

DESIGN OF HYBRID PLASMONIC NANOSTRUCTURES FOR ENHANCED PHOTOCATALYTIC ACTIVITY

GAGANDEEP KAUR

A thesis submitted for the partial fulfillment of

the degree of Doctor of Philosophy



Institute of Nano Science and Technology

Sector-81, Knowledge City, Sahibzada Ajit Singh Nagar, Punjab, 140306

Indian Institute of Science Education and Research Mohali

Knowledge City, Sector 81, SAS Nagar, Manauli PO, Mohali 140306, Punjab, India.

June 2023

*Dedicated to my
Beloved Family*

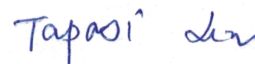
DECLARATION

The work presented in the thesis “Design of hybrid plasmonic nanostructures for enhanced photocatalytic activity” has been carried out by me under the guidance of Dr. Tapasi Sen at the Institute of Nano Science and Technology Mohali. This work has not been submitted in part or in full for a degree, a diploma, or a fellowship to any other university or institute. Whenever contributions of others are involved, every effort is made to indicate this clearly, with due acknowledgement of collaborative research and discussions. This thesis is a bonafide record of original work done by me and all sources listed within have been detailed in the bibliography.



GAGANDEEP KAUR

In my capacity as the supervisor of the candidate's thesis work, I certify that the above statements by the candidate are true to the best of my knowledge.



Dr. TAPASI SEN

ACKNOWLEDGEMENTS

Writing a thesis is a significant achievement and requires an immense amount of hard work, dedication, and support. I am deeply grateful for the Almighty and people who helped me reach this milestone.

To begin, I would like to show gratitude and thanks to God, the Almighty, who has provided me with countless resources, opportunities, and insights that have helped me finish this thesis.

My gratitude extends to **Dr. Tapasi Sen**, my mentor at INST Mohali, for having faith in my research abilities and providing me with the amazing opportunity to investigate the fascinating field of plasmonic nanomaterials. She has been a constant source of wisdom and encouragement. I couldn't have finished my thesis without her insightful suggestions, technical knowledge, and support. Her vast scientific expertise and boundless curiosity have served as an inspiration to me. She let me do whatever scientific research I wanted and helped me out whenever I hit a snag. I consider myself very fortunate to have such a mentor who has provided me with wonderful experience over the past five years.

I would like to express my gratitude to the Institute of Nano Science and Technology for enabling me to conduct successful research by providing a pleasant working environment, excellent facilities, and useful resources. I would also like to thank IISER Mohali for providing the facility with the necessary infrastructure.

I wish to express my heartfelt gratitude to the director of INST **Prof. Amitava Patra**, and **Prof. H. N Ghosh** who gave me the opportunity to be a part of this prestigious institute and then for all the motivation, support and facilities provided during my PhD tenure. I'd also like to express my respect and appreciation to my doctoral committee members, **Dr. Debabrata Patra** and **Dr. Prakash P. Neelakandan**, for their insightful comments and unwavering encouragement throughout the course of my research. I'd also like to give props to **Dr. Sangeeta Saini** (Kurukshetra university), conducting a simulation study that corroborated our results. My special words of thank towards our collaborators **Dr. Krishna Kanta Halder** (Central University Punjab) and **Dr. Asifkhan Shanavas** (INST

Mohali) for their dedication to our research projects and their positive, supportive, and inspiring attitudes throughout the work.

I also express my sincere thanks to my lab seniors **Dr. Swati Tanwar**, and **Ms. Vishaldeep Kaur**. The time and energy they put into instructing me in synthesis, instrument handling and data analysis is priceless. I also want to thank my juniors **Ms. Charanleen Kaur**, **Ms. Shikha Rai**, **Ms. Mridu Sharma**, and **Ms. Priyanka Singhmar** who helped me a lot in the lab during my work.

There's a lot I owe to my wonderful grandparents, **Mr. Jarnail Singh**, **Mrs. Surjit Kaur** **Late Mr. Baldev Singh**, and **Mrs. Amarjit Kaur**. Their selflessness and blessings have made it possible for me to have a prosperous future. I owe hugely to my dear parents, **Mr. Baljeet Singh** and **Mrs. Karamjeet Kaur**. Their permanent love and confidence in me have encouraged me to go ahead in my study and career. They always inspire me to aim high and go after my goals, so I'm eternally grateful. I learned the value of commitment, self-control, sacrifice, tolerance, and perseverance from them. I never would have considered pursuing a doctoral degree without their support. I'd also like to express my deepest love to my brothers **Mr. Manpreet Singh** and **Mr. Akashdeep Singh** for always being there for me, providing emotional support and strength to tackle any obstacle on my way. They always teach me to keep my feet on the ground even as I aim for the stars. I am eternally grateful to my sister-in-law **Mrs. Mandeep Kaur** who has been there for me and helped me out more than any older sister could have. The utmost love to my adorable little nephew **Sehraab** for his little and stress relieving talks with me during tough days of my PhD time and making me laugh. I wish to express my gratitude to my uncle **Mr. Baljinder Singh** and aunt **Mrs. Paramjeet Kaur** for immense love and support. I would like to thank my cousins for having fun during family gatherings and functions in last 5 years which has been a great way to relieve stress. My deepest appreciation goes out to my relatives, who have helped me in many ways during this journey.

Without the unflinching backing of my friends, I never would have been able to complete this endeavor. My heartfelt generosity goes to **Ashish**, who was there for me through

thick and thin, always providing a listening ear and a comforting word when I needed it the most. I would like to say thanks to **Bandana** and **Mahima** for being there for me emotionally and helping me deal with the stress. It was pleasant when we all went our separate ways during our PhD studies, but we all came together to help one another through the tough times. **Sonali** and **Mamta**, my extraordinary friends, made my time as a doctoral student much more rewarding. During the darkest points of my research journey, their support, laughter, and friendship were the only things that kept me going. I would like to acknowledge my batchmates and friends **Dr. Navpreet**, **Dr. Rakesh**, **Chirag**, **Dr. Kamaljit**, **Arpna**, **Neethu**, **Ridhima**, **Dr. Ajit**, and **Sourav** for their support, love and motivational talks. My school friends **Jagdeep**, **Arshveer**, **Simran** deserve a special thank for providing strength, motivation, push to keep moving forward. My B.Sc. and M.Sc. friends **Jasveer**, **Navneet**, earn deep gratitude for having motivational messages, long and relaxing talks over the phone during off days.

I also want to thank all Administrative staff, Technical, Non-teaching staff and Security staff of INST Mohali for their valuable contribution towards the completion of my PhD. Special thank to **Butta Singh Ji** for serving tea during my yearly evaluations and **Vikram Singh** for providing delicious food in the INST mess back when we were at the old campus.

At last, I would like to thank **Col. Mohan Singh Ghuman** and **Mrs. Gurdish Kaur**, my landlords, who went above and beyond to ensure my comfort and all the help they've given me is greatly appreciated.

I also would also like to extend my gratitude to the many others who, whether directly or indirectly, have helped make this journey a success.

GAGANDEEP KAUR

TABLE OF CONTENTS

Contents	Page No.
List of Figures	I
List of Schemes	IX
List of Tables	XI
Abbreviations	XIII
Nomenclature	XV
Abstract	XVII
 Chapter 1: Introduction	
1.1 Plasmonic nanomaterials	3
1.2 Metal nanoparticles	4
1.3 Optical properties of plasmonic metal nanoparticles	4
1.3.1 The emergence of surface plasmon resonance	5
1.3.2 Effect of size, shape, and surrounding environment on optical properties	8
1.3.3 Optical properties of plasmonic metal nanoshells	12
1.3.4 Optical properties of plasmonic bimetallic core-shell nanoparticles	14
1.3.5 Optical properties of hybrid plasmonic metal-semiconductor core-shell nanostructures	15
1.4 Interaction of light with plasmonic metal nanoparticles	16
1.4.1 Radiative plasmon decay	17
1.4.2 Non- radiative plasmon decay	19
1.5 Fabrication of assembled plasmonic metal nanoparticles	21
1.5.1 Assembly of plasmonic metal nanostructures on DNA origami	22
1.6 Applications of plasmonic nanoparticles	24
1.6.1 Plasmon induced photocatalysis	25
1.6.2 SERS as a monitoring tool for plasmonic photocatalysis	27
1.6.2.1 Surface-enhanced Raman spectroscopy (SERS)	27
1.6.2.1.1 Mechanisms of SERS	28
1.6.2.1.1.1 Electromagnetic enhancement (EM) and enhancement factor (EF) in SERS	29
1.6.2.1.1.2 Chemical enhancement (CE) in SERS	31
1.6.2.2 SERS substrates for plasmonic photocatalysis	33
1.6.2.3 SERS for small molecules detection	35
1.6.3 Photothermal therapy	37
1.6.4 Photochemical water splitting	40
1.6.5 Electrocatalysis	42
References	45

Chapter 2: Methodology & Instrumentation

2.1	Synthesis of Au nanoparticles	55
2.1.1	Synthesis of anisotropic-shaped nanostructures	55
2.1.1.1	Seeds mediated approach for synthesis of anisotropic shaped Au nanoparticles	56
2.1.2	Synthesis of bimetallic nanoparticles	57
2.1.3	Synthesis of metallic nanoshells	58
2.1.4	Synthesis of hybrid metal-semiconductor nanostructures	60
2.2	Synthesis of rectangular DNA origami	61
2.3	Fabrication of DNA origami assembled plasmonic nanoparticles	62
2.4	Characterization techniques	63
2.4.1	UV-Vis spectroscopy	63
2.4.2	Dynamic light scattering (DLS) and zeta potential study	64
2.4.3	Powder X-ray diffraction (XRD)	67
2.4.4	Fourier transform infrared (FTIR) spectroscopy	68
2.4.5	Raman spectroscopy	69
2.4.6	Atomic force microscopy (AFM)	72
2.4.7	Transmission electron microscopy (TEM)	73
2.4.7.1	HAADF-STEM (high-angle annular dark-field scanning transmission electron microscopy)	75
2.4.8	X-ray Photoelectron spectroscopy (XPS)	76
2.4.9	Electrochemical studies	78
2.4.9.1	Electrode configuration: Three electrode setup	78
2.4.9.2	Electrochemical techniques	79
2.4.9.2.1	Linear and cyclic sweep voltammetry	79
2.4.9.2.2	Electrochemical impedance spectroscopy (EIS)	79
2.4.9.2.3	Stability	80
	References	81

Chapter 3: Interfacial design of gold/silver core-shell nanostars for plasmon-enhanced photocatalytic coupling of 4-aminothiophenol

3.1	Introduction	85
3.2	Experimental section	88
3.2.1	Materials	88
3.2.2	Experimental procedures	88
3.2.2.1	Synthesis of silver coated gold nanostars (Au/Ag nanostars)	88
3.2.2.2	Catalysis of PATP to p,p'-Dimercaptoazobisbenzene (DMAB)	89
3.2.2.3	pH dependent studies	89
3.2.2.4	Time-dependent studies	89
3.2.2.5	Raman measurements	90
3.2.2.6	FDTD (finite difference time domain) simulation	90

3.3	Results and discussion	90
3.3.1	Optical and structural characterizations of Au/Ag NSs	90
3.3.2	SERS measurements	97
3.3.2.1	Au/Ag NSs as SERS substrate and photocatalyst for conversion reaction	97
3.3.2.2	Effect of thickness of Ag coating on SERS spectra of DMAB	101
3.3.2.3	Effect of pure metal counter parts on SERS spectra of DMAB	104
3.3.2.4	Effect of nanostructure morphology on SERS spectra of DMAB	107
3.3.2.5	Effect of incubation time on SERS spectra of DMAB	108
3.3.2.6	Effect of excitation laser wavelength on SERS spectra of DMAB	110
3.3.3	FDTD simulation study	110
3.3.4	Insight into the catalytic conversion of PATP to DMAB using Au/Ag NSs	111
3.4	Conclusion	115
	References	116

Chapter 4: Design of silica@Au hybrid nanostars for enhanced SERS and photothermal effect

4.1	Introduction	121
4.2	Experimental section	123
4.2.1	Materials	123
4.2.2	Experimental procedures	123
4.2.2.1	Synthesis of spherical core-shell SiO ₂ @Au NPs	123
4.2.2.1.1	Preparation of silica nanoparticles (SiO ₂ -NPs)	123
4.2.2.1.2	Preparation of aminated silica nanoparticles (SiO ₂ -NH ₂ NPs)	124
4.2.2.1.3	Synthesis of THPC Au NPs suspension	124
4.2.2.1.4	Synthesis of Au plating solution	124
4.2.2.2	Synthesis of SiO ₂ @Au NSs	125
4.2.2.3	Raman measurements	126
4.2.2.4	Photothermal transduction efficiency (η) studies	126
4.2.2.5	Hemocompatibility studies	127
4.2.2.6	In vitro studies	127
4.2.2.7	In vitro biocompatibility	127
4.2.2.8	In vitro photothermal therapy	128
4.2.2.9	Cellular uptake study	128
4.2.2.10	Cell morphology analysis	129
4.3	Results and discussion	129
4.3.1	Optical and structural characterizations of SiO ₂ @Au NSs	129
4.3.2	SERS performance of SiO ₂ @Au NSs	134
4.3.2.1	Effect of laser wavelength on SERS performance of	136

	SiO ₂ @Au NSs	
4.3.3	Photothermal efficiency of SiO ₂ @Au NSs	137
4.3.4	In vitro studies	139
4.4	Plausible mechanism of photothermal effect of SiO ₂ @Au NSs	142
4.5	Conclusion	143
	References	144

Chapter 5: Design of plasmonic - semiconductor hybrid nanostructures for photochemical water splitting

5.1	Introduction	149
5.2	Experimental section	151
5.2.1	Materials	151
5.2.2	Experimental procedures	151
	5.2.2.1 Synthesis of Au nanostars	151
	5.2.2.2 Synthesis of Au@ZnO NCs	151
	5.2.2.3 Photocatalytic water splitting experiments	152
5.3	Results and discussion	153
5.3.1	Optical and structural characterizations of Au@ZnO NCs	153
5.3.2	Photocatalytic water splitting	158
	5.3.2.1 Au@ZnO NCs as photocatalyst for H ₂ and O ₂ evolution reactions	158
	5.3.2.2 Recycling tests of catalyst Au@ZnO NCs for H ₂ and O ₂ production activity	159
5.3.3	Plausible mechanism for the photocatalytic water splitting	159
5.4	Conclusion	161
	References	162

Chapter 6: DNA origami-templated bimetallic core-shell nanostructures for enhanced OER

6.1	Introduction	167
6.2	Experimental section	169
6.2.1	Materials	169
6.2.2	Experimental procedures	170
	6.2.2.1 Synthesis of Au nanostars and Au nanostars coated with Ag layer (Au@Ag nanostars)	170
	6.2.2.2 Synthesis of rectangular DNA Origami	170
	6.2.2.3 Synthesis of ss-DNA functionalized Coated Au@Ag nanostars	170
	6.2.2.4 Synthesis of DNA origami templated Au@Ag nanostars assemblies	171
	6.2.2.5 Preparation of TEM samples	171
	6.2.2.6 Preparation of AFM samples	172

6.2.2.7	Electrochemical measurements	172
6.3	Results and discussion	173
6.3.1	Structural and optical characterizations of DNA origami templated Au@Ag nanostars	173
6.3.2	Electrochemical OER performance	179
6.3.2.1	Stability studies	186
6.3.2.2	Effect of OER on morphology of Au@Ag nanostars	188
6.3.2.3	Most possessable mechanistic pathway for OER activity	189
6.4	Conclusion	189
	References	191

Chapter 7: Conclusions

7.1	Summary of the work	197
7.2	Scope for the future work	200

Appendix A	201
Publications	213
Conference presentations	215
Vita	217

LIST OF FIGURES

Chapter 1: Introduction

Figure No.		Page No.
Figure 1.1	Photograph showing the colors of Au nanoparticles for different particle sizes in aqueous solution	5
Figure 1.2	Schematic depiction of localized surface plasmon oscillation for a sphere metal nanoparticle, showing the displacement of the conduction electrons cloud relative to the nuclei	6
Figure 1.3	Normalized UV-vis extinction spectra of Au nanoparticles (blue curve), and Ag nanoparticles (red curve).	6
Figure 1.4	UV-Vis extinction spectra of spherical Au nanoparticles of different size range from 30 nm to 100 nm	9
Figure 1.5	(a) Schematic depiction of SPR excitation for Au nanorods along and perpendicular to long, (b) Normalized extinction spectra of Au nanorods with different aspect ratios, and (c) corresponding digital image of Au nanorods	10
Figure 1.6	(a) Diagrammatic depiction of the concept of plasmon hybridization of core and tip plasmons in the nanostar, (b) Normalized UV-Vis-NIR spectra of different sized Au nanostars having different positions of LSPRs, and (c) corresponding digital image of Au nanostars	12
Figure 1.7	UV-Vis-NIR spectra of metal nanoshells (silica core, Au shell) calculated theoretically over a range of core radius/shell thickness ratios	13
Figure 1.8	(a) Diagrammatic illustration of a nanoshell as the fusion of a sphere and a cavity, (b) An energy-level diagram of hybridization of sphere and cavity plasmons resulting in antibonding (ω_+) and bonding (ω_-) plasmon modes, and (c) energy level diagram for the effect of shell thickness on the plasmon interaction	14
Figure 1.9	UV-visible extinction spectra of a physical mixture of the same amount of Ag nanoparticles and Au nanoparticles, and spherical core-shell Au-Ag bimetallic nanoparticles	15
Figure 1.10	UV-vis spectra of Ag and Ag@SnO ₂ metal semiconductor core shell nanoparticles	16
Figure 1.11	A diagrammatic representation of the mechanisms of plasmon enhancement, radiative effects: (a) far-field scattering, and (b) near-field coupling, and non-radiative effects: (c) hot electron transfer, and (d) plasmon induced resonant energy transfer	17

Figure 1.12	Distributions of simulated electric fields for (a) nanospheres, (b) nanorods, (c) nanotriangles, (d) nanocubes, (e) nanotripods, and (f) nanostars, when exposed to incident light	19
Figure 1.13	Energy band diagram of transfer of hot electrons from plasmonic metal nanoparticle to a) conduction band of semiconductor, and (b) LUMO of adsorbed molecule	20
Figure 1.14	The two-dimensional DNA origami nano scale structures. (a) A rectangle, (b) a star, (c) a disk with three holes, and (d) a triangle	23
Figure 1.15	(a) DNA origami assembled Au nanoparticle dimers (Reprinted with permission from ref.108, 2014 American Chemical Society), and (b) Bowtie nanoantenna on DNA origami	24
Figure 1.16	Diagrammatic illustration of plasmonic nanoparticle applications	25
Figure 1.17	Schematic representation of (a) activation of metal oxide support for catalysis via electron transfer during plasmonic metal nanoparticle excitation, (b) non-plasmonic metal nanoparticle acting as a catalyst on illuminated plasmonic metal nanoparticle support, and (c) plasmonic metal nanoparticle itself acting as a catalyst on illumination with a light source	26
Figure 1.18	Schematic demonstration of (a) H ₂ dissociation on the Au nanoparticle surface, and hot electron excitation in Au nanoparticle on light illumination along with transfer of hot electron to antibonding orbital of adsorbed H ₂ molecule, and (b) electrons generated by plasmon activation in Ag nanocubes exposed to visible light utilized to hydrogenate carbonyls.	27
Figure 1.19	A simplified representation of electromagnetic and chemical enhancements in SERS	29
Figure 1.20	Mechanistic illustration of basic EM SERS. The AuNP (1) strengthens both the incident laser field (a) and the scattered field (b), significantly increasing the intensity of scattered Raman signal from a neighboring molecule	30
Figure 1.21	EM enhancement contours of (a) a nanosphere, (b) a nanotriangle, (c) a nanorod in logarithmic scale, and (d) EELS intensity map of a nanostar	31
Figure 1.22	Schematic description of the three contributors to CE mechanism	33
Figure 1.23	(a) The time-dependent SERS of DMAB at molecular concentration, M, and (b) Transformation of PATP adsorbed on Ag electrode to DMAB during electrochemical SERS measurement and corresponding SERS spectra	34

Figure 1.24	(a) Illustration of the plasmon-driven decarboxylation of 4-MBA to TP, (b) SERS spectra collected before 4-MBA decarboxylation, and (c) SERS spectra collected after decarboxylation of 4-MBA into TP	35
Figure 1.25	Representation of Au nanoflowers utilized for the SERS enhancement of Raman signals of rhodamine 6G dye	36
Figure 1.26	SERS spectra of TR dye bound to Au nanostar dimers assembled on DNA origami with average gaps of 7 nm (i) and 13 nm (ii)), and TR dye bound to Au nanostar monomer on DNA origami (iii) and bulk TR dye (iv)	37
Figure 1.27	(a) Schematic representation of photothermal effect by plasmonic metal nanostructures, and (b) PTT is represented by irradiating plasmonic nanoparticles with NIR light to generate heat and kill the surrounding tumor tissue	38
Figure 1.28	The four most common AuNP shapes for PTT are silica/Au core – shell nanostructures, Au nanorods, hollow Au nanocages, and Au nanostars	40
Figure 1.29	Photocurrent curves of Au@ZnO core–shell nanostructures and pure ZnO nanoparticles at an applied potential of 0.5 V vs. Ag/AgCl under simulated sunlight irradiation during on/off cycles within 300 s	41
Figure 1.30	Polarization curves for HER and OER	43
Figure 1.31	Linear sweep polarization curves performed for Au@Co ₃ O ₄ , Co ₃ O ₄ , and Au nanocrystals	44

Chapter 2: Methodology & Instrumentation

Figure No.		Page No.
Figure 2.1	Depiction of UV-Vis spectrophotometer set up	63
Figure 2.2	Transitions on an electronic level between bonding and anti-bonding states	64
Figure 2.3	Illustration of the Dynamic Light Scattering apparatus	65
Figure 2.4	Schematic representation of zeta potential	66
Figure 2.5	Bragg's law of diffraction	68
Figure 2.6	Three different ways of re-emitting incident light	69
Figure 2.7	Energy level diagram indicating the transitions involved in Raman scattering	70
Figure 2.8	Schematic depiction of Raman spectrometer	71
Figure 2.9	Depiction of an atomic force microscope	72
Figure 2.10	Diagrammatic representation of a transmission electron microscope	74
Figure 2.11	Schematic representation of ray diagram of HAADF	76
Figure 2.12	The fundamental parts of a monochromatic XPS setup	78

Chapter 3: Interfacial design of gold/silver core-shell nanostars for plasmon-enhanced photocatalytic coupling of 4-aminothiophenol

Figure No.		Page No.
Figure 3.1	UV-Vis extinction spectra of as synthesized (a) Au nanostars, and (b) Au/Ag nanostars	91
Figure 3.2	TEM images of (a, b) Au NSs and (c, d) Au/Ag NSs	92
Figure 3.3	TEM images of Au/Ag nanostars (a) wide view, (b) single Au/Ag NSs, and (c) the corresponding inverted TEM image, respectively	92
Figure 3.4	High resolution TEM images of Au/Ag NS showing the thickness of Ag over the preformed Au NSs	93
Figure 3.5	HRTEM images of (a) single Au/Ag NSs, and (b) and (c) IFFT of marked area x and y of picture (a); (d) HAADF-STEM image, and (e, f) elemental mapping of Au/Ag nanostars	94
Figure 3.6	TEM-EDX (Energy dispersive X-ray) spectrum of Au/Ag NSs	95
Figure 3.7	(a) UV-Vis extinction spectra of as synthesized Au/Ag nanostars under acidic and basic conditions. TEM images of Au/Ag nanostars under (b) basic, and (c) acidic pH. Insets: High resolution images of Au/Ag nanostars	95
Figure 3.8	XPS spectra of Au/Ag NSs: (a) Ag 3d, and (b) Au 4f	96
Figure 3.9	Normal Raman spectrum of solid PATP	97
Figure 3.10	(a) Concentration dependent SERS spectra of DMAB formed from PATP at different concentrations of Au/Ag NSs under neutral conditions and, (b) Time dependent SERS spectra of DMAB formed from PATP at 36 pM concentration of Au/Ag NSs	98
Figure 3.11	(a) Concentration dependent SERS spectra of DMAB formed from PATP at different concentrations of Au/Ag NSs under basic conditions and, (b) Time dependent SERS spectra of DMAB formed from PATP at 9 pM concentration of Au/Ag NSs	99
Figure 3.12	Concentration dependent SERS spectra of DMAB formed from PATP at different concentrations of Au/Ag nanostars under acidic conditions	100
Figure 3.13	TEM images of Au/Ag NSs after catalytic reaction of PATP to DMAB	101
Figure 3.14	UV-Vis extinction spectra and TEM images of Au/Ag NSs with lower Ag coating (a, b) and with higher Ag coating (c, d)	102
Figure 3.15	Time dependent SERS spectra of DMAB formed from PATP at 36 pM concentration of Au/Ag NSs with a) lower Ag coating (1.9 ± 0.5 nm), b) moderate Ag coating (3.5 ± 0.5 nm), and c) higher Ag coating (7 ± 0.5 nm)	103

Figure 3.16	SERS spectra of DMAB formed from PATP at incubation time of 512s using 45 pM concentration of Au NS (a), and Au/Ag NSs (a'); 63 pM concentration of Au NS (b), and Au/Ag NSs (b'); 81 pM concentration of Au NS (c), and Au/Ag NSs (c'); and 180 pM concentration of Au NS (d), and Au/Ag NSs (d').	105
Figure 3.17	a) Normalized UV-Vis extinction spectrum, and b) TEM image of as prepared Ag NSs	106
Figure 3.18	SERS spectra of DMAB formed from PATP at incubation time of 512s using different concentrations of a) Au/Ag NSs, and b) Ag NSs	106
Figure 3.19	a) UV-Vis extinction spectrum b) TEM image of as prepared spherical Au nanoparticles	107
Figure 3.20	SERS spectra of DMAB formed from PATP using spherical Au NPs at 45 pM (a), 63 pM (b), 81 pM (c), 180 pM (d) concentration at incubation time 512s	108
Figure 3.21	SERS spectra of DMAB formed from PATP at 180pM concentration of Au/Ag NSs at a) zero second incubation time and b) 512 seconds incubation time	109
Figure 3.22	SERS spectra of DMAB formed from PATP at 180pM concentration of Au NSs at a) zero second incubation time and b) 512 seconds incubation time	109
Figure 3.23	SERS spectra of DMAB formed from PATP at incubation time of 512s using different concentrations of Au NSs at a) 532 nm laser, and b) 633 nm laser	110
Figure 3.24	The magnitude of electric field $ E $ in xy plane passing through the centre of nanostar at $\lambda=540$ nm for (a) Au-nanostar (b) silver coated Au-nanostar. A plane wave source has been used for FDTD calculations. The incident wave-vector is perpendicular to plotted xy cross-section. Note the difference in color-coding scale for both plots	111
Figure 3.25	(a) SERS spectra measured under neutral conditions at concentration 6 pM in inert atmosphere. Raman spectrum of (b) Au/Ag NSs, (c) mixture of PATP and NaCl, and, (d) mixture of Au/Ag NSs and NaCl	112
Figure 3.26	ATR-FTIR spectra of (a) PATP and (b) DMAB formed from PATP in presence of Au/Ag NSs	114

Chapter 4: Design of silica@Au hybrid nanostars for enhanced SERS and photothermal effect

Figure No.		Page No.
Figure 4.1	(a) Dynamic light scattering spectra of SiO ₂ and SiO ₂ -NH ₂ NPs, (b) XRD pattern of SiO ₂ NPs, (c) Zeta potential, (d) Fourier-transform infrared spectra (FTIR) of SiO ₂ and SiO ₂ -NH ₂ NPs, and (e, f) TEM images of SiO ₂ NPs	130
Figure 4.2	(a) UV-Vis extinction spectra of THPC Au NPs suspension, Au NPs decorated on SiO ₂ NPs and SiO ₂ @Au NPs, (b) XRD pattern of SiO ₂ @Au NPs, (c) DLS spectrum of THPC Au NPs suspension, (d) DLS spectra Au NPs decorated on SiO ₂ NPs and SiO ₂ @Au NPs, and (e, f) TEM images of Au NPs decorated on SiO ₂ NPs	132
Figure 4.3	(a) UV- Vis-NIR spectrum of SiO ₂ @Au NSs, (b) Low resolution TEM images of SiO ₂ @Au NSs, and (c) TEM image of single SiO ₂ @Au NS.	133
Figure 4.4	(a) HAADF-STEM image, (b,c) elemental mapping, (d) Line scan analysis of SiO ₂ @Au NS, and (e) EDX spectrum of SiO ₂ @Au NSs	134
Figure 4.5	(a) Raman spectrum of RhB dye, and (b) SERS spectrum of 100μM RhB dye in SiO ₂ @Au NSs using 785 nm laser	135
Figure 4.6	(a) Raman spectrum of RhB dye, and (b) SERS spectrum of 100μM RhB dye in SiO ₂ @Au NSs using 633 nm laser	137
Figure 4.7	(a) Heating curves of various concentrations of SiO ₂ @Au NSs under laser irradiation and, (b) Photostability of SiO ₂ @Au NSs under three cycles of laser irradiation	137
Figure 4.8	(a) Biocompatibility of SiO ₂ @Au NSs with L929 cells, and (b) Hemocompatibility of SiO ₂ @Au NSs	139
Figure 4.9	Cytotoxicity of SiO ₂ @Au NSs (a) at varying concentrations with and without 5 min of laser irradiation, (b) at varying concentrations with laser irradiation for 10 min, (c) cell viability at different laser irradiation time (conc.200 μg/mL), and (d) time dependent cellular uptake of SiO ₂ @Au NSs	140
Figure 4.10	Confocal microscopic images of (i) untreated, (ii) SiO ₂ @Au NSs treated L929 cells (a), and (i) untreated, (ii) SiO ₂ @Au NSs, (iii) SiO ₂ @Au NSs + laser treated MDA-MB-231 cells (b).	141

Chapter 5: Design of plasmonic - semiconductor hybrid nanostructures for photochemical water splitting

Figure No.		Page No.
Figure 5.1	Normalized UV-vis extinction spectra of Au nanostars (black), ZnO nanoparticles (red), and Au@ZnO NCs (blue)	153
Figure 5.2	Powder XRD pattern of Au@ZnO NCs	154
Figure 5.3	(a) wide XPS survey spectrum of Au@ZnO NCs, High resolution XPS spectra of (b) Au 4f, Zn 3p, (c) Zn 2p, and (d) O 1s elements present in Au@ZnO NCs	155
Figure 5.4	(a-b) TEM images of Au/ZnO core shell nanostructures, (c) HRTEM image of Au/ZnO, and (d) Zoom in image showing the inter planer d spacing of marked area in (c)	156
Figure 5.5	EDX spectrum of Au@ZnO NCs	157
Figure 5.6	(a) HAADF-STEM image of single Au@ZnO NC and corresponding EDX elemental mapping of Au (b), Zn (c), and O (d)	157
Figure 5.7	(a) Time-dependent photocatalytic hydrogen and oxygen gas production profiles of Au@ZnO NCs (Error bars indicate standard deviation for three measurements), and (b) Impedance spectrum of Au@ZnO NCs	158
Figure 5.8	Stability of Au@ZnO NCs for photocatalytic H ₂ (a), and O ₂ gas production (b) for five cycles	159
Figure 5.9	(a) Tauc plot indicating optical band gap, (b) UPS spectrum indicating work function, and XPS valence band spectrum indicating position of VB from E _f of catalyst Au@ZnO NC.	160
Figure 5.10	Schematic diagram of band alignments in Au@ZnO NC and mechanism of photo-generated charge separation for (a) H ₂ evolution reaction, and (b) O ₂ evolution reaction	161

Chapter 6: DNA origami-templated bimetallic core-shell nanostructures for enhanced OER

Figure No.		Page No.
Figure 6.1	(a, b) AFM images of rectangular DNA origami, (c) corresponding height profile, and (d, e) TEM images of rectangular DNA origami	174
Figure 6.2	UV-vis extinction spectra of Au nanostars and Au@Ag nanostars (the inset shows digital images of nanostar solutions)	175
Figure 6.3	TEM images of Au nanostars (a and b), and Au@Ag nanostars (c and d)	176
Figure 6.4	(a) HAADF-STEM image, and (b, c) the elemental	177

	mapping images of Au@Ag nanostars	
Figure 6.5	Energy Dispersive X-Ray (EDX) spectrum of Au@Ag nanostars	177
Figure 6.6	UV-Vis extinction spectra of Au@Ag nanostars before and after ss-DNA functionalization	178
Figure 6.7	(a) AFM images of DNA origami-templated Au@Ag nanostar assemblies (the inset shows the corresponding height profile) and (b and c) TEM images of DNA origami-templated Au@Ag nanostar assemblies	179
Figure 6.8	(a) Polarization curves (LSV) and (b) corresponding Tafel plots of Au nanostars, IrO ₂ , Au@Ag nanostars, ss-DNA-functionalized Au@Ag nanostars, and DNA origami-templated Au@Ag nanostars. (c) Electrochemical impedance spectra of the catalysts recorded at 350 mV (Ag/AgCl)	180
Figure 6.9	(a) polarization curves (LSV), and (b) corresponding Tafel plots of DNA origami templated Au nanostars, ss-DNA functionalized Au nanostars and Au nanostars, respectively. (c) Electrochemical impedance spectra of the catalysts at 350 mV (Ag/AgCl)	181
Figure 6.10	(a-b) Cyclic voltammetry curves and (d-e) plot of anodic current density (J_a) and cathodic current density (J_c) against scan rate for the determination of double layer capacitance (C_{dl}) of DNA origami templated Au@Ag nanostars, ss-DNA functionalized Au@Ag nanostars and Au@Ag nanostars, respectively	183
Figure 6.11	(a-b) Cyclic voltammetry curves and (d-e) plot of anodic current density (J_a) and cathodic current density (J_c) against scan rate for the determination of double layer capacitance (C_{dl}) of DNA origami templated Au nanostars, ss-DNA functionalized Au nanostars and Au nanostars, respectively	184
Figure 6.12	Stability test: LSV curves of DNA origami-templated Au@Ag nanostars of first and 2500th cycles of continuous operation	187
Figure 6.13	Chronoamperometry study of (a) Au@Ag nanostars (using binder) at an overpotential of 309 mV for 15 h, (b) DNA origami templated Au@Ag nanostars at an overpotential of 266 mV for 15 h, and (c) Chronopotentiometric study of DNA origami templated Au@Ag nanostars for OER activity in 1.0 M KOH as a function of current density (20-100 mA/cm ²)	188
Figure 6.14	TEM images of DNA origami templated Au@Ag nanostars after chronoamperometry stability	188

LIST OF SCHEMES

Chapter 2: Methodology & Instrumentation

Scheme No.		Page No.
Scheme 2.1	Schematic illustration of seed-mediated synthesis of Au nanostars	57
Scheme 2.2	Schematic depiction for synthesis of Ag coated Au nanorod	58
Scheme 2.3	Schematic illustration of synthesis of silica-Au nanoshells	59
Scheme 2.4	Schematic representation of synthesis hybrid metal-semiconductor nanostructures	61
Scheme 2.5	Schematic representation of fabrication of rectangular DNA origami	61
Scheme 2.6	Schematic representation of immobilization of Au nanoparticle on DNA origami	62

Chapter 3: Interfacial design of gold/silver core-shell nanostars for plasmon-enhanced photocatalytic coupling of 4-aminothiophenol

Scheme No.		Page No.
Scheme 3.1	Schematic depiction of the synthesis of Ag coated Au nanostar	89
Scheme 3.2	Schematic depiction of the catalytic conversion of PATP into DMAB using Au/Ag nanostars	89
Scheme 3.3	Schematic illustration for the reaction mechanism depicting the oxidation of PATP into DMAB	113

Chapter 4: Design of silica@Au hybrid nanostars for enhanced SERS and photothermal effect

Scheme No.		Page No.
Scheme 4.1	Schematic depiction of synthesis of SiO ₂ @Au NSs	125
Scheme 4.2	Schematic for the mechanism of the photothermal effect of SiO ₂ @Au NSs to kill cancer cells on laser illumination	142

Chapter 5: Design of plasmonic - semiconductor hybrid nanostructures for photochemical water splitting

Scheme No.		Page No.
Scheme 5.1	Schematic depiction for synthesis of Au@ZnO NCs	152

Chapter 6: DNA origami-templated bimetallic core-shell nanostructures for enhanced OER

Scheme No.		Page No.
Scheme 6.1	Schematic illustration for the synthesis of ss-DNA functionalized Au@Ag nanostars	171
Scheme 6.2	Schematic illustration for the synthesis of DNA origami templated Au@Ag nanostar assemblies	171

LIST OF TABLES

Chapter 3: Interfacial design of gold/silver core-shell nanostars for plasmon-enhanced photocatalytic coupling of 4-aminothiophenol

Table No.		Page No.
Table 3.1	ICP-MS (Inductively coupled plasma mass spectrometry) of Au/Ag nanostars	97
Table 3.2	The atomic percentage of Au and Ag in Au/Ag NSs from TEM- Energy dispersive X-ray (EDX) analysis	103
Table 3.3	ATR-FTIR frequency data (cm ⁻¹) of PATP and DMAB	114

Chapter 4: Design of silica@Au hybrid nanostars for enhanced SERS and photothermal effect

Table No.		Page No.
Table 4.1	Enhancement factor comparison with literature	136
Table 4.2	Photothermal Transduction Efficiency (η) comparison with literature	138

Chapter 6: DNA origami-templated bimetallic core-shell nanostructures for enhanced OER

Table No.		Page No.
Table 6.1	Summary of electrochemical OER performance of Au nanostars, Au@Ag nanostars, and ss-DNA functionalized Au@Ag nanostars, and DNA origami templated Au@Ag nanostars catalysts in 1 M KOH	185
Table 6.2	Comparison of OER activity of as synthesized DNA origami templated Au@Ag nanostars with some reported Au or Ag or DNA based catalysts	186

ABBREVIATIONS

AFM	Atomic Force Microscopy
DNA	Deoxyribonucleic acid
EIS	Electrochemical Impedance Spectroscopy
EDX	Energy Dispersive X-ray spectroscopy
EF	Enhancement factor
FT-IR	Fourier Transform Infrared
GCE	Glassy Carbon Electrode
HRTEM	High-resolution Transmission Electron Microscopy
IBM	International Business Machines
LSPR	Localized Surface Plasmon Resonance
LSV	Linear Sweep Voltammetry
NPs	Nanoparticles
NSs	Nanostars
OER	Oxygen Evolution Reaction
PXRD	Powder X-ray Diffraction
pH	The negative logarithm of hydronium-ion concentration ($-\log_{10} [\text{H}_3\text{O}^+]$)
RHE	Reversible Hydrogen Electrode
SERS	Surface Enhanced Raman Spectroscopy
SEM	Scanning Electron Microscopy
SPR	Surface Plasmon Resonance
STM	Scanning Tunneling Microscope
TEM	Transmission Electron Microscopy
UV-Vis	UV-Visible Spectroscopy

NOMENCLATURE

mV	Milli Volt
λ	Wavelength
α	Alpha
σ	Sigma
\AA	Angstrom
π	Pi
ε	Extinction coefficient
θ	Theta
Hz	Hertz
$^{\circ}\text{C}$	Degree Centigrade
η	Overpotential
mg	Milligram
mA	Milli Ampere
F	Faraday Constant
pM	Picomolar
nM	Nanomolar
μM	Micromolar
mM	Millimolar
q	Charge
μL	microlitre
mL	Millilitre
nm	Nanometer
μm	Micrometer

ABSTRACT

The utilization of gold and silver plasmonic nanostructures has recently emerged as a booming field of research due to their fascinating optical properties attributable to a unique phenomenon known as localized surface plasmon resonance (LSPR). LSPR is defined as the confinement of a surface plasmon in a nanoparticle of size comparable to or smaller than the wavelength of light used to excite the plasmon. After being resonantly excited by the light, the LSP produces a strong electric field that is localized near the metal surfaces. During both the excitation and decay processes of LSP, the electron-hole pairs, the strong electric field, and the heat generated can serve as potential excitation sources for the molecules present in proximity to the metal nanoparticles. LSPR can be tuned by altering the shape and size of plasmonic nanostructures. As a result, the optical properties of these materials can be tailored to accomplish the requirements of a particular application. Tuning plasmon resonance can be achieved with remarkable precision by manipulating the shape of metal nanoparticles. By changing the size of nanoparticle, surface plasmon resonances in spheres can be tuned over a narrow wavelength range (a few tens of nm), but shape anisotropy adds an additional level of flexibility for tuning these wavelengths over a wide range. Due to their one-of-a-kind optical properties, plasmonic nanoparticles have the potential to be utilized in a wide range of areas, including biosensing, SERS, photocatalysis, photothermal therapy, and many others. When two or more distinct types of plasmonic metal nanostructures are combined, they have the potential to produce extraordinary plasmonic capabilities. The integration of two or three different components within the same nanostructure not just adds up the properties of the individual components but also imparts novel properties upon the hybrid nanostructure as a result of the synergistic effect. Enhanced reactivity, product selectivity, and optical sensitivity are all benefits that come from utilizing hybrid plasmonic core-shell type integrated nanostructures. These capabilities make them an attractive candidate for several applications. DNA origami has emerged as a reliable technique for the assembly of a wide variety of nanostructures, allowing for precise control over the position of nanoparticles. Compared to top-down lithographic methods, such assembly methods are simple and cost-effective. This means that nanostructures

templated on DNA origami can be used for a wide range of purposes, from sensing to optical applications.

In line with the background information provided above, the first part of the thesis consists of an interfacial designing procedure for the fabrication of a class of bimetallic hybrid nanomaterials as a profoundly active photocatalyst for the conversion of para-aminothiophenol (PATP) into 4,4'-dimercaptoazobenzene (DMAB). To accomplish this goal, core-shell nanostars composed of gold (core) and silver (shell) (Au/Ag NSs) have been synthesized which served as both a surface-enhanced Raman scattering substrate and a plasmon driven catalyst when subjected to laser excitation at a wavelength of 532 nm. The surface-enhanced Raman scattering (SERS) efficiency of PATP is shown to be exceptionally high by Au/Ag NSs with sharp tips. Using the SERS technique, we were able to determine that PATP undergoes a rapid transformation into its dimerized product DMAB within a few seconds as a result of a surface photochemical reaction occurring in the Au–Ag heterojunction of core-shell nanostars. Au/Ag NSs with multiple sharp tips exhibit intense LSPR, and these tips also create exceptionally strong electric fields, which enable the generation of hot electrons that are responsible for the rapid conversion reaction. These interfacial bimetallic nanostars could have potential applications in SERS, biosensing, and photoinduced surface catalysis when they were designed and constructed adequately.

In the following chapter of the thesis, core-shell nanostructures of silicon oxide@noble metal were synthesized and utilized for enhanced SERS and photothermal effect. These core-shell nanostructures have piqued a lot of researchers' interest due to their unique properties, as well as their low toxicity and remarkable biocompatibility. Plasmonic nanoparticles are being used as a SERS based detection of pollutants and photothermal (PT) agents in cancer therapy. This is possible due to the unique property of localized surface plasmon resonance (LSPR), which plasmonic nanoparticles possess. The synthesis of multifunctional silica core - Au nanostars shell (SiO₂@Au NSs) nanostructures using surfactant free aqueous phase method is presented and demonstrated in this chapter. Using Rhodamine B (RhB) dye as a Raman probe, the SERS performance of the as-synthesized anisotropic core-shell NSs was evaluated, and the results showed a

significant enhancement factor of 1.37×10^6 . In addition, SiO₂@Au NSs were utilized in the process of PT killing of breast cancer cells, and these nanoparticles demonstrated a concentration-dependent increase in the intensity of the photothermal effect. The incredible photothermal conversion efficiency of up to 72% has been displayed by the SiO₂@Au NSs, which sets a new benchmark. As an outcome, our synthesized NIR active SiO₂@Au nanostructures are of pivotal significance to have their dual applications in SERS enhancement and PT effect.

Apart from the metal core-metal shell nanostructures and dielectric core-metal shell nanostructures described earlier, the next chapter of the thesis presents nanostructures of the metal core-semiconductor shell type. Due to their enhanced plasmonic fields of plasmonic metal nanoparticles, metal-semiconductor core-shell nanostructures have recently been investigated for their potential to facilitate efficient photocatalytic water splitting. Therefore, we have developed a new type of nanostructure of Au nanostar core ZnO nanopetals composite (Au@ZnO). The as-synthesized Au@ZnO nanocomposites (NCs) were characterized utilizing different spectroscopic and microscopic techniques. Powder X-ray diffraction (XRD) and X-ray photoelectron spectroscopy (XPS) studies clearly confirm the formation of highly crystalline Au/ZnO composite structure. The transmission electron microscopy (TEM) images clearly show that Au is present in the core and ZnO in the surrounding. The fabricated Au@ZnO NCs were used as a catalyst for photocatalytic water splitting. Au@ZnO NCs exhibited hydrogen and oxygen evolution up to 518.36 and 177.86 $\mu\text{mol g}^{-1}$, respectively. The observed enhanced photocatalytic activity of Au-ZnO NCs is associated with the efficient suppression of the recombination of photogenerated charge carriers in ZnO due to the strong electron scavenging activity of Au nanoparticles combined with the improved sun light utilization capability of Au@ZnO NCs coming from the plasmonic response of Au core surrounded with ZnO nanostructures.

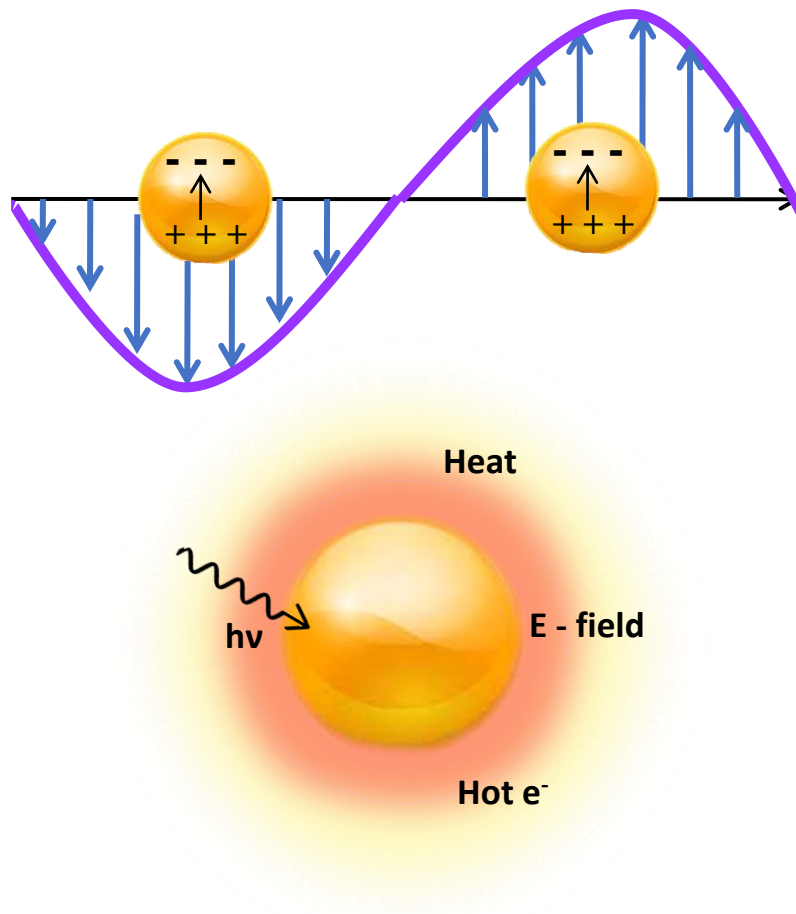
In addition to the applications of plasmonic metal nanoparticles based on LSPR that were mentioned earlier, the last part of the thesis covers another unusual application of noble metal nanostructures which is to act as electrocatalyst for Oxygen Evolution Reaction (OER). The kinetically slow anodic OER is a cause for concern when considering the

feasibility of large-scale hydrogen synthesis from electrochemical water splitting as a means of producing clean energy that can replace fossil fuels. Hence, the development of highly active electrocatalysts is of immense interest for improving the efficiency of gas evolution. In this chapter, we present the design of a monomer structure of Ag-coated Au nanostars (core-shell-type Au@Ag nanostars) assembled on rectangular DNA origami and investigate their electrocatalytic activities through OER. Our designed DNA origami-templated bimetallic nanostar catalyst showed excellent OER activity and high stability without using any external binder and exhibited a current density of 10 mA cm^{-2} at a low overpotential of 266 mV, which was smaller than those of ss-DNA-functionalized Au@Ag nanostars and DNA origami templated pure Au nanostars. Our results reveal that DNA origami-assembled core-shell Au@Ag nanostars show better electrocatalytic performance as compared to pure-core Au nanostars immobilized on DNA origami, owing to the presence of a highly conductive Ag layer. Such controlled assembly of bimetallic nanostructures on a DNA origami template can provide additional electrochemical surface area and a higher density of active sites resulting in enhanced electrocatalysis.

The research presented in this thesis is part of an ongoing effort to create new plasmonic hybrid nanomaterials with promising photocatalytic, energy, and medical applications. A discussion of potential follow-up studies is included in the investigation as well.

Chapter 1

Introduction



1.1. Plasmonic nanomaterials

Plasmonic nanomaterials are a class of materials that exhibit distinctive optical properties as a result of the collective oscillation of free electrons at their surface, which is known as plasmons. There are many different kinds of plasmonic nanomaterials available,^{1, 2} in addition to the noble metals. Such nanomaterials provide a broad range of options which can be developed in fusion with numerous different components based on the objective of an implementation and cost efficacy.^{3, 4} Semiconductors, in general, exhibit resonance which is redshifted in comparison to the visible and near-infrared range of the majority of metallic nanomaterials. As a result, semiconductor nanoparticles with a small size (<10 nm), such as quantum dots, can indeed be utilized in biomedical applications. On the other hand, noble metal nanoparticles, particularly gold and silver, provide the strongest resonance intensity, which makes on-resonance applications easier to implement. Hence, plasmonic nanomaterials typically consist of noble metals, and their sizes range anywhere from one to one hundred nanometers (nm). As a result of the localized surface plasmon resonance (LSPR)⁵ of the free electrons that are located at their surface, they possess unusual optical properties. When the size of the particles is nearly equivalent to the the incident light's wavelength, this interaction affects the absorption and scattering of light, and consequently, the color of the particle.⁶ This had already widely recognized experimentally between old Roman glass makers because they had been utilizing silver and gold in the glass production which resulted in diversely colored glasses based on the path the of light, and the most well documented case of Lycurgus cup.⁷ However, in 1857, Faraday conducted an experiment that led to the development of the first scientific method for determining the color of small metallic particles. He demonstrated that gold colloids have a color similar to ruby,⁸ and Mie subsequently provided a theoretical explanation for this observation.⁹ Since that time, a large number of studies have been conducted to investigate the optical properties of fine metallic particles, and a growing number of possible applications that make use of these particles have come into existence. Plasmonic nanomaterials have superior performance to that of conventional nanomaterials. All such plasmonic noble metal nanoparticles have considerable benefits thanks to their high absorption and scattering cross sections, potent field enhancement, and straightforward formation

of a variety of distinct morphologies that can be reproduced. Modifications in the size and shape of the plasmonic metal nanoparticles produce resonance bands that range from the visible to the infrared regions. Hence, nanostructured materials' plasmonic behavior has led to extensive research into their applications in areas as diverse as catalysis¹⁰, energy harvesting,¹¹ and biomedical field.¹²

1.2. Metal nanoparticles

Owing to their particle size, metallic nanoparticles have captivated attention of scientists for over an era in the field of material science. Synthesis methods of metal nanoparticles are currently being explored by researchers due to their remarkable properties and their application in physics, chemistry, biology, medicine, photocatalysis, optoelectronics, biosensing, and sensor technology.¹³⁻¹⁷ Various kinds of metallic nanoparticles and their variants have received considerable interest. This includes gold (Au), silver (Ag), copper (Cu), nickel (Ni), iron (Fe), platinum (Pt), and zinc (Zn) metal nanoparticles which own different applications in various fields. Iron oxide nanoparticles have been studied for biomedical applications like contrast-enhancing agents in MRI, hyperthermia, drug delivery, early cancer detection, and diabetes due to their magnetic and biocompatible properties.¹⁸ Zinc oxide nanoparticles are also known to have utilizations as biosensors,¹⁹ drug delivery,²⁰ bio imaging,²¹ food packaging material,²² and solar photocatalyst²³ because they are less expensive, and non-toxic. Implementations of Cu and Cu-based nanoparticle in the field of electrocatalysis, photocatalysis, gas phase catalysis, and organic conversion reactions have sparked a lot of interest which are based on the low-cost and high abundance of copper metal.²⁴ In the last two decades, Au and Ag nanoparticles are also been extensively employed for biomedical,²⁵ photocatalytic applications,²⁶ and chemical analysis²⁷ owing to their unique optical properties.

1.3. Optical properties of plasmonic metal nanoparticles

Optical property is one of the most basic and significant characteristic of metal nanoparticles. For example, at nanoscale Ag nanoparticles show yellowish gray color, Pt and palladium (Pd) nanoparticles display black color. The most striking example is of

Au nanoparticles which are able to show a range of orange to red colors depending on the size (Figure 1.1).

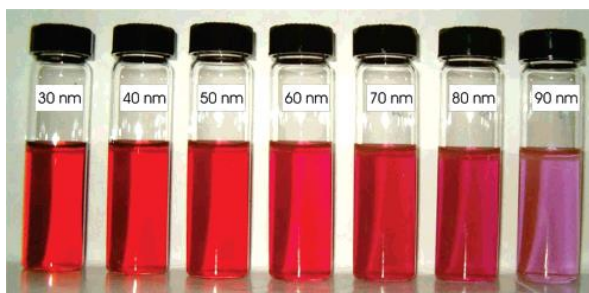


Figure 1.1. Photograph showing the colors of Au nanoparticles for different particle sizes in aqueous solution (Reprinted with permission from ref.²⁸, 2007 American Chemical Society).

Mie, in his work in 1908, mathematically explained the intense red color of Au nanoparticles by solving maxwell equations for absorption and scattering spectra for spherical metallic nanoparticles.⁹ He was able to demonstrate the changeable color of Au colloids as the size of the Au spheres increased, which was afterward defined in terms of surface plasmon resonances. According to this captivating theory by Mie, size, shape of metal nanoparticles, and surrounding environment around metal nanoparticles have a significant effect on the color of colloidal solution of metal nanoparticles resulting in unique optical properties of metal nanoparticles. The distinct colors of metal nanoparticles are caused by surface plasmon resonance, which is prompted by collaborative oscillations of free electrons on the surface of metal nanoparticles when exposed to resonant light. The exitance of surface plasmon resonance is demonstrated by R. H. Ritchie for the first time in 1957.²⁹

1.3.1. The emergence of surface plasmon resonance

Metals have free electrons on their surfaces which move throughout the material, especially d electrons in case of Au and Ag. Collective oscillations of these free electrons are known as plasmons.³⁰ When the size of metal nanoparticles (mainly noble metals) is less than the wavelength ($d \ll \lambda$) of incident light on surface of metal nanoparticle, the electric field of incident light can pass through the metal and as a

result polarization of conduction electrons of metal take place. These electron oscillations are not propagating, rather these are distributed in the metal nanoparticle volume only provided the metal nanoparticles are smaller than the wavelength of incident light. These non-propagating electron oscillations are known as localized surface plasmon resonance (LSPR) as shown in Figure 1.2. When the resonance takes place between the oscillation frequency of conduction electrons and electric field of incident light, then this gives rise to the intense absorption band in UV-vis region.³¹

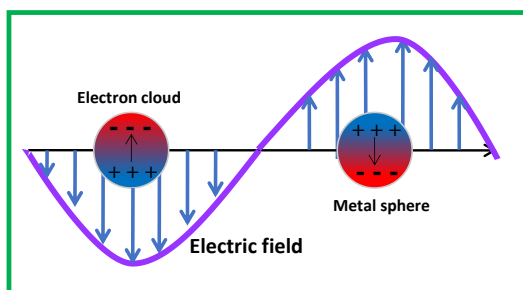


Figure 1.2. Schematic depiction of localised surface plasmon oscillation for a sphere metal nanoparticle, showing the displacement of the conduction electrons cloud relative to the nuclei.

For Au and Ag nanoparticles, the value of LSPR is at ~ 520 nm and ~ 420 nm respectively which are responsible for vivid colors (ruby red for Au nanoparticles and yellow grey for Ag nanoparticles) of noble metal nanoparticles (Figure 1.3).

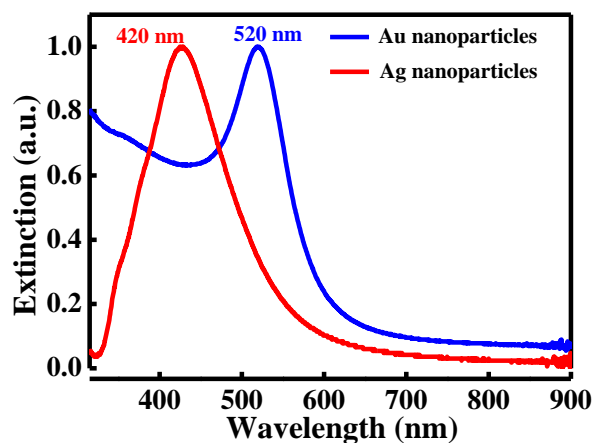


Figure 1.3. Normalized UV-vis extinction spectra of Au nanoparticles (blue curve), and Ag nanoparticles (red curve).

The SPR is estimated utilizing scattering and absorption spectroscopy and is affected by multiple factors such as size, shape of metal nanoparticles, their electron densities, and dielectric constant of the material of metal nanoparticle, and the dielectric constant of the surrounding environment of metal nanoparticle.^{31, 32}

The quasi-steady expression of the extinction coefficient σ_{Ext} (sum of absorption and scattering) for spherical metal nanoparticles is given by Mie's theory (Equation 1.1).^{30, 33}

$$\sigma_{Ext} = \frac{18\pi NV \varepsilon_m^{3/2}}{\lambda} \times \frac{\varepsilon''}{(\varepsilon' + \chi \varepsilon_m)^2 + \varepsilon''^2}$$

Equation 1.1

Where N is number of particles in volume V, and λ is wavelength of incident light which is absorbed, ε_m is dielectric constant of non-absorbing surrounding medium of whose imaginary part is equal to zero, ε' and ε'' are the real and imaginary part of dielectric constant of material of which the metal nanoparticle is formed, χ is the form factor which depends on the shape of spheroid, ranging from 2 for a sphere to 17 for a spheroid with an aspect ratio of 5:1.³⁴

$$\varepsilon(\omega) = \varepsilon'(\omega) + i \varepsilon''(\omega)$$

Equation 1.2

ε is a complex dielectric function which depends upon the angular frequency(ω) of incident light (Equation 1.2).

Any metal's plasmonic properties are defined by its $\varepsilon(\omega)$. The value of σ_{Ext} is maximum for spherical metal nanoparticles when the Equation 1.3 holds. ($\chi = 2$ for spherical metal nanoparticles)

$$\varepsilon'(\omega) = -\chi \varepsilon_m$$

Equation 1.3

The Equation 1.3 is known as Fröhlich condition at which the LSPR occurs. This occurs in visible range of electromagnetic spectrum for Au and Ag nanoparticles.

When magnitude of dielectric constant of surrounding medium increases, the red shift in LSPR position takes place owing to the accumulation of polarization charges at the interface, resulting in the weakening of total restoring force. Hence, it is clear that LSPR frequency is highly tunable with variation in the ε_m of surrounding medium. Mie

theory was employed to deduce the optical properties of spherical nanoparticles and was afterward widened to Gans theory³⁵ and Maxwell-Garnett equations to explore other shapes and core-shell nanostructures.³⁶ Nanoparticle geometry affects the LSPR's restoring force because of charge accumulation on the surface of the particle. Gans modification of Mie theory predicted the splitting of plasmon resonance for non-spherical geometry.³⁵

1.3.2. Effect of size, shape, and surrounding environment on optical properties

The SPR is immensely susceptible to variations in nanoparticle shape or size. With change in size or shape of nanoparticle, the surface geometry varies which tends to cause a change in electric field density on the surface. Hence, the oscillation frequency of surface electrons is changed resulting different cross sections for the optical properties inclusive of absorption and scattering.³⁷ This gives rise to different positions of SPR. For particle sizes smaller than about 20 nm, it is well known that the bandwidth is inversely proportional to the radius r of the particle. For large size nanoparticles usually > 25 nm for Au nanoparticles, the extinction coefficient clearly tends to depend on the size of nanoparticle as the wavelength of incident light approaches the nanoparticle dimension. When the size of Au nanoparticles is comparable to the wavelength of incident light, then the distribution of the electric field along the particle is generally uniform, polarisation of electron cloud is coherent in all points of the metal, and dipolar plasmon resonance oscillations are excited. In contrast, when the size of the Au NP is nearly equivalent to or larger than the wavelength of interacting light, the electric field distribution on the surface of particle is non-uniform, polarisation of electron cloud is no longer congruent at each point of the metal, and hence results in excitations of multi-polar plasmon oscillations.³⁰ These type of size effects are known as extrinsic size effects which appear in the absorption spectrum of as broadening and red shift of SPR with increasing the size of Au nanoparticles. This is fully expressed by the Mie's theory. Generally, the expanding of the plasmon band is attributed to retardation effects.³⁸ The size variations in spherical Au nanoparticles allow for the attuning of SPR wavelengths (λ_{SPR}) above 60 nm by different particle sizes between 10

and 100 nm³⁹ and this can be explained by the equation 1.4, where d_{av} is average diameter of particles.⁴⁰

$$\lambda_{SPR} = 382.6 + 1.18d_{av} \quad \text{Equation 1.4}$$

The Figure 1.4 shows the red shifted positions of SPR for spherical Au nanoparticles with the increase in size.

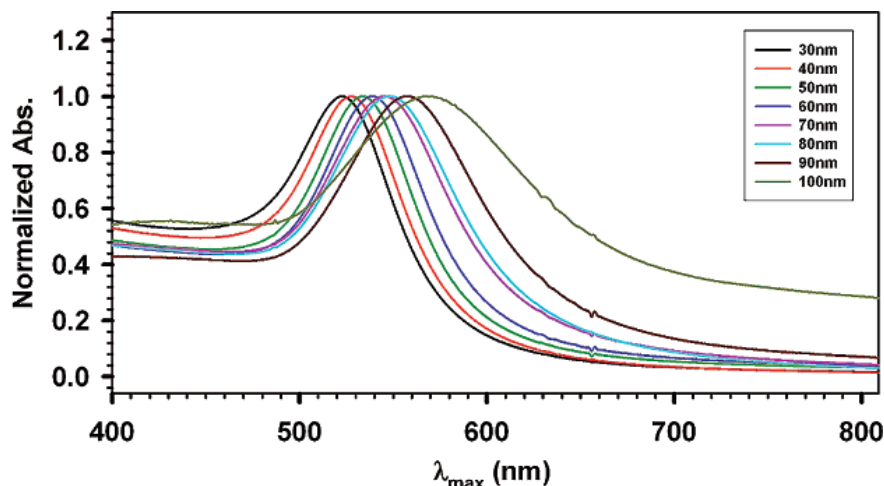


Figure 1.4. Normalized UV-Vis Absorption spectra of spherical Au nanoparticles of different size range from 30 nm to 100 nm. (Adapted with permission from ref.²⁸, 2007 American Chemical Society).

Improvements in the synthesis and characterization of plasmonic nanostructures have enabled the recognition of nanoparticles with a wide range of shapes, which would include nanoshells, nanowires, nanocubes, nanostars, nanoprisms, nanopyramids, nanotriangles, and nanocones.^{34, 41} The shape of the metal nanoparticle has a significant influence on the SPR band. By reduction in geometry of nanoparticle, the position and intensity of plasmon band can be tuned over arrange of wavelengths in UV-Vis-NIR regions. The new plasmon band/bands originate by changing the shape have common feature that they are positioned at lower frequency/energy or higher wavelength than the corresponding sphere. For illustration, spherical Au nanoparticles with sizes ranging from 2 to 50 nm exhibit just one plasmon band centring around 520 nm, whereas two different plasmon bands appear when the nanoparticle symmetry is altered from spherical Au nanoparticles to Au nanorods.^{42, 43} The SPR band for Au nanorods or

nanowires divided into two plasmon bands, depending upon the oscillations of free electrons in diverse directions.^{44, 45} The SPR band at higher wavelength as compared to its equivalent spherical is originated due the oscillations of free electron along the long axis which is known as Longitudinal SPR and the other band at lower wavelength is due the free electron oscillations perpendicular to long axis known as Transverse SPR (Figure 1.5a).

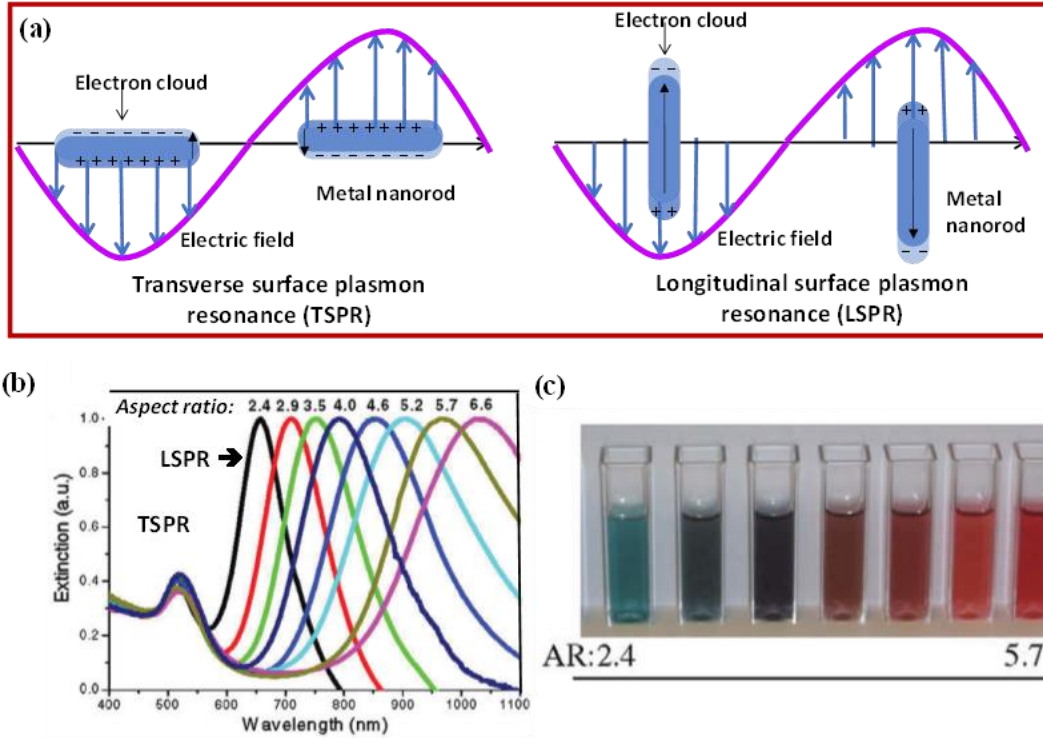


Figure 1.5. (a) Schematic depiction of SPR excitation for Au nanorods along and perpendicular to long axis (Adapted with permission from ref.⁴⁶, 2014 Elsevier), (b) Normalized extinction spectra of Au nanorods with different aspect ratios, and (c) corresponding digital image of Au nanorods. (b and c are reprinted with permission from ref.⁴⁷, 2010 Elsevier).

The Transverse SPR mode is positioned nearly at 520 nm likewise for spherical Au nanoparticles. Meanwhile the Longitudinal SPR at longer wavelength is very susceptible to the change in aspect ratio of the nanorod. The aspect ratio is described as the ratio of the nanorod length to its width. The Longitudinal SPR can be relocated from

the visible to the NIR range by increasing the aspect ratio of the nanorod while retaining the transverse SPR position at 510-520 nm (Figure 1.5 b and c).^{48, 49}

The wavelength of longitudinal SPR is linearly related with the dielectric constant of medium (ϵ_m) and the aspect ratio (AR) of nanorods⁴⁵ (Equation 1.5).

$$\lambda_{LSPR} = (33.34AR - 46.31)\epsilon_m + 472.31 \quad \text{Equation 1.5}$$

Even for a monodisperse sample of rods, the aspect ratio does not distinctively decide the extinction spectrum (absorption + scattering) of a nanorod as it depends upon the ϵ_m . It must be highlighted once again that a repositioning of plasmon band occurs by approximately 150 nm when the dielectric function of medium is increased by just one. The extinction spectra or optical properties of cylinders with hemi-spherical, hemi-ellipsoidal, or flat ends and ellipsoids are incredibly unique.

Apart from the Au nanospheres and nanorods, the optical properties can be tuned by other structural modifications to more complex structures such as Au nanostars and Au nanoshells. The response to incident light of these complex nanostructures can be understood in terms of hybridization of plasmons of complex shaped metal nanostructures. The optical properties of Au nanostars are extremely sensitive to the size and length of tips. The Au nanostar exhibit the plasmon band which is the hybridization of plasmons of core and the those existing in the tips of a nanostar.⁵⁰ Figure 1.6a shows that when the hybridization takes place between the plasmon of core and tips of a nanostar and splitting of resonances takes place between bonding plasmons of lower energy and antibonding plasmons of higher energy. The lower energy bonding plasmons are mostly comprised of tip plasmons, with a small participation from core plasmons. This hybridization of tip and core plasmon modes results in significantly increased bonding plasmon excitation cross-sections, resulting in extremely intense nearby electric field enhancements across sharp corners, edges, or tips. Because of this high extinction cross-section of such sharp nanostructures, the interaction of resonant light with metal nanostars is immensely fascinating.⁵¹ Even though the main body of a metal nanostructure is important in providing electrons to tips that amplify the electric field, the tips play a significant role in the main plasmonic features of these

sharp nanostructures.^{52, 53} The localized surface plasmon resonance resonances of Au nanostars are highly tunable (Figure 1.6 b and c) and can be red shifted as the tip length increases, thus generating intense local electric field at sharp tips.^{54, 55}

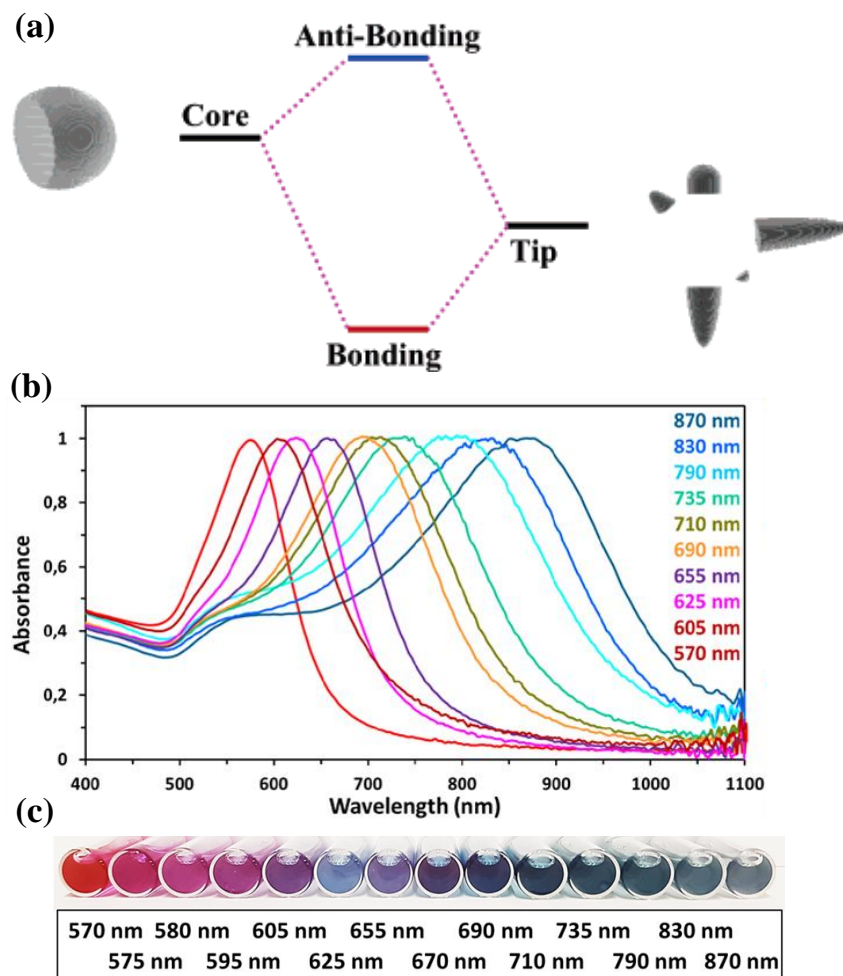


Figure 1.6. (a) Diagrammatic depiction of the concept of plasmon hybridization of core and tip plasmons in the nanostar (Permission to reprint from ref.⁵⁰, 2007 American Chemical Society), (b) Normalized UV-Vis-NIR spectra of different sized Au nanostars having different positions of LSPRs, and (c) corresponding digital image of Au nanostars. (b and c are reprinted with permission from ref.⁵⁵, 2018 American Chemical Society).

1.3.3. Optical properties of plasmonic metal nanoshells

Aside from shape and size, the optical properties of metal nanostructures are strongly influenced by the design of nanostructure. Metal nanoshells are a novel type of

nanoparticle with highly variable optical properties. Metal nanoshells can be comprised of dielectric core, magnetic core or metallic core.^{56, 57} When the metal nanoshell has dielectric core then a new type of composite nanostructure is formed, with immensely observable optical properties. The optical properties of these such core-shell nanostructures are highly predictable based on relative thickness of the dielectric core and metallic shell in the nanostructure. By adjusting the core-shell thickness ratio, one can have complete control over the SPR position of these types of nanostructures, which can then be tuned to suit the application. As a result, the position of the plasmon band can be tuned from UV-Vis to NIR region of electromagnetic spectrum (Figure 1.7).

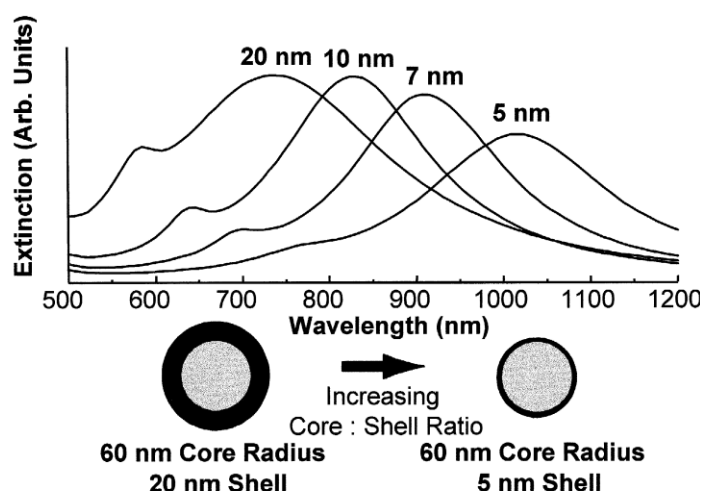


Figure 1.7. UV-Vis-NIR spectra of metal nanoshells (silica core, Au shell) calculated theoretically over a range of core radius/shell thickness ratios (Reprinted with permission from ref.⁵⁸, 1998 Elsevier).

As the ratio of core to shell thickness is changed from 3 to 12, the plasmon band can be positioned across a range of wavelengths from UV-Vis to NIR region. As a result, a few nanometer variations in shell thickness can result in the exceptional optical properties of metal shells. However, this is not observed in the upside-down nanostructure, which consists of a metal core and a dielectric shell.⁵⁸ So, there is something about the metallic shell morphology that inevitably leads to this unique property. This can be explained based on the concept of “hybridization of plasmons” as discussed by Halas and the group.^{59, 60} Nanoshell can be expressed as a combination of sphere and cavity (Figure 1.8). So, the plasmons of the sphere and the cavity interact with each other and this

plasmon hybridization gives rise to the low energy bonding and high energy antibonding plasmon modes. Only the low energy bonding plasmon mode interacts with the incident light. The degree of interaction among cavity and sphere plasmons is greatly impacted by metal shell thickness (Figure 1.8c).

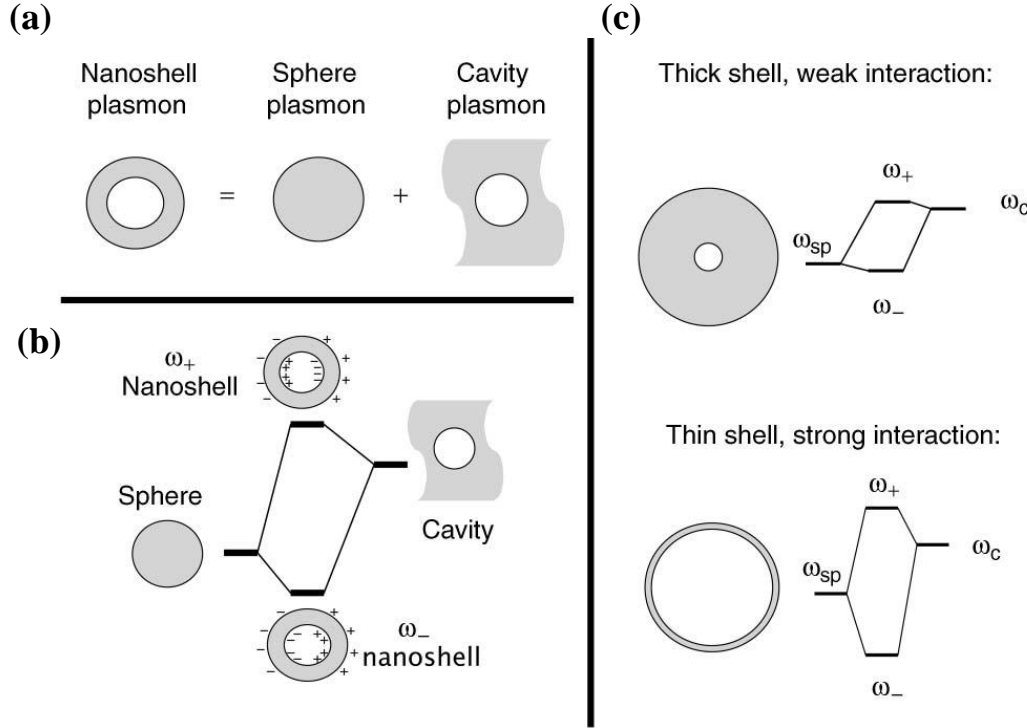


Figure 1.8. (a) Diagrammatic illustration of a nanoshell as the fusion of a sphere and a cavity, (b) An energy-level diagram of hybridization of sphere and cavity plasmons resulting in antibonding (ω_+) and bonding (ω_-) plasmon modes, and (c) energy level diagram for the effect of shell thickness on the plasmon interaction (Adapted with permission from ref.⁶⁰, 2005 Springer Nature).

1.3.4. Optical properties of plasmonic bimetallic core-shell nanoparticles

Bimetallic nanoparticles, in which two different kinds of materials are incorporated, have very distinctive characteristics. These unique features are significantly different from the corresponding individual components. The combination of two discrete materials results in the improvement in properties such as enhanced optical and magnetic properties,^{61, 62} enhanced catalytic properties.⁶³ Such outstanding properties result from the bimetallic structure's electronic and architectural effects.⁶⁴ Because these

features are highly influenced by the structure, morphology, and composition of the bimetallic nanostructures, designing these nanoparticles with precise control over structures, morphologies, and combinations is a useful goal.⁶⁵ It has been illustrated that the optical properties of bimetallic Au-Ag core-shell nanoparticles can be effortlessly tailored by modifying the ratio of Ag to Au.^{66, 67} The plasmon band of spherical Au-Ag core-shell lies in between that of the physical mixture of Au nanospheres and Ag nanospheres (Figure 1.9). As a result, depending upon the application, control over the SPR band can be achieved by playing with the thickness of shell.⁶⁸ Such control over optical properties makes Au/Ag core-shell nanoparticles of significant importance in catalytic applications,⁶⁹ photocatalysis⁷⁰ and electrochemical reactions.^{65, 71}

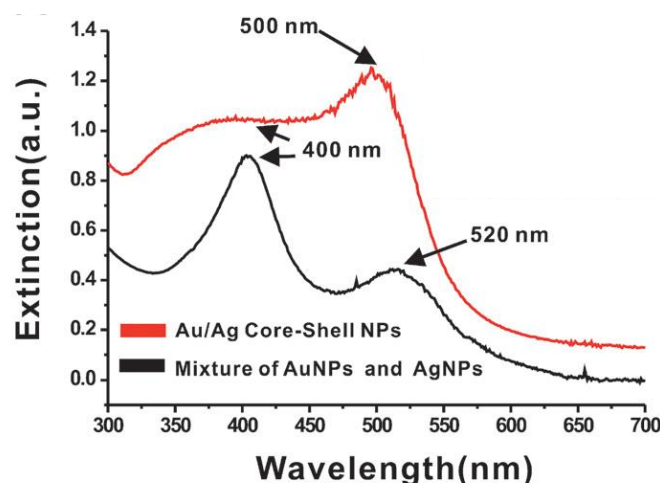


Figure 1.9. UV-visible extinction spectra of a physical mixture of the same amount of Ag nanoparticles and Au nanoparticles, and spherical core-shell Au-Ag bimetallic nanoparticles (Reprinted with permission from ref.⁶⁸, 2008 Royal Society of Chemistry).

1.3.5. Optical properties of hybrid plasmonic metal-semiconductor core-shell nanostructures

The hybrid nanostructures consisting of metal as a core and semiconductor as a shell are a significant category of nanocomposite frameworks that could possess a fusion of characteristics from the participant parts and provide improved tunability of properties. Even new synergistic properties emerge predominantly from interactions between both

the widely divergent components i.e., noble metal and semiconductor.⁷² Optical properties are highly dependent on the surrounding material of the metal nanoparticle.⁷³ As a result, shell components with a higher refractive index induce a relatively large red-shift as compared to pure metal nanoparticle parts and widening of SPR band position (Figure 1.10).^{74, 75}

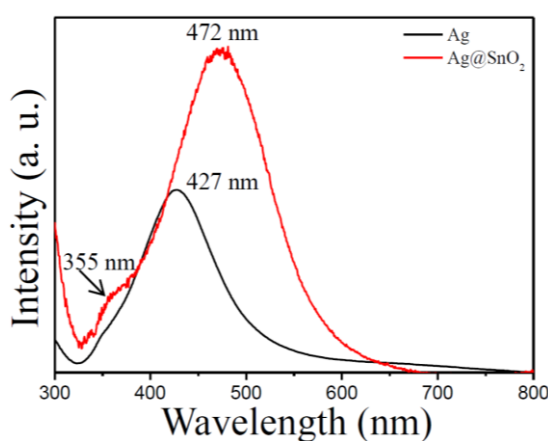


Figure 1.10. UV-vis spectra of Ag and Ag@SnO₂ metal semiconductor core shell nanoparticles (Adapted with permission from ref.⁷⁶, 2015 Royal Society of Chemistry).

1.4. Interaction of light with plasmonic metal nanoparticles

When plasmonic metal nanoparticles interact with light, resonant conditions lead to the generation of LSPR which may undergo decay either in radiative or non-radiative way.^{30, 77} In radiative decay, the LSPR relaxes to re-radiate the light in close vicinity of metal nanoparticle or the plasmonic metal nanoparticles behave as a secondary source of light to promote nearby electric fields. Hence, strong electric fields are generated in surroundings of metal nanoparticles in radiative decay of LSPR. In non-radiative decay, and hot electron hole pairs are generated on relaxation of LSPR in plasmonic nanoparticles which can be transferred to the molecule (chemical molecule or semiconductor) present in close contact of metal nanoparticle. In this relaxation process, the metal nanoparticles act as a photo sensitizer and the process of hot electron transfer to nearby molecule is known as photosensitization. When spectral overlap exists between the LSPR of plasmonic metal nanoparticle and absorption of nearby semiconductor, the process is known as plasmon induced resonant energy transfer (PIRET) or plasmon resonant energy transfer (PRET). Thus, four mechanisms take

place in plasmonic enhancements in which electromagnetic fields and light scattering are classified as radiative effects, and the other two mechanisms, hot electron transfer and plasmon resonant energy transfer, are considered as non-radiative effects (Figure 1.11).

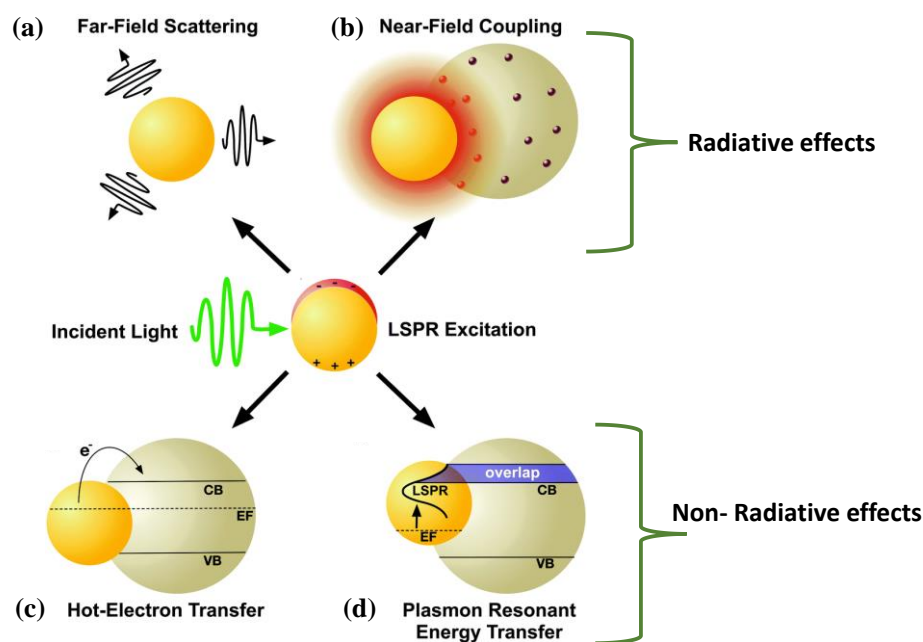


Figure 1.11. A diagrammatic representation of the mechanisms of plasmon enhancement, radiative effects: (a) far-field scattering, and (b) near-field coupling, and non-radiative effects: (c) hot electron transfer, and (d) plasmon induced resonant energy transfer (Adapted with permission from ref.⁷⁸ , 2016 Royal Society of Chemistry).

1.4.1. Radiative plasmon decay

The radiative decay of excited LSP either results in the generation of electromagnetic fields in the "near-field" of the nanostructures or in the scattering of light in the "far-field" of the nanostructures. Hence, during the radiative decay the plasmonic nanoparticles act as an additional source of light. In far field scattering, when light hits metal nanostructures with a high enough albedo, it gets scattered into the far field of nanostructure. The scattering cross section can be up to an order of magnitude higher than the nanostructure's physical cross-section, depending on the particle's geometry

and material properties.⁷⁷ Light scattered in the far field can be reabsorbed by the sensitizer molecule or semiconductor, allowing for greater absorption of light by the molecules present at distances of many hundreds of nanometres. In this far field scattering, scattered photons from individual nanoparticles can interact with multiple scattering from nearby nanoparticles, resulting in an increase in the total amount of trapped light thus enhancing the light harvesting.⁷⁷ The ability of metal nanostructures to scatter light is directly related to their size as described by Mie theory.⁷⁹ The scattering cross-section of a metal nanosphere with radius (a) is given by following Equation 1.6.

$$\sigma_{scat} = \frac{8\pi}{3} k^4 a^6 \left| \frac{\epsilon_{metal} - \epsilon_{medium}}{\epsilon_{metal} + 2\epsilon_{medium}} \right|^2 \quad \text{Equation 1.6}$$

Where, k is $2\pi/\lambda$, and ϵ_{metal} and ϵ_{medium} are the permittivity of metal and surrounding medium, respectively. The scattering cross section increases proportionally with the size of the metal nanoparticle. In order to maximize light harvesting, the size of nanoparticle can be altered to attain the ideal scattering properties. Size is not the only factor in determining how much light a metal nanostructure scatters in the far field; the nanostructure's shape, attributable to its augmented polarizability, also plays a role.^{39, 80, 81} Nanostructures with pointed corners and tips, which include nanostars, nanopyramids, nanorods, nanocubes, and patterned concentric nanostructures, in which polarizability is improved at the metal-dielectric junction of each layer, are particularly susceptible to the influence of polarizability. In addition, the composition of nanostructures affects the light scattering properties, with Ag having stronger radiative properties than Au.

The term "near-fields" refers to the enhanced electromagnetic fields in close proximity to a nanostructure as a result of the interaction of incident light with plasmonic nanostructures. Plasmonic metal nanostructures serve as nano - size light concentrators by focusing the incident light on surface of nanostructure within a narrow volume. These fields typically have intensities that are several orders of magnitude larger than that of incident light. As a result, one is able to imagine nanostructures functioning as a secondary light source, thereby intensifying the photon flow and the total light absorption⁸² which generate the strong electric fields in surrounding of nanostructures.

In a manner similar to that of far-field scattering, the near-fields produced by LSPR are controlled by the size, shape, and composition of the plasmonic nanostructure.^{81, 83, 84} Nanostars, nanorods, nanocubes as well as other non-spherical plasmonic nanostructures with sharp characteristics create an intense electromagnetic field because of the highly concentrated charges at their sharp edges and corners.^{85, 86} Finite difference time domain (FDTD) simulation studies have shown that the morphology and composition of nanostructures have an effect on the intensities of the localized electromagnetic field at sharp edges (Figure 1.12).

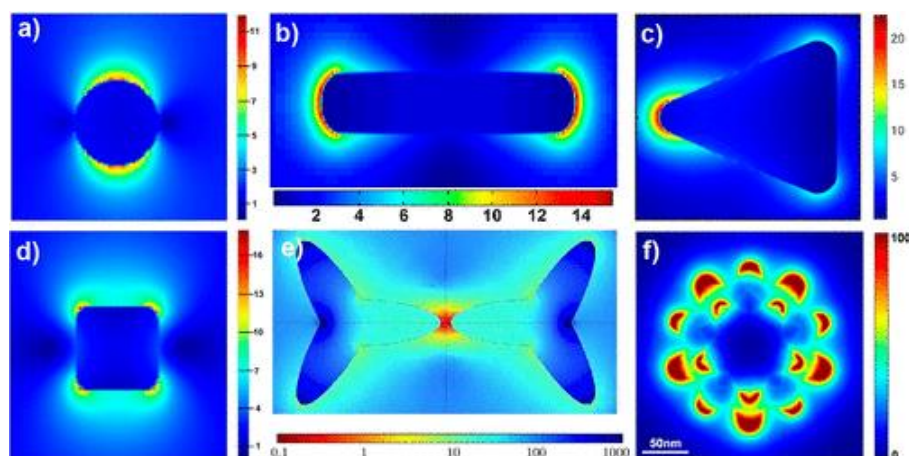


Figure 1.12. Distributions of simulated electric fields for (a) nanospheres, (b) nanorods, (c) nanotriangles, (d) nanocubes, (e) nanotripods, and (f) nanowires and (f) nanostars, when exposed to incident light (Adapted with permission from ref.⁸⁶ 2022, American Chemical Society).

1.4.2. Non- radiative plasmon decay

Non-radiative effects also contribute to plasmonic enhancements. Hot-electron transfer and PRET/PIRET processes boost carrier generation non-radiatively. During plasmonic nanoparticle excitation, short-lived localized surface plasmons (LSPs) decay non-radiatively, generating hot electrons and holes. Landau damping, a quantum mechanical effect investigated with femtosecond spectroscopy, redistributes LSP energy to hot electrons and holes in 1-100 fs.⁸⁷ Hot electrons are not thermally balanced with plasmonic material atoms. Hot electrons are formed by intra-band excitations in the conduction band or inter-band excitations from d-band transitions in noble

nanostructures like Au and Ag.³⁰ Since the energy level of the d-band in Au is only 2.4 eV well below Fermi energy, so inter-band transitions can play a significant role in the production of hot carriers. Meanwhile, in case of Ag, hot electrons are created by intra-band excitations because the d-band in Ag is 4 eV below Fermi energy.⁸⁸ Transferring electrons to the semiconductor or adsorbed molecule can occur via indirect hot electron transfer (Figure 1.13). Hot electrons can directly enter the conduction band of neighboring semiconductors if their energy is high enough to overcome the Schottky barrier between metal and semiconductor.⁸⁹ Hot electron transfer can occur without spectral overlap between the metal nanostructure and the semiconductor because the energy required is less than the semiconductor's bandgap. Hot electron transfer requires the metal and semiconductor's Fermi levels to be in equilibrium and electrons to freely move between them.⁹⁰

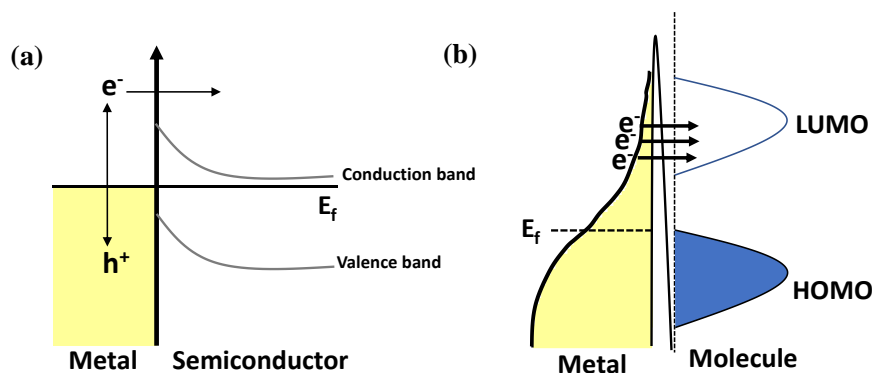


Figure 1.13. Energy band diagram of transfer of hot electrons from plasmonic metal nanoparticle to a) conduction band of semiconductor, and (b) LUMO of adsorbed molecule. (LUMO: lowest unoccupied molecular orbital, E_f : Fermi level, e^- : electron, and h^+ : hole)

In the indirect hot-electron transport pathway, hot electrons are transported from the Fermi level of plasmonic metal to adsorbed molecule via an inelastic electron tunneling process, resulting in the development of a transient negative ion state of the adsorbed molecule.^{87, 91} After the transient negative ion states are formed, the chemical reactions induced by plasmons occur through vibrational excitation. In plasmon chemistry using metal surfaces, the indirect hot-electron transfer pathway has been used to explain

mechanisms of most of the reactions.⁸⁷ Also, it was revealed through an investigation that hot-hole transfer could be a way for reactions to happen.⁹²

Morphology of plasmonic metal nanostructures determines their ability to efficiently generate hot electrons. Hot carriers with energies near the Fermi level are more likely to be generated as the particle's size increases, as shown by Manjavacas et al.⁸⁸ Furthermore, metal nanostructures with complicated multilayer or strongly non-homogeneous nanostructures, can also serve as favorable generators of hot electrons. The hot electrons generated in plasmonic nanostructures eventually cool down via electron–electron scattering (~100 fs) and electron–phonon collisions (1-10 ps) by transferring their energy into the lattice through the vibrational relaxation, which results in the dissipation of heat.^{87, 93} Reportedly, the surface temperature of the system increased to around 300°C when LSP of Au Nanoparticles deposited on zinc oxide nanorods is excited.⁹⁴ This generated heat is enough to cross the energy barrier of many molecules, making them useful for the conversion reactions. This concept has indeed been utilized to a great extent in photothermal cancer treatments.^{95, 96}

Besides hot electron transfer, PRET is another non-radiative decay pathway which is crucial to plasmonic enhancements. This transfer process requires spectral overlap between semiconductor's absorption and nanostructure's LSPR. Dipole–dipole coupling from metal to semiconductor generates electron–hole pairs near the semiconductor's band edge.^{97, 98} The PRET mechanism has extensive practical applications in photovoltaics, photocatalysis, and photoelectrochemical cells.^{78, 98, 99}

During the excitation, and radiative and non-radiative decay of LSP, strong electric field, hot electron-hole pairs and heat generated, can be used by adjacent molecules as excitation sources and hence can be employed in multidisciplinary applications. The extent of applications also depend upon the self-assembled nanostructures on the templates.

1.5. Fabrication of assembled plasmonic metal nanoparticles

Metal nanoparticles' interactions with surrounding molecules are strongly influenced by their spatial arrangement over a template, making this a powerful method for

systematically controlling their catalytic properties and revealing novel phenomena. In order to achieve this goal, considerable efforts were put in to develop approaches that allow for precise control over the assembled structure of metal nanoparticles. The top down approaches electron-beam lithography and focused ion beam etching have been used to assemble metal nanoparticles over templates. Despite their sophistication and flexibility, lithographic techniques have many drawbacks, including the inadequacy to develop 3D structures, high production costs, and time-consuming multistep synthesis. Bottom-up approaches start with colloidal synthesis of metal nanoparticles and self-assemble them using methods like controlled solvent evaporation or transferring nanoparticles dispersed in organic solvents to water to form a monolayer after evaporation. Solution-based assembly of metal nanoparticles yields high-yield nanostructures.

1.5.1. Assembly of plasmonic metal nanostructures on DNA origami

DNA origami has emerged as a highly effective template for the arrangement of various nanostructures, allowing for exact control over the arrangement of nanoparticles.¹⁰⁰ In 1980, Ned Seeman proposed using DNA as construction material to create different structures using short-staple DNA sequences in careful stoichiometry.¹⁰¹ Yan et al. used directed nucleation of DNA tiles around a scaffold DNA strand to create a DNA barcode lattice in 2003.¹⁰² Later, Shih et al. used synthetic oligonucleotides to fold a 1.7 kb DNA strand into an octahedron.¹⁰³ In 2006, Paul Rothemund proposed "scaffolded DNA origami," a versatile "one-pot" method for synthesising self-assembled DNA nanostructures.¹⁰⁴ Hence, DNA origami refers to the practice of folding a single long DNA scaffold strand into a variety of nanoscale designs with the help of hundreds of short DNA oligonucleotides (staple strands). The bases of nucleic acids pair up in a very specific and predictable way thanks to Watson and Crick base pairing. As a result of manipulating the Watson–Crick base pairing, scaffold strands can be designed into a variety of shapes with the assistance of short staple strands, which leads to the formation of DNA origami nanoscale structures (Figure 1.14).

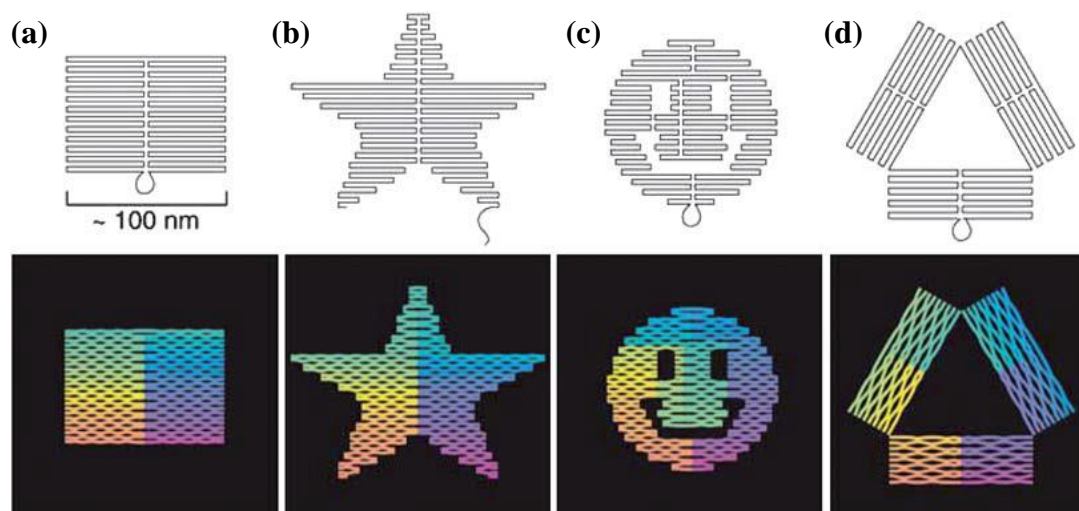


Figure 1.14. The two-dimensional DNA origami nano scale structures. (a) A rectangle, (b) a star, (c) a disk with three holes, and (d) a triangle (adapted with permission from ref.¹⁰⁴, 2006 Nature Publishing Group).

The ability to accurately and efficiently arrange nanoparticles on DNA origami templates has enabled the construction of plasmonic structures with fascinating optical properties. When compared to the top-down lithographic techniques that are typically used, these assembly techniques are less complicated and more cost-effective to place metal nanoparticles. Due to their easy conjugation with DNA oligonucleotides via Au-thiol bond, Au NPs have been the best material for self-assembly. In 2012, Ding used DNA origami to build 3D plasmonic chiral nanostructures with strong plasmon-induced circular dichroism (CD).¹⁰⁵ Since then, many examples of using DNA origami to assemble spherical and anisotropic nanoparticles in prespecified patterns have been reported.^{106, 107} Focusing and controlling light within extremely small, deep-subwavelength volumes was the driving force behind the use of DNA origami as a template for fabricating metal nanoparticles.

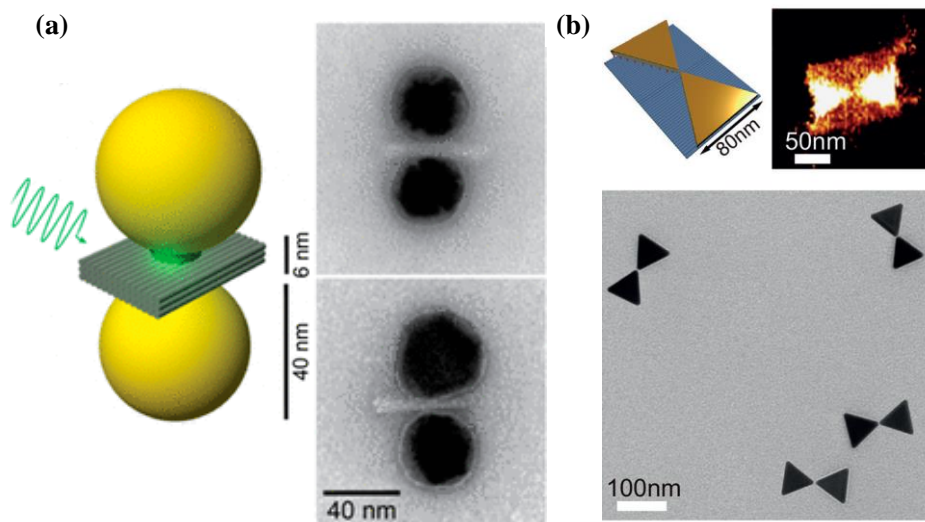


Figure 1.15. (a) DNA origami assembled Au nanoparticle dimers (Reprinted with permission from ref.¹⁰⁸, 2014 American Chemical Society), and (b) Bowtie nanoantenna on DNA origami (Reprinted with permission from ref.¹⁰⁹, 2018 Wiley-VCH Verlag GmbH & Co. KGaA).

Kuhler et al. showed the fabrication of assembled Au nanoparticles on DNA origami, (Figure 1.15a).¹⁰⁸ In other example, Zhan et al. illustrated the assembly of Au bowtie nanoantennas on DNA origami (Figure 1.15b).¹⁰⁹ These fabricated assemblies can be used for SERS applications.

1.6. Applications of plasmonic nanoparticles

Plasmonic noble nanoparticles have piqued the attention of many researchers because of their distinctive optical properties,¹¹⁰ which are now widely used in enhanced spectroscopies such as surface enhanced infrared absorption spectroscopy (SEIRAS), SERS,⁸⁷ and surface plasmon fluorescence spectroscopy (SPFS),^{111, 112} biosensing and chemical sensing,¹¹³ nanomedicine,¹¹⁴ solar cells,¹¹⁵ analytical applications,¹¹⁶ and photovoltaic devices¹¹⁷ (Figure 1.16).

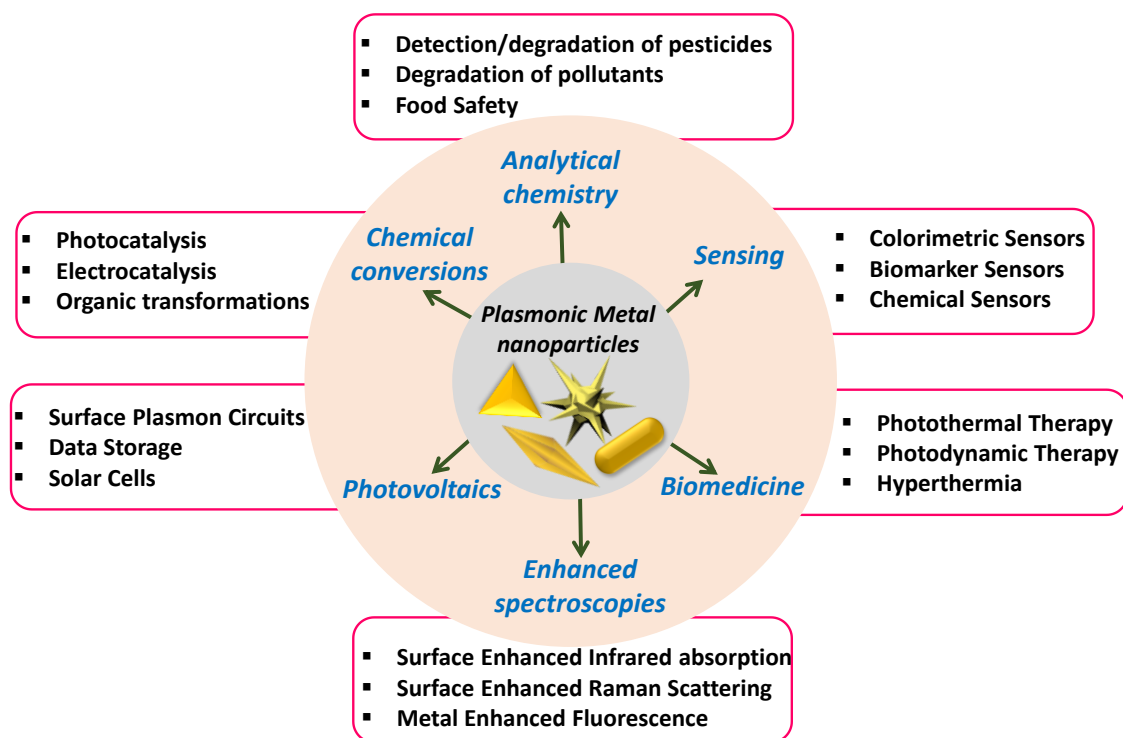


Figure 1.16. Diagrammatic illustration of plasmonic nanoparticle applications.

Plasmonic nanomaterials have recently been recognized as favorable platforms for catalytic applications.^{118, 119} The LSPR of plasmonic metal nanoparticles itself serves as the catalyst to drive chemical processes for various applications with enhanced efficiency.^{91, 120-123} The direct interaction of LSPR generated in plasmonic metal nanoparticles and nearby molecules present in close proximity to plasmonic metal nanoparticles aids in inducing, triggering, or enhancing chemical transformations/reactions/processes. Following pioneering research on plasmonic-based nanocatalysts in the early 2000s, there has been a surge in interest in LSPR-driven catalysis over the two decades. Tian et al. opened up a way for the development of a new type of photocatalyst using plasmonic Au NPs as a photosensitizer for TiO₂ films used in visible light induced photooxidation of methanol and ethanol.¹²⁴

1.6.1. Plasmon induced photocatalysis

When Awazu et al. observed the photocatalytic degradation of methylene blue prompted by plasmonic Ag nanoparticles incorporated with titanium dioxide films, they introduced the term "plasmonic photocatalysis."¹²⁵ Taking motivation from such

beginning works, a wide range of metal nanoparticle-based catalysts have been examined, hence broadening the range of reactions induced or enhanced by LSPR of plasmonic metal nanoparticles. Control over catalytic applications of noble plasmonic metal nanoparticles is achieved by controlling and modulating the optical properties with modification in shape and size. Interestingly, plasmonic metal nanocatalysts can be developed as entirely free nanoparticles or as fully supported nanoparticles that can be arranged on supports like as metal oxide support, semiconductors, or another non plasmonic metal nanoparticle (Figure 1.17). The plasmonic photocatalysis relies on the activation of LSPR of metal nanoparticle on resonant light excitation.

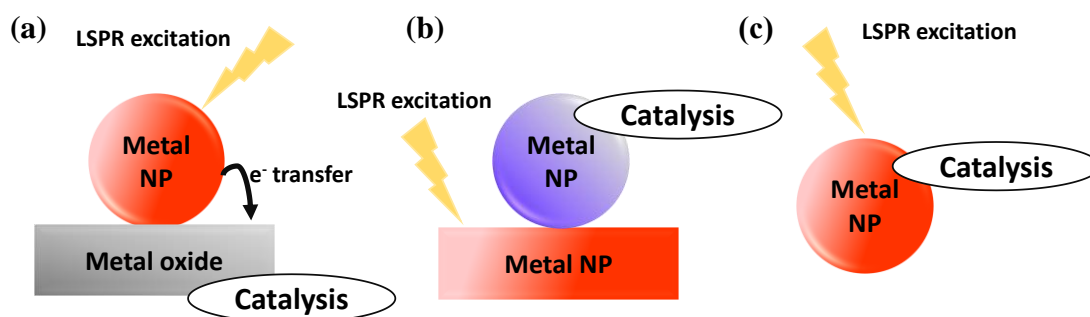


Figure 1.17. Schematic representation of (a) activation of metal oxide support for catalysis via electron transfer during plasmonic metal nanoparticle excitation, (b) non-plasmonic metal nanoparticle acting as a catalyst on illuminated plasmonic metal nanoparticle support, and (c) plasmonic metal nanoparticle itself acting as a catalyst on illumination with a light source.

The surface plasmon assisted oxidation^{126, 127} and reductive coupling reactions¹²⁸ can be carried out by using only plasmonic metal nanoparticles without assistance of catalytic and support materials. The Halas group demonstrated the potential of hot electrons generated in metal nanoparticles for plasmon induced dissociation of H₂ gas on the Au nanoparticles by LSPR at room temperature (Figure 1.18a).¹²⁹

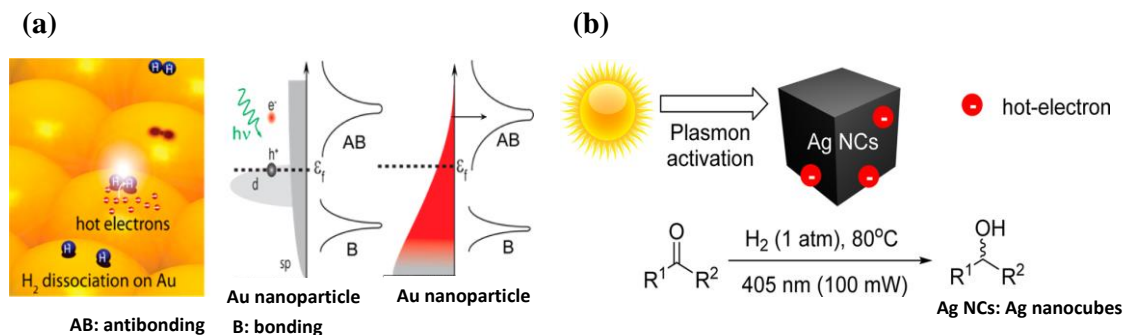


Figure 1.18. Schematic demonstration of (a) H₂ dissociation on the Au nanoparticle surface, and hot electron excitation in Au nanoparticle on light illumination along with transfer of hot electron to antibonding orbital of adsorbed H₂ molecule (Reprinted with permission from ref.¹²⁹, 2013 American Chemical Society), and (b) electrons generated by plasmon activation in Ag nanocubes exposed to visible light utilized to hydrogenate carbonyls (Adapted with permission from ref.¹³⁰, 2017 American Chemical Society).

Landry et al. also demonstrated that at atmospheric pressure, Ag nanoparticles are effective photocatalysts for converting ketones and aldehydes to corresponding alcohols (Figure 1.18b).¹³⁰ Transfer of Hot electron to antibonding orbital of H₂ was followed by homoleptic cleavage to activate hydrogen gas. After that, the alcohol was eventually formed because of transfer of the adsorbed hydrogens.

1.6.2. SERS as a monitoring tool for plasmonic photocatalysis

Moreover, the majority of the findings on plasmonic photocatalysis were conducted using ex situ or indirect strategies.^{129, 131, 132} So, in situ techniques for identifying the basic steps of plasmon-assisted photocatalysis must be established. This requirement is met by using SERS, which emerges from SPR and has exceptionally high sensitivity.¹³³⁻¹³⁵

1.6.2.1. Surface-enhanced Raman spectroscopy (SERS)

Molecules scatter light elastically (Rayleigh scattering) or inelastically (Raman scattering). The energy of incident photon on the molecule and the state of the molecule after the scattering phenomena are unaffected in the elastic case. Thus, Rayleigh scattering does not reveal molecular state structure. However, in inelastic scattering,

photons of incident monochromatic light change frequency when they interact with a molecule's vibrational states.¹³⁶ Smekal et al. proposed the Raman effect theoretically in 1923,¹³⁷ but Indian physicist C.V. Raman discovered it experimentally in 1928 in an experiment using the sun as a light source.^{138, 139} This type of phenomenon is then known as Raman spectroscopy, named after C.V. Raman, and won the Nobel Prize in Physics in 1930 for this discovery. The major drawback of Raman effect is that it is an intrinsically weak phenomenon. Raman scattering occurs in about one out of every 10^7 photons. As a result of low analyte concentrations or due to poor Raman scattering cross-section of most molecules, the intensity of Raman signal is extremely low. The high fluorescence of the molecule can sometimes mask the Raman signals. This problem is solved by SERS which is a non-invasive spectroscopic technique that involves the enhancement of Raman signals from molecules over several orders of magnitude when they are adsorbed on metal nanoparticles or rough surfaces of metals. The discovery of the SERS effect was a watershed moment in Raman spectroscopy. Fleischmann and colleagues unintentionally discovered it in 1974 while measuring the Raman signals of pyridine adsorbed on rough Ag electrodes, and they attributed this enhancement in Raman signal to a surface-area effect.¹⁴⁰ Jeanmaire and Van Duyne,¹⁴¹ as well as Albrecht and Creighton,¹⁴² individually recognized that the enhanced intensities observed could not be explained merely by an increase in the number of adsorbed molecules as surface area increased, and they proposed that amplification of intensity of Raman signal occurred in the adsorbed state. With the addition of the LSPR effect, the intensity of Raman signal corresponding to adsorbed molecules on metal surfaces can be significantly increased. The SERS effect enables Raman spectroscopy to be used as an in situ analytic method for evaluating the details of molecular arrangement and alignment of surface species. SERS-based measurements are used in material science, chemistry, forensic science, biology, and biotechnology to analyze and provide molecular-level information on a wide range of chemical, biological, and physical processes on surfaces and interfaces.

1.6.2.1.1. Mechanism of SERS

Despite SERS's rapid growth, its mechanism is still unclear. Jeanmaire and Van Duyne suggested an electric field enhancement mechanism to amplify Raman signals, while

Albrecht and Creighton suggested resonance Raman scattering by electronic states of molecules broadened by molecule-metal surface interaction. Nowadays, two mechanisms have gained wide acceptance: electromagnetic enhancement and chemical enhancement (Figure 1.19).

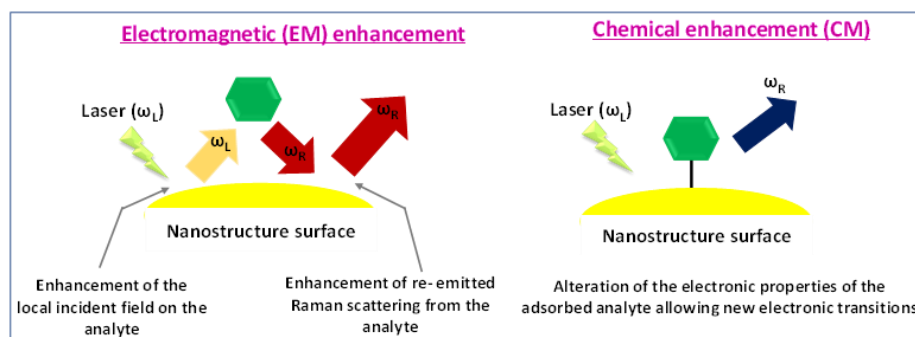


Figure 1.19. A simplified representation of electromagnetic and chemical enhancements in SERS.

It is widely assumed that the intensity boosting of Raman signals is caused primarily by electromagnetic enhancement, with contribution from charge transfer due to interactions between both the metal nanoparticle and adsorbate molecule.¹⁴³⁻¹⁴⁶

1.6.2.1.1.1 Electromagnetic enhancement (EM) and enhancement factor (EF) in SERS

When electromagnetic radiation excites LSPs in plasmonic metal nanoparticles, far-field incident light accumulates at sharp corners, tips, or curves, increasing the local electromagnetic field. The SERS effect is caused by electromagnetic enhancement, which improves EM fields during excitation and scattering to up to 10^{10} . SERS electromagnetic field enhancement involves two steps. (Figure 1.20).¹⁴⁷

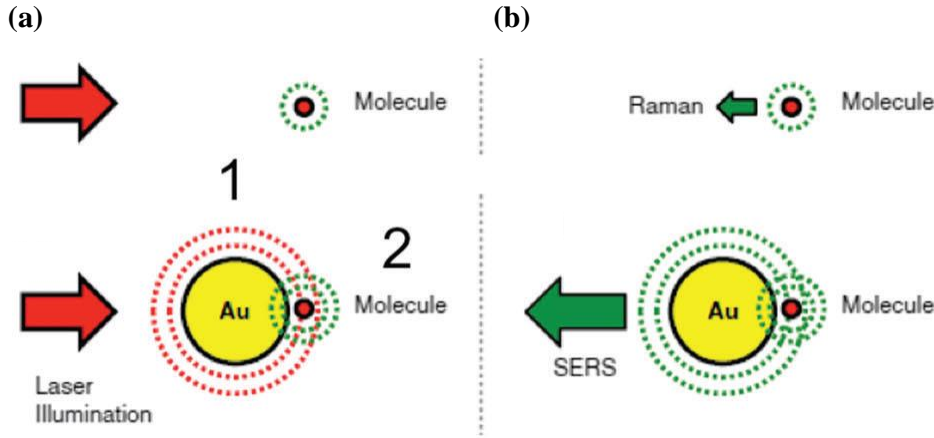


Figure 1.20. Mechanistic illustration of basic EM SERS. The AuNP (1) strengthens both the incident laser field (a) and the scattered field (b), significantly increasing the intensity of scattered Raman signal from a neighbouring molecule (2) (Reproduced with permission from ref.¹⁴⁸, 2012 IOP Publishing).

First, the local electromagnetic field around the plasmonic metal nanoparticle increases at the incident frequency (ω_0). Thus, plasmonic metal nanoparticles act as receiving optical nano-antennae to convert far field incident light to near field. In the second step, the mutual reciprocity excitation between the induced dipole of molecules near metal nanoparticles and their dipoles enhanced the electromagnetic field. Thus, plasmonic metal nanoparticles act as optical nano-antennae by transferring the near field to the far field at the Raman scattered frequency (ω_R). The total SERS EF is determined by the EF of both the first $G_1(\omega_0)$ and the second step $G_2(\omega_R)$ and, is determined by the equation below (Equation 1.7).

$$G = G_1(\omega_0) G_2(\omega_R) = \frac{|E_{loc}(\omega_0)|^2 |E_{loc}(\omega_R)|^2}{|E_0(\omega_0)|^2 |E_0(\omega_R)|^2} \approx \frac{|E_{loc}(\omega_R)|^4}{|E_0(\omega_0)|^4} \quad \text{Equation 1.7}$$

Where E_0 and E_{loc} are the local electric fields produced when plasmonic metal nanoparticles are absent and present, respectively. As indicated by the Equation 1.7, SERS EF is nearly proportional to the fourth power of the local electric field enhancement. As a result, the stronger the intensity of the generated electric field, the higher will be SERS EF.^{149, 150} The distance between the metal nanoparticle and nearby molecule, its size and shape, and the nearby molecule's alignment with the plasmonic metal nanoparticle's surface all affect EF intensity. The most common nanoparticles

have spherical morphology and moderate Raman signal enhancement due to their high symmetry. Thus, "plasmonic hotspots" made from spherical nanostructures have moderate SERS activity. However, rationally designed nanoparticles with sharp edges and corners, such as Au and Ag nanoflowers, nanocubes, nanostars, and mesocages, have much higher SERS activity than spherical ones.¹⁵¹ Figure 1.21 a, b, and c depicts the enhancement of EM field intensity contours of different shaped Au nanostructures such as nanosphere, nanotriangle, and nanorod procured from finite-difference time-domain simulations (FDTD) studies.¹⁵² Also, the energy loss spectroscopy (EELS) map indicates higher localization of SPR at the sharp tips of Au nanostar (Figure 1.21d).¹⁵³

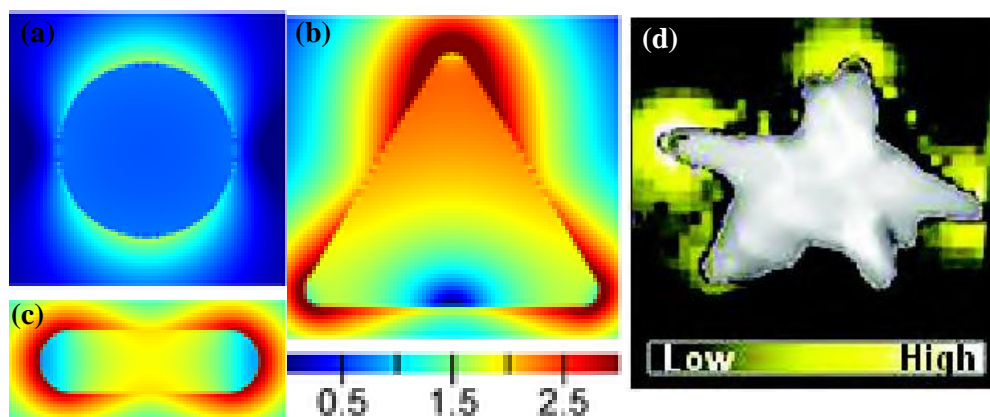


Figure 1.21. EM enhancement contours of (a) a nanosphere, (b) a nanotriangle, and (c) a nanorod in logarithmic scale (Adapted with permission from ref.¹⁵², 2014 Wiley-VCH Verlag GmbH & Co. KGaA, Weinheim), (d) EELS intensity map of a nanostar (Reprinted with permission from ref.¹⁵³, 2009 American Chemical Society).

Due to their unique structure, Au nanostars have higher SERS EFs than spherical, nanorod, or nanotriangle morphologies. SERS EFs of 10^9 - 10^{10} can be achieved using sharp-tipped Au nanostars.^{153, 154} Due to these important properties, Au nanostars are used in many SERS-based sensing/detection, catalysis, and other applications.^{151, 155, 156}

1.6.2.1.1.2 Chemical enhancement (CE) in SERS

Although EM field enhancement should be the only nonselective amplifying factor for Raman scattering for all molecules bound on a metal nanostructure surface, CO and N₂ SERS intensities vary by a factor of 200 under identical experimental conditions. This finding is hard to explain with EM enhancement alone. This finding suggests that apart

from the EM enhancement which relies on the LSPR effect, there is an additional type of SERS enhancement that is usually described as chemical enhancement (CE).¹⁵⁷ The CE mechanism in SERS is related to electron transfer among both adsorbed molecule and nanoparticle substrate. Its existence is still debated¹⁵⁰ and the contribution of CE mechanism is considered to be much smaller than that of EM enhancement. The CE mechanism is largely dependent on the adsorbed molecule on the SERS substrate (Equation 1.8).^{150, 158}

$$G_{SERS}^{CE} = \frac{\sigma_K^{ads}}{\sigma_K^{free}} \quad \text{Equation 1.8}$$

σ_K^{ads} and σ_K^{free} are indeed the Raman cross sections of the adsorbed and free molecule's K^{th} vibrational modes, respectively.

CE mechanism can be categorized into three types of significant contributions.^{159, 160} (Figure 1.22). (1) A Raman resonance effect caused by resonance of incident light with an electronic transition in the adsorbed molecule, (2) A charge-transfer effect in which incident light resonates with a molecule - metal or metal - molecule transition, and (3) A non-resonant CE effect caused by overlapping of orbitals in ground states of an adsorbed molecule and the metal. The input of the charge-transfer effect (2) to SERS is significantly stronger than the other two modes (1, and 3) and is based primarily on changes in polarizability of an adsorbed molecule on the metal nanoparticle surface, which can result in the formation of a new metal-analyte complex. The electronic orbitals of newly formed chemical complexes are drastically altered in comparison to the analyte's original orbital configuration, allowing intrinsic electronic transitions to occur within the metal-molecule complexes.¹⁶¹ This effect is observed due to the energy difference that exists between the highest occupied molecular orbital (HOMO) of a metal nanoparticle and the lowest unoccupied molecular orbital (LUMO) of the adsorbed molecule. Creighton, for example, discovered in 1986 that SERS spectrum of pyridine molecule absorbed on the surface of Cu and Ag substrates has four intense peaks at 629, 1005, 1210, and 1590 cm^{-1} , as opposed to the normal Raman spectrum of pyridine, which has very weak peaks at 629, 1210, and 1590 cm^{-1} and a strong peak at

1005 cm^{-1} . This enhancement in the a_1 modes of pyridine has been credited to charge transfer effect from the metal to pyridine's lowest unoccupied π^* orbital.¹⁶²

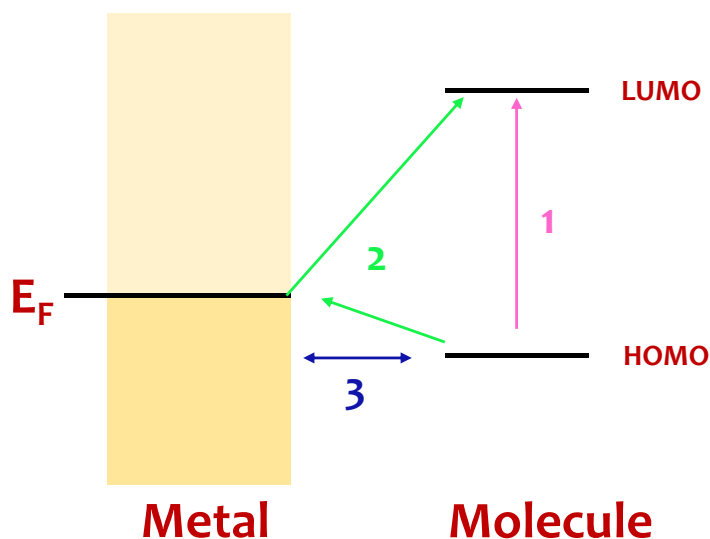


Figure 1.22. Schematic description of the three contributors to CE mechanism.

Highlights of enhancement mechanisms:

1. EM is much stronger than the CE.
2. The severe EM field is confined in sub-nm gaps between plasmonic nanoparticles or at the sharp edges of nanostructures.
3. The combination of localized and extended surface plasmons can result in much stronger enhancements due to significantly increased Raman cross sections.

1.6.2.2. SERS substrates for plasmonic photocatalysis

Because SERS and plasmon assisted reactions share the same origin i.e., SPR, SERS has the ability to impart in situ fingerprinting of surface adsorbates during plasmonic photocatalysis. As a result, the plasmon assisted chemical reactions have been demonstrated since 2010. Based on theoretical and experimental findings, the Sun group evidenced from SERS that the dimerized product p,p'-dimercaptoazobenzene (DMAB) is formed from p-aminothiophenol (PATP) by selective catalytic oxidation reaction of PATP on Ag nanoparticles (Figure 1.23a).¹⁶³ SERS is regarded as a non-invasive approach for providing fingerprint vibrational information of the adsorbed surface molecules. Tian's research group demonstrated, using SERS, that PATP

molecules can undergo chemical transformation i.e., oxidative coupling reaction to produce DMAB on silver electrodes (Figure 1.23b).¹⁶⁴

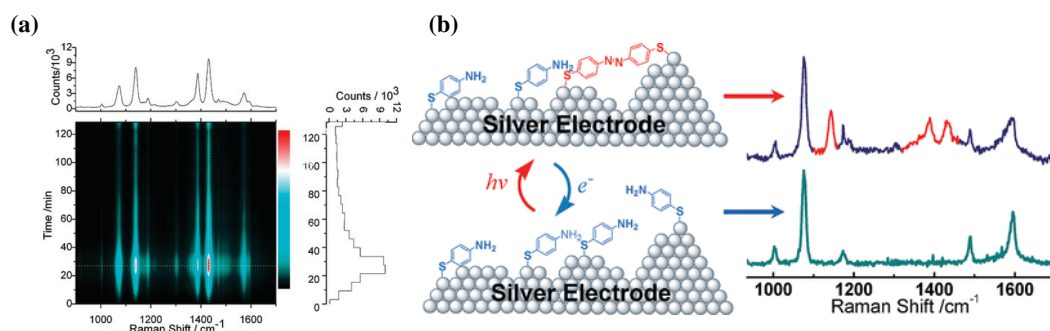


Figure 1.23. (a) The time-dependent SERS of DMAB at molecular concentration, M (Adapted with permission from ref.¹⁶³, 2010 American Chemical Society), and (b) Transformation of PATP adsorbed on Ag electrode to DMAB during electrochemical SERS measurement and corresponding SERS spectra (Reprinted with permission from ref.¹⁶⁴, 2010 American Chemical Society).

Decarboxylation reaction is another well-known example of plasmon photocatalysis that has sparked significant attention in organic synthesis. Many research groups have carried out the decarboxylation reaction catalysed by metals, but rough conditions such as toxic metals and harsh organic solvents have been involved.¹⁶⁵⁻¹⁶⁷ For the decarboxylation reaction, 4-mercaptobenzoic acid (4-MBA) has been chosen as the SERS probe because of its strong interaction with noble metals, primarily via S-metal bonds, contribute to improved SERS signals. Zong et al. were the first group to report on the plasmon-induced decarboxylation of 4-MBA.¹⁶⁸ As a source of SPR, they developed a uniform monolayer film of Au nanoparticles and adsorbed MBA molecules onto the Au nanoparticles. The new Raman peaks observed in SERS spectra that differ significantly from the reactant SERS spectra are recognised as the peaks corresponding to decarboxylation product i.e., thiophenol (TP) (Figure 1.24).

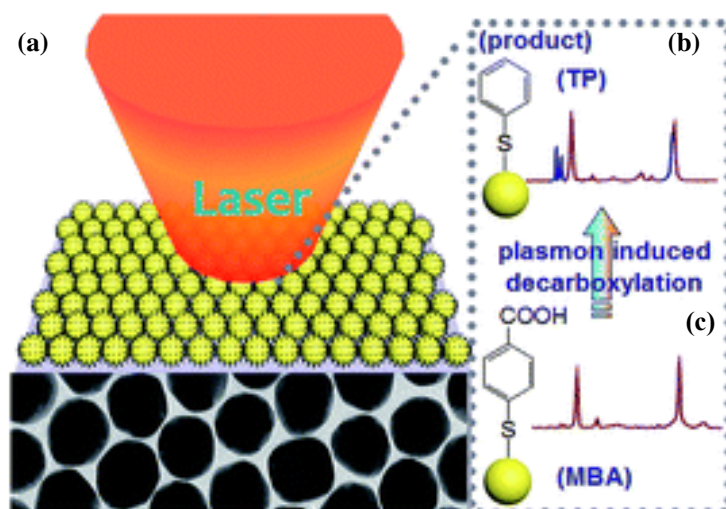


Figure 1.24. (a) Illustration of the plasmon-driven decarboxylation of 4-MBA to TP, (b) SERS spectra collected before 4-MBA decarboxylation, and (c) SERS spectra collected after decarboxylation of 4-MBA into TP (Adapted from ref.¹⁶⁸, 2014 Royal Society of Chemistry).

The plasmonic metals serve two functions in above mentioned plasmon induced chemical conversion reactions: (1) harvest light to generate hot carriers that will catalyze the chemical reaction, and (2) act as a SERS substrate to boost the Raman signal. In this type of plasmonic photocatalysis, both the CE and EM mechanisms are involved. The former is in responsible of converting the reactant into the required product, with characteristic peaks in the SERS spectrum that differ from the product peaks. The latter mechanism is in charge of increasing the intensity of the product's characteristic Raman peaks.

1.6.2.3. SERS for small molecules detection

High-performance liquid chromatography or gas chromatography, combined with mass spectrometry, quantifies environmental pollutants and dyes. Despite their high specificity, sensitivity, and accuracy, all these techniques require complex equipment and lengthy procedures. On-site analysis requires sensitive, simple, and easy detection methods. SERS is one of the most powerful and versatile analytical techniques due to its high sensitivity (till single molecule detection), unique "fingerprint" accuracy, and non-destructive molecule sensing.¹⁶⁹ These advantages make SERS a good platform for

environmental monitoring, food analysis, disease diagnosis, and more.^{159, 170, 171} Because of ongoing breakthroughs in nanofabrication methods, it is now possible to develop rationally designed plasmonic metal nanomaterials.^{172, 173} Specifically, SERS substrates made of Au and Ag plasmonic metal nanoparticles are widely acknowledged to be essential for effective Raman signal enhancement owing to their unique property of LSPR. Thus, EF depends heavily on the LSPR position, which is affected by shape, size, and medium. Due to higher electric field generation, sharp and tipped anisotropic nanoparticle edges are preferred over smooth surfaces. Because of their shapes and sizes, anisotropic nanoparticles create massive hotspots for sensing analyte molecules.¹⁷⁴⁻¹⁷⁸ Patel et al. utilized the Au nanoflowers for SERS based sensing and Raman signal enhancement of rhodamine 6G dye (Figure 1.25).¹⁷⁹

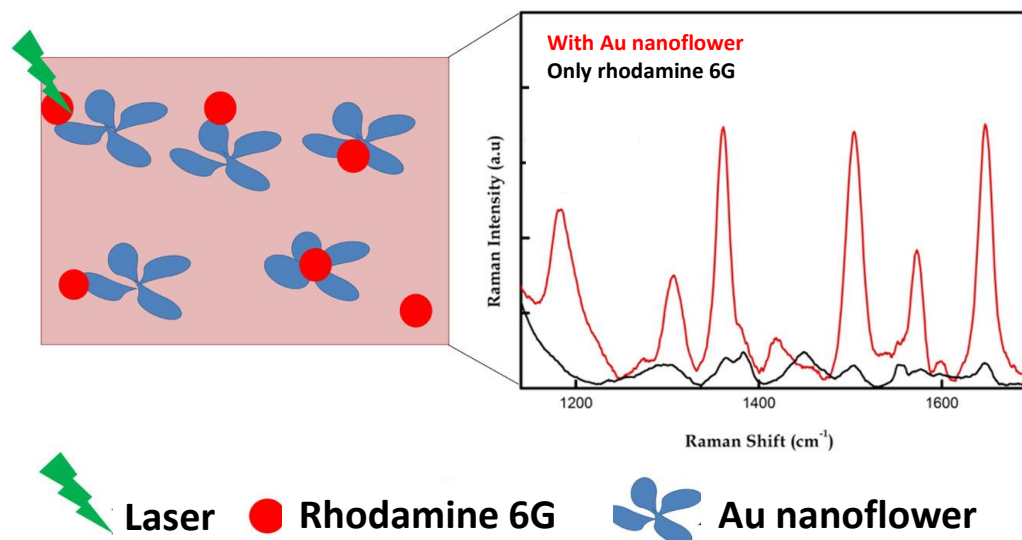


Figure 1.25. Representation of Au nanoflowers utilized for the SERS enhancement of Raman signals of rhodamine 6G dye (Adapted from ref.¹⁷⁹, 2018 Elsevier).

At 10^{-10} M concentrations, Au nanoflowers detected rhodamine 6G dye molecules. Au nanoflowers boost Raman signal enhancement with EFs of 10^6 . Au nanoflowers show the SERS effect, but Au nanospheres do not improve Raman signals. Au nanoflowers' sharp corners explain their high EF value compared to Au nanospheres. Nanoflower edges increase electromagnetic field, which interacts with adsorbed molecules and boosts Raman signal.

SERS can detect single molecules by positioning plasmonic nanoparticles over templates like DNA origami, which allow precise control over nanoparticle position and

gap. This gap between nanoparticles creates a strong plasmonic hotspot with higher electric field enhancements to detect analyte molecules with more sensitivity. Swati et al. demonstrated the synthesis of Au nanostar dimers with tunable interparticle gap and controlled stoichiometry assembled on DNA origami for single analyte detection of Texas red (TR) dye with EF of 2×10^{10} and 8×10^9 for interparticle gap 7 nm and 13 nm using 633 nm laser, respectively (Figure 1.26).¹⁰⁰

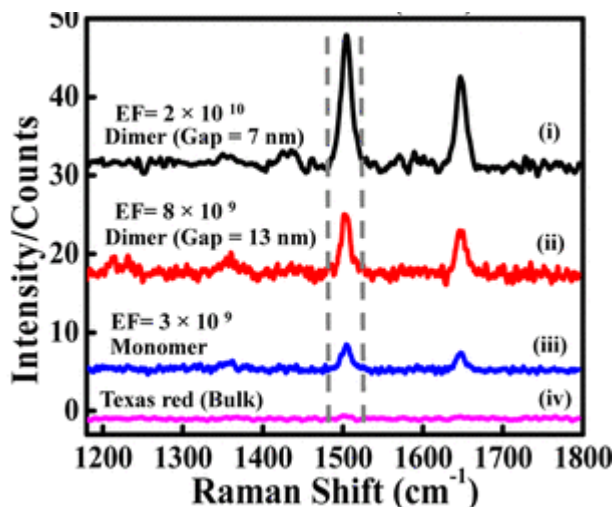


Figure 1.26. SERS spectra of TR dye bound to Au nanostar dimers assembled on DNA origami with average gaps of 7 nm (i) and 13 nm (ii), and TR dye bound to Au nanostar monomer on DNA origami (iii) and bulk TR dye (iv) (Adapted from ref.¹⁰⁰, 2016 American Chemical Society).

Such anisotropic nanostructures can be used for the identification of biomarkers, the detection of dyes and pesticides in food, and the detection of environmental pollutants with high accuracy and simple experimental setups that would otherwise be time-consuming.

1.6.3. Photothermal therapy

Photothermal therapy is a major use of plasmonic nanomaterials. Plasmonic nanoparticles' large optical cross sections absorb and scatter light. Photothermal effect occurs when absorbed light is converted into heat energy by photophysical processes like electron-electron or electron-phonon relaxations.¹⁸⁰ These femtosecond- and

picosecond-scale relaxation processes cause the surface of a metal to become extremely hot. Surface temperature decreases due to relaxation brought on by phonon-phonon interaction. It means that the nanoparticles radiate heat into their surroundings, warming any molecules or species nearby. (Figure 1.27a).

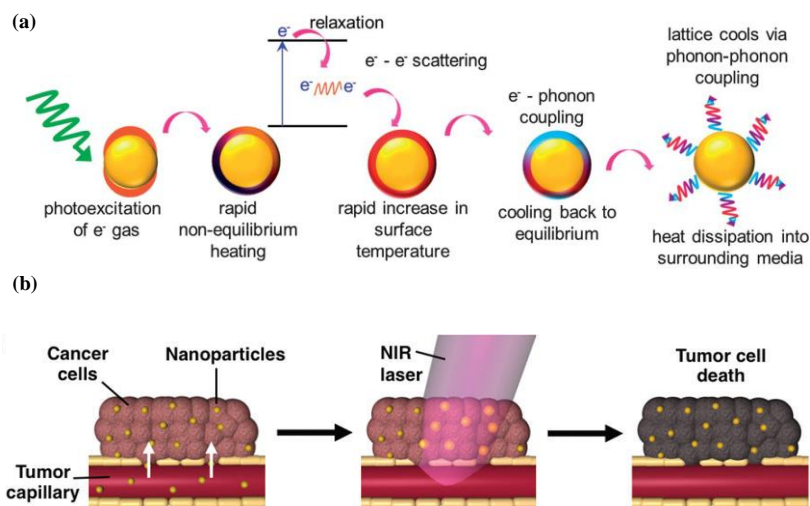


Figure 1.27. (a) Schematic representation of photothermal effect by plasmonic metal nanostructures (Adapted from ref.¹⁸¹, 2014 RSC Publishing), and (b) PTT is represented by irradiating plasmonic nanoparticles with NIR light to generate heat and kill the surrounding tumor tissue (Reprinted with permission from ref.¹⁸², 2017 Wiley-VCH Verlag GmbH & Co. KGaA).

This photothermal effect of plasmonic nanoparticles is known as plasmonic photothermal therapy (PTT) when used to destroy cancer cells attached or present in close contact to nanoparticles (Figure 1.27b).¹⁸³ Au nanoparticles are of particular significance among the noble plasmonic metal nanoparticles due to its biological and chemical stability, minimal toxicity in biological systems, and a wide range of surface functionalizations with ligands like as proteins, DNA, and antibodies.¹⁸⁴ As the photothermal effect is highly depends upon the nanoparticle's absorption and scattering cross sections which are strongly reliant on nanoparticle's size and shape as well as the wavelength of light used.¹⁸⁵ Jain et al. explored the size and shape dependent changes in scattering and absorption behaviour utilizing Mie theory calculations.¹⁸⁶ It was discovered that as the size of Au nanospheres increased from 20 to 80 nm, the comparative contribution of absorption to total extinction (Extinction cross-section =

Absorbance cross-section + Scattering cross-section)¹⁸⁷ decreased while the contribution of scattering increased. As a result, increasing the size of Au nanospheres from 20 to 80 nm red shifts the plasmon band from 520 to 580 nm, which is in the visible region. Although Au nanoshells have a similar extinction cross-section as Au nanospheres for same size,¹⁸⁶ tuning the thickness of the nanoshell causes a large red shift in the plasmon absorption band towards the NIR region (biological window) which is advantageous for photothermal therapy. The Halas group had developed core-shell nanostructures composed of silica core of size 100 to 150 nm and thin Au shell with thickness 5 to 20 nm.⁵⁸ The absorption band is red-shifted for thinner shells.¹⁸⁸ Au nanorods absorb NIR light like Au nanospheres and nanoshells because their SPR band position is sensitive to aspect ratio (length/width). Redshift the longitudinal plasmon band by manipulating nanorod length. In addition to Au nanospheres, nanoshells, and nanorods, Au nanocages^{189, 190} and Au nanostars^{191, 192} (Figure 1.28) have been revealed in photothermal therapies because of their enhanced light absorption in the visible and NIR regions owing to their SPR oscillations. Sharp tips, spikes, and edges in nanostructures increase the electromagnetic field and temperature distribution at the tip head, transducing plasmonic heat for non-invasive photothermal abscission of cancer cells.¹⁹² Due to their high absorption cross-sections, Au nanostars are better for photothermal effect than Au nanorods with the same longitudinal plasmon bands.¹⁹¹

Hence, photothermal effect is highly dependent on the

1. Extinction cross- section (mainly absorption cross- section) of nanoparticles.
2. Size of nanoparticles.
3. Shape of nanoparticles.

When the frequency of incident light matches the NIR absorption band of Au nanoparticle, enhanced absorption occurs, contributing to higher photothermal conversion efficiency. The "photothermal conversion efficiency" of a nanoparticle determines its scattering and absorption efficiency. Thus, PTT material selection has become increasingly dependent on photothermal (light to heat) conversion efficiency. Maestro et al. examined the heating efficiency of Au nanorods, nanoshells, nanostars, and nanocages with LSPR band positions in NIR (~ 808 nm, within the first biological window).¹⁹³





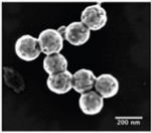
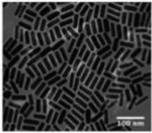
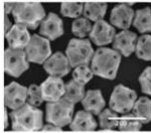
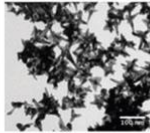
	Nanoshells	Nanorods	Nanocages	Nanostars
Schematic				
SEM				
Size for PTT	~150 nm diameter	~10 nm x 40 nm	~40-60 nm length	~45-120 nm
Stage of development	Clinical trials: lung, head & neck, and prostate cancer	Preclinical	Preclinical	Preclinical
Unique features	Core:shell structure	Two resonance peaks	Drug loading capabilities	Large surface area for bioconjugation

Figure 1.28. The four most common AuNP shapes for PTT are silica/Au core – shell nanostructures, Au nanorods, hollow Au nanocages, and Au nanostars (Reprinted with permission from ref.¹⁸², 2017 Wiley-VCH Verlag GmbH & Co. KGaA).

1.6.4. Photochemical water splitting

Nowadays, scientists have been inspired to establish renewable and environmentally friendly energies as they become more aware of the depletion of fossil fuels as well as the degradation of the natural ecosystem. Because of its high energy potential and environmentally friendly nature, hydrogen (H₂) is recognized as the easiest and most appealing fuel for power generation. Photocatalytic water splitting using solar energy to produce H₂ and O₂ is intriguing. Semiconductors are known for splitting water molecules into oxygen and hydrogen.¹⁹⁴ Fujishima and Honda's 1970 photochemical water splitting demonstration under ultraviolet irradiation piqued researchers' interest.¹⁹⁵ Since then, the TiO₂ semiconductor has unquestionably known to be among the best catalysts for photochemical water splitting.¹⁹⁶ Because of large band-gap of semiconductors (3.2 eV for TiO₂¹⁹⁷ and 3.37 eV for ZnO¹⁹⁸), they can be excited by UV or near UV radiation only, which accounts for only 4% of the light coming from the sun on Earth. In order to effectively exploit the visible part of light, semiconductors are decorated with plasmonic metal nanoparticles to enhance their photochemical

efficiencies. Designing Au@semiconductor core-shell nanoparticles not just protect the Au nanoparticle core from agglomeration and chemical corrosion during the harsh reaction conditions, but they also provide an optimum and intimate interaction between semiconductor and Au nanoparticle, which really is essential for plasmon - exciton interactions and as well as charge transfer between the core and shell.^{199, 200} Combining Au nanoparticles with ZnO semiconductor enables the absorption of visible light through LSPR effect. The high chemical stability of Au nanoparticles also aids in the reduction of inherent photo - corrosion problem encountered while using only ZnO.²⁰¹ Moreover, integrating plasmonic Au nanoparticles with ZnO in a well-defined core-shell nanostructure are extremely desirable in order to better comprehend optical absorption, charge transfer, and other properties.

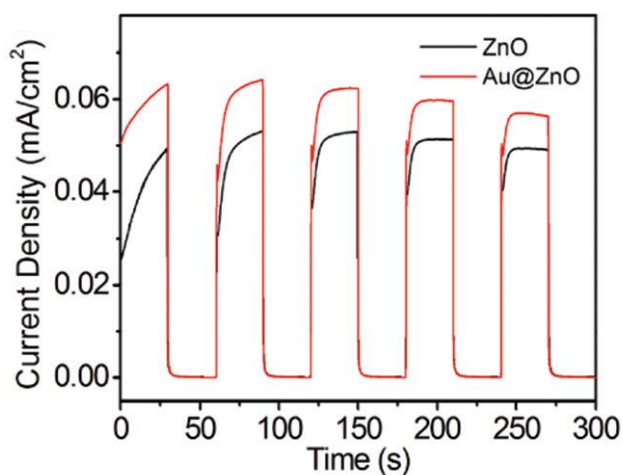


Figure 1.29. Photocurrent curves of Au@ZnO core-shell nanostructures and pure ZnO nanoparticles at an applied potential of 0.5 V vs. Ag/AgCl under simulated sunlight irradiation during on/off cycles within 300 s (reprinted with permission from ref.²⁰², 2016 Royal Society of Chemistry).

Shao et al. prepared core-shell Au@ZnO nanostructures for visible-light photocatalytic and photoelectrochemical properties.²⁰² Further to that, they observed that when exposed to simulated sunlight, Au@ZnO as a photo-electrode material exhibits an elevated photocurrent density as compared to pure ZnO nanoparticles (Figure 1.29). This enhancement is due to harvesting of visible light by plasmonic core Au

nanoparticles. By optimizing the size and shape of the metal nanoparticle and semiconductor, photocatalysts with improved efficiencies can be designed for enhanced photochemical water splitting.^{203, 204}

1.6.5. Electrocatalysis

Apart from photochemistry, electrochemistry has emerged as a renewable energy pathway capable of meeting the ever-increasing demand for energy. Hence, Electrocatalysis is, without a shadow of a doubt, a very significant field of study. There is a rising motivation to establish highly stable, durable, active, and budget friendly electrocatalysts because even a slight improvement in efficiency will result in a recognisably significant difference. The noble metals platinum (Pt), palladium (Pd), iridium (Ir), rhodium (Rh), and gold (Au) have great electrocatalytic potential. It is well established that the surface properties of noble metallic nanoparticles significantly impact their overall catalytic behaviour.²⁰⁵ Conventional catalysts such as Iridium oxide (IrO_2) and Ruthenium oxide (RuO_2) in acid media have proven to be the most effective electrocatalysts for oxygen evolution reaction (OER) to date.²⁰⁶ On the other hand, nanoparticles of Pt have proven to be the most cutting-edge electrocatalysts for hydrogen evolution reaction (HER),²⁰⁷ oxygen reduction reaction (ORR),²⁰⁸ and hydrogen oxidation reaction (HOR).²⁰⁹ The electrochemical production of hydrogen through water splitting is one of these plausible processes that has the potential to effectively and efficiently mitigate the ongoing global energy crisis and lead to a solution that is both sustainable and efficient. Regrettably, due to the slow kinetics of the anodic OER, large-scale synthesis of hydrogen from electrochemical water splitting is still a cause for concern.²¹⁰ Since the cathodic HER is a two-electron-transfer reaction process and OER is a complex four-electron-proton coupled reaction,²⁰⁶ a relatively high overpotential is required to overcome the kinetic energy pathway for OER than it is for HER (high overpotential (η), $\eta_a > \eta_c$, where η_a and η_c are anodic and cathodic overpotentials, respectively (Figure 1.30).

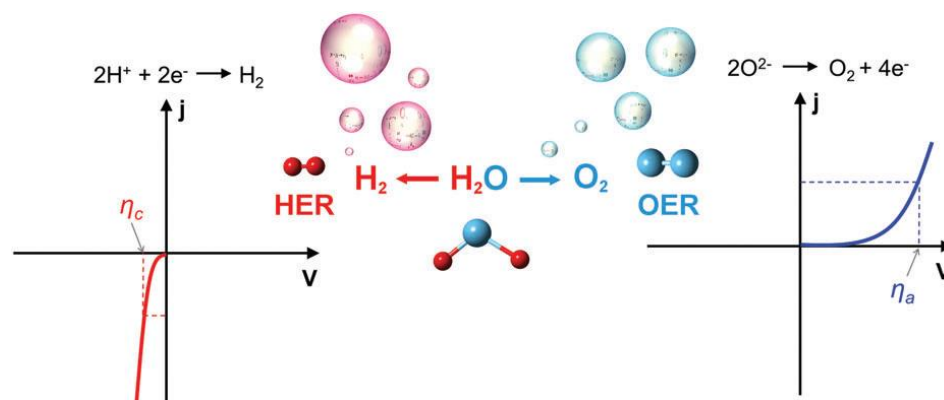


Figure 1.30. Polarization curves for HER and OER (reprinted with permission from ref.²⁰⁶, 2017 Royal Society of Chemistry).

Standard electrocatalysts for OER include IrO_2 and RuO_2 , which perform well in both alkaline and acidic electrolytes. However, such environments easily oxidize these catalytic materials, which are scarce and unsustainable. Recent research has focused on transition metal oxide catalytic activities. Due to their multi-functionality and synergistic effects, noble metals have also been studied for their potential use in many catalytic processes.⁹³ Due to synergistic effects among two or more components, composite nanomaterials typically illustrate distinctive catalytic and electrocatalytic properties when compared with their individual counterparts.²¹¹ The performance of the catalysts is heavily influenced by the characteristics of the interface that exists between the active materials and the matrix.²¹² Hence, in order to achieve conducive interfaces that will result in increased catalytic activity, some core-shell nanomaterials have been synthesized.²¹³ Au is unquestionably the most common core metal to enhance the OER performance of an electrocatalyst owing to its higher conductivity²¹⁴ and ability to adsorb hydroxide ions,²¹⁵ which are essential for the OER process to occur. Zhuang et al. synthesized core-shell nanocatalyst comprised of $\text{Au@Co}_3\text{O}_4$ with uniform particle size and shell thickness.²¹⁶ The resultant catalyst exhibited an efficient synergistic effect between the core and shell material. As a result, The $\text{Au@Co}_3\text{O}_4$ nanocrystals showed a current density in the OER that was 7 times higher than a mixture of Au and Co_3O_4 nanocrystals or Co_3O_4 nanocrystals alone, and 55 times higher than Au nanocrystals alone (Figure 1.31).

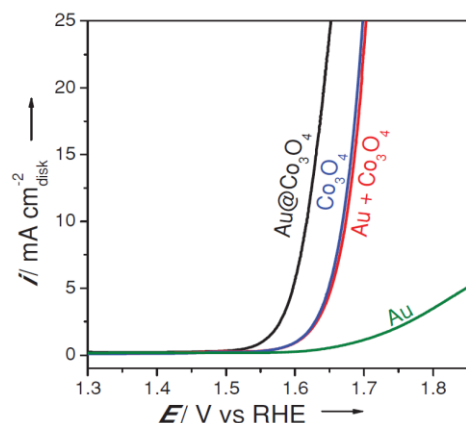


Figure 1.31. Linear sweep polarization curves performed for $\text{Au@Co}_3\text{O}_4$, Co_3O_4 , and Au nanocrystals (reprinted with permission from ref.²¹⁶ 2014, Wiley-VCH Verlag GmbH & Co. KGaA).

There is a one-to-one relationship between the surface area of the nanoparticles and their OER activities. The complex nanostructures such nanowires, nanofibers, and flower shaped nanostructures provide much higher active surface area which contribute to better performance of catalysts towards electrochemical processes.²¹⁷⁻²¹⁹ Catalysts' active sites are the sites of electrochemical interactions, where charges are stored and/or transferred. Therefore, improved performance is a direct result of increased electrochemically active surface area because more electrolyte ions can reach the surface, where they can participate in electrochemical reactions.²²⁰ Moreover, Au nanostructures, with their potential surface-sensitive applications, have recently attracted a lot of attention.²²¹

The noble nanomaterials have attracted a lot of attention due to their exceptional absorption, scattering, and field enhancement providing widespread use in fields as diverse as biomedicine, energy, and sensing devices. Despite noble nanomaterial's remarkable potential, it has not yet been fully exploited to bring fabricated nanomaterials from research papers to commercial uses. There is a substantial scope for further development.

References

1. A. Comin and L. Manna, *Chemical Society Reviews*, 2014, **43**, 3957-3975.
2. G. V. Naik, V. M. Shalaeve and A. Boltasseva, *Advanced Materials*, 2013, **25**, 3264-3294.
3. A. Agrawal, S. H. Cho, O. Zandi, S. Ghosh, R. W. Johns and D. J. Milliron, *Chemical Reviews*, 2018, **118**, 3121-3207.
4. Y. Li, Z. Li, C. Chi, H. Shan, L. Zheng and Z. Fang, *Advanced Science*, 2017, **4**, 1600430.
5. K. A. Willets and R. P. Van Duyne, *Annu. Rev. Phys. Chem.*, 2007, **58**, 267-297.
6. M. Quinten, *Applied Physics B*, 2001, **73**, 317-326.
7. F. Wagner, S. Haslbeck, L. Stievano, S. Calogero, Q. Pankhurst and K.-P. Martinek, *Nature*, 2000, **407**, 691-692.
8. M. Faraday, *Philosophical Transactions of the Royal Society of London*, 1857, 145-181.
9. G. Mie, *Annalen der Physik*, 1908, **330**, 377-445.
10. S. Ezendam, M. Herran, L. Nan, C. Gruber, Y. Kang, F. Gröbmeyer, R. Lin, J. Gargiulo, A. Sousa-Castillo and E. Cortés, *ACS Energy Letters*, 2022, **7**, 778-815.
11. A. Kumar, P. Choudhary, A. Kumar, P. H. Camargo and V. Krishnan, *Small*, 2022, **18**, 2101638.
12. J.-H. Han, D. Kim, J. Kim, G. Kim, P. Fischer and H.-H. Jeong, *Advanced Materials*, **n/a**, 2107917.
13. J. Spivey, 2014.
14. A. Roucoux, J. Schulz and H. Patin, *Chemical Reviews*, 2002, **102**, 3757-3778.
15. O. V. Salata, *Journal of Nanobiotechnology*, 2004, **2**, 3.
16. Z. Jiang, N. D. B. Le, A. Gupta and V. M. Rotello, *Chemical Society Reviews*, 2015, **44**, 4264-4274.
17. H. Malekzad, P. S. Zangabad, H. Mirshekari, M. Karimi and M. R. Hamblin, *Nanotechnology Reviews*, 2017, **6**, 301-329.
18. V. V. Mody, R. Siwale, A. Singh and H. R. Mody, *Journal of Pharmacy & Bioallied Sciences*, 2010, **2**, 282-289.
19. D. Chen, X. Zou, F. Dong, C. Zhen, D. Xiao, X. Wang, Q. Wu, Y. Cao and J. Tu, *ACS Applied Materials & Interfaces*, 2021, **13**, 33006-33014.
20. J. Wang, H. Wang, H. Wang, S. He, R. Li, Z. Deng, X. Liu and F. Wang, *ACS Nano*, 2019, **13**, 5852-5863.
21. J. E. Eixenberger, C. B. Anders, K. Wada, K. M. Reddy, R. J. Brown, J. Moreno-Ramirez, A. E. Weltner, C. Karthik, D. A. Tenne, D. Fologea and D. G. Wingett, *ACS Applied Materials & Interfaces*, 2019, **11**, 24933-24944.
22. M. Zare, K. Namratha, S. Ilyas, A. Sultana, A. Hezam, S. L. M. A. Surmeneva, R. A. Surmenev, M. B. Nayan, S. Ramakrishna, S. Mathur and K. Byrappa, *ACS Food Science & Technology*, 2022, **2**, 763-781.
23. C. B. Ong, L. Y. Ng and A. W. Mohammad, *Renewable and Sustainable Energy Reviews*, 2018, **81**, 536-551.
24. M. B. Gawande, A. Goswami, F.-X. Felpin, T. Asefa, X. Huang, R. Silva, X. Zou, R. Zboril and R. S. Varma, *Chemical Reviews*, 2016, **116**, 3722-3811.
25. G. A. Sotiriou, *Wiley Interdisciplinary Reviews: Nanomedicine and Nanobiotechnology*, 2013, **5**, 19-30.
26. A. Gellé and A. Moores, *Current Opinion in Green and Sustainable Chemistry*, 2019, **15**, 60-66.
27. J. Krajczewski, K. Kołataj and A. Kudelski, *RSC Advances*, 2017, **7**, 17559-17576.

28. P. N. Njoki, I. I. S. Lim, D. Mott, H.-Y. Park, B. Khan, S. Mishra, R. Sujakumar, J. Luo and C.-J. Zhong, *The Journal of Physical Chemistry C*, 2007, **111**, 14664-14669.
29. R. H. Ritchie, *Physical Review*, 1957, **106**, 874-881.
30. S. A. Maier, *Plasmonics: Fundamentals and Applications*, Springer, 2007.
31. M. E. Stewart, C. R. Anderton, L. B. Thompson, J. Maria, S. K. Gray, J. A. Rogers and R. G. Nuzzo, *Chemical Reviews*, 2008, **108**, 494-521.
32. K. A. Willets and R. P. Van Duyne, *Annual Review of Physical Chemistry*, 2007, **58**, 267-297.
33. V. Amendola, R. Pilot, M. Frasconi, O. M. Maragò and M. A. Iatì, *Journal of Physics: Condensed Matter*, 2017, **29**, 203002.
34. A. J. Haes, C. L. Haynes, A. D. McFarland, G. C. Schatz, R. P. Van Duyne and S. Zou, *MRS Bulletin*, 2005, **30**, 368-375.
35. R. Gans, *Annalen der Physik*, 1915, **352**, 270-284.
36. G. C. Papavassiliou, *Progress in Solid State Chemistry*, 1979, **12**, 185-271.
37. S. Eustis and M. A. El-Sayed, *Chemical Society Reviews*, 2006, **35**, 209-217.
38. U. Kreibig and M. Vollmer, *Optical Properties of Metal Clusters*, Springer Science & Business Media, 2013.
39. P. K. Jain, K. S. Lee, I. H. El-Sayed and M. A. El-Sayed, *The Journal of Physical Chemistry B*, 2006, **110**, 7238-7248.
40. A. A. Ashkarran and A. Bayat, *International Nano Letters*, 2013, **3**, 50.
41. Y. Xia and N. J. Halas, *MRS bulletin*, 2005, **30**, 338-348.
42. N. Harris, M. J. Ford, P. Mulvaney and M. B. Cortie, *Gold Bulletin*, 2008, **41**, 5-14.
43. S. W. Prescott and P. Mulvaney, *Journal of Applied Physics*, 2006, **99**, 123504.
44. L. M. Liz-Marzán, in *Colloidal Synthesis of Plasmonic Nanometals*, Jenny Stanford Publishing, 2020, pp. 1-13.
45. S. Link and M. A. El-Sayed, *The Journal of Physical Chemistry B*, 1999, **103**, 8410-8426.
46. J. Cao, T. Sun and K. T. V. Grattan, *Sensors and Actuators B: Chemical*, 2014, **195**, 332-351.
47. X. Huang and M. A. El-Sayed, *Journal of Advanced Research*, 2010, **1**, 13-28.
48. P. K. Jain, I. H. El-Sayed and M. A. El-Sayed, *Nano Today*, 2007, **2**, 18-29.
49. E. K. Payne, K. L. Shuford, S. Park, G. C. Schatz and C. A. Mirkin, *The Journal of Physical Chemistry B*, 2006, **110**, 2150-2154.
50. F. Hao, C. L. Nehl, J. H. Hafner and P. Nordlander, *Nano Letters*, 2007, **7**, 729-732.
51. R. Alvarez-Puebla, L. M. Liz-Marzán and F. J. García de Abajo, *The Journal of Physical Chemistry Letters*, 2010, **1**, 2428-2434.
52. M. Liebrau, M. Sivi, A. Feist, H. Lourenço-Martins, N. Pazos-Pérez, R. A. Alvarez-Puebla, F. J. G. de Abajo, A. Polman and C. Ropers, *Light Sci Appl*, 2021, **10**, 82.
53. M. Sivi, N. Pazos-Perez, R. Yu, R. Alvarez-Puebla, F. J. García de Abajo and C. Ropers, *Communications Physics*, 2018, **1**, 13.
54. S. Barbosa, A. Agrawal, L. Rodríguez-Lorenzo, I. Pastoriza-Santos, R. A. Alvarez-Puebla, A. Kornowski, H. Weller and L. M. Liz-Marzán, *Langmuir*, 2010, **26**, 14943-14950.
55. N. Pazos-Perez, L. Guerrini and R. A. Alvarez-Puebla, *ACS Omega*, 2018, **3**, 17173-17179.
56. R. Ghosh Chaudhuri and S. Paria, *Chemical Reviews*, 2012, **112**, 2373-2433.
57. Q. Zhang, J. Ge, J. Goebel, Y. Hu, Y. Sun and Y. Yin, *Advanced Materials*, 2010, **22**, 1905-1909.
58. S. Oldenburg, R. Averitt, S. Westcott and N. Halas, *Chemical Physics Letters*, 1998, **288**, 243-247.
59. E. Prodan, C. Radloff, N. J. Halas and P. Nordlander, *Science*, 2003, **302**, 419-422.

60. N. Halas, *MRS Bulletin*, 2005, **30**, 362-367.
61. P. Srinoi, Y.-T. Chen, V. Vittur, M. D. Marquez and T. R. Lee, *Applied Sciences*, 2018, **8**, 1106.
62. S. Duan and R. Wang, *Progress in Natural Science: Materials International*, 2013, **23**, 113-126.
63. K. Sytwu, M. Vadai and J. A. Dionne, *Advances in Physics: X*, 2019, **4**, 1619480.
64. J. Gao, X. Ren, D. Chen, F. Tang and J. Ren, *Scripta Materialia*, 2007, **57**, 687-690.
65. X. Liu and D. Astruc, *Advanced Materials*, 2017, **29**, 1605305.
66. V. Vongsavat, B. M. Vittur, W. W. Bryan, J.-H. Kim and T. R. Lee, *ACS Applied Materials & Interfaces*, 2011, **3**, 3616-3624.
67. A. M. Fales, H. Yuan and T. Vo-Dinh, *The Journal of Physical Chemistry C*, 2014, **118**, 3708-3715.
68. D.-K. Lim, I.-J. Kim and J.-M. Nam, *Chemical Communications*, 2008, DOI: 10.1039/B810195G, 5312-5314.
69. K. K. Haldar, S. Kundu and A. Patra, *ACS Applied Materials & Interfaces*, 2014, **6**, 21946-21953.
70. A. C. P. Melet, S. Chandren and W. Dungchai, *eProceedings Chemistry*, 2019, **4**.
71. P. N. Njoki, M. E. Roots and M. M. Maye, *ACS Applied Nano Materials*, 2018, **1**, 5640-5645.
72. R. Costi, A. E. Saunders and U. Banin, *Angewandte Chemie International Edition*, 2010, **49**, 4878-4897.
73. P. Rai, *Sustainable Energy & Fuels*, 2019, **3**, 63-91.
74. P. Rai, R. Khan, S. Raj, S. M. Majhi, K.-K. Park, Y.-T. Yu, I.-H. Lee and P. K. Sekhar, *Nanoscale*, 2014, **6**, 581-588.
75. S. M. Majhi, P. Rai and Y.-T. Yu, *ACS Applied Materials & Interfaces*, 2015, **7**, 9462-9468.
76. P. Rai, S. M. Majhi, Y.-T. Yu and J.-H. Lee, *RSC Advances*, 2015, **5**, 17653-17659.
77. C. F. Bohren and D. R. Huffman, *Absorption and Scattering of Light by Small Particles*, John Wiley & Sons, 2008.
78. W. R. Erwin, H. F. Zarick, E. M. Talbert and R. Bardhan, *Energy & Environmental Science*, 2016, **9**, 1577-1601.
79. X. Zhang, Y. L. Chen, R.-S. Liu and D. P. Tsai, *Reports on Progress in Physics*, 2013, **76**, 046401.
80. K.-S. Lee and M. A. El-Sayed, *The Journal of Physical Chemistry B*, 2006, **110**, 19220-19225.
81. K. L. Kelly, E. Coronado, L. L. Zhao and G. C. Schatz, *The Journal of Physical Chemistry B*, 2003, **107**, 668-677.
82. J. A. Schuller, E. S. Barnard, W. Cai, Y. C. Jun, J. S. White and M. L. Brongersma, *Nature Materials*, 2010, **9**, 193-204.
83. I. O. Sosa, C. Noguez and R. G. Barrera, *The Journal of Physical Chemistry B*, 2003, **107**, 6269-6275.
84. C. Sönnichsen, T. Franzl, T. Wilk, G. Von Plessen and J. Feldmann, *New Journal of Physics*, 2002, **4**, 93.
85. M. Haggui, M. Dridi, J. Plain, S. Marguet, H. Perez, G. C. Schatz, G. P. Wiederrecht, S. K. Gray and R. Bachelot, *ACS Nano*, 2012, **6**, 1299-1307.
86. N. M. Ngo, H.-V. Tran and T. R. Lee, *ACS Applied Nano Materials*, 2022, **5**, 14051-14091.
87. E. Kazuma and Y. Kim, *Angewandte Chemie International Edition*, 2019, **58**, 4800-4808.
88. A. Manjavacas, J. G. Liu, V. Kulkarni and P. Nordlander, *ACS Nano*, 2014, **8**, 7630-7638.

-
89. X.-C. Ma, Y. Dai, L. Yu and B.-B. Huang, *Light: Science & Applications*, 2016, **5**, e16017-e16017.
 90. M. W. Knight, H. Sobhani, P. Nordlander and N. J. Halas, *Science*, 2011, **332**, 702-704.
 91. M. L. Brongersma, N. J. Halas and P. Nordlander, *Nature Nanotechnology*, 2015, **10**, 25-34.
 92. A. E. Schlather, A. Manjavacas, A. Lauchner, V. S. Marangoni, C. J. DeSantis, P. Nordlander and N. J. Halas, *The Journal of Physical Chemistry Letters*, 2017, **8**, 2060-2067.
 93. S. Li, P. Miao, Y. Zhang, J. Wu, B. Zhang, Y. Du, X. Han, J. Sun and P. Xu, *Advanced Materials*, 2021, **33**, 2000086.
 94. T. Bora, D. Zoepfl and J. Dutta, *Scientific Reports*, 2016, **6**, 26913.
 95. X. Huang, P. K. Jain, I. H. El-Sayed and M. A. El-Sayed, *Lasers in Medical Science*, 2008, **23**, 217-228.
 96. M. Kim, J. H. Lee and J. M. Nam, *Advanced Science*, 2019, **6**, 1900471.
 97. S. K. Cushing, J. Li, J. Bright, B. T. Yost, P. Zheng, A. D. Bristow and N. Wu, *The Journal of Physical Chemistry C*, 2015, **119**, 16239-16244.
 98. J. Li, S. K. Cushing, F. Meng, T. R. Senty, A. D. Bristow and N. Wu, *Nature Photonics*, 2015, **9**, 601-607.
 99. Z. Zheng, W. Xie, B. Huang and Y. Dai, *Chemistry—A European Journal*, 2018, **24**, 18322-18333.
 100. S. Tanwar, K. K. Haldar and T. Sen, *Journal of the American Chemical Society*, 2017, **139**, 17639-17648.
 101. N. C. Seeman, *Journal of Theoretical Biology*, 1982, **99**, 237-247.
 102. H. Yan, T. H. LaBean, L. Feng and J. H. Reif, *Proceedings of the National Academy of Sciences*, 2003, **100**, 8103-8108.
 103. W. M. Shih, J. D. Quispe and G. F. Joyce, *Nature*, 2004, **427**, 618-621.
 104. P. W. Rothmund, *Nature*, 2006, **440**, 297-302.
 105. X. Shen, C. Song, J. Wang, D. Shi, Z. Wang, N. Liu and B. Ding, *Journal of the American Chemical Society*, 2012, **134**, 146-149.
 106. Y. Tian, T. Wang, W. Liu, H. L. Xin, H. Li, Y. Ke, W. M. Shih and O. Gang, *Nature Nanotechnology*, 2015, **10**, 637-644.
 107. A. Cecconello, L. V. Besteiro, A. O. Govorov and I. Willner, *Nature Reviews Materials*, 2017, **2**, 17039.
 108. P. Kühler, E.-M. Roller, R. Schreiber, T. Liedl, T. Lohmüller and J. Feldmann, *Nano Letters*, 2014, **14**, 2914-2919.
 109. P. Zhan, T. Wen, Z.-G. Wang, Y. He, J. Shi, T. Wang, X. Liu, G. Lu and B. Ding, *Angewandte Chemie International Edition*, 2018, **57**, 2846-2850.
 110. D. J. de Aberasturi, A. B. Serrano-Montes and L. M. Liz-Marzán, *Advanced Optical Materials*, 2015, **3**, 602-617.
 111. J.-F. Li, C.-Y. Li and R. F. Aroca, *Chemical Society Reviews*, 2017, **46**, 3962-3979.
 112. X. Yang, Z. Sun, T. Low, H. Hu, X. Guo, F. J. García de Abajo, P. Avouris and Q. Dai, *Advanced Materials*, 2018, **30**, 1704896.
 113. K. Saha, S. S. Agasti, C. Kim, X. Li and V. M. Rotello, *Chemical Reviews*, 2012, **112**, 2739-2779.
 114. G. Doria, J. Conde, B. Veigas, L. Giestas, C. Almeida, M. Assunção, J. Rosa and P. V. Baptista, *Sensors*, 2012, **12**, 1657-1687.
 115. X. Liu, J. Iocozzia, Y. Wang, X. Cui, Y. Chen, S. Zhao, Z. Li and Z. Lin, *Energy & Environmental Science*, 2017, **10**, 402-434.
 116. J. Boken, P. Khurana, S. Thatai, D. Kumar and S. Prasad, *Applied Spectroscopy Reviews*, 2017, **52**, 774-820.
 117. H. A. Atwater and A. Polman, *Nature Materials*, 2010, **9**, 205-213.

118. Y. Xu, L. Chen, X. Wang, W. Yao and Q. Zhang, *Nanoscale*, 2015, **7**, 10559-10583.
119. R. S. Geonmonond, A. G. D. Silva and P. H. Camargo, *Anais da Academia Brasileira de Ciências*, 2018, **90**, 719-744.
120. S. Linic, P. Christopher and D. B. Ingram, *Nature Materials*, 2011, **10**, 911-921.
121. K. Watanabe, D. Menzel, N. Nilius and H.-J. Freund, *Chemical Reviews*, 2006, **106**, 4301-4320.
122. M. J. Kale, T. Avanesian and P. Christopher, *ACS Catalysis*, 2014, **4**, 116-128.
123. Y. Zhang, S. He, W. Guo, Y. Hu, J. Huang, J. R. Mulcahy and W. D. Wei, *Chemical Reviews*, 2018, **118**, 2927-2954.
124. Y. Tian and T. Tatsuma, *Journal of the American Chemical Society*, 2005, **127**, 7632-7637.
125. K. Awazu, M. Fujimaki, C. Rockstuhl, J. Tominaga, H. Murakami, Y. Ohki, N. Yoshida and T. Watanabe, *Journal of the American Chemical Society*, 2008, **130**, 1676-1680.
126. A. G. da Silva, T. S. Rodrigues, V. G. Correia, T. V. Alves, R. S. Alves, R. A. Ando, F. R. Ornellas, J. Wang, L. H. Andrade and P. H. Camargo, *Angewandte Chemie International Edition*, 2016, **55**, 7111-7115.
127. L.-B. Zhao, X.-X. Liu, M. Zhang, Z.-F. Liu, D.-Y. Wu and Z.-Q. Tian, *The Journal of Physical Chemistry C*, 2016, **120**, 944-955.
128. E. M. van Schrojenstein Lantman, T. Deckert-Gaudig, A. J. Mank, V. Deckert and B. M. Weckhuysen, *Nat Nanotechnol*, 2012, **7**, 583-586.
129. S. Mukherjee, F. Libisch, N. Large, O. Neumann, L. V. Brown, J. Cheng, J. B. Lassiter, E. A. Carter, P. Nordlander and N. J. Halas, *Nano Letters*, 2013, **13**, 240-247.
130. M. J. Landry, A. Gellé, B. Y. Meng, C. J. Barrett and A. Moores, *ACS Catalysis*, 2017, **7**, 6128-6133.
131. P. Christopher, H. Xin and S. Linic, *Nature Chemistry*, 2011, **3**, 467-472.
132. H. Zhu, X. Ke, X. Yang, S. Sarina and H. Liu, *Angewandte Chemie International Edition*, 2010, **49**, 9657-9661.
133. E. C. L. Ru and P. G. Etchegoin, *Annual Review of Physical Chemistry*, 2012, **63**, 65-87.
134. K. Kneipp, Y. Wang, H. Kneipp, L. T. Perelman, I. Itzkan, R. R. Dasari and M. S. Feld, *Physical Review Letters*, 1997, **78**, 1667-1670.
135. E. Garcia-Rico, R. A. Alvarez-Puebla and L. Guerrini, *Chemical Society Reviews*, 2018, **47**, 4909-4923.
136. W. H. Weber and R. Merlin, *Raman Scattering in Materials Science*, Springer Science & Business Media, 2000.
137. A. Smekal, *Naturwissenschaften*, 1923, **11**, 873-875.
138. C. V. Raman and K. S. Krishnan, *Nature*, 1928, **121**, 501-502.
139. R. Krishnan and R. Shankar, *Journal of Raman Spectroscopy*, 1981, **10**, 1-8.
140. M. Fleischmann, P. J. Hendra and A. J. McQuillan, *Chemical Physics Letters*, 1974, **26**, 163-166.
141. D. L. Jeanmaire and R. P. Van Duyne, *Journal of Electroanalytical Chemistry and Interfacial Electrochemistry*, 1977, **84**, 1-20.
142. M. G. Albrecht and J. A. Creighton, *Journal of the American Chemical Society*, 1977, **99**, 5215-5217.
143. P. L. Stiles, J. A. Dieringer, N. C. Shah and R. P. V. Duyne, *Annual Review of Analytical Chemistry*, 2008, **1**, 601-626.
144. M. Moskovits, *Reviews of Modern Physics*, 1985, **57**, 783.
145. E. Le Ru, P. Etchegoin and M. Meyer, *The Journal of Chemical Physics*, 2006, **125**, 204701.

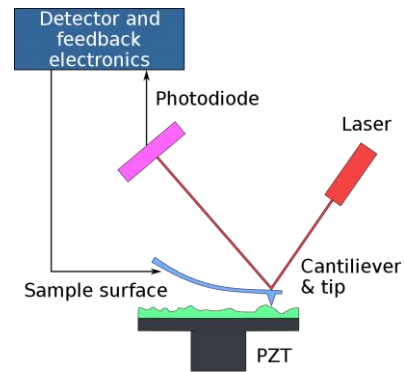
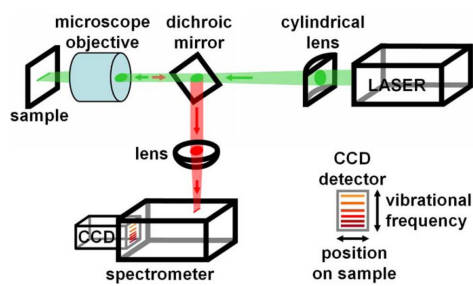
-
146. K. Kneipp, M. Moskovits and H. Kneipp, *Surface-enhanced Raman Scattering: Physics and Applications*, Springer Science & Business Media, 2006.
147. Y. S. Yamamoto, Y. Ozaki and T. Itoh, *Journal of Photochemistry and Photobiology C: Photochemistry Reviews*, 2014, **21**, 81-104.
148. N. C. Lindquist, P. Nagpal, K. M. McPeak, D. J. Norris and S. H. Oh, *Rep Prog Phys*, 2012, **75**, 036501.
149. E. Le Ru and P. Etchegoin, *Chemical Physics Letters*, 2006, **423**, 63-66.
150. E. Le Ru and P. Etchegoin, *Principles of Surface-Enhanced Raman Spectroscopy: and related Plasmonic Effects*, Elsevier, 2008.
151. J. Reguera, J. Langer, D. Jiménez de Aberasturi and L. M. Liz-Marzán, *Chemical Society Reviews*, 2017, **46**, 3866-3885.
152. R. Jiang, B. Li, C. Fang and J. Wang, *Advanced Materials*, 2014, **26**, 5274-5309.
153. L. Rodríguez-Lorenzo, R. A. Álvarez-Puebla, I. Pastoriza-Santos, S. Mazzucco, O. Stéphan, M. Kociak, L. M. Liz-Marzán and F. J. García de Abajo, *Journal of the American Chemical Society*, 2009, **131**, 4616-4618.
154. A. D. S. Indrasekara, S. Meyers, S. Shubeita, L. Feldman, T. Gustafsson and L. Fabris, *Nanoscale*, 2014, **6**, 8891-8899.
155. A. L. Siegel and G. A. Baker, *Nanoscale Advances*, 2021, **3**, 3980-4004.
156. P. Priece, H. A. Salami, R. H. Padilla, Z. Zhong and J. A. Lopez-Sanchez, *Chinese Journal of Catalysis*, 2016, **37**, 1619-1650.
157. S. Y. Ding, X. M. Zhang, B. Ren and Z. Q. Tian, *Encyclopedia of Analytical Chemistry: Applications, Theory and Instrumentation*, 2006, 1-34.
158. R. Aroca, *Surface-Enhanced Vibrational Spectroscopy*, John Wiley & Sons, 2006.
159. S. Schlücker, *Angewandte Chemie International Edition*, 2014, **53**, 4756-4795.
160. S. Cong, X. Liu, Y. Jiang, W. Zhang and Z. Zhao, *The Innovation*, 2020, **1**, 100051.
161. S. Fateixa, H. I. S. Nogueira and T. Trindade, *Physical Chemistry Chemical Physics*, 2015, **17**, 21046-21071.
162. J. Creighton, *Surface Science*, 1986, **173**, 665-672.
163. Y. Fang, Y. Li, H. Xu and M. Sun, *Langmuir*, 2010, **26**, 7737-7746.
164. Y.-F. Huang, H.-P. Zhu, G.-K. Liu, D.-Y. Wu, B. Ren and Z.-Q. Tian, *Journal of the American Chemical Society*, 2010, **132**, 9244-9246.
165. L. J. Gooßen, W. R. Thiel, N. Rodríguez, C. Linder and B. Melzer, *Advanced Synthesis & Catalysis*, 2007, **349**, 2241-2246.
166. L. J. Gooßen, C. Linder, N. Rodríguez, P. P. Lange and A. Fromm, *Chemical Communications*, 2009, 7173-7175.
167. L. Xue, W. Su and Z. Lin, *Dalton Transactions*, 2011, **40**, 11926-11936.
168. Y. Zong, Q. Guo, M. Xu, Y. Yuan, R. Gu and J. Yao, *RSC Advances*, 2014, **4**, 31810-31816.
169. M. Fan, G. F. Andrade and A. G. Brolo, *Analytica Chimica Acta*, 2020, **1097**, 1-29.
170. Z. Lin and L. He, *Current Opinion in Food Science*, 2019, **28**, 82-87.
171. B. Sharma, R. R. Frontiera, A.-I. Henry, E. Ringe and R. P. Van Duyne, *Materials Today*, 2012, **15**, 16-25.
172. P. A. Mosier-Boss, *Nanomaterials*, 2017, **7**, 142.
173. C. Hamon and L. M. Liz-Marzán, *Journal of Colloid and Interface Science*, 2018, **512**, 834-843.
174. T. H. Chow, N. Li, X. Bai, X. Zhuo, L. Shao and J. Wang, *Accounts of Chemical Research*, 2019, **52**, 2136-2146.
175. Z. Zhang, W. Shen, J. Xue, Y. Liu, Y. Liu, P. Yan, J. Liu and J. Tang, *Nanoscale Research Letters*, 2018, **13**, 1-18.
176. C. Wang and C. Yu, *Reviews in Analytical Chemistry*, 2013, **32**, 1-14.

177. Y. Yang, S. Matsubara, L. Xiong, T. Hayakawa and M. Nogami, *The Journal of Physical Chemistry C*, 2007, **111**, 9095-9104.
178. L. Vigderman and E. R. Zubarev, *Langmuir*, 2012, **28**, 9034-9040.
179. A. S. Patel, S. Juneja, P. K. Kanaujia, V. Maurya, G. V. Prakash, A. Chakraborti and J. Bhattacharya, *Nano-Structures & Nano-Objects*, 2018, **16**, 329-336.
180. S. Link and M. A. El-Sayed, *Annual Review of Physical Chemistry*, 2003, **54**, 331-366.
181. J. A. Webb and R. Bardhan, *Nanoscale*, 2014, **6**, 2502-2530.
182. R. S. Riley and E. S. Day, *Wiley Interdiscip Rev Nanomed Nanobiotechnol*, 2017, **9**.
183. X. Huang and M. A. El-Sayed, *Alexandria Journal of Medicine*, 2011, **47**, 1-9.
184. D. A. Giljohann, D. S. Seferos, W. L. Daniel, M. D. Massich, P. C. Patel and C. A. Mirkin, *Angewandte Chemie International Edition*, 2010, **49**, 3280-3294.
185. E. Polo, M. F. Navarro Poupard, L. Guerrini, P. Taboada, B. Pelaz, R. A. Alvarez-Puebla and P. del Pino, *Nano Today*, 2018, **20**, 58-73.
186. P. K. Jain, K. S. Lee, I. H. El-Sayed and M. A. El-Sayed, *The Journal of Physical Chemistry B*, 2006, **110**, 7238-7248.
187. M. Hlaing, B. Gebear-Eigzabher, A. Roa, A. Marcano, D. Radu and C.-Y. Lai, *Optical Materials*, 2016, **58**, 439-444.
188. C. Loo, A. Lin, L. Hirsch, M.-H. Lee, J. Barton, N. Halas, J. West and R. Drezek, *Technology in Cancer Research & Treatment*, 2004, **3**, 33-40.
189. J. Chen, B. Wiley, Z. Y. Li, D. Campbell, F. Saeki, H. Cang, L. Au, J. Lee, X. Li and Y. Xia, *Advanced Materials*, 2005, **17**, 2255-2261.
190. M. Hu, H. Petrova, J. Chen, J. M. McLellan, A. R. Siekkinen, M. Marquez, X. Li, Y. Xia and G. V. Hartland, *The Journal of Physical Chemistry B*, 2006, **110**, 1520-1524.
191. X. Wang, G. Li, Y. Ding and S. Sun, *RSC Advances*, 2014, **4**, 30375-30383.
192. H. Chatterjee, D. S. Rahman, M. Sengupta and S. K. Ghosh, *The Journal of Physical Chemistry C*, 2018, **122**, 13082-13094.
193. L. M. Maestro, P. Haro-González, A. Sánchez-Iglesias, L. M. Liz-Marzán, J. García Solé and D. Jaque, *Langmuir*, 2014, **30**, 1650-1658.
194. M. R. Hoffmann, S. T. Martin, W. Choi and D. W. Bahnemann, *Chemical Reviews*, 1995, **95**, 69-96.
195. A. Fujishima and K. Honda, *Nature*, 1972, **238**, 37-38.
196. S. U. Khan, M. Al-Shahry and W. B. Ingler Jr, *Science*, 2002, **297**, 2243-2245.
197. C. Chen, W. Cai, M. Long, B. Zhou, Y. Wu, D. Wu and Y. Feng, *ACS Nano*, 2010, **4**, 6425-6432.
198. M. Kim, J.-H. Seo, U. Singiseti and Z. Ma, *Journal of Materials Chemistry C*, 2017, **5**, 8338-8354.
199. C.-H. Kuo, Y.-C. Yang, S. Gwo and M. H. Huang, *Journal of the American Chemical Society*, 2011, **133**, 1052-1057.
200. M. Misra, P. Kapur and M. L. Singla, *Applied Catalysis B: Environmental*, 2014, **150**, 605-611.
201. J. B. Lee, S. Choi, J. Kim and Y. S. Nam, *Nano Today*, 2017, **16**, 61-81.
202. X. Shao, B. Li, B. Zhang, L. Shao and Y. Wu, *Inorganic Chemistry Frontiers*, 2016, **3**, 934-943.
203. L. Zhang, L. O. Herrmann and J. J. Baumberg, *Scientific Reports*, 2015, **5**, 1-12.
204. M. J. Sampaio, J. W. L. Oliveira, C. I. L. Sombrio, D. L. Baptista, S. R. Teixeira, S. A. C. Carabineiro, C. G. Silva and J. L. Faria, *Applied Catalysis A: General*, 2016, **518**, 198-205.
205. C. Xie, Z. Niu, D. Kim, M. Li and P. Yang, *Chemical Reviews*, 2020, **120**, 1184-1249.
206. N.-T. Suen, S.-F. Hung, Q. Quan, N. Zhang, Y.-J. Xu and H. M. Chen, *Chemical Society Reviews*, 2017, **46**, 337-365.

-
207. I. Ledezma-Yanez, W. D. Z. Wallace, P. Sebastián-Pascual, V. Climent, J. M. Feliu and M. T. M. Koper, *Nature Energy*, 2017, **2**, 17031.
208. X. X. Wang, M. T. Swihart and G. Wu, *Nature Catalysis*, 2019, **2**, 578-589.
209. E. S. Davydova, S. Mukerjee, F. Jaouen and D. R. Dekel, *ACS Catalysis*, 2018, **8**, 6665-6690.
210. C. C. L. McCrory, S. Jung, I. M. Ferrer, S. M. Chatman, J. C. Peters and T. F. Jaramillo, *Journal of the American Chemical Society*, 2015, **137**, 4347-4357.
211. J.-M. Yan, X.-B. Zhang, T. Akita, M. Haruta and Q. Xu, *Journal of the American Chemical Society*, 2010, **132**, 5326-5327.
212. J. Zhou, B. Duan, Z. Fang, J. Song, C. Wang, P. B. Messersmith and H. Duan, *Advanced Materials*, 2014, **26**, 701-705.
213. W. Luc, C. Collins, S. Wang, H. Xin, K. He, Y. Kang and F. Jiao, *Journal of the American Chemical Society*, 2017, **139**, 1885-1893.
214. A. L. Strickler, M. a. Escudero-Escribano and T. F. Jaramillo, *Nano Letters*, 2017, **17**, 6040-6046.
215. B. N. Wanjala, J. Luo, R. Loukrakpam, B. Fang, D. Mott, P. N. Njoki, M. Engelhard, H. R. Naslund, J. K. Wu, L. Wang, O. Malis and C.-J. Zhong, *Chemistry of Materials*, 2010, **22**, 4282-4294.
216. Z. Zhuang, W. Sheng and Y. Yan, *Advanced Materials*, 2014, **26**, 3950-3955.
217. T. Y. Ma, S. Dai, M. Jaroniec and S. Z. Qiao, *Journal of the American Chemical Society*, 2014, **136**, 13925-13931.
218. C. Ranaweera, C. Zhang, S. Bhoyate, P. Kahol, M. Ghimire, S. Mishra, F. Perez, B. K. Gupta and R. K. Gupta, *Materials Chemistry Frontiers*, 2017, **1**, 1580-1584.
219. V. D. Silva, T. A. Simões, J. P. F. Grilo, E. S. Medeiros and D. A. Macedo, *Journal of Materials Science*, 2020, **55**, 6648-6659.
220. A. Roy, A. Ray, S. Saha, M. Ghosh, T. Das, M. Nandi, G. Lal and S. Das, *International Journal of Energy Research*, 2021, **45**, 16908-16921.
221. M. Zhu, B. Lei, F. Ren, P. Chen, Y. Shen, B. Guan, Y. Du, T. Li and M. Liu, *Scientific Reports*, 2014, **4**, 5259.

Chapter 2

Methodology & Instrumentation



Chapter 2 includes the synthesis of anisotropic-shaped Au nanostars, Ag-coated Au nanostars, silica core - Au nanostar shell type nanostructures, Au nanostar - ZnO nanopetal shaped hybrid core-shell structures, and DNA origami. This chapter also provides an introduction to the fundamental principles and theories underlying the wide variety of instruments employed for the work included in this thesis.

2.1. Synthesis of Au nanoparticles

Michael Faraday provided a detailed description of the synthetic protocol for the synthesis of colloidal gold nanoparticles in the year 1857.¹ He made use of white phosphorus to reduce the gold salt, and carbon disulfide was used as a stabilizing agent. The synthesis of spherical Au nanoparticles utilizing trisodium citrate as a reducing agent was first proposed by Turkevich et al. in 1951^{2, 3} and later improved by Frens.⁴ This technique, also known as the citrate reduction method, is now widely used. Since then, several synthetic approaches have been suggested for developing gold nanoparticles in both spherical and anisotropic shapes.

2.1.1. Synthesis of anisotropic-shaped nanostructures

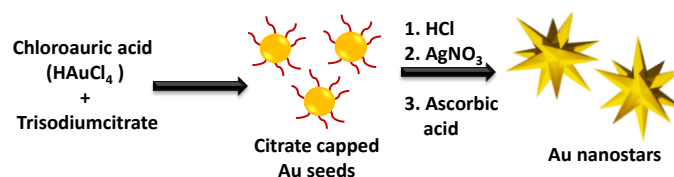
For the synthesis of anisotropic-shaped Au nanostructures, two types of approaches have been employed: top-down approach and bottom-up approach.⁵ Developing nanoscale structures from bulk materials by selective removal, which can be attained via lithographic techniques⁶ or chemically based modes,⁷ is what the top-down approach entails. The most problematic aspect of this method is the imperfection of the surface structures, as well as the crystallographic malfunction to produce patterns. This leads to high costs for fabrication, variations in particle shape and morphology, and a wide range of sizes across the product.⁸ The "bottom-up" process involves the arrangement of nanoscale basic components like nanoparticles, which have been derived from their molecular precursors via colloidal chemistry. This method offers control over the morphology as well as the polydispersity of the final product. When using the bottom-up method, the first step is nucleation, which is then accompanied by two growth mechanisms that are controlled either thermodynamically or kinetically. The simple and direct reduction of metallic ions has a tendency to nucleate as well as

grow into thermodynamically stable nanoparticles, which ultimately leads to the development of minimum-energy spherical or near-spherical nanostructures. Anisotropic growth occurs as a result of directional growth over those low energy crystallographic facets when kinetic control is used to direct the growth of the material.⁹ This is accomplished through the selective adsorption of ligands, polymers, ions, or surfactants onto selective facets of the substrate.¹⁰ Synthesis of anisotropic metal nanoparticles has been accomplished through the use of a variety of chemical synthetic approaches up to now. These approaches include seed-mediated synthesis,¹¹ electrochemical synthesis,¹² template mediated synthesis,^{13, 14} polyol synthesis,¹⁵ and photoinduced synthesis.¹⁶ The seed-mediated methodology is by far the most common one, and it is responsible for producing metal nanostructures in a variety of interesting shapes like wires, rods, stars, pyramids, triangles, and flowers.

2.1.1.1. Seeds mediated approach for synthesis of anisotropic shaped Au nanoparticles

The first demonstration of seed-mediated approach was carried out by Jana et al. for the development of Au nanorods and nanowires.¹⁷ Since that time, it's been put to use in the process of synthesizing metal nanoparticles in a variety of shapes, including nanorods, nanocubes, nanostars, and many others. The conventional seed-mediated strategy consists of two steps in general. In the first step, small spheroidal nanoparticles known as seeds are synthesized by the reducing metal salts with the help of a stronger reducing agent. The next step is to grow seeds nanoparticle into the required shape by adding a shape guiding agent or surfactant and a moderate reducing agent like ascorbic acid. Surfactants in the growth solution are meant to bind preferentially to specific crystal facets of the seed, thereby preventing growth at such facets. When it comes to the synthesis of anisotropically shaped nanoparticles, the surfactants such as hexadecylcetyltrimethylammonium bromide (CTAB) and poly(vinylpyrrolidone) (PVP) are the ones that are used most commonly.^{18, 19} Among the various different anisotropic shapes of Au nanoparticles, the synthesis of nanostar morphology has been mainly driven by significance of their optical and structural properties.²⁰ As a result, over the course of the past few years, a variety of procedures for chemical synthesis

Au nanostars have been introduced.²¹ For seed-mediated growth of Au nanostars, Kumar et al. prepared the PVP capped small spherical Au seeds along with N,N-dimethylformamide (DMF) in which PVP capping restricted the growth along (110) direction resulting into star like morphology.²² The nanostars shrank in size and had a reduced number of spikes as the concentration of Au seeds in the growth solution decreased. Without the use of surfactants and organic solvents, Yuan et al. proposed a simple seed-mediated method for the synthesis of Au nanostars with remarkable monodispersity (Scheme 2.1).²³



Scheme 2.1. Schematic illustration of seed-mediated synthesis of Au nanostars.

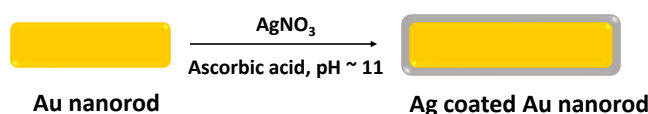
It was discovered that Au nanostar size could be controlled by adjusting the seed concentration in the growth solution.

The work presented in this thesis involves the seed-mediated synthesis of Au nanostars.

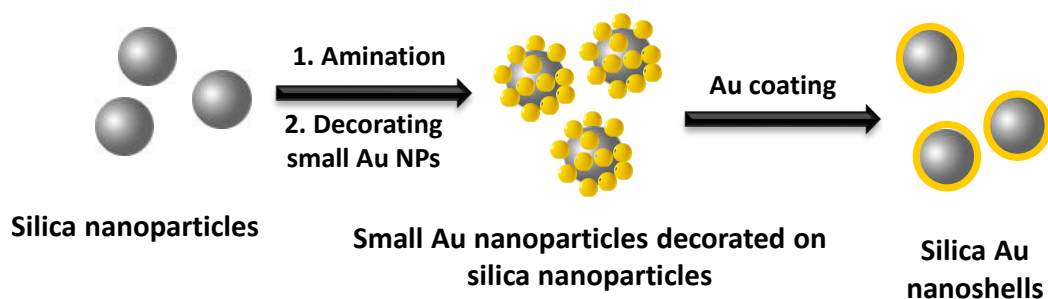
2.1.2. Synthesis of bimetallic nanoparticles

The synthesis of bimetallic type nanostructures has received a lot of attention because of their superior photocatalytic performance and high SERS activities as compared to single counter parts.^{24, 25} Synthesis of bimetallic type nanostructures can be accomplished through a number of different methods, including²⁶ (a) coreduction, in which two different type of metal salts are parallelly reduced via refluxing in suitable solvent solutions using a stabilizing agent; (b) successive reduction in which one metal ions has a reduction potential that is significantly different from that of the other (in this instance, the metal ion with the more negative reduction potential is reduced first, being followed by the second metal); (c) thermal decomposition in which refluxing of required metal ions is carried out in presence of suitable solvents and stabilizing agents. the refluxing temperature should be high enough to allow the nucleation and growth of nanoparticles. In each method, the reaction conditions are adjusted so that monodisperse

bimetallic NPs with the targeted morphology are produced. Such synthetic methods result in the production of bimetallic nanoparticles of three distinguishable types, each of which possesses a distinct set of characteristics as well as plasmonic properties of their very own. These include hollow particles, core-shell particles, and particles with an alloy composition. Ferrer et al. fabricated Au-Pd core shell nanoparticles with the help of a polyol synthesis method which were stabilized by polymers.²⁷ Masaharu et al. prepared Au-Ag core-shell nanoparticles by a microwave assisted polyol method through the two-step reduction of AuCl_4^- and Ag^+ ions in the presence of poly(vinylpyrrolidone) (PVP) as a capping reagent.²⁸ Hence, it is clear that two steps are required in the synthesis of bimetallic core-shell nanostructures: the first is the preparation of the core material, and the second is the coating of another material by adding the appropriate metal salt for nucleation over the core. Fu et al. developed a method for synthesis of Ag coated Au nanorods.²⁹ They prepared Au nanorods to serve as the core material, after which they coated the nanorods with Ag under basic conditions using AgNO_3 as a source of Ag, ascorbic acid as a mild reducing Ag(I) as shown in scheme 2.2.



layer of metallic material. The first metallic nanoshell was developed by Zhou and colleagues which was comprised of gold sulphide (Au_2S) dielectric core surrounded by a Au shell.³⁴ Chloroauric acid (HAuCl_4) and sodium sulfide (Na_2S) are mixed together in a single step to grow these nanoparticles. Au- Au_2S nanoshells with varying core and shell thicknesses can be grown by adjusting the proportions of HAuCl_4 and Na_2S added. Subsequent to this, Oldenburg et al. created a new nanoparticle, a silica gold core-shell nanostructures (Scheme 2.3).³³ Firstly, Stober method was used to develop a dielectric silica core. In this method, tetraethylorthosilicate (TEOS) was reduced in ethanol under basic conditions, which results in the nucleation and development of spherical and extremely monodisperse silica colloid. Through a reaction with aminopropyltriethoxysilane (APTES), silica core surfaces were subsequently functionalized with amine groups. After that, small Au nanoparticles of size on the order of 1–2 nm were adsorbed onto amine functionalized surface of Silica core. The small Au nanoparticles attached over the surface of silica cores act as nucleation sites for further reduction of Au which was accomplished by reduction of Au in a solution of HAuCl_4 . When more Au is reduced, the coating on the surface of silica nanoparticle thickens and eventually forms a complete Au spherical shell.

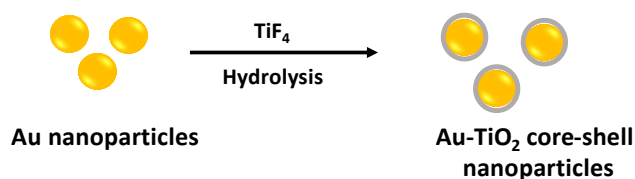


Scheme 2.3. Schematic illustration of synthesis of silica-Au nanoshells.

It is reported in chapter 4 of the present thesis that the above protocol can be used to develop a rational methodology for the synthesis of shell type Au nanostars over silica cores.

2.1.4. Synthesis of hybrid metal-semiconductor nanostructures

In recent years, significant efforts have been directed toward the synthesis of heteronanostructures by combining plasmonic metal nanoparticles and semiconductors. This is due to the fact that these heteronanostructures have demonstrated superior performance in a variety of photocatalytic reactions, such as the production of hydrogen, in comparison to the semiconductor analogues.³⁵⁻³⁷ Several different strategies and procedures are employed to develop metal-semiconductor hybrid nanostructures. The following includes the strategies for preparation of Au nanoparticle-semiconductor hybrid nanostructures that are used most frequently:³⁶ (a) deposition–precipitation method in which supporting material is submerged in an aqueous solution of HAuCl_4 , which is then followed by the addition of NaOH solution in order to bring the resultant suspension to the desired pH value under constant stirring for particular time. The catalyst precursor is filtered, and washed with deionized water and calcinated at various temperatures; (b) photoreduction method in which a semiconductor is irradiated with appropriate wavelength light, the photoexcited electrons in the conduction band do the reduction of Au^{3+} to Au^0 on the surface of semiconductor, while the scavenger captures holes left behind in valence band to prevent positive charge accumulation; (c) encapsulation is not a common technique for the preparation of catalysts; rather, it is merely a way to organize or fabricate catalyst composites, which is typically accomplished through the application of other methods. Encapsulation, on the other hand, is extremely beneficial because it inhibits the aggregation and growth of Au nanoparticles, which ultimately leads to an improvement in the stability of nanostructure. Zhang et al. developed and manufactured a sandwich-structured $\text{SiO}_2@\text{Au}@\text{TiO}_2$ plasmonic-semiconductor core-shell hybrid nanostructures by combining simple and direct sol–gel and calcination procedures.³⁸ Nanostructures with a Au core and a titanium dioxide (TiO_2) shell are prepared hydrothermally and come in a variety of morphologies,^{39, 40} in which, firstly, spherical Au nanospheres are developed by reducing HAuCl_4 with trisodium citrate, and then shell of TiO_2 is formed on the as prepared Au nanoparticles by hydrolyzing TiF_4 in a hydrothermal environment (Scheme 2.4). The concentration of TiF_4 present enables one to manipulate the shape of the TiO_2 shell.⁴¹

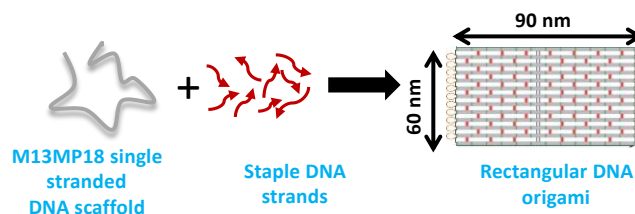


Scheme 2.4. Schematic representation of synthesis hybrid metal-semiconductor nanostructures.

In chapter 5 of the current thesis, it is reported that the methodology described above can be utilized to develop a rational procedure for the synthesis of unique nanopetal shape of ZnO surrounding Au nanostar.

2.2. Synthesis of rectangular DNA origami

To construct rectangular DNA origami, M13mp18 single-stranded bacteriophage genomic DNA with 7249 nucleotides served as a scaffold DNA as well as 213 short staple DNA sequences were employed to direct its folding (Scheme 2.5). The plan replicated the one described in Paul Rothemund's pioneering paper on DNA origami.⁴²



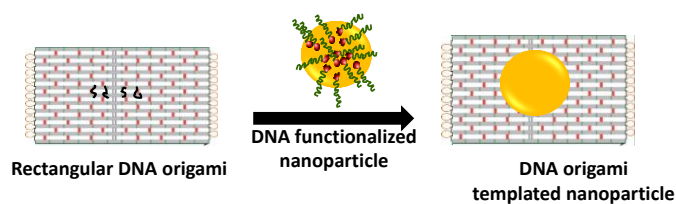
Scheme 2.5. Schematic representation of fabrication of rectangular DNA origami.

The thermal annealing method was used for the self-assembly of DNA origami structures. Scaffold DNA was heated to 90°C together with folding staple strands in a single pot for the reaction, which was then cooled to 20°C. Due to the presence of random complementary bases, a single-stranded scaffold DNA has several internal secondary and tertiary structures.⁴³ At room temperature, these structures prevent staple strands from binding. On heating at 90°C, all internal structures are removed, leaving the scaffold DNA stretched.⁴⁴ All staples bind to scaffold DNA to form the designed structure with the lowest energy configuration on slow cooling. A Bio-Rad PCR thermocycler (Model no.C1000 Touch) using a 1.5-hour folding program folded the DNA origami structures. The folding reaction mixture volume was 50 μ L,

with scaffold DNA, modified staple strands, and unmodified staple strands at 2, 10, and 20 nM in 1xTAE-Mg²⁺ buffer (40 mM Tris, 20 mM Acetic acid, 2 mM EDTA and 12.5 mM Magnesium chloride, pH 8.0). The folding staple concentration was higher than the scaffold concentration so that all scaffold strands could access all staple strands, leading to correctly folded structures. Divalent cations like Mg²⁺ in the 10–20 mM (generally, 12.5 mM concentration is suitable for folding) range help origami structures fold by counteracting the negative charges of the phosphates in the DNA backbone and reducing the repulsion between scaffold and staple strands.⁴⁴ Rectangle DNA origami structures aggregate due to strong stacking interactions of blunt ends present on the left and right edges of structures.⁴² Eliminating the edge staples (12 each side) keeps the scaffold DNA unfolded and inhibits aggregation.⁴⁵

2.3. Fabrication of DNA origami assembled plasmonic nanoparticles

DNA origami has proven as an efficient method for the programmable self-assembly of nanoparticles, making it one of the most promising recent developments in the field.⁴⁶ Throughout DNA origami structure, the sequence used in each folding staple is unique, and the position of each staple is predefined to bind to a particular position on the scaffold.⁴⁷ An individual binding site on the template can be created by modifying and extending the sequence of a folding staple.⁴⁸ Nanoparticles that have been functionalized with a sequence that is complementary to the linker DNA (denoted by black curvy lines on the surface of DNA origami having bases complementary to bases of single stranded DNA functionalized with metal nanoparticle) are guided to a particular location on a pre-assembled DNA origami template, where they bind (Scheme 2.6).



Scheme 2.6. Schematic representation of immobilization of Au nanoparticle on DNA origami. (Black curvy lines indicate short staple strands and green lines on nanoparticle indicate single stranded DNA)

In this thesis, fabrication of DNA origami-templated Ag coated Au nanostars was carried out and reported in chapter 6.

2.4. Characterization techniques

2.4.1. UV-Vis spectroscopy

To analyze the presence or absence of species in a sample that absorb light in the near-ultraviolet (180-390 nm) or visible range, ultraviolet-visible (UV-Vis) spectroscopy can be used which is a quantification characterization technique. A typical UV-VIS spectrophotometer setup is shown in Figure 2.1.

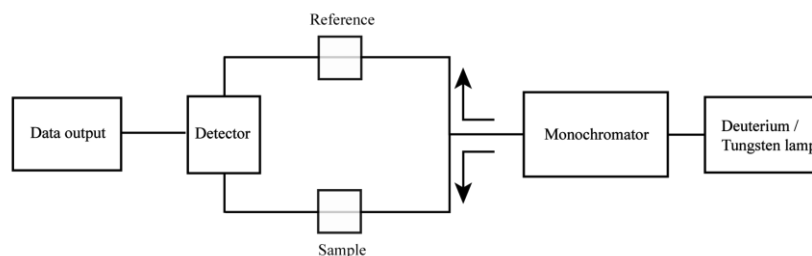


Figure 2.1 Depiction of UV-Vis spectrophotometer set up. (Image taken from Wikipedia).

The energy needed to excite the molecules from ground state to excited state dictates the wavelength of absorption. When less energy is needed for excitation, a longer wavelength of absorption is observed, and vice versa when more energy is needed. The Beer-Lambert law underlies the fundamental operation of UV-Vis spectrophotometers. This law states that the rate at which a beam of monochromatic light loses intensity as it passes through a solution containing an absorbing substance is proportional to the concentration and thickness of the solution and the incident radiation. Beer-Lambert law is represented by equation 2.1.

$$A = \log_{10} \left(\frac{I_0}{I} \right) = \epsilon c l \quad \text{Equation 2.1}$$

In this equation, A is the absorbance value, I_0 is the incident light intensity on a sample cell, I is the transmitted light intensity, l is the path length through the sample (usually 1 cm), c is the concentration of the absorbing species, and ϵ is a constant known as

extinction coefficient or molar absorptivity. This constant, defined in units of $M^{-1}cm^{-1}$, is a fundamental property of molecules in a specific solvent at a fixed temperature and pressure.

If a molecule takes in enough energy in the visible or ultraviolet spectrum, the absorbed photons will cause an electron to jump to a higher energy molecular orbital, creating an excited state. It is postulated that there are four different kinds of transitions take place: $\pi-\pi^*$, $n-\pi^*$, $\sigma-\sigma^*$, and $n-\sigma^*$ (Figure 2.2). The plot of absorbance (A) versus wavelength (λ) that is produced by a UV-Vis spectrophotometer is referred to as a spectrum. This instrument measures the degree of absorption that a sample exhibits at various wavelengths. The maximum amount of light absorbed by a sample at a particular wavelength is referred to as the λ_{max} .

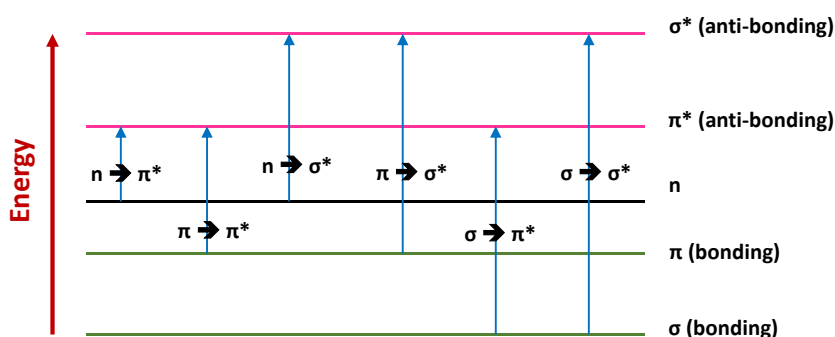


Figure 2.2. Transitions on an electronic level between bonding and anti-bonding states.

In this thesis, UV-visible spectroscopy was utilized to record the UV-visible absorption spectra of spherical Au nanoparticles, Au nanostars, bimetallic Au@Ag bimetallic nanostars, Au nanoparticles decorated on Silica nanoparticles, spherical $SiO_2@Au$ nanoparticles, $SiO_2@Au$ nanostars, and hybrid Au@ZnO nanostructures. Every single UV-Vis spectrum was captured by a Shimadzu UV-2600 spectrophotometer.

2.4.2. Dynamic light scattering (DLS) and zeta potential study

Dynamic Light Scattering is a method for measuring the size of particles, typically in the sub-micron range. This method is also known as Photon Correlation Spectroscopy and Quasi-Elastic Light Scattering. Brownian motion is measured by DLS, and the size of the particles is determined based on this measurement. Brownian motion refers to the

random movement of particles that occurs as a result of the particles being bombarded by the surrounding solvent molecules. These collisions cause a transfer of energy among the particles, which in turn causes the particles to move in some direction. When dealing with larger particles, the Brownian motion will decrease accordingly. Particles with a smaller diameter are "kicked" further by the molecules of the solvent, and as a result, they move at a faster rate. Brownian motion is described by a property generally regarded as the translational diffusion coefficient (D), which determines the velocity of the Brownian motion. The Stokes-Einstein equation describes the relationship between the speed at which the particles travel and the particle size (Equation 2.2).

$$d(H) = \frac{kT}{3\pi\eta D} \quad \text{Equation 2.2}$$

Where $d(H)$ denotes the hydrodynamic diameter, k denotes the Boltzmann's constant, D denotes the translational diffusion coefficient, η denotes the viscosity of the sample medium, and T denotes the temperature of the system. DLS is typically applied to the measurement of particles that are suspended in a liquid. A typical DLS instrument looks like the one depicted in Figure 2.3 and is made up of a single frequency laser which is aimed at a sample in a cuvette. The incident laser scatters in all directions and can be detected at a specific angle after a certain amount of time has passed. By applying the Stokes-Einstein equation (Equation 2.2) to the scattered light, one can calculate the diffusion coefficient as well as the size of the particles. In DLS, analysis of the scattered light intensity is done as a function of time.

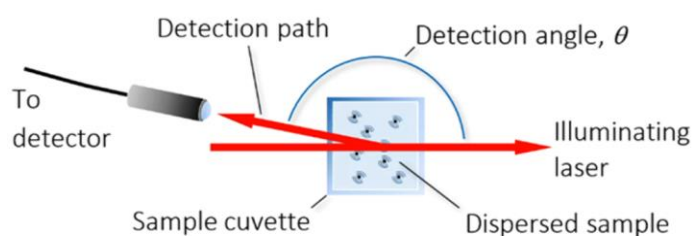
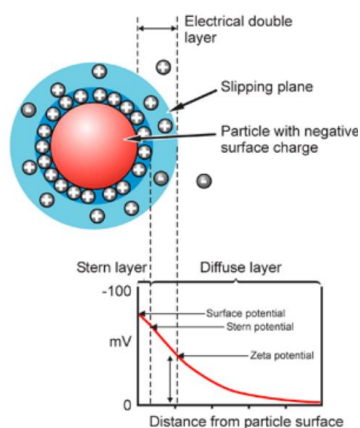


Figure 2.3. Illustration of the Dynamic Light Scattering apparatus.⁴⁹

The zeta potential of a particle can be thought of as a physical property which is shared by all particles in suspension. It is possible to employ it in the process of formulating optimal suspensions and emulsions. Additionally, it is helpful in determining the

possibility of long-term stability. There are two parts of the liquid layer that surrounds the particle: an inner region known as the Stern layer, which is where the ions are strongly bound, and an outer region known as the diffuse region, where they are associated with each other less firmly (Figure 2.4). There is a notional boundary located inside the diffuse layer. Inside this boundary, the ions and particles combine to form a stable entity. Ions within the boundary move particles due to gravity. The bulk dispersant retains ions beyond the boundary. This boundary potential (surface of hydrodynamic shear) is referred to as the zeta potential.



*Figure 2.4. Schematic representation of zeta potential.*⁵⁰

The strength of the zeta potential can be interpreted as an indication of the colloidal system's potential stability. If all of the particles in suspension have a large zeta potential that is either negative or positive, then they will have the tendency to repel each other, and there will be no tendency for the particles to come together. If, on the other hand, the particles have low zeta potential values, there will be no force to prevent the particles from coming together and they flocculate.

For the current thesis, DLS measurements were carried out for the purpose of determining the hydrodynamic diameter of silica nanoparticles, as well as spherical SiO₂@Au nanoparticles. Additionally, the zeta potential of only silica nanoparticles and amine-functionalized silica nanoparticles was measured using DLS. The Malvern zetasizer nano ZSP instrument equipped with a HeNe laser was used to carry out the DLS measurements.

2.4.3. Powder X-ray diffraction (XRD)

X-ray powder diffraction (XRD) is a relatively quick analytical method that is primarily utilized for figuring out the atomic and molecular structure of a crystal. When an X-ray beam is directed at a crystalline sample, the crystallized structure of the sample causes the incident X-rays to diffract into a range of different directions. A crystallographer is able to generate a three-dimensional view of the density of electrons inside a crystal by determining the intensities and angles of these diffracted beams. The average positions of the atoms in the crystal, the chemical bonds between them, the crystallographic disorder, and a variety of other pieces of information can be deduced from the electron density of the crystal.

Bragg's law

The diffraction of X-rays by a crystal was first explained by Lawrence Bragg, who did so by modeling the crystal as a collection of discrete parallel planes that were separated by a constant parameter d . He proposed that when X-ray radiation with a wavelength comparable to the atomic spacings 2–3 Å is incident on a crystalline system, the radiation will scatter from the lattice planes that are separated by the interplanar distance d . Bragg's peak is seen to appear whenever the scattered waves go through the process of constructive interference. The term "constructive interference" refers to a situation in which the path lengths of the two waves are equal to an integer multiple of the wavelength of the X-rays that are incident. The difference in path length between the two waves that are interacting due to interference can be expressed as $2d\sin\theta$, where θ is the glancing angle (Figure 2.5). In Bragg's law, the condition on that must be met for the constructive interference to be at its highest is represented by the equation 2.3.

$$2d\sin\theta = n\lambda \quad \text{Equation 2.3}$$

Where n is greater than zero and is the wavelength of incident light. The wavelength of X-rays that is most commonly used is the characteristic $K\alpha$ radiation, which has a value of $\lambda = 1.5418 \text{ Å}$ and is emitted by copper.

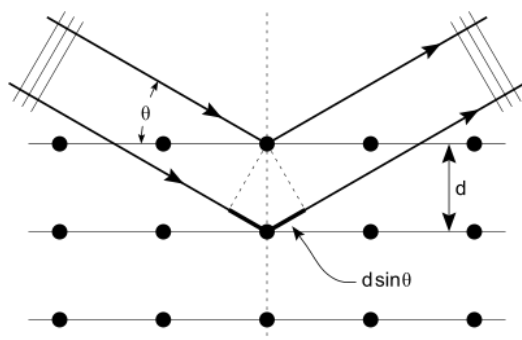


Figure 2.5. Bragg's law of diffraction. (Image take from Wikipedia).

For the purpose of recording the X-ray diffraction pattern of silica nanoparticles, spherical $\text{SiO}_2\text{@Au}$ nanoparticles, and hybrid Au@ZnO nanostructures, powder XRD was utilized in this thesis. XRD patterns were captured by a Bruker Eco D8 setup illuminated by Cu $K\alpha$ radiation ($\lambda = 0.154056 \text{ nm}$).

2.4.4. Fourier transform infrared (FTIR) spectroscopy

Infrared spectroscopy (IR), is a technique which has been employed extensively for the identification and structural analysis of various chemical compounds. Infrared radiation is a type of electromagnetic radiation that has a wavelength range from 700 nm to 1 mm. This region of the electromagnetic spectrum is known as the infrared region. The IR spectrum can be split into three bands: the near IR 0.8-2.5 μm ($12500\text{-}4000 \text{ cm}^{-1}$), the mid IR 2.5-25 μm ($4000\text{-}400 \text{ cm}^{-1}$), and the far IR 25-1000 μm ($400\text{-}10 \text{ cm}^{-1}$). When molecules are subjected to infrared irradiation, the molecules' dipole moments shift because of the absorption of radiation at a certain wavelength. A peak appears in the infrared spectrum when the absorbed radiation's frequency coincides with the vibrational frequencies. The frequency of vibration can be calculated using equation 2.4.

$$\gamma = \frac{1}{2\pi} \sqrt{\frac{k}{\mu}} \quad \text{Equation 2.4}$$

Where k is the force constant and μ is the reduced mass. The excitation of vibrational modes of the chemical bonds and functional groups present in the molecules is represented by peaks in the IR spectrum of a sample, which can be found by using an

infrared spectrometer. Therefore, the IR spectrum of a compound reveals information about its structure and is frequently referred to as the compound's "fingerprint." Because the majority of inorganic and organic compounds show absorption in this region, an IR spectrum is typically recorded from $4000\text{--}400\text{ cm}^{-1}$ in normal practice. FTIR spectrometers are capable of collecting data with a high spectral resolution across a broad spectral range. The high signal-to-noise ratio, the high accuracy of the wavenumber readings, the shorter scan times, and the wider scan ranges that FTIR spectrometers offer are some of their advantages.

In this thesis, FTIR was used for determining the surface functionalities of the synthesized Si nanoparticles. The FTIR measurements were carried out on an Agilent technologies Cary 600 series spectrometer.

2.4.5. Raman spectroscopy

The term "Raman spectroscopy" refers to a spectroscopic technique that is based on vibrational molecular spectroscopy and originates from an inelastic scattering of incident light. This technique was named after the Indian physicist C.V. Raman. In the process of Raman spectroscopy, a monochromatic beam of light from laser source is scattered by the molecules, which causes the energy of the laser photon to either decrease or increase or same (Figure 2.6).

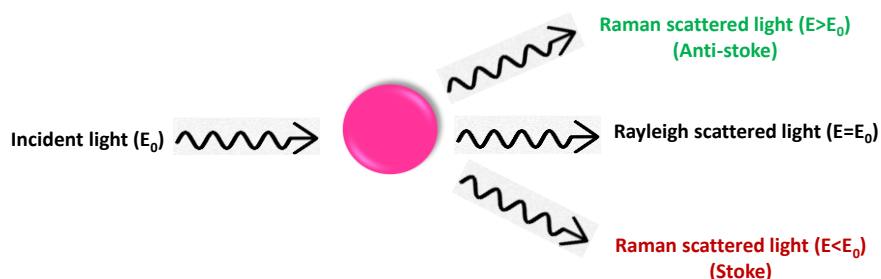


Figure 2.6. Three different ways of re-emitting incident light.

The amount of energy lost can be observed as a change in the energy (wavelength) of the incident photon. In the case where the scattered photons have nearly the same energy as the incident photons, the scattering process is considered elastic and is called Rayleigh scattering. When nuclear motion is induced while the scattering process is

taking place, energy will either be transferred from the incident photon to the molecule or from the molecule to the photon that was scattered. As a consequence of this, the energy of the scattered photon is either less than or greater than the energy of the photons that initially entered the system. The term "Raman scattering" is used to describe this type of scattering. If the frequency of the scattered photon is becoming lower, this is referred to as the Stokes frequency, and if the frequency ends up being higher, this is referred to as the anti-Stokes frequency. This energy loss/gain is unique to a specific bond in the molecule and is a characteristic of the bond (Figure 2.7).

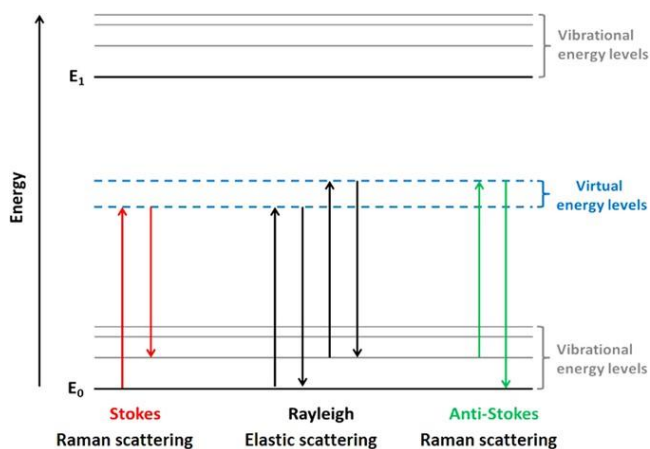


Figure 2.7. Energy level diagram indicating the transitions involved in Raman scattering.⁵¹

The scattered photons of light consist almost exclusively of Rayleigh and only contain a negligible amount of Raman scattered light about only one in every 10^6 – 10^8 photons. Though not all molecular or vibrational motions are Raman active, motions that cause a shift in the polarizability ellipsoid display strong Raman scattering. The most noticeable shifts and scattering typically result from symmetric vibrations. Raman is best understood as the generation of a precise spectral fingerprint, specific to a molecule or, more accurately, a specific molecular structure. Thus, it is comparable to Fourier transform infrared (FT-IR) spectroscopy, which is more common. In contrast to FT-IR, Raman has a number of distinct benefits: (1) Since Raman is not affected by the large water absorption effects seen in FT-IR technique, it has the potential to analyze aqueous solutions; (2) In solution, the concentration of a species determines how strongly its

spectral features are exhibited; (3) Almost no sample preparation is necessary for Raman. Nujol and KBr matrices are unnecessary. Both Raman and mid-infrared spectroscopies are complemented to each other. In general, symmetric vibrations of non-polar groups are best analyzed using Raman spectroscopy, whereas asymmetric vibrations of polar groups are best analyzed using infrared spectroscopy.

A Raman system includes the following four major components (Figure 2.8): a laser excitation source, a sample illumination system and light collection optics, a wavelength selector (either a filter or spectrophotometer), and a detector (photodiode array, CCD or PMT). Laser beams with wavelengths in the ultraviolet (UV), visible (Vis), or near infrared (NIR) ranges are typically used to illuminate a sample. In order to obtain the Raman spectrum of a sample, scattered light must first be collected using a lens, after which it must be passed through an interference filter or spectrophotometer.

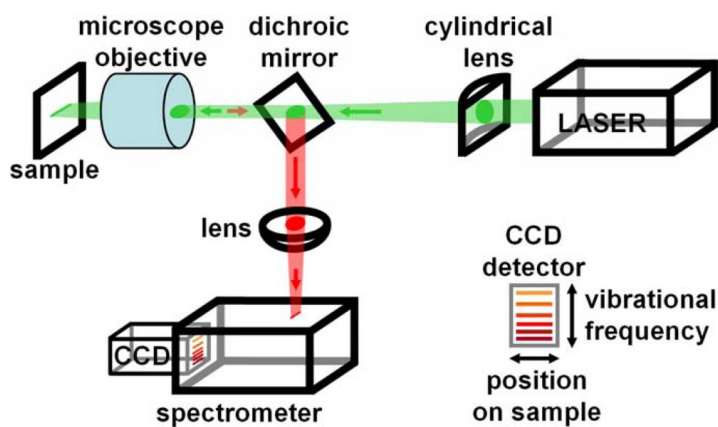


Figure 2.8. Schematic depiction of Raman spectrometer.⁵²

In chapters 3 and 4 of this thesis, a confocal Raman microscope was used to monitor the photocatalytic conversion of PATP molecules in DMAB through SERS measurements and also recorded SERS of rhodamine B dye using $\text{SiO}_2\text{@Au}$ nanostars. Throughout the investigation, a confocal Raman microscope (Witec alpha 300 R) that was paired with an upright optical microscope (Zeiss) was utilized. The measurements were taken in air with lasers having wavelengths of 532, 633, and 785 nm and using objectives of 10 \times , 50 \times , and 100 \times .

2.4.6. Atomic force microscopy (AFM)

Atomic force microscopy, also known as scanning force microscopy (SFM), is a type of scanning probe microscopy (SPM) that has a very high resolution. It has a resolution that has been demonstrated to be on the order of fractions of a nanometer, and is more than 1000 times better than the optical diffraction limit. Using a mechanical probe, the information is collected by "feeling" or "touching" the surface of the object. Images are produced by an AFM by moving a cantilever (Figure 2.9), which is relatively small, across the surface of a sample. The cantilever is bent when it makes contact with the surface because the sharp tip at the end of the cantilever presses against the surface. This causes a change in the amount of laser light that is reflected into the photodiode. After that, the height of the cantilever is tuned in order to regain the response signal. This action causes the calibrated cantilever height to trace the surface.

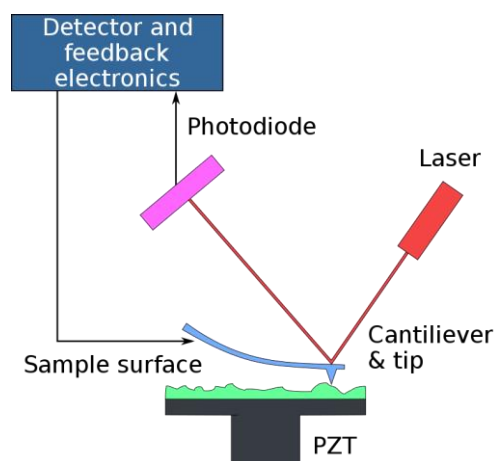


Figure 2.9. Depiction of an atomic force microscope. (Image collected from Wikipedia).

The operation of an AFM can typically be categorized into one of three modes based on the type of tip motion being performed: contact mode, tapping mode, and non-contact mode. In the contact mode, the tip is raster-scanned all over the surface, and the lever is deflected as it moves across the topography of the surface. Because the cantilever is kept at a distance of less than 10^{-10} m from the sample during the experiment, the interatomic force that acts between the sample and the cantilever is repelling. In the non-contact mode, the spacing between the cantilever and the sample surface is in the range of tens to hundreds of Å. In this mode, the interatomic forces exert an attractive

force on the system. The tapping mode is a type of intermittent mode that moves back and forth between the contact and non-contact modes.

In chapter 6 of this thesis, tapping mode AFM imaging of DNA origami and DNA origami templated Au@Ag nanostars was done. Mica disks were used for the preparation of AFM samples (V1 quality). The Bruker Multimode 8 scanning probe microscope, silicon cantilever from Bruker, and Budget sensors (Tap150Al-G) with a force constant of 5 N/m were used in this study.

2.4.7. Transmission electron microscopy (TEM)

The transmission electron microscope is an extremely effective instrument in the field of material science. Since it is a quantitative technique, it reveals specifics about the size, shape, and distribution of nanostructures, among other structural characteristics. An electron beam with a high energy is shone across a very thin sample and the morphological features of the sample can be observed based on the interactions that occur between the atoms and the electrons. The image is produced through the use of the electrons that are transmitted. TEM is based on the same fundamental principles as the light microscope, but it utilizes electrons rather than light. The wavelength of electrons is significantly shorter than that of light, so the optimal resolution that can be achieved with TEM images is many several orders of magnitude superior than that which can be achieved with a light microscope. Therefore, TEM can show even the most minute aspects of a material's internal structure. When applied to visible light, Abbe's equation can produce an approximation of a resolution limit (d) of approximately 200 nm in a light microscope which is limited by wavelength of photons (Equation 2.5).

$$d = \frac{1.22\lambda}{2NA} \quad \text{Equation 2.5}$$

Where, λ is wavelength of light and NA is numerical aperture. According to the theory of Louis-Victor de Broglie, electrons possess both wave and particle properties. Because electrons behave like waves, a beam of electrons can be focused and diffracted in a manner that is analogous to how light behaves. Using the de Broglie equation, one

can determine a relationship between the wavelength of electrons and their kinetic energy (Equation 2.6).

$$\lambda_e = \frac{h}{\sqrt{2m_0E(1+\frac{E}{2m_0c^2})}} \quad \text{Equation 2.6}$$

Where, h is Planck's constant, m_0 is electron rest mass, and c is speed of light. Electrons are accelerated using various accelerating voltages and focused using electromagnetic and electrostatic lenses on the sample. The electron density, periodicity, and phase can all be determined from the transmitted beam of electrons, which is then used to create an image. Accelerating voltages between 80 and 120 kV are typically used on biological samples. Samples with lower sensitivities can tolerate higher voltages around 200 kV. The typical instrumentation set up of TEM is shown below (Figure 2.10).

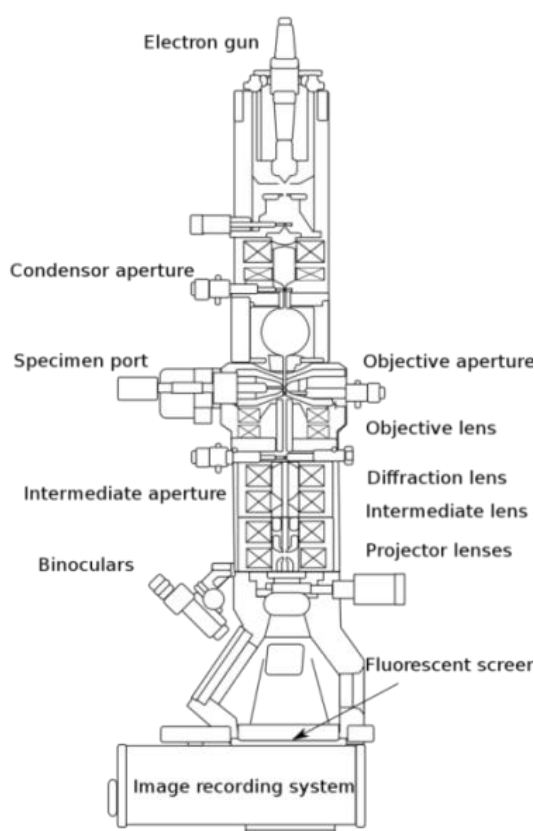


Figure 2.10. Diagrammatic representation of a transmission electron microscope. (Image collected from Wikipedia).

The electron gun and the condenser system are the two components that make up the lighting system. An electron beam is produced by the electron gun, and it is directed toward the sample. Crystals of lanthanum hexaboride (LaB₆) serve as the electron source in modern TEM. The electron beam that was generated is concentrated on the sample by the condenser system. The objective lens, the condenser lens, the intermediate lens, the projector lens, and the movable specimen stage make up the image-producing system. The primary beam is formed by the condenser lens, and the image is initially magnified by the objective lens. The image produced by the objective lens is then magnified by the intermediate lenses after it has passed through the objective lens. At long last, the projector lens broadens the beam so that it can be projected onto a fluorescent screen. TEM has an image recording system that consists of a fluorescent screen and a CCD camera. The fluorescent screen is used to view the sample, and the CCD camera converts this electron image in to digital image.

2.4.7.1 HAADF-STEM (high-angle annular dark-field scanning transmission electron microscopy)

High-angle annular dark-field scanning transmission electron microscopy (HAADF-STEM) is a STEM technique that utilizes an annular dark-field (ADF) detector to gather inelastically scattered electrons or thermal diffuse scattering (TDS) at high angles (~50 to appropriately high angle). Displaying the electrons' integrated intensities in synchronization with the incident probe position yields a STEM image. Due to the HAADF's image intensity being proportional to the square of the atomic number, heavier atoms can be easily observed due to their greater brightness, while lighter atoms are more challenging to observe due to their lower intensity. There are two main factors that make the HAADF image simple and easy to understand: (1) Due to the small size of the TDS scattering cross section at the high angles required for imaging, no multiple scattering occurs. (2) For imaging purposes, the electron interference effect is suppressed (non-interference image). The diameter of the incident probe on the specimen determines the resolution of the HAADF image. Better than 0.05 nm resolution is achievable with a high-performance STEM instrument. A schematic representation of ray diagram of HAADF is shown in Figure 2.11.

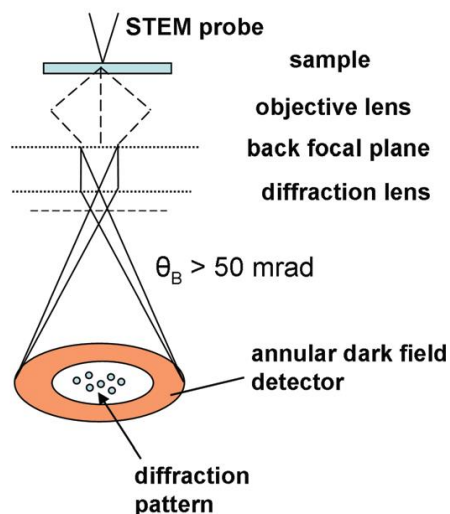


Figure 2.11. Schematic representation of ray diagram of HAADF. (Reproduced with permission from ref.⁵³, 2012 American Vacuum Society)

In this thesis, TEM has been utilized for the purpose of determining the size and morphology of as synthesized Au nanoparticles, silica nanoparticles, DNA origami, and Au-ZnO hybrid nanostructures. Imaging biological samples without first staining them can be challenging owing to the fact that the scattering effect is related to the square of the atomic number. Therefore, negative staining with uranyl acetate was performed in order to image DNA origami. The transmission electron microscopy (TEM), high-resolution transmission electron microscopy (HRTEM), electron dispersive x-ray spectroscopy (EDX), and scanning transmission electron microscope - electron dispersion x-ray spectroscopy (STEM-EDX) were performed with a JEOL model 2100 instrument at an accelerating voltage of 200 kV for nanoparticles and 120 kV for DNA origami. The JEOL JEM 200F system was used to acquire HAADF-STEM mapping images of Au@Ag nanostars, SiO₂@Au nanostars, and Au@ZnO nanocomposites, and the accelerating voltage was set to 200 kV throughout the process.

2.4.8. X-ray Photoelectron spectroscopy (XPS)

X-ray Photoelectron spectroscopy (XPS) is a technique that uses X-rays to irradiate a sample's surface and then measures the photoelectrons' kinetic energy as they escape the sample (XPS). By employing this technique, researchers are able to examine the surface of a sample in detail, learning about its chemical bonds, and the elements along with

their oxidation states which make up its composition. It is basically a surface analytical method as it can be used on a wide variety of materials and offers useful quantitative and chemical state details from the surface of the sample being analyzed. XPS works by using the guidelines of photoelectric effect: When X-ray beam having sufficient energy hits the sample, i.e., if photon energy is higher than the binding affinity of the core electron, the core electrons become excited, leave the atom, and emit out of the surface. Binding energy of solids is calculated by the following equation (Equation 2.7).

$$BE = h\nu - KE - (\phi) \quad \text{Equation 2.7}$$

Where BE represents the binding energy of the atom from which the electron has been ejected, KE stands for the kinetic energy of the electron, and Φ stands for the work function. In the XPS, the sample is subjected to irradiation by soft X-rays with an energy range of between 200 and 2000 eV to remove the electron from core. Ultra violet rays have the ability to eject valence electrons, which, in turn, provides information about the bonding in molecules. This technique is referred to as "Ultraviolet Photoelectron Spectroscopy (UPS)". The monochromatic beam is able to penetrate the sample to a depth of a few nanometers (between 3 and 10 nm for an Al K α), and the emitted electrons are then directed to the analyzer by means of magnetic or electrostatic lenses. When the number of electrons ejected is plotted against their binding energy, an XPS spectrum is produced. In an XPS spectrum, a group of peaks appear; these peaks further assist in determination of the chemical state as well as the electronic state of the material being observed. Figure 2.12 illustrates the components that are included in a commercially available XPS system. These components include a source of X-rays, an electron collection lens, an ultra-high vacuum (UHV) stainless steel chamber with UHV pumps, an electron energy analyzer, an electron detector system, Mu-metal magnetic field shielding, a modest vacuum sample introduction chamber, a sample stage, sample mounts, and a set of stage manipulators.

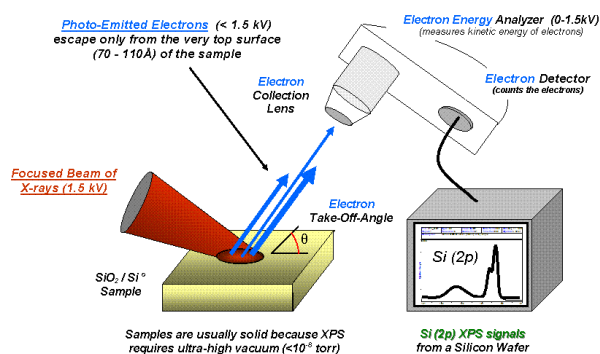


Figure 2.12. The fundamental parts of a monochromatic XPS setup. (Image is taken from Wikipedia).

In the present this we have used X-ray photoelectron spectroscopy (XPS) on ECSA: 220-IXL with $\text{MgK}\alpha$ is used for further investigation of elements. The $\text{MgK}\alpha$ used is non-monochromated X-ray beam with photon energy 1253.6 eV.

2.4.9. Electrochemical Studies

Electrochemical methods typically involve the use of an electrochemical cell with an electrolyte and conducting electrodes dipped in the electrolyte to measure the reaction to an electric input. Oxidation and reduction are two different types of chemical reactions that occur as a result of charge transport via the electrode-electrolyte interface.

2.4.9.1. Electrode configuration: Three electrode setup

The working electrode, the reference electrode, and the counter electrode consider as components of the setup. The glassy carbon (GC) electrode fulfills the role of the working electrode, Ag/AgCl (3M KCl) electrode serves as the function of the reference electrode, and platinum electrode plays the role of the counter electrode. When measuring the voltage between the working electrode and the reference electrode, the reference electrode is also connected to the working electrode. If the surface area of the counter electrode is not greater than that of the working electrode, then the rate of the reaction will be slowed down, which is a limiting factor. In most cases, potential difference is applied between the working electrode and the counter electrode. The

configuration only measures one half of the cell, but it enables a more accurate study of the specific reaction.

In chapter 6 of this thesis, all the electrochemical measurements were carried out using Metrohm Autolab (Multichannel-204) connected to a standard three-electrode electrochemical cell using Nova 2.1.4 software. For the electrochemical measurements, the samples were coated on a GC electrode which acted as the working electrode. Platinum (Pt) and Ag/AgCl (3M KCl) electrodes were used as counter electrode and reference electrode for the electrochemical OER studies, respectively.

2.4.9.2. Electrochemical techniques

2.4.9.2.1. Linear and cyclic sweep voltammetry

The linear sweep voltammetry (LSV) illustrates the sweeping of voltage at a constant rate to potential range. This is done by measuring the voltage across the potential window. If the same scan is performed multiple times in a row, the method is known as cyclic voltammetry, and the voltammogram is a representation of the data recorded in the form of current versus potential. The LSV recorded at a slow scan speed can serve as a valuable method for obtaining the Tafel slope, and it can also define the mechanism by which the reaction proceeds. In cyclic voltammetry, surface properties such as oxide formation, mass loading, and morphology of the catalyst are evaluated via the electrode-electrolyte interface. The number of cycles, scan rate, and potential range are the other factors that are taken into consideration in this evaluation. The repeated cycles are used to determine the durability of the catalyst, which is something that can be demonstrated more convincingly through long-term electrolysis at a particular current density.

2.4.9.2.2. Electrochemical impedance spectroscopy (EIS)

Electrochemical impedance spectroscopy is a useful technique that elucidates the electrochemical properties of various coatings, surfaces, catalysts, and interfaces etc. It is now unavoidable to not use EIS in a variety of subfields of energy research where current, potential, and charge all play important roles in determining performance. EIS correlates activity trends by measuring charge transfer resistances (R_{ct}). The R_{ct} values

of the various electrocatalysts that were investigated primarily serve the purpose of benchmarking the activity. By deducting the resistance (iR) from the applied potential (E), one can arrive at the corrected potential ($E_{\text{corrected}}$). The corrected potential is known as “ iR corrected” (Equation 2.8).

$$E_{\text{Corrected}} = E - iR \quad \text{Equation 2.8}$$

Where, iR is the total circuit resistance.

2.4.9.2.3 Stability

It is essential to consider both electrocatalytic activity and long-term stability when choosing materials or electrocatalysts for an electrochemical reaction. Because of its high efficiency, an electrocatalyst is used, but it also needs to be resistant to corrosion and stable in aggressive environments such as highly acidic and basic conditions during OER and HER reactions.

In this thesis, LSV cycles at a constant scan rate were used to test the electrocatalysts' stability. Furthermore, designed catalysts' stability was examined across a broad range of applied potential and current in chronopotentiometry and chronoamperometric studies, respectively.

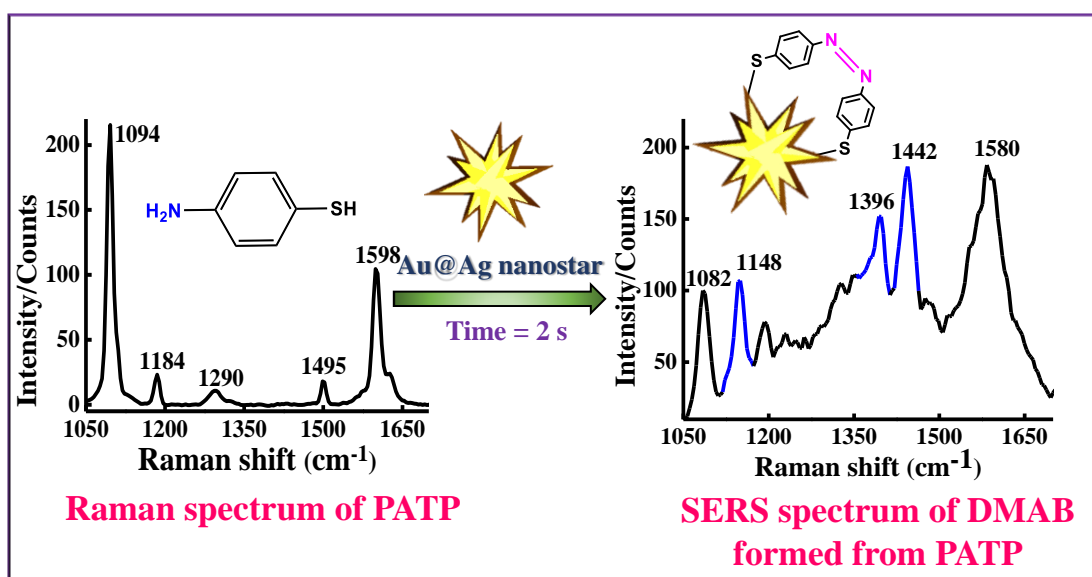
References

1. M. Faraday, *Philosophical Transactions of the Royal Society of London*, 1857, 145-181.
2. J. Turkevich, *Gold Bulletin*, 1985, **18**, 125-131.
3. J. Turkevich, P. C. Stevenson and J. Hillier, *Discussions of the Faraday Society*, 1951, **11**, 55-75.
4. G. Frens, *Nature Physical Science*, 1973, **241**, 20-22.
5. A. Biswas, I. S. Bayer, A. S. Biris, T. Wang, E. Dervishi and F. Faupel, *Advances in Colloid and Interface Science*, 2012, **170**, 2-27.
6. Z. Tang and A. Wei, *ACS Nano*, 2012, **6**, 998-1003.
7. M. J. Mulvihill, X. Y. Ling, J. Henzie and P. Yang, *Journal of the American Chemical Society*, 2010, **132**, 268-274.
8. N. Abid, A. M. Khan, S. Shujait, K. Chaudhary, M. Ikram, M. Imran, J. Haider, M. Khan, Q. Khan and M. Maqbool, *Adv Colloid Interface Sci*, 2022, **300**, 102597.
9. A. K. Pearce, T. R. Wilks, M. C. Arno and R. K. O'Reilly, *Nature Reviews Chemistry*, 2021, **5**, 21-45.
10. G. Berhault, M. Bausach, L. Bisson, L. Becerra, C. Thomazeau and D. Uzio, *The Journal of Physical Chemistry C*, 2007, **111**, 5915-5925.
11. Y. Xiong and Y. Xia, *Advanced Materials*, 2007, **19**, 3385-3391.
12. S. P. McDarby, C. J. Wang, M. E. King and M. L. Personick, *Journal of the American Chemical Society*, 2020, **142**, 21322-21335.
13. E. H. Hill, N. Claes, S. Bals and L. M. Liz-Marzán, *Chemistry of Materials*, 2016, **28**, 5131-5139.
14. M. R. Jones, K. D. Osberg, R. J. Macfarlane, M. R. Langille and C. A. Mirkin, *Chemical Reviews*, 2011, **111**, 3736-3827.
15. F. Fiévet, S. Ammar-Merah, R. Brayner, F. Chau, M. Giraud, F. Mammeri, J. Peron, J. Y. Piquemal, L. Sicard and G. Viau, *Chemical Society Reviews*, 2018, **47**, 5187-5233.
16. J. Zhu, Y. Shen, A. Xie, L. Qiu, Q. Zhang and S. Zhang, *The Journal of Physical Chemistry C*, 2007, **111**, 7629-7633.
17. N. R. Jana, L. Gearheart and C. J. Murphy, *Chemical Communications*, 2001, 617-618.
18. N. R. Jana, L. Gearheart and C. J. Murphy, *Advanced Materials*, 2001, **13**, 1389-1393.
19. Y. Zhai, J. S. DuChene, Y.-C. Wang, J. Qiu, A. C. Johnston-Peck, B. You, W. Guo, B. DiCiaccio, K. Qian and E. W. Zhao, *Nature Materials*, 2016, **15**, 889-895.
20. W. Niu, Y. A. A. Chua, W. Zhang, H. Huang and X. Lu, *Journal of the American Chemical Society*, 2015, **137**, 10460-10463.
21. A. Guerrero-Martínez, S. Barbosa, I. Pastoriza-Santos and L. M. Liz-Marzán, *Current Opinion in Colloid & Interface Science*, 2011, **16**, 118-127.
22. P. S. Kumar, I. Pastoriza-Santos, B. Rodríguez-González, F. J. G. De Abajo and L. M. Liz-Marzán, *Nanotechnology*, 2007, **19**, 015606.
23. H. Yuan, C. G. Khoury, H. Hwang, C. M. Wilson, G. A. Grant and T. Vo-Dinh, *Nanotechnology*, 2012, **23**, 075102.
24. R. Borah and S. W. Verbruggen, *The Journal of Physical Chemistry C*, 2020, **124**, 12081-12094.
25. N. Blommaerts, H. Vanrompay, S. Nuti, S. Lenaerts, S. Bals and S. W. Verbruggen, *Small*, 2019, **15**, 1902791.
26. K. J. Major, C. De and S. O. Obare, *Plasmonics*, 2009, **4**, 61-78.
27. D. Ferrer, A. Torres-Castro, X. Gao, S. Sepúlveda-Guzmán, U. Ortiz-Méndez and M. José-Yacamán, *Nano Letters*, 2007, **7**, 1701-1705.
28. M. Tsuji, N. Miyamae, K. Matsumoto, S. Hikino and T. Tsuji, *Chemistry Letters*, 2005, **34**, 1518-1519.

29. Q. Fu, D. Zhang, M. Yi, X. Wang, Y. Chen, P. Wang and H. Ming, *Journal of Optics*, 2012, **14**, 085001.
30. L. R. Hirsch, A. M. Gobin, A. R. Lowery, F. Tam, R. A. Drezek, N. J. Halas and J. L. West, *Annals of Biomedical Engineering*, 2006, **34**, 15-22.
31. A. L. Aden and M. Kerker, *Journal of Applied Physics*, 1951, **22**, 1242-1246.
32. S. J. Oldenburg, R. D. Averitt, S. L. Westcott and N. J. Halas, *Chemical Physics Letters*, 1998, **288**, 243-247.
33. R. Averitt, D. Sarkar and N. Halas, *Physical Review Letters*, 1997, **78**, 4217.
34. H. S. Zhou, I. Honma, H. Komiyama and J. W. Haus, *Physical Review B*, 1994, **50**, 12052-12056.
35. L. Ma, S. Chen, Y. Shao, Y.-L. Chen, M.-X. Liu, H.-X. Li, Y.-L. Mao and S.-J. Ding, *Catalysts*, 2018, **8**, 634.
36. C. Wang and D. Astruc, *Chemical Society Reviews*, 2014, **43**, 7188-7216.
37. L. Liu, S. Ouyang and J. Ye, *Angewandte Chemie*, 2013, **125**, 6821-6825.
38. Q. Zhang, D. Q. Lima, I. Lee, F. Zaera, M. Chi and Y. Yin, *Angewandte Chemie International Edition*, 2011, **50**, 7088-7092.
39. X.-F. Wu, H.-Y. Song, J.-M. Yoon, Y.-T. Yu and Y.-F. Chen, *Langmuir*, 2009, **25**, 6438-6447.
40. N. Zhang, S. Liu, X. Fu and Y.-J. Xu, *The Journal of Physical Chemistry C*, 2011, **115**, 9136-9145.
41. R. Jiang, B. Li, C. Fang and J. Wang, *Advanced Materials*, 2014, **26**, 5274-5309.
42. P. W. K. Rothmund, *Nature*, 2006, **440**, 297-302.
43. H.-K. Nguyen and E. M. Southern, *Nucleic Acids Research*, 2000, **28**, 3904-3909.
44. J. J. Schmied, M. Raab, C. Forthmann, E. Pibiri, B. Wünsch, T. Dammeyer and P. Tinnefeld, *Nature Protocols*, 2014, **9**, 1367-1391.
45. R. Jungmann, M. Scheible, A. Kuzyk, G. Pardatscher, C. E. Castro and F. C. Simmel, *Nanotechnology*, 2011, **22**, 275301.
46. P. Wang, T. A. Meyer, V. Pan, P. K. Dutta and Y. Ke, *Chem*, 2017, **2**, 359-382.
47. T. Tørring, N. V. Voigt, J. Nangreave, H. Yan and K. V. Gothelf, *Chemical Society Reviews*, 2011, **40**, 5636-5646.
48. S. Takabayashi, W. P. Klein, C. Onodera, B. Rapp, J. Flores-Estrada, E. Lindau, L. Snowball, J. T. Sam, J. E. Padilla and J. Lee, *Nanoscale*, 2014, **6**, 13928-13938.
49. A. V. Malm and J. C. W. Corbett, *Scientific Reports*, 2019, **9**, 13519.
50. T. A. T. Mohd, M. Z. Jaafar, A. A. A. Rasol and M. F. Hamid, *MATEC Web of Conferences*, 2017.
51. K. J. I. Ember, M. A. Hoeve, S. L. McAughtrie, M. S. Bergholt, B. J. Dwyer, M. M. Stevens, K. Faulds, S. J. Forbes and C. J. Campbell, *npj Regenerative Medicine*, 2017, **2**, 12.
52. A. Downes and A. Elfick, *Sensors*, 2010, **10**, 1871-1889.
53. F. H. Baumann, *Journal of Vacuum Science & Technology B, Nanotechnology and Microelectronics: Materials, Processing, Measurement, and Phenomena*, 2012, **30**, 041804.

Chapter 3

Interfacial design of gold/silver core-shell nanostars for plasmon-enhanced photocatalytic coupling of 4-aminothiophenol



3.1. Introduction

Tuning the size and shape of nanostructures made of noble metals like gold (Au) and silver (Ag) is a proven method for attributing their physical and chemical properties for use in a wide range of fields, including physics, chemistry, biology, and materials science. The surface plasmon resonance (SPR) has made plasmonic metal nanostructures of great interest and led to their widespread use in a variety of applications such as catalysis, surface plasmon resonance sensors,¹ photothermal therapy² and SERS.³ In particular, localized surface plasmon resonance (LSPR) assisted catalysis has shown potential as a novel route for studying chemical responses on plasmonic metal nanostructures with the aid of SERS. Various SPR-assisted chemical reactions such as photochemical isomerization,⁴ polymerization,⁵ photocatalytic reactions,^{6,7} and photodissociation⁸ have been examined using SERS. SERS is typically amplified by plasmonic metal nanostructures, which can produce fingerprint information down to the single molecular level with extreme precision and sensitivity.⁹

Surface plasmon resonance (SPR) driven photocatalytic reactions have received a lot of interest because of their convenient approach, as well as the highly energetic hot charge carriers (electrons and holes) produced by the decaying of SPR in contrast to the electrons generated by conventional photocatalytic materials.¹⁰ Previous research concentrated primarily on utilizing different morphologies of monometallic metal nanostructures, such as spheres and nanorods with tunable SPR band positions. However, the catalytic activity of such plasmon-based photocatalysis highly depends on the rational design of the plasmonic nanomaterials. In addition to studies showing the development of monometallic nanomaterials, a few studies have shown the development of bimetallic nanostructures, such as alloy and core-satellite superstructures, that increase photocatalytic activity by tuning the SPR. bimetallic nanostructures comprised of plasmonic nanoparticles were used to induce or enhance the oxidation¹¹ and facilitate coupling reactions¹² due to its enhanced reactivity, product selectivity, specificity and optical sensitivity via binary structures formation.¹³

Plasmonic nanostructures have been utilized for understanding the plasmon-driven chemical reactions by taking a model coupling reaction, the conversion of *p*-aminothiophenol (PATP) into 4,4'-dimercaptoazobenzene (DMAB) monitored through SERS measurements. PATP molecules have attracted a lot of attention because of their potential uses in electronic systems and their function as a Raman probe molecule that generates a potent SERS signal upon intense interaction with plasmonic metallic nanostructures.¹⁴ The catalytic conversion reaction from PATP to DMAB monitored through SERS is used for gaining an understanding of the dynamics of hot carriers and charge transfer from the metal surface to the molecule.¹⁵ Pioneering works on the dimerization of conversion of PATP to DMAB were reported using spherical Au and Ag nanoparticles based on the SERS technique as PATP is a Raman active molecule, and the new vibrational modes which are generated due to the formation of DMAB can be enhanced by Au and Ag nanostructures.¹⁶⁻¹⁸ For example, Osawa and co-workers recorded the SERS of PATP and they found that new peaks were emerging which were then considered as enhanced so-called “b₂” modes of PATP molecule.¹⁹ Later on, other groups^{20, 21} have shown that new peaks were appearing as a result of the dimerization of PATP molecule into its dimeric product DMAB. This conversion procedure occurs through the charge transfer of LSPR excited electrons to oxygen which adsorbed at the metal surface, enabling the utilization of visible light for oxidation reactions.²¹⁻²⁶ Recently, Anderson *et al* reported the use of multimetallic Au/AgAu nanorattles which contained a nanosphere within a nanoshell, towards SPR mediated oxidations by utilizing the plasmon concoction idea.¹⁸ However, even though a variety of monometallic¹⁷ and bimetallic²⁷ nanostructured materials have been exploited for plasmonic catalytic conversion of PATP to DMAB, still relatively little focus has been placed on the investigation of bimetallic gold (core) and silver (shell) nanostars (Au/Ag NSs) shape structure in the chemical reaction. Multiple studies showed that compared to spherical or rod-shaped Au nanostructures, Au nanostars with sharp tips significantly increase the catalytic efficiency of semiconducting material in the visible and NIR region. The reason is that there are more hot electrons near the interface because of the extremely enhanced electromagnetic field surrounding the sharp spikes.²⁸ As a result of the strong field enhancement at the nanostars' pointed tips, this shape is well suited for

SERS applications.²⁹ In addition, by simply varying the thickness of the Ag coating over the Au nanostars, the LSPR band can be tuned over a range of wavelengths, bringing together the enhanced plasmonic properties of Ag and the chemical stability of Au in a single bimetallic Au/Ag nanostructure.³⁰ As both optical and catalytic properties of such nanostructures can be tuned by controlling the morphology (such as the sharpness and number of tips surrounding the core) and varying shell thickness of the nanostructures, controlled design of nanomaterials like these open the door to plasmonic catalysis's potential for mechanistic insight and efficiency improvement.

In this chapter, We have included synthesis of anisotropically shaped Ag coated Au nanostars, i.e., bimetallic Au/Ag nanostars, and carried out spectral, structural, and microscopic studies. In bimetallic nanostructures, strong plasmon mixing between the Au and Ag segments of the Au/Ag nanostars can prompt a great extent in electromagnetic and chemical enhancements compared to its individual counterparts in a controllable manner without relying on the unbridled assembly among individual nanostructures. Hence, this unique shape of bimetallic Au core/Ag shell nanostars was used in a plasmon-driven photocatalytic reaction using a model oxidative coupling reaction i.e., conversion of PATP into DMAB on the Au/Ag nanostars surface. The emergence of “b₂” modes related to –N=N– vibrational modes in SERS spectrum of PATP in Au/Ag nanostar solution predicted the formation of dimerized product of PATP. In order to gain insight into their plasmonic catalytic efficiency of Au/Ag nanostars, the concentration dependent SERS was recorded under neutral, basic and acidic conditions. The time dependent SERS performances were also carried out in order to get the completion time for this conversion. This chapter demonstrates the efficiency of Au/Ag nanostars in promoting the conversion of PATP to DMAB, as well as whether Au/Ag nanostars are superior to their pure metal counterparts or not. Therefore, the research provided in this chapter paves way to new opportunities for the application of plasmonic photocatalysis in conversion reactions and the synthesis of organic molecules.

3.2. Experimental Section

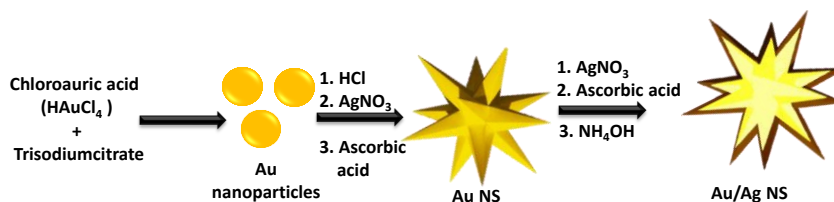
3.2.1. Materials

L- Ascorbic acid, Gold chloride trihydrate ($\text{HAuCl}_4 \cdot 3\text{H}_2\text{O}$), Sodium dodecyl sulphate (SDS), Silver nitrate (AgNO_3), Ammonium hydroxide solution (NH_4OH) 25%, Hydrochloric acid (HCl), Trisodium citrate dihydrate, Sodium hydroxide (NaOH), Para-aminothiophenol (PATP), and Sodium chloride (NaCl) were purchased from Sigma-Aldrich. Ethanol (absolute for analysis) was purchased from Merck. All the reagents were used without further purification. Milli-Q (MQ) water was used during the experiment.

3.2.2. Experimental procedures

3.2.2.1. Synthesis of silver coated gold nanostars (Au/Ag nanostars)

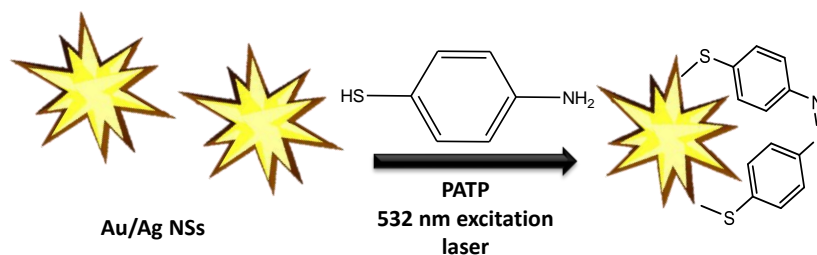
Synthesis of Au/Ag nanostars was achieved by applying an Ag coating to seed-mediated synthesized Au nanostars (Scheme 3.1). Au seeds were prepared by citrate reduction method³¹ as discussed in chapter 2 of the thesis. Briefly, to 12.5 mL of boiling 1 mM HAuCl_4 solution, 2 mL of 1.5% trisodium citrate was added while stirring vigorously. Within 10 minutes, light yellow solution turned wine red, indicating the formation of 12-15 nm sized Au nanoparticles. After color stabilization, heating was stopped and cooled at room temperature with stirring. Then, Au nanostars were prepared by adding 150 μL of above prepared Au seed solution to growth solution containing 12.5 mL of 0.2 mM HAuCl_4 , 12.5 μL of 1 M HCl, and 40 μL of 0.01 M AgNO_3 . Upon addition of 62.5 μL of 0.1 M ascorbic acid, color was changed to blue indicating the formation of Au nanostars.³² The prepared Au nanostars were coated with silver according to modified protocol.³⁰ After 10 minutes of stirring of Au nanostars solution, coating with silver was done by adding 24 μL of 0.1 M AgNO_3 , 24 μL of 0.1 M ascorbic acid, 24 μL of NH_4OH solution. After 10 minutes of addition, color was changed to yellowish purple and then 0.5 mL of 0.1 M SDS was added. The reaction mixture was further stirred for 10 minutes followed by centrifugation at 4500 RPM for 10 minutes and resuspended in MQ water.



Scheme 3.1. Schematic depiction of the synthesis of Ag coated Au nanostar

3.2.2.2. Catalysis of PATP to *p,p'*-Dimercaptoazobisbenzene (DMAB)

To carry out the conversion reaction of PATP into its dimerized product DMAB by using Au/Ag nanostars (Scheme 3.2), 1 μM ethanolic solution of PATP was prepared. 20 μL of Au/Ag nanostars solutions were added to 800 μL of 1 μM PATP solution to have different final concentrations of reaction mixtures.



Scheme 3.2. Schematic depiction of the catalytic conversion of PATP into DMAB using Au/Ag nanostars.

3.2.2.3. pH dependent studies

To show the effect of neutral, acidic and basic environments on the conversion reaction, the reaction mixtures of PATP and Au/Ag nanostars were adjusted to pH ~ 7 , ~ 4 , ~ 10 , respectively. The pH was adjusted using HCl and NaOH solutions. Then, the Raman spectra were measured.

3.2.2.4. Time-dependent studies

In order to conclude the completion of conversion reaction of PATP into DMAB, time dependent SERS spectra were measured. For time dependent studies, 20 μL of Au/Ag nanostars solution was added to 800 μL of PATP solution. At different time intervals (incubation time of Au/Ag nanostars solution with PATP solution) such as 0 second, 2

seconds, 4 seconds, 8 seconds, 16 seconds, 32 seconds, 64 seconds, 128 seconds, 246 seconds, 512 seconds, and 1024 seconds, NaCl solution was added to reaction mixture to form solid aggregates. Zero incubation time (0s) means that NaCl solution was added to Au/Ag nanostars solution followed by addition of PATP solution. The solid precipitates were collected through centrifugation, dried and SERS spectra were recorded.

3.2.2.5. Raman measurements

Raman measurements were recorded with a confocal Raman microscope (Witec alpha 300 R) equipped with an upright optical microscope (Zeiss). The measurements were performed in air using laser light at 532 nm laser (6mW) using 10 × objective (NA = 0.25) to a diffraction limited spot/laser spot diameter of about 2.6µm.

3.2.2.6. FDTD (finite difference time domain) simulation

The electric field magnitude, $|E|$ is computed through three-dimensional finite-difference time-domain (FDTD) modelling for Au nanostar as well as for Ag coated Au nanostar using commercial-grade simulator Lumerical Software (<https://www.lumerical.com/products/-fdtd/>).

Optical and structural characterization of as synthesized Au nanostars, Ag nanostars, Au/Ag nanostars, were performed by UV-Vis spectrophotometer, XPS, and TEM as described in chapter 2 of this thesis.

3.3. Results and discussion

3.3.1. Optical and structural characterizations of Au/Ag NSs

The Au/Ag nanostars shape (Au/Ag NSs), a unique family of bimetallic nanostructured materials, used in this chapter were synthesized in aqueous medium under mild condition. Our preparation technique depends on consolidating two key ideas, first, the utilization of Au nanostar as the core for Ag coating; second, an appropriate addition variety of the Ag salt in the reaction medium during the fabrication procedure. The

nucleation of Ag coating onto Au NSs was monitored by measuring UV-visible extinction spectra after washing of as prepared Au NSs solution (Figure 3.1).

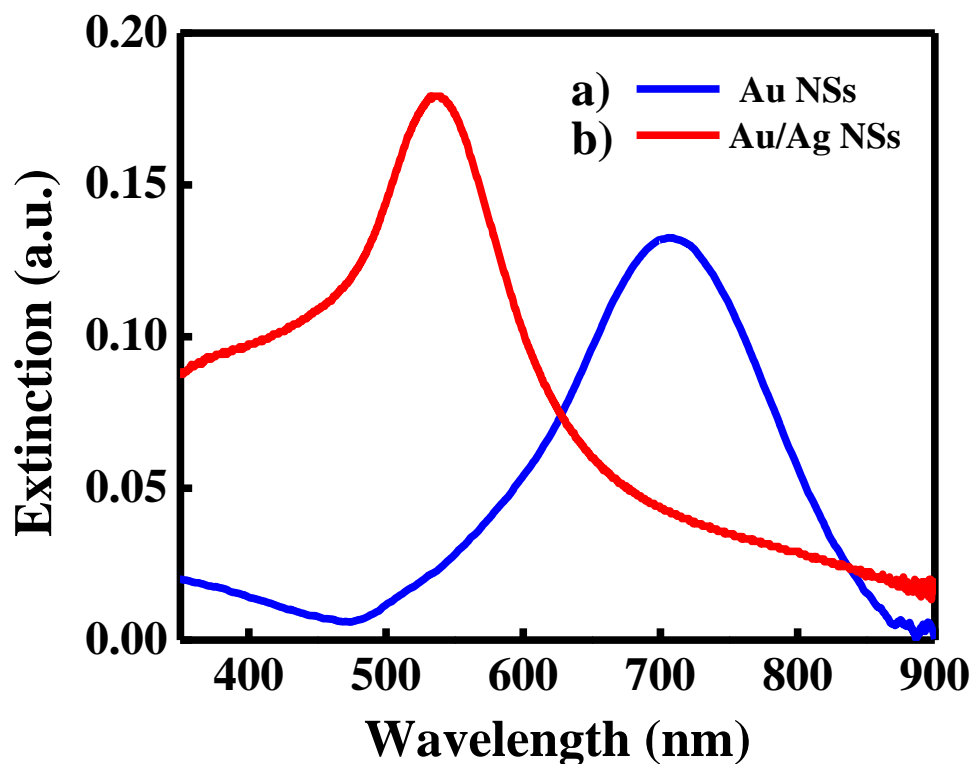


Figure 3.1. UV-Vis extinction spectra of as synthesized (a) Au nanostars, and (b) Au/Ag nanostars.

Figure 3.1a displays the UV-Vis spectrum of Au NSs where the plasmon peak appeared at 710 nm. However, in case of Au/Ag NSs, the absorbance band arises at 538 nm (Figure 3.1b). The plasmon band of the Au/Ag NSs blue-shifts from around 710 nm down toward 538 nm is attributed to the formation of bimetallic Au/Ag nanostars shape. The TEM images of Au nanostars without Ag coating and with Ag coating are shown in Figure 3.2. As it is clear from TEM images that on the as prepared Au nanostars, coating of Ag is carried out without any morphological change of Au nanostar structure. The tips of Au nanostars remain intact.

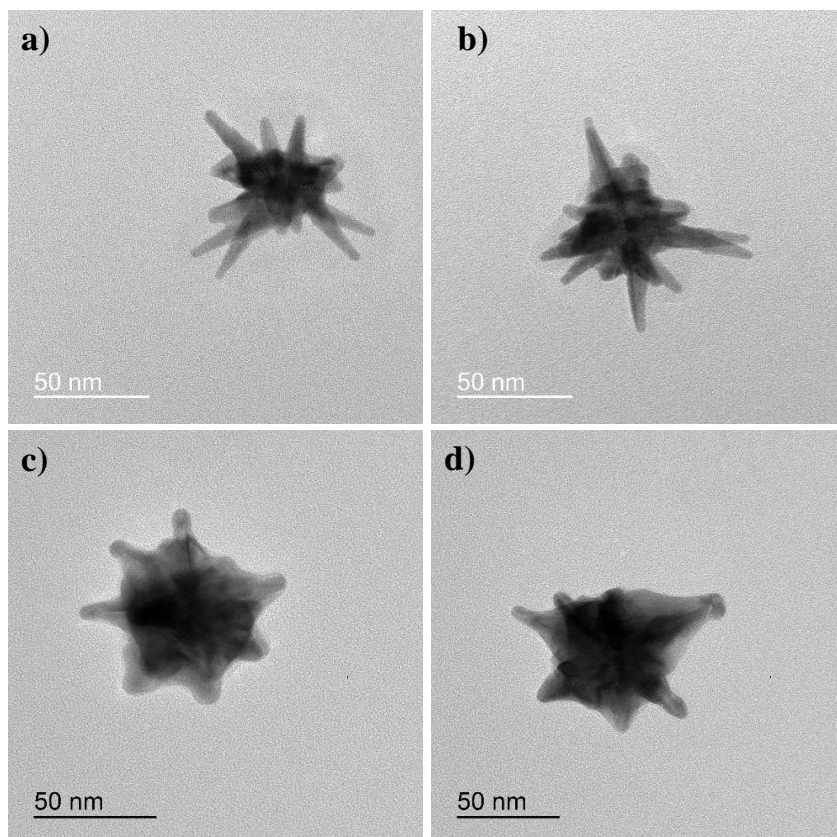


Figure 3.2. TEM images of (a, b) Au NSs and (c, d) Au/Ag NSs.

The morphology and particle size of as synthesized Au/Ag NSs were characterized by using transmission electron microscopy (TEM) at neutral pH (Figure 3.3)

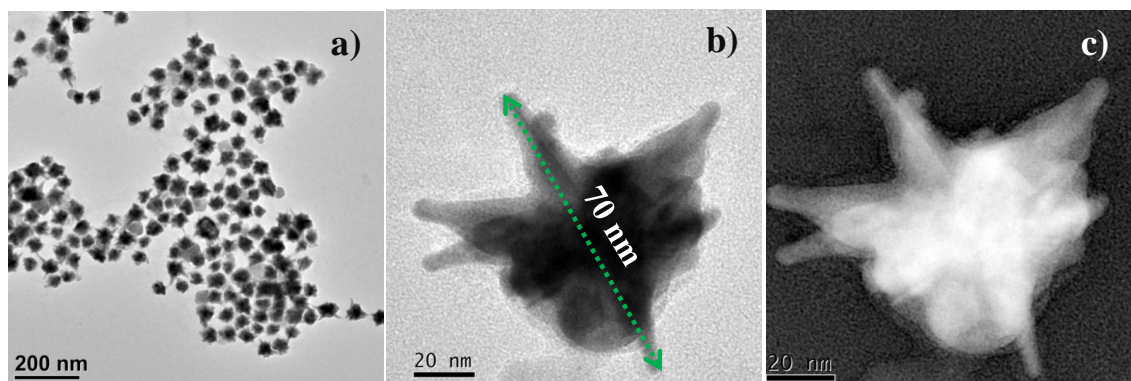


Figure 3.3 TEM images of Au/Ag nanostars (a) wide view, (b) single Au/Ag NSs, and (c) the corresponding inverted TEM image, respectively.

Figure 3.3a reveals a panoramic view of the TEM pictures demonstrating bimetallic Au/Ag nanostars. Without size sorting, the Au/Ag NSs nanocrystals acquired here demonstrated great monodispersity. The designed bimetallic Au/Ag nanostars structures had a profoundly crystalline structure. It has also been seen that the average size of Au/Ag NSs was found to be 70 ± 5 nm (Figure 3.3b). The inverted TEM picture of a single Au/Ag NS (Figure 3.3c) has obviously shown that during the progress of the reaction, Ag coated on the preformed Au nanostar leads to a 3D bimetallic Au/Ag nanostars shape composite nanostructure. The thickness of Ag coating over the Au NSs was found to be an average of 3.5 ± 0.5 nm (Figure 3.4).

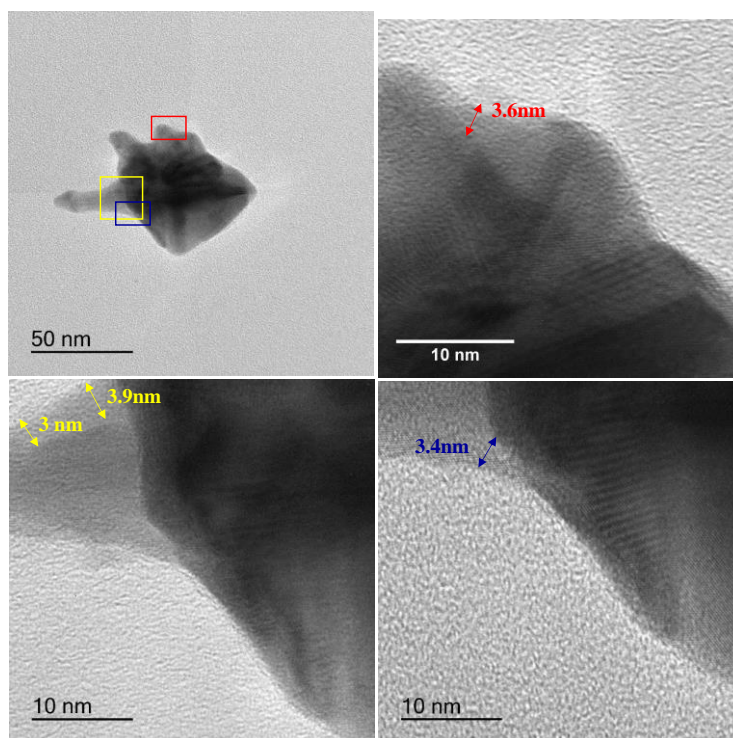


Figure 3.4. High resolution TEM images of Au/Ag NS showing the thickness of Ag over the preformed Au NSs.

To further confirm the Au/Ag NSs, we have investigated as-prepared samples via the high-resolution transmission electron microscopy (HR-TEM) and HAADF-STEM analysis. Figure 3.5a displays the HRTEM image of an Au/Ag NS and corresponding inverse fast fourier transform (IFFT) patterns of the area marked as ‘x’ and ‘y’ (Figure 3.5b and c), demonstrating that the lattice spacing of the observed lattice planes are

around 2.38 and 2.05 Å, which are well suited with the spacing for the (111) and (200) planes of face centred cubic of noble metals. Strikingly, the d-spacing values of 2.38 and 2.05 Å relate to (111) and (200) plane for both cubic Au and Ag nanocrystals, respectively, and it is difficult to distinguish both the lattice fringe at the same time.

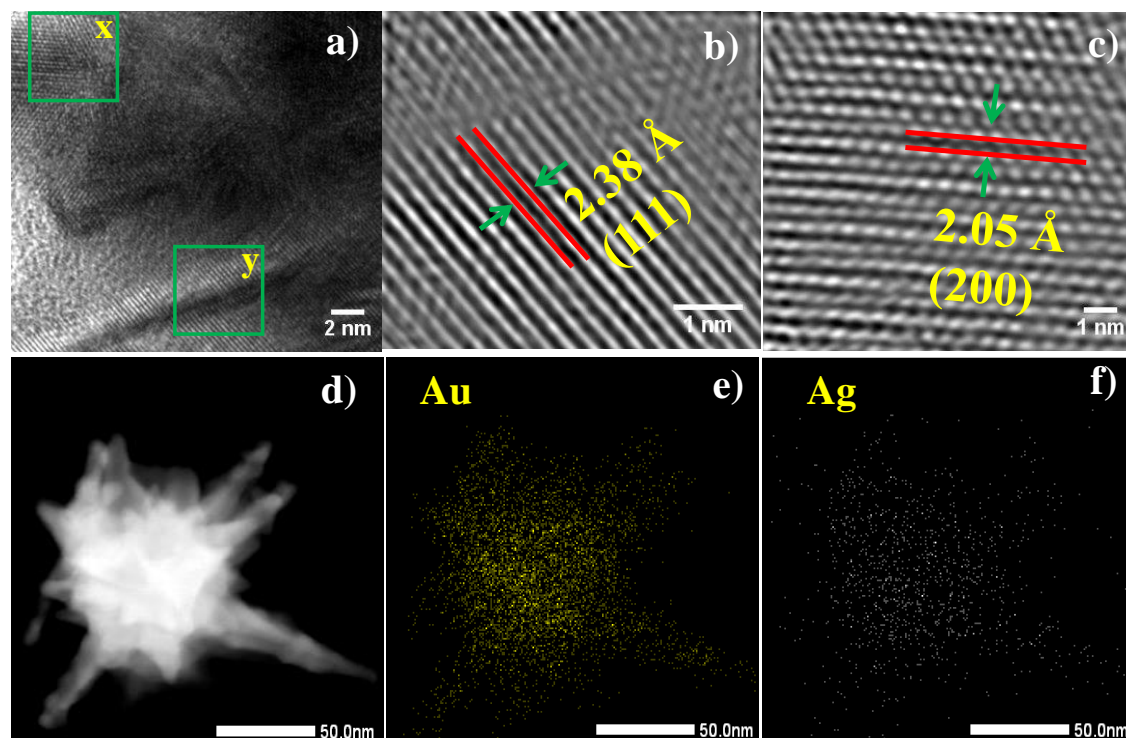


Figure. 3.5. HRTEM images of (a) single Au/Ag NSs, and (b) and (c) IFFT of marked area x and y of picture (a); (d) HAADF-STEM image, and (e, f) elemental mapping of Au/Ag nanostars.

However, it is believed that the d-value obtained here might correspond to the lattice planes of cubic Ag as Ag is coated over Au nanostar. These Au/Ag NSs bimetallic structures were additionally investigated to get more compositional information by HAADF-STEM (Figure 3.5d-f). The elemental mapping study unmistakably indicated that Au, and Ag are the essential components exist (Figure. 3.5e-f) in Au/Ag NSs bimetallic structures and it was additionally seen that Ag components are uniformly distributed all throughout Au nanostar structures. These observations successfully prove that Au/Ag NSs bimetallic structures are formed by the uniform coating of Ag onto Au

nanostar surface. The TEM- Energy dispersive X-ray (EDX) analysis also revealed the atomic percentages of Au and Ag in Au/Ag nanostars which are found to be 53.97% and 46.07%, respectively (Figure 3.6).

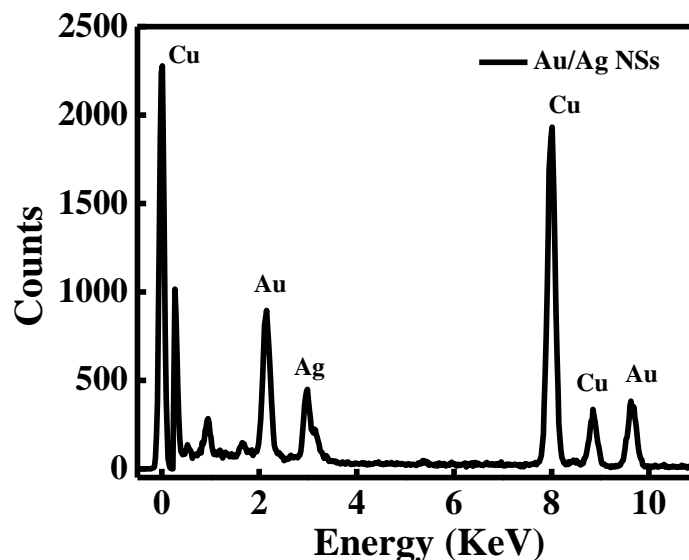


Figure 3.6. TEM-EDX (Energy dispersive X-ray) spectrum of Au/Ag NSs.

In addition, we have also taken UV-vis spectra (Figure 3.7a) and TEM images under basic (Figure 3.7b, at pH=10) and acidic (Figure 3.8c, at pH=4) conditions and the results demonstrated that bimetallic Au/Ag NSs are stable and there is no structural deformation of bimetallic nanostructures with tuning their pH.

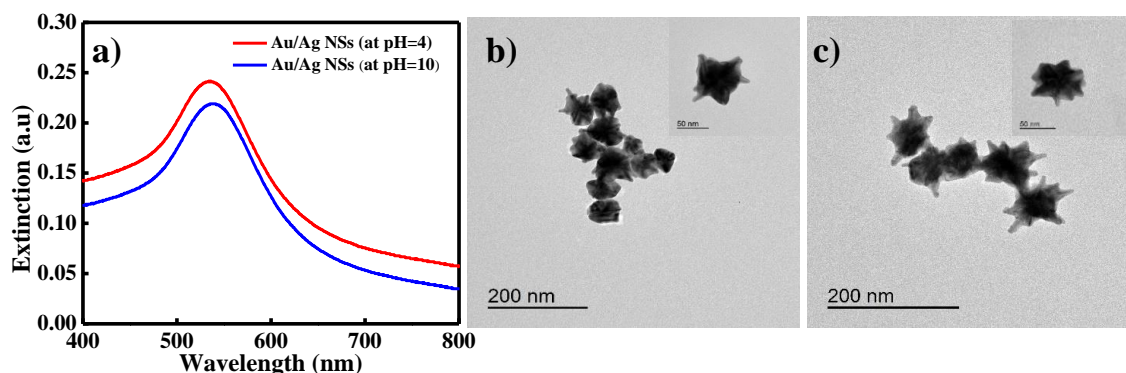


Figure 3.7. (a) UV-Vis extinction spectra of as synthesized Au/Ag nanostars under acidic and basic conditions. TEM images of Au/Ag nanostars under (b) basic, and (c) acidic pH. Insets: High resolution images of Au/Ag nanostars.

Further to know the chemical composition and valence states of the as synthesized Au/Ag NSs, we have examined the X-ray photoelectron spectroscopy (XPS) studies (Figure 3.8). Peaks centered at the binding energy of 368.14 eV and 374.05 eV (Figure 3.8a) are attributed to Ag 3d_{3/2} and Ag 3d_{5/2}, indicating the existence of metallic Ag i.e., Ag⁰ in the Au/Ag NSs.³³⁻³⁵ However, XPS spectrum of Au 4f area exhibits two peaks at binding energy values of 84.11 eV and 87.69 eV which are assigned to Au 4f_{5/2} and Au 4f_{7/2}, respectively (Figure 3.8b), and confirms the presence of Au at zero oxidation state i.e., Au⁰ in the as Au/Ag NSs.^{36, 37} No peak at the binding energy of 84.9 eV corresponding to Au⁺ were observed indicating that the Au atoms are in metallic form in this Au/Ag NSs core-shell type nanostructure.³⁸ Thus, from the XPS analysis it is believed that all of the gold and silver ions used for the fabrication of Au/Ag nanostars are fully reduced and are in the metallic state.

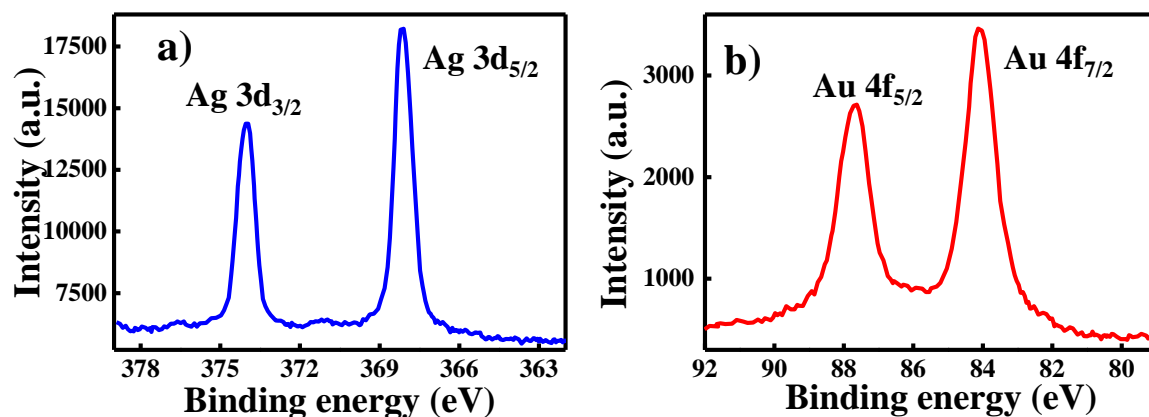


Figure 3.8. XPS spectra of Au/Ag NSs: (a) Ag 3d, and (b) Au 4f.

The Au and Ag content in Au/Ag nanostars is provided in Table 3.1, representing the core-shell Au/Ag nanostars in which atomic ratio of Au and Ag is 51.1% and 48.9%, respectively as quantified from inductive coupled plasma mass spectrometry (ICP-MS). Au and Ag concentrations are determined from ICP-MS and their atomic ratio is calculated by dividing the Au and Ag concentration with molar mass of Au (196.97 g mol⁻¹) and Ag (107.87g mol⁻¹)

Table 3.1. ICP-MS (Inductively coupled plasma mass spectrometry) of Au/Ag nanostars.

Nanoparticles	Au conc. (mg/l)	Ag conc. (mg/l)	Atomic percentage
Au/Ag NSs	0.42	0.22	Au: 51.1% and Ag: 48.9%

3.3.2. SERS measurements

3.3.2.1. Au/Ag NSs as SERS substrate and photocatalyst for conversion reaction

Our SERS-based DMAB formation from PATP investigations included the utilization of intentionally fabricated, bifunctional bimetallic Au/Ag NSs as the SERS active substrate as well as plasmonic photocatalyst. The Au/Ag NSs were then explored to investigate the dimerization reaction of PATP molecule into DMAB. First, in absence of Au/Ag NSs, normal Raman spectrum (NRS) of PATP was recorded by using excitation wavelength 532 nm (Figure 3.9), showing clearly a strong peak at 1095 cm^{-1} which corresponds to ν_{CS} and ν_{CC} vibrations. The Raman signal appear at 1290 cm^{-1} corresponds to vibrations of ν_{CN} . The signals arise at 1184 cm^{-1} and 1598 cm^{-1} are designated to Raman vibrations of ν_{CH} and ν_{CC} of benzene ring, respectively. Also, Raman signal at 1495 cm^{-1} is attributed to β_{CH} and ν_{CC} vibrations.³⁹ All these vibrational modes are considered as so-called “ a_1 ” symmetric vibrations of PATP.⁴⁰

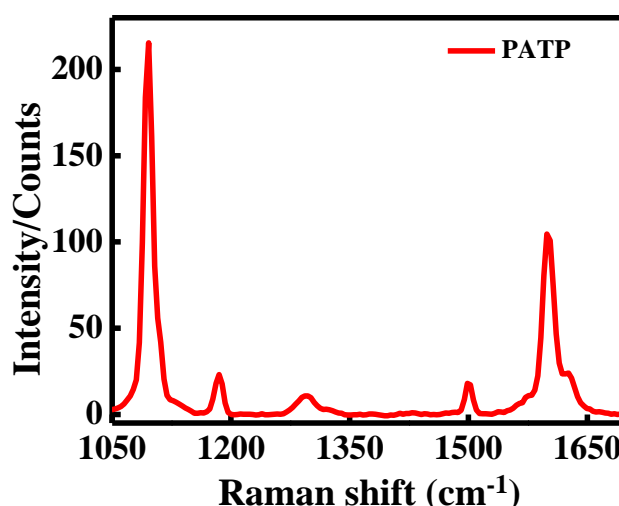


Figure 3.9. Normal Raman spectrum of solid PATP.

It is well known that the SERS of PATP adsorbed on metal surface emphatically rely upon the concentration PATP molecules as well as delay time and also metal nanoparticles present in reaction medium. Hence, for comparison reason, we have performed concentrations dependent SERS study of PATP with Au/Ag NSs under neutral pH (Figure 3.10). Along with all the characteristic peaks of PATP, the emergence of three new peaks at 1140, 1392 and 1440 cm^{-1} which are characteristic peaks of DMAB indicating the formation of dimerized product of PATP. This result also demonstrated that Raman signal of DMAB decreased with lowering the Au/Ag NSs concentration. This outcome additionally showed that minimum concentration of Au/Ag NSs which is required to trigger the chemical dimerization of PATP was found to be 36 pM.

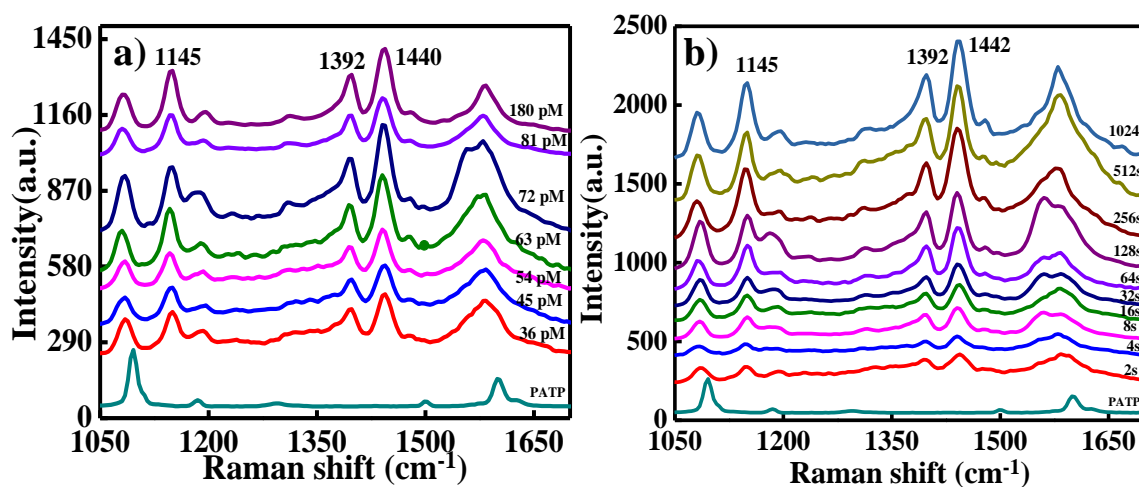


Figure. 3.10. (a) Concentration dependent SERS spectra of DMAB formed from PATP at different concentrations of Au/Ag NSs under neutral conditions and, (b) Time dependent SERS spectra of DMAB formed from PATP at 36 pM concentration of Au/Ag NSs.

Again, SERS spectra was recorded at different time intervals (Figure 3.10b) at constant concentration (36 pM) of Au/Ag NSs to know the acquisition time required the production of DMAB from PATP. Within 2 seconds of incubation time (at solution phase) of Au/Ag nanostars solution with PATP solution, the emergence of three new peaks at 1140, 1392 and 1440 cm^{-1} indicate that the reaction has been started

immediately. We have observed that the Raman signal became most intense at incubation time of about 256 seconds and intensity became constant afterwards. The intensity of characteristic peaks of DMAB became strongest at incubation time of about 256 seconds and got saturated afterwards, indicating the completion of reaction. Similarly, by adjusting the pH of reaction mixture to basic, concentration dependent and time dependent SERS spectra were recorded. It was found that under basic conditions minimum concentration of Au/Ag nanostars which is required to trigger the conversion of PATP into DMAB was 9 pM (Figure 3.11a) and the characteristic peaks corresponding to product DMAB were found to be emerging just after 2 seconds of incubation of Au/Ag nanostars solution with PATP solution and getting saturated after 128 seconds of incubation time indicating the completion of conversion reaction (Figure 3.11b).

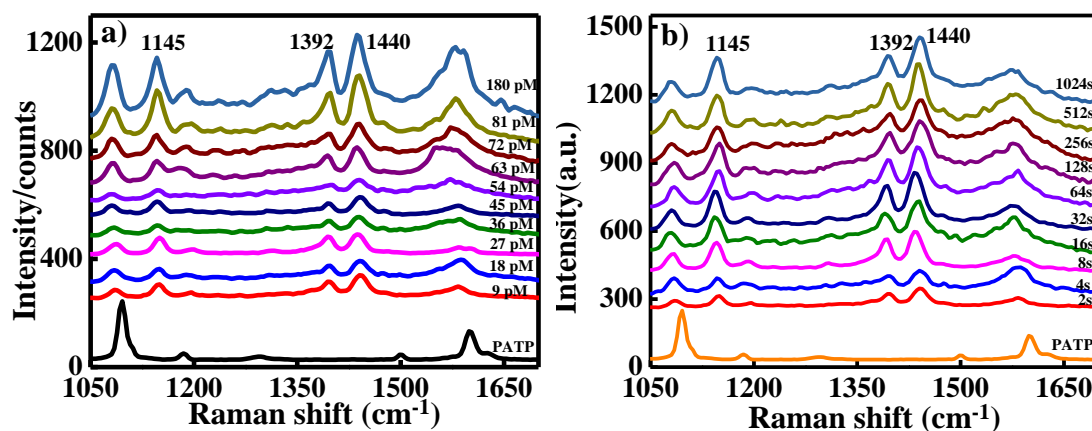


Figure 3.11. (a) Concentration dependent SERS spectra of DMAB formed from PATP at different concentrations of Au/Ag NSs under basic conditions and, (b) Time dependent SERS spectra of DMAB formed from PATP at 9 pM concentration of Au/Ag NSs.

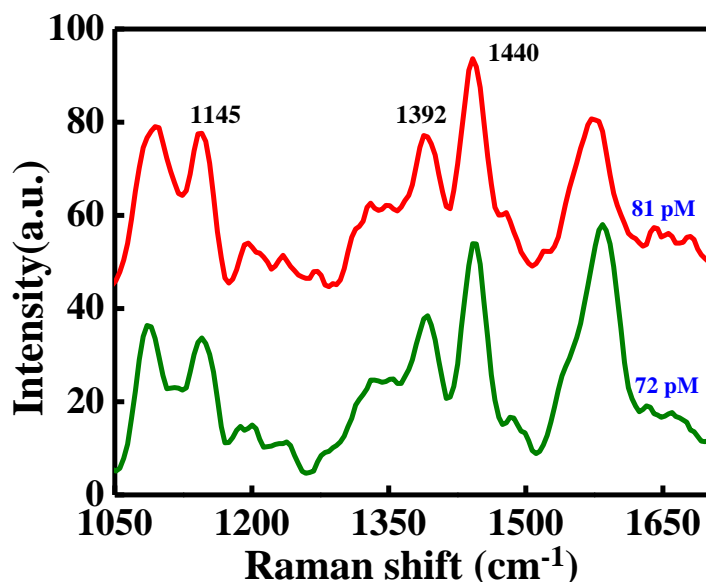


Figure 3.12. Concentration dependent SERS spectra of DMAB formed from PATP at different concentrations of Au/Ag nanostars under acidic conditions.

When the pH of reaction mixture was adjusted to acidic, then its concentration dependent SERS spectra were recorded. It was found that under such acidic conditions, the minimum concentration of Au/Ag NSs which is required to carry out the conversion reaction of PATP to DMAB was 72 pM (Figure 3.12). Below the concentration of 72 pM at acidic conditions, no peaks correspond to DMAB was observed. The concentration value at acidic condition is higher than the concentration values in case of neutral and basic conditions. This indicated that the conversion reaction is more efficient in basic conditions because -NH_2 group of PATP can be deprotonated easily and further oxidized to DMAB which is difficult under acidic conditions due to large abundance of H^+ ions.⁴¹ For neutral and basic conditions, new peaks are emerging within 2 seconds of incubation time indicating formation of DMAB which is much faster than previous reports.⁴²

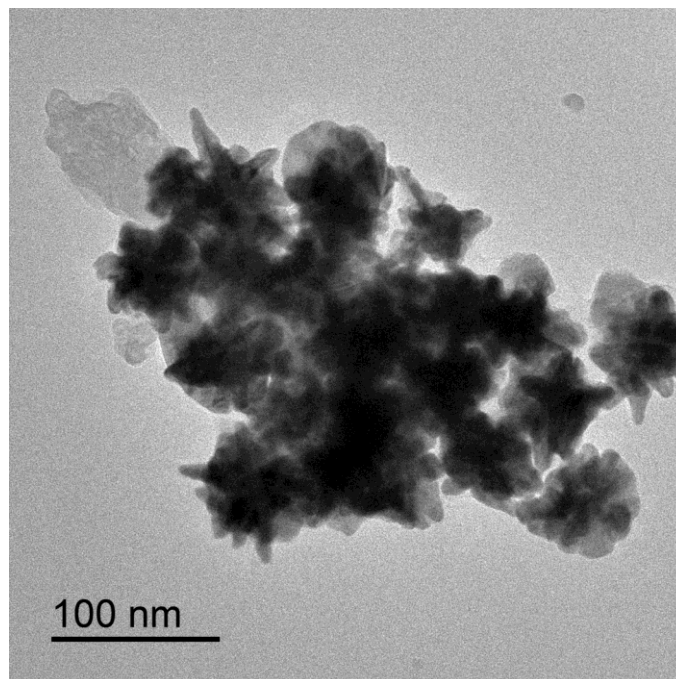


Figure 3.13. TEM images of Au/Ag NSs after catalytic reaction of PATP to DMAB.

TEM images (Figure 3.13) of Au/Ag NSs after SERS measurement indicate that no structural deformation occur due to catalytic conversion of PTAP to DMAB. It is believed that the chemical enhancement emerges from the static charge transfer at the ground state because of the interaction between PATP molecules and the Au/Ag NSs. This charge transfer creates an increase in the electronic static polarizability resulting enhancement of the SERS signal.²⁷ From the control Raman measurements, it is revealed that the oxidative dimerization of PATP into DMAB product can be carried out by surface photochemistry reactions using Au/Ag NSs. The high photocatalytic activity on the Au/Ag NSs interface is a result of the generation of hot electrons, which is enabled by the presence of significantly enhanced electric fields at the sharp tips of Au/Ag NSs.

3.3.2.2. Effect of thickness of Ag coating on SERS spectra of DMAB

To understand the effect of various thickness of Ag coating on photocatalytic conversion of PATP into DMAB, Au/Ag NSs with variation in Ag coating were

prepared. The UV-vis extinction spectra and TEM images of Au/Ag NSs with less and more Ag coating are included in Figure 3.14.

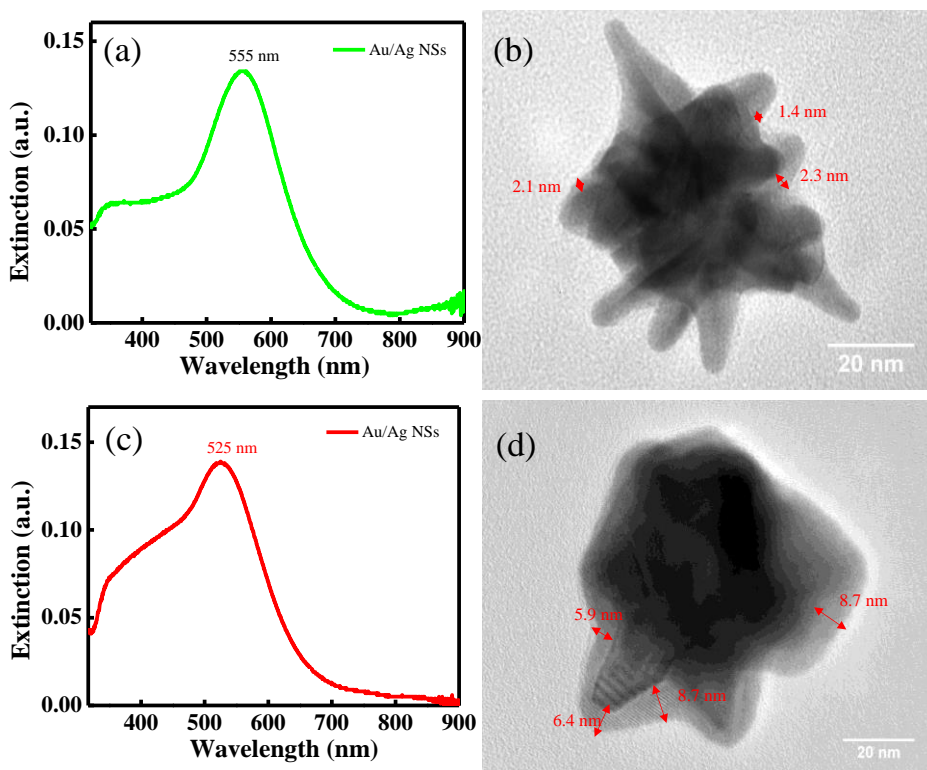


Figure 3.14. UV-Vis extinction spectra and TEM images of Au/Ag NSs with lower Ag coating (a, b) and with higher Ag coating (c, d).

For less Ag coating, the plasmon band was shifted to value 555 nm towards the plasmon band of Au NSs (Figure 3.14a). For less Ag coating, average thickness of Ag shell around the Au NSs core was found to be 1.9 ± 0.5 nm. It was found that for less Ag coating, the coating is not uniform around the Au NS core and tips as some tips were found to be not coated as depicted in TEM image (Figure 3.14b). This observation is in consistent with the previous report by Fales et al.³⁰ For more Ag coating around the Au NS core, the plasmon band got shifted to value 525 nm away from plasmon band of Au NSs (Figure 3.14c). For more Ag coating, uniform Ag layer was present on both core and tips of the Au nanostar with an average thickness of Ag shell around the Au core of $\sim 7 \pm 0.5$ nm (Figure 3.14d). Our observations on such Au/Ag NS systems with different Ag coating are in well agreement with the literature.^{30, 43} The TEM- Energy

dispersive X-ray (EDX) analysis also revealed the atomic percentages of Au and Ag in Au/Ag nanostars with less and more Ag coating (Table 3.2). The atomic percentages of Au and Ag in Au/Ag NSs with less Ag coating are found to be 70.48% and 29.14%, respectively. Also, the atomic percentages of Au and Ag in Au/Ag NSs with more Ag coating are found to be 41.15% and 58.85%, respectively.

Table 3.2. The atomic percentage of Au and Ag in Au/Ag NSs from TEM- Energy dispersive X-ray (EDX) analysis is shown below.

Nanoparticles	Atomic percentage (%) of Au and Ag	
Au/Ag NSs (lower coating)	Au: 70.84%	Ag: 29.14%
Au/Ag NSs (higher coating)	Au: 41.15%	Ag: 58.85%

Afterwards to understand the effect of thickness of Ag coating on photocatalytic reaction, time dependent SERS based photocatalytic dimerization of PATP into DMAB was investigated by varying the thickness of Ag coating over Au NSs. In all cases, the particle concentration (Au/Ag NSs) was kept fixed i.e. 36 pM (Figure 3.15).

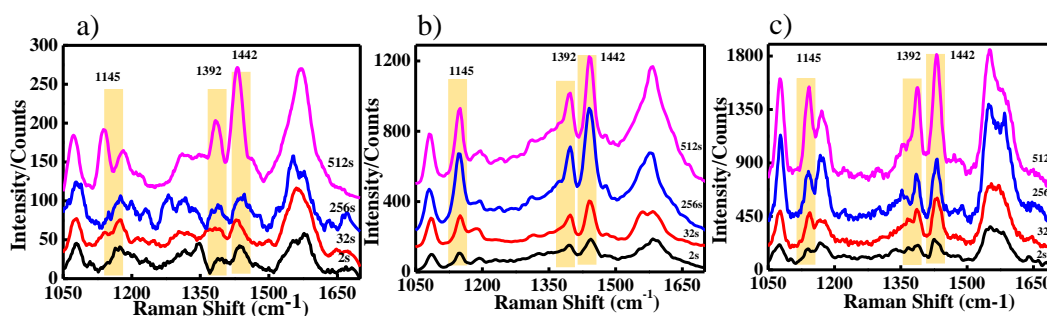


Figure 3.15. Time dependent SERS spectra of DMAB formed from PATP at 36 pM concentration of Au/Ag NSs with a) lower Ag coating (1.9 ± 0.5 nm), b) moderate Ag coating (3.5 ± 0.5 nm), and c) higher Ag coating (7 ± 0.5 nm).

It was found that for less Ag coating, intensity of characteristic peaks of DMAB is much less as compared to the moderate and more Ag coating (Figure 3.15a). This indicates that less Ag coating is not much effective for the photocatalytic conversion of PATP into DMAB as the tips are not coated with Ag layer. In case of moderate and

more Ag coating, intensity of characteristic peaks of DMAB are maximum at incubation time of 246 seconds and got saturated afterwards (Figure 3.15b, 3.15c). Further to compare the SERS intensities at different Ag coatings, the intensity at peak 1440 cm^{-1} was investigated for incubation time of 512 seconds. The ratio of intensities at 1440 cm^{-1} for moderate and less Ag coating $I_{(\text{moderate Ag coating})} / I_{(\text{less Ag coating})}$ was found to be 3.6. The ratio of intensities at 1440 cm^{-1} for more and moderate Ag coating $I_{(\text{more Ag coating})} / I_{(\text{moderate Ag coating})}$ was found to be 1.8. Hence it can be seen that in case of more Ag coating, intensity of characteristic peaks of DMAB are higher. However, the enhancement factor in peak intensity in case of moderate to higher Ag coating (1.8 fold) is less than that of lower to moderate Ag coating (3.6 fold). It was also found that the intensity of required peaks is getting saturated at the incubation time of 256 seconds indicating the completion of reaction at same time in the case of both moderate and more Ag coating. The higher intensity of characteristic peaks of DMAB is in case of more Ag coating which may be due to better electromagnetic enhancement SERS activity of Ag. This indicates that optimum thickness of Ag shell was found to be $\sim 7 \pm 0.5\text{ nm}$ for this photocatalytic reaction. On further increasing the thickness of Ag coating can lead to complete coverage of Au NS tips which results in the loss of the sharp tips (behaving like spherical Au/Ag nanostructures) and can diminish the SERS activity of such structures as mentioned by Fales group.³⁶ Therefore, our experimental findings suggest that the Ag coating of $\sim 7 \pm 0.5\text{ nm}$ thickness is the optimum coating for the SERS based photocatalytic conversion of PATP into DMAB.

3.3.2.3. Effect of pure metal counter parts on SERS spectra of DMAB

Also, we have performed SERS measurements in which only Au NSs were used to carry out the catalytic conversion of PATP to DMAB at concentrations 180 pM, 81 pM, 63 pM and 45 pM of Au NSs. The recorded SERS spectra (Figure 3.16) demonstrated that only the higher concentrations of 180 pM and 81 pM were able to convert PATP into DMAB and with lower concentrations of 63 pM and 45 pM, the characteristic peaks of DMAB which are positioned at 1140, 1392 and 1440 cm^{-1} are missing. These results indicate that lower concentrations of Au NSs are unable to catalyze the dimerization reaction of PATP into DMAB showing that Au/Ag NSs are much more

efficient than only Au NSs. It has been also observed from the SERS spectra (Figure 3.16) that, for the same laser power and same concentration of Au/Ag NSs and Au NSs i.e., 180 pM and 81 pM, intensity of characteristic peaks of DMAB is much more in case of Au/Ag NSs indicating higher efficiency of Au/Ag NSs for the photocatalytic conversion of PATP into DMAB.

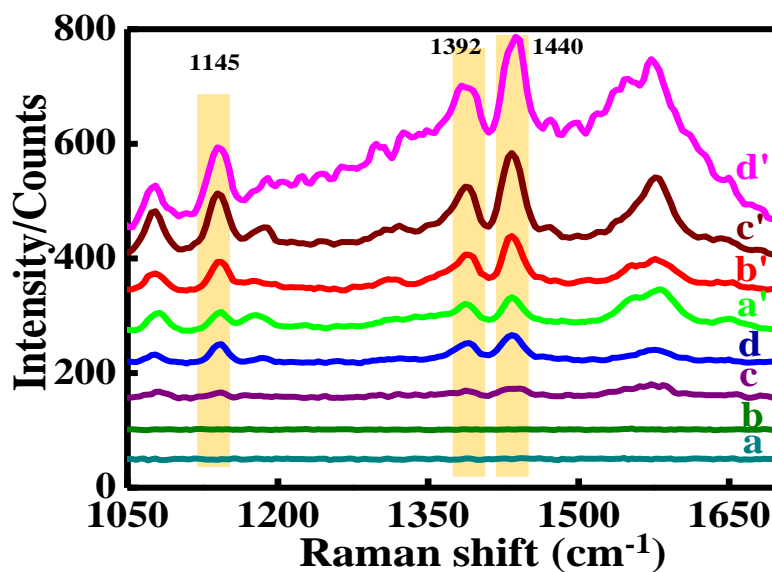


Figure 3.16. SERS spectra of DMAB formed from PATP at incubation time of 512 seconds using 45 pM concentration of Au NS (a), and Au/Ag NSs (a'); 63 pM concentration of Au NS (b), and Au/Ag NSs (b'); 81 pM concentration of Au NS (c), and Au/Ag NSs (c'); and 180 pM concentration of Au NS (d), and Au/Ag NSs (d').

Ag NSs were synthesized according to protocol reported by Garcia-Leis *et al.*⁴⁴ UV-Vis spectrum and TEM image are shown in Figure 3.17 indicates the successful synthesis of Ag NSs.

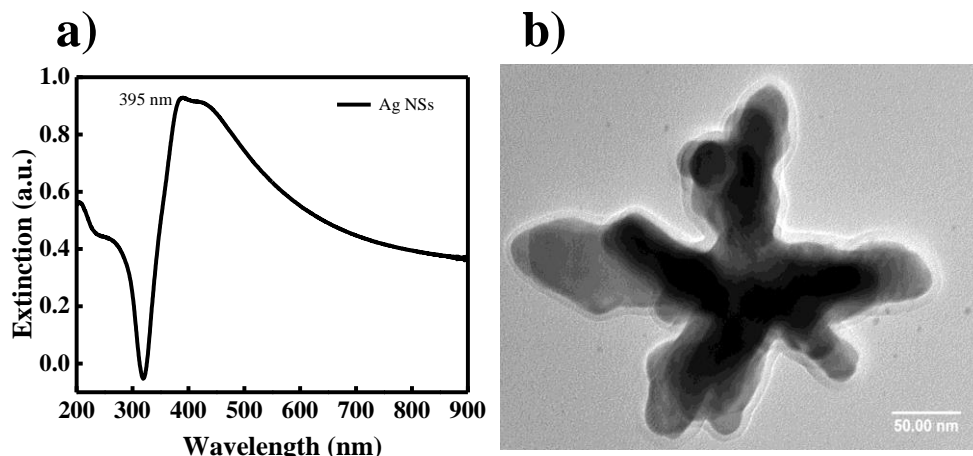


Figure 3.17. a) Normalized UV-Vis extinction spectrum, and b) TEM image of as prepared Ag NSs.

SERS spectra of DMAB formed from PATP were recorded using Ag NSs at different concentrations of 180, 81, 63, 45 pM (Figure 3.18). With comparison to Au/Ag NSs, the intensity of characteristic peaks of DMAB is much less for Ag NSs. For lower concentration (45 pM), the required peaks of DMAB were missing in case of Ag NSs. In case of Ag NSs, the intensity of characteristic peaks of DMAB is more indicating better SERS activity of Ag NSs as compared to pure Au NSs.

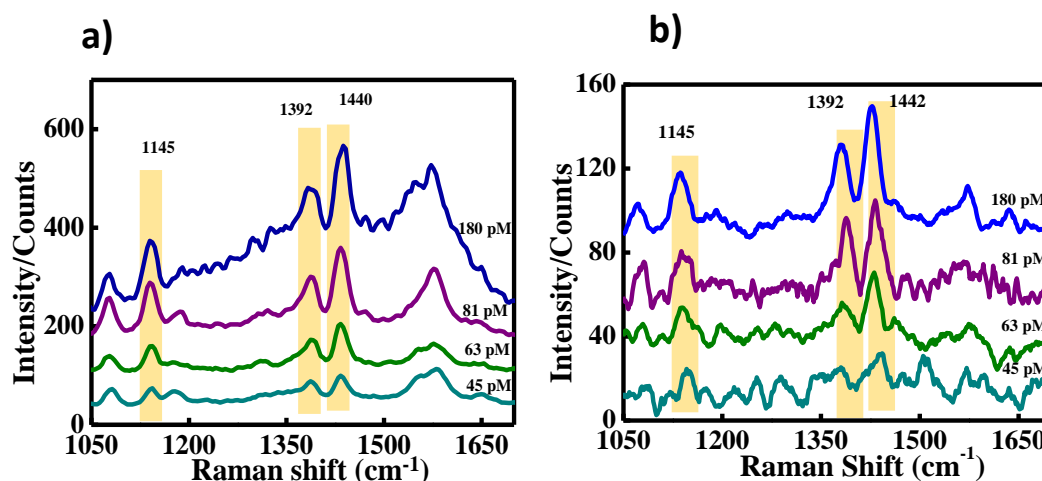


Figure 3.18. SERS spectra of DMAB formed from PATP at incubation time of 512 seconds using different concentrations of a) Au/Ag NSs, and b) Ag NSs.

These results indicate that the prepared Au/Ag NSs are demonstrating better photocatalytic activity as compared to their pure metal counter parts i.e., only Au NSs and Ag NSs.

3.3.2.4. Effect of nanostructure morphology on SERS spectra of DMAB

We also have carried out the similar reactions using spherical Au nanoparticles with similar size of nanostar to unveil the effect of nanostructure morphology on photocatalytic activity. For the morphological comparison, we have prepared spherical Au nanoparticles of similar size of Au nanostars i.e., 75 ± 5 nm. We have given the UV-Vis extinction spectrum and TEM image of as prepared spherical Au nanoparticles (Figure 3.19).

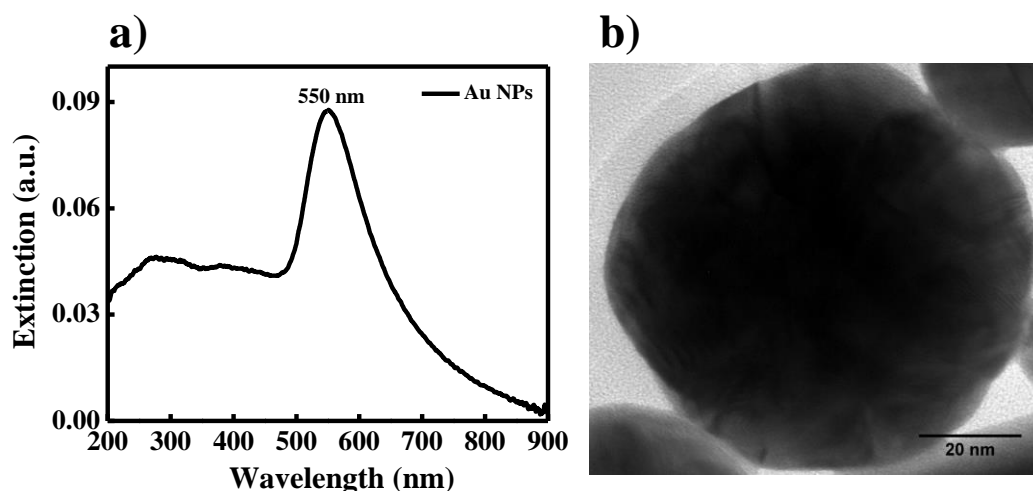


Figure 3.19. a) UV-Vis extinction spectrum b) TEM image of as prepared spherical Au nanoparticles.

The prepared spherical Au NPs were used to carry out the conversion reaction of PATP into DMAB at different concentration 180, 81, 63, 45 pM at 512 seconds incubation time of Au NPs solution with ethanolic PATP solution. It was observed from the SERS spectra that the characteristic peaks of DMAB $1142, 1382, 1442 \text{ cm}^{-1}$ were visible in the SERS spectra for 180 pM concentration of Au NPs in total reaction mixture (Figure 3.20). For the lower concentration of Au NPs, these peaks were missing indicating that the conversion reaction is not occurring at these lower concentrations. Here, we have

provided SERS spectra of DMAB formed from PATP at different concentrations of Au NPs at same incubation time of 512 seconds. The higher catalytic activity and higher Raman signal enhancement obtained in case of nanostar compared to spherical nanoparticles may be due to presence of sharp tips surrounding the Au core. The strong plasmon coupling between tips and cores of nanostar,³² further results in creation of lots of “hotspots” required for highly significant SERS enhancement.

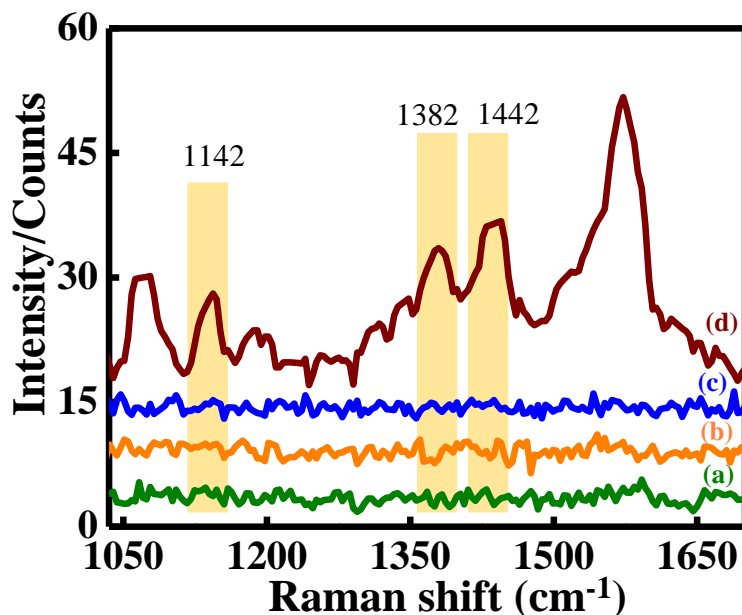


Figure 3.20. SERS spectra of DMAB formed from PATP using spherical Au NPs at 45 pM (a), 63 pM (b), 81 pM (c), 180 pM (d) concentration at incubation time 512 seconds.

3.3.2.5. Effect of incubation time on SERS spectra of DMAB

SERS spectrum of Au/Ag NSs at zero incubation time (0 second incubation at solution phase) with PATP solution compared to SERS spectrum of Au/Ag NSs at 512 seconds incubation time with PATP (Figure 3.21). It is clear that from the comparison spectra that with higher incubation time the characteristic peaks of DMAB are more intense as compared to zero incubation. With Au NSs also (Figure 3.22), similar observation was made. With zero incubation time, the characteristic peaks of DMAB are missing but with higher time of 512 seconds, peaks of dimerized product of PATP are present. It

reveals that solution phase incubation of both nanostar solution and PATP solution before addition of NaCl is playing a crucial role for triggering the dimerization reaction efficiently.

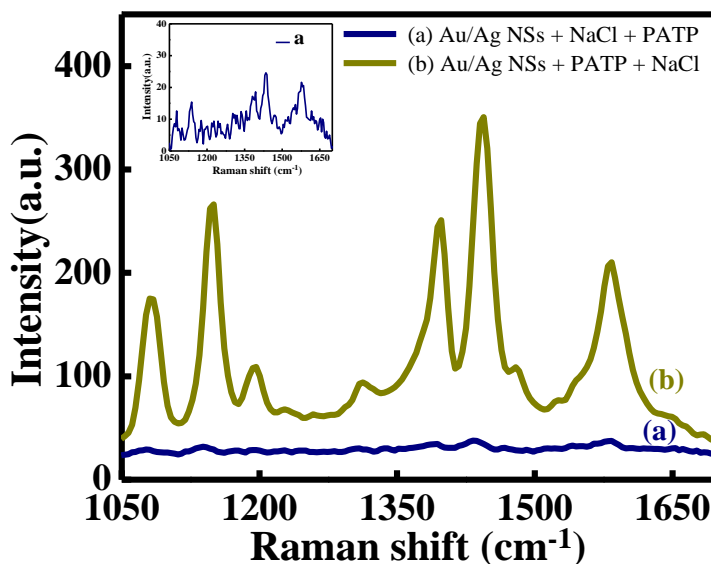


Figure 3.21. SERS spectra of DMAB formed from PATP at 180pM concentration of Au/Ag NSs at a) zero second incubation time and b) 512 seconds incubation time.

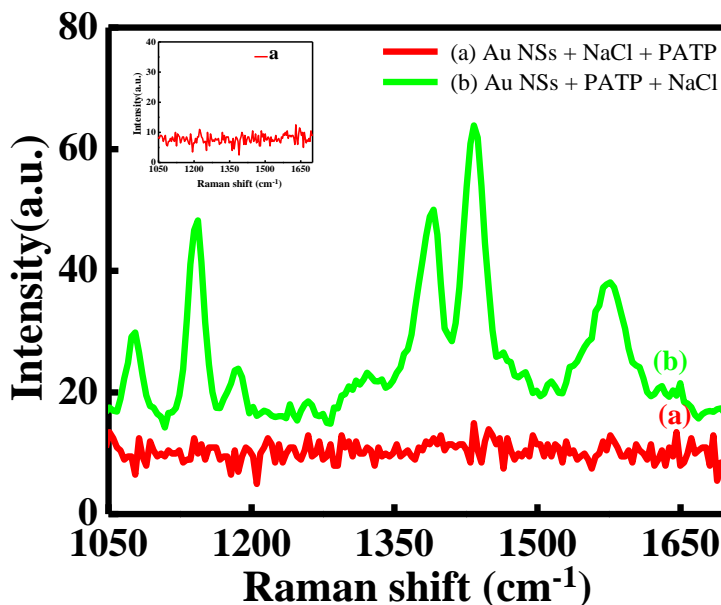


Figure 3.22. SERS spectra of DMAB formed from PATP at 180pM concentration of Au NSs at a) zero second incubation time and b) 512 seconds incubation time.

3.3.2.6. Effect of excitation laser wavelength on SERS spectra of DMAB

To see whether the better performance of Au/Ag NSs was originated from the resonant laser excitation or not, SERS measurements were carried out for DMAB formed from PATP at different concentrations of Au NSs with 633 nm laser excitation source (Figure 3.23).

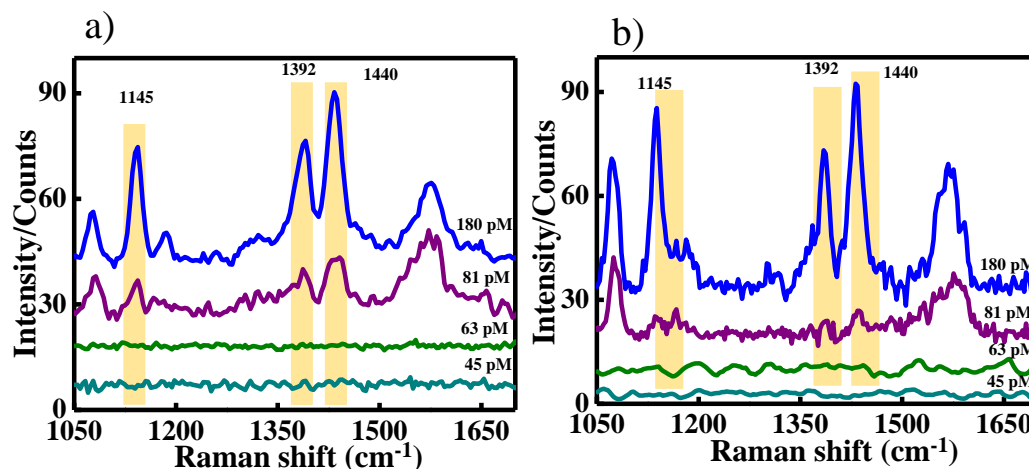


Figure 3.23. SERS spectra of DMAB formed from PATP at incubation time of 512 seconds using different concentrations of Au NSs at a) 532 nm laser, and b) 633 nm laser.

It was found that the intensity of characteristic peaks of DMAB using Au NSs are almost comparable to the intensity obtained using 532 nm laser excitation. But lower concentrations of Au NSs are unable to produce the characteristic signals of DMAB even at the resonant laser excitation (633 nm). This implies that lower concentrations of Au NSs are still unable to catalyze the conversion reaction of PATP into DMAB.

3.3.3. FDTD simulation study

We have performed the finite difference time domain (FDTD) simulations for Au NSs and Au/Ag NSs to provide the electric field distribution of nanostars near the sharp tips (Figure 3.24). The electric field magnitude, $|E|$ is computed through three-dimensional finite-difference time-domain (FDTD) modelling for Au nanostar as well as for Ag coated Au nanostar. The plots indicate increase in $|E|$ at tips for Ag coated Au nanostar

as compared to uncoated pure Au nanostar. The enhancement in electric field as obtained from Au core/Ag shell NS compared to pure Au NS will result in higher SERS enhancement of DMAB formed from PATP for Au core/Ag shell nanostar than that of Au nanostar which are in good agreement with experimental findings.

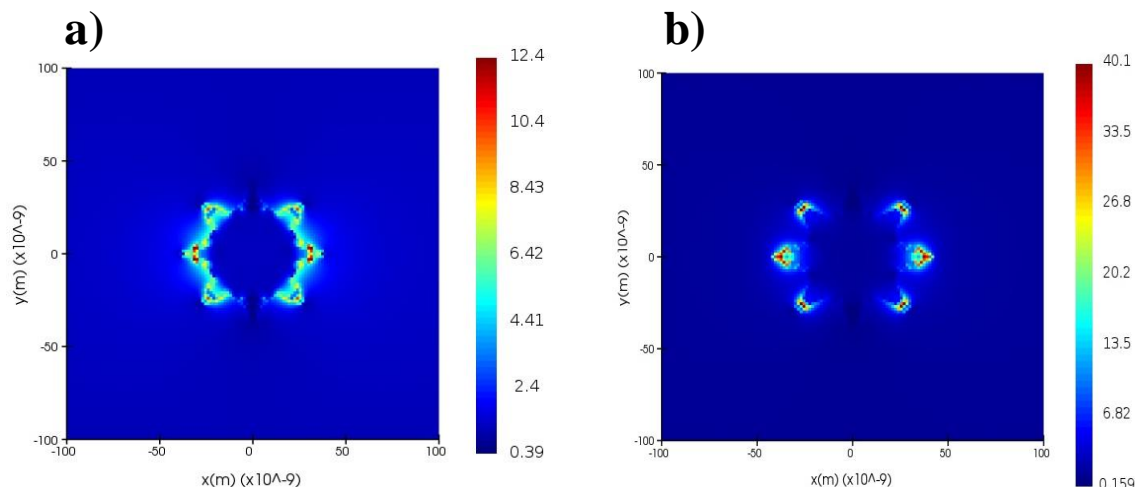


Figure 3.24. The magnitude of electric field $|E|$ in xy plane passing through the centre of nanostar at $\lambda=540$ nm for (a) Au-nanostar (b) silver coated Au-nanostar. A plane wave source has been used for FDTD calculations. The incident wave-vector is perpendicular to plotted xy cross-section. Note the difference in color-coding scale for both plots.

3.3.4. Insight into the catalytic conversion of PATP to DMAB using Au/Ag NSs

In order to gain a better understanding of the potential mechanism of plasmon-driven catalytic dimerization of PATP into DMAB in the presence of Au/Ag NSs, several control experiments were carried out by recording the SERS spectra of PATP. It is established that PATP is converted into DMAB by its oxidation and the oxidation process that can take place either with the help of holes or hot electrons generated in plasmonic metal nanoparticles.^{21, 39} It is also reported that hot holes can directly oxidize or hot electrons first activate the atmospheric oxygen and later the activated oxygen can oxidize the PATP into its dimerized product DMAB. Hence, in order to observe the role of O_2 in this photocatalytic reaction, the reaction was carried out under inert atmosphere. The recorded SERS spectrum showing no peaks indicates that the

conversion reaction is not taking place in absence of O_2 (Figure 3.25a). Thus, it confirms that O_2 is involved in the oxidation process of PATP which means that hot electrons are participating in conversion process. To understand the potentiality of Au/Ag NSs as SERS substrate we found that no peaks was observed in Raman spectrum of Au/Ag NSs only (Figure 3.25b) under illumination of same 532 nm laser which reveals that there is no resonance effect. Control Raman experiments were also carried out to confirm the formation of DMAB from PATP in presence of metal nanostructures only. Raman spectrum of mixture of PATP and NaCl (Figure 3.25c) shows PATP peaks only. Raman spectrum of mixture of Au/Ag NSs and NaCl was also recorded and there were also no peaks of DMAB product (Figure 3.25d).

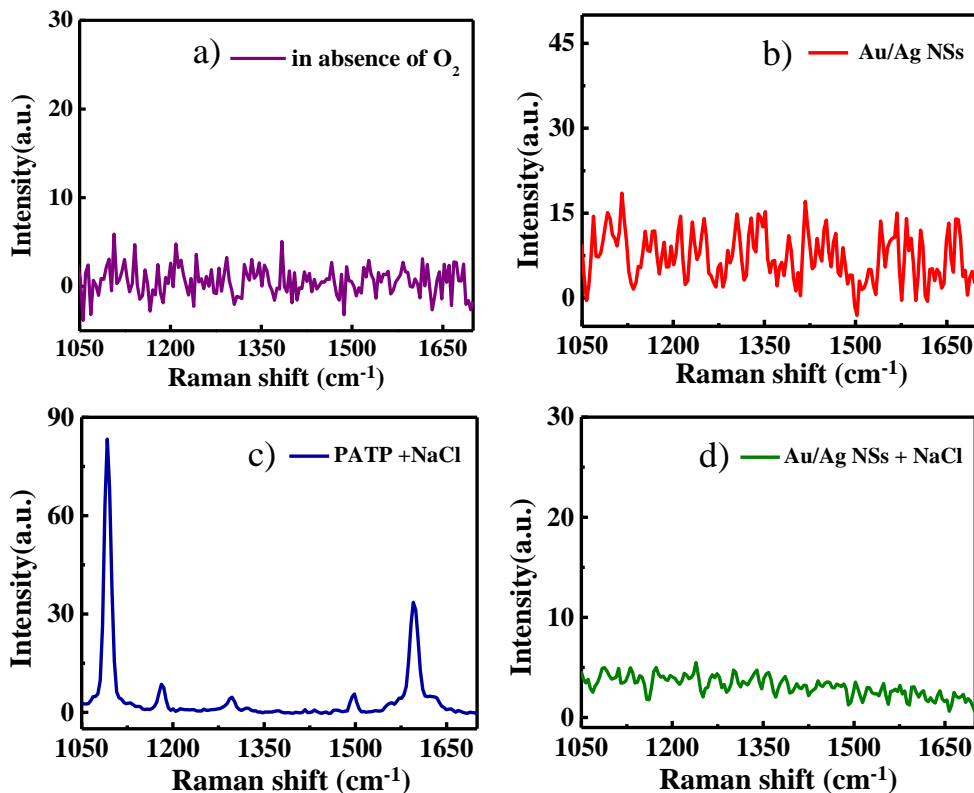
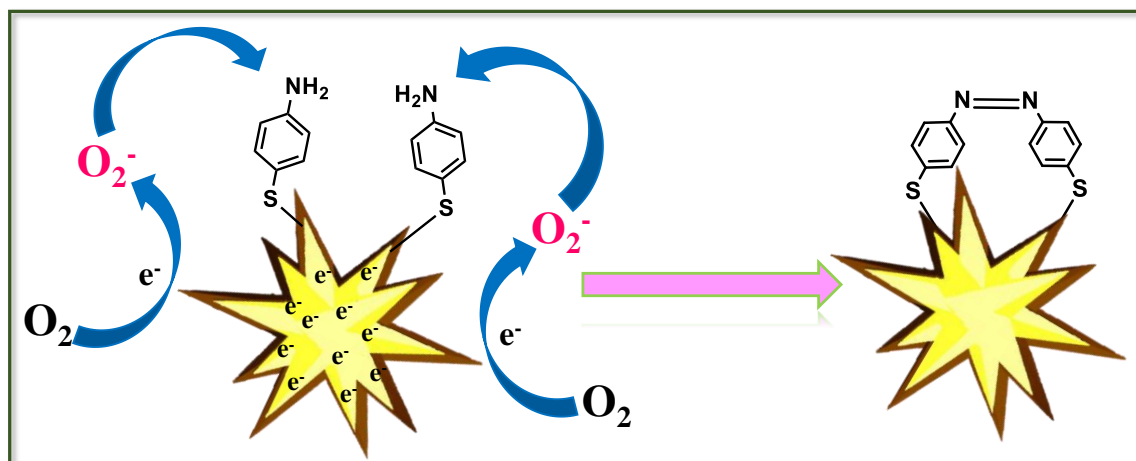


Figure 3.25. (a) SERS spectra measured under neutral conditions at concentration 6 pM in inert atmosphere. Raman spectrum of (b) Au/Ag NSs, (c) mixture of PATP and NaCl, and, (d) mixture of Au/Ag NSs and NaCl.



Scheme 3.3. Schematic illustration for the reaction mechanism depicting the oxidation of PATP into DMAB.

Schematic representation of the process by which PATP is transformed into DMAB by means of Au/Ag NSs is depicted in Scheme 3.3.

Finally, to further confirm the formation of DMAB by oxidation of PATP in presence of Au/Ag nanostars, we have conducted the attenuated total reflectance-fourier-transform infrared (ATR-FTIR) spectroscopic study of pure PATP and DMAB (Figure 3.26). Figure 3.26a represents the ATR-FTIR spectra of PATP, where the peaks at 3418 and 3206 cm^{-1} are assigned to N-H stretching vibration.^{45, 46} The peaks appeared at 3021 and 2982 cm^{-1} due to the asymmetric and symmetric stretching vibration of aromatic C-H bond,⁴⁷ respectively, while the peaks corresponding to S-H stretching vibration were observed at 2597 and 2560 cm^{-1} .^{45, 48} Peaks centered at 1587 and 1488 cm^{-1} were attributed to the stretching vibration of C=C bonds of the aromatic ring.⁴⁹ Bands at 1278, 1174 and 1123 cm^{-1} could be allotted to C-N stretching vibration.^{50, 51} Peaks located at 1006 and 952 cm^{-1} is credited to the C-S stretching vibration.^{50, 52}

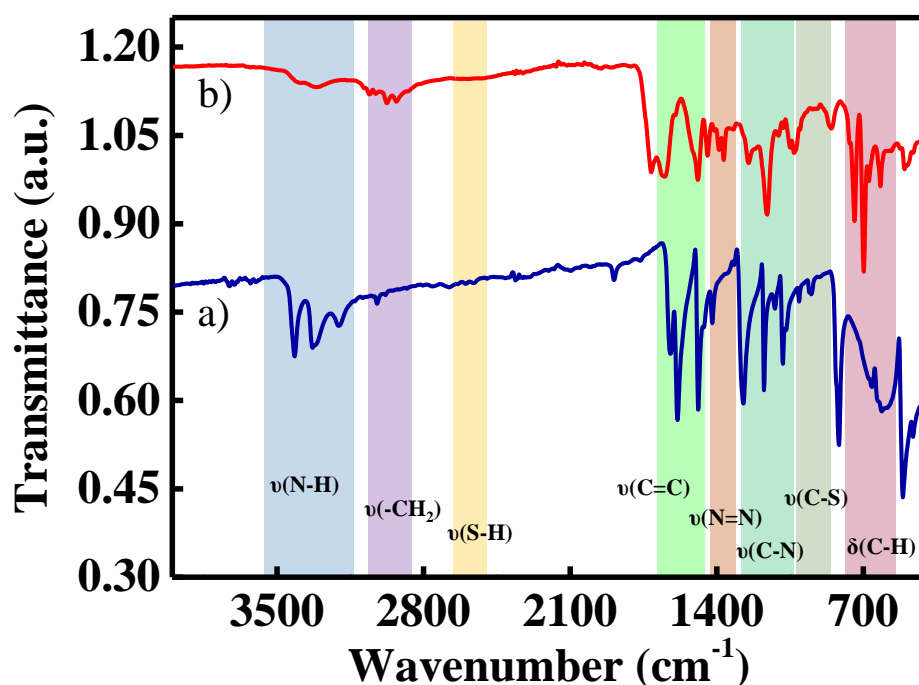


Figure 3.26. ATR-FTIR spectra of (a) PATP and (b) DMAB formed from PATP in presence of Au/Ag NSs.

The ATR-FTIR spectra of DMAB also indicates that all the peaks corresponding to stretching vibration of N-H, C-H, S-H, C=C, C-N and C-S bonds (details are in Table 3.3) (Figure 3.26b). Notably, the additional peaks at 1444 and 1389 cm^{-1} are attributed to the stretching vibration of N=N bond⁴⁵ (Figure 3.26b) which proves the formation of DMAB from PATP via N-N coupling mechanism in presence of Au/Ag nanostars.

Table 3.3. ATR-FTIR frequency data (cm^{-1}) of PATP and DMAB.

Assignments	PATP ATR-FTIR frequency (cm^{-1})	DMAB ATR-FTIR frequency (cm^{-1})	References
$\nu\text{N-H}$	3418, 3320, 3206	3404, 3318	45, 46
$\nu\text{C-H}$	3021 2982	2976 2828	47
$\nu\text{S-H}$	2597 2560	Not detected	45, 48

$\nu\text{C}=\text{C}$	1587 1488	1653 1491	49
$\nu\text{N}=\text{N}$	-	1444 1389	45
$\nu\text{C}-\text{N}$	1273 1174 1123 1084	1367 1248 1160	50, 51
$\nu\text{C}-\text{S}$	1006 952	1050 1031	53
$\nu\text{C}-\text{H}$ rocking and out-of- plane bending	816 614	742 698 618	54

3.4. Conclusion

In conclusion, we have shown that Au/Ag core-shell nanostars serve as an extremely effective SERS substrate and plasmon driven catalyst for the plasmon mediated dimerization reaction of PATP. Bimetallic nanostars are more effective than their single-metal counterparts i.e., pure Au and Ag nanostars. the anisotropic star morphology is superior to the spherical shape. The surface photocatalytic coupling reaction of PATP conversion to DMAB occurs more efficiently on Au/Ag nanostars because they generate a significantly strong electric field surrounding their sharp tips. Potential applications for these Au/Ag NSs-based LSPRs include the development of new plasmon-driven photocatalytic frameworks for the synthesis of other organic molecules.

Note:

- ✓ Authors and the paper's corresponding author gave their approval for inclusion of this work in present thesis. The corresponding publication is:

Gagandeep Kaur, Swati Tanwar, Vishaldeep Kaur, Rathindranath Biswas, Sangeeta Saini, Krishna Kanta Halder, and Tapasi Sen “Interfacial design of gold/silver core–shell nanostars for plasmon-enhanced photocatalytic coupling of 4-aminothiophenol” *Journal of Materials Chemistry C* 2021, 9 (42), 15284-15294.

References

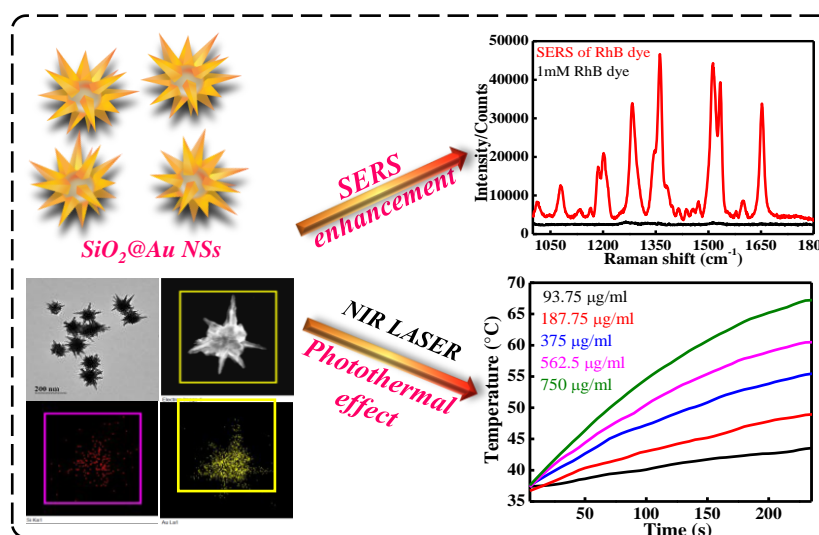
1. J. M. Brockman, B. P. Nelson and R. M. Corn, *Annual Review of Physical Chemistry*, 2000, **51**, 41-63.
2. S. Lal, S. E. Clare and N. J. Halas, *Accounts of Chemical Research*, 2008, **41**, 1842-1851.
3. C. Kuttner, R. P. Höller, M. Quintanilla, M. J. Schnepf, M. Dulle, A. Fery and L. M. Liz-Marzán, *Nanoscale*, 2019, **11**, 17655-17663.
4. C. Hubert, A. Rumyantseva, G. Lerondel, J. Grand, S. Kostcheev, L. Billot, A. Vial, R. Bachelot, P. Royer, S.-H. Chang, S. K. Gray, G. P. Wiederrecht and G. C. Schatz, *Nano Letters*, 2005, **5**, 615-619.
5. K. Ueno, S. Juodkazis, T. Shibuya, Y. Yokota, V. Mizeikis, K. Sasaki and H. Misawa, *Journal of the American Chemical Society*, 2008, **130**, 6928-6929.
6. D.-Y. Wu, L.-B. Zhao, X.-M. Liu, R. Huang, Y.-F. Huang, B. Ren and Z.-Q. Tian, *Chemical Communications*, 2011, **47**, 2520-2522.
7. M. Sun, Y. Hou and H. Xu, *Nanoscale*, 2011, **3**, 4114-4116.
8. C. J. Chen and R. M. Osgood, *Physical Review Letters*, 1983, **50**, 1705-1708.
9. K. Kneipp, Y. Wang, H. Kneipp, L. T. Perelman, I. Itzkan, R. R. Dasari and M. S. Feld, *Physical Review Letters*, 1997, **78**, 1667-1670.
10. S. Li, P. Miao, Y. Zhang, J. Wu, B. Zhang, Y. Du, X. Han, J. Sun and P. Xu, *Advanced Materials*, 2021, **33**, 2000086.
11. T. Balcha, J. R. Strobl, C. Fowler, P. Dash and R. W. J. Scott, *ACS Catalysis*, 2011, **1**, 425-436.
12. S. Sarina, H. Zhu, E. Jaatinen, Q. Xiao, H. Liu, J. Jia, C. Chen and J. Zhao, *Journal of the American Chemical Society*, 2013, **135**, 5793-5801.
13. K. Sytwu, M. Vadai and J. A. Dionne, *Advances in Physics: X*, 2019, **4**, 1619480.
14. X. Ren, E. Cao, W. Lin, Y. Song, W. Liang and J. Wang, *RSC Advances*, 2017, **7**, 31189-31203.
15. E. M. van Schrojenstein Lantman, T. Deckert-Gaudig, A. J. G. Mank, V. Deckert and B. M. Weckhuysen, *Nature Nanotechnology*, 2012, **7**, 583-586.
16. C. Zhan, X.-J. Chen, Y.-F. Huang, D.-Y. Wu and Z.-Q. Tian, *Accounts of Chemical Research*, 2019, **52**, 2784-2792.
17. M. He, B. Cao, X. Gao, B. Liu and J. Yang, *Journal of Materials Research*, 2019, **34**, 2928-2934.
18. A. G. M. da Silva, T. S. Rodrigues, V. G. Correia, T. V. Alves, R. S. Alves, R. A. Ando, F. R. Ornellas, J. Wang, L. H. Andrade and P. H. C. Camargo, *Angewandte Chemie International Edition*, 2016, **55**, 7111-7115.
19. M. Osawa, N. Matsuda, K. Yoshii and I. Uchida, *The Journal of Physical Chemistry*, 1994, **98**, 12702-12707.
20. Y.-F. Huang, H.-P. Zhu, G.-K. Liu, D.-Y. Wu, B. Ren and Z.-Q. Tian, *Journal of the American Chemical Society*, 2010, **132**, 9244-9246.
21. Y.-F. Huang, M. Zhang, L.-B. Zhao, J.-M. Feng, D.-Y. Wu, B. Ren and Z.-Q. Tian, *Angewandte Chemie International Edition*, 2014, **53**, 2353-2357.
22. P. Christopher, H. Xin and S. Linic, *Nature Chemistry*, 2011, **3**, 467.
23. J. Wang, R. A. Ando and P. H. Camargo, *Angewandte Chemie International Edition*, 2015, **54**, 6909-6912.
24. J. Wang, R. A. Ando and P. H. Camargo, *ACS Catalysis*, 2014, **4**, 3815-3819.
25. L.-B. Zhao, M. Zhang, Y.-F. Huang, C. T. Williams, D.-Y. Wu, B. Ren and Z.-Q. Tian, *The Journal of Physical Chemistry Letters*, 2014, **5**, 1259-1266.

26. A. G. da Silva, T. S. Rodrigues, J. Wang, L. K. Yamada, T. V. Alves, F. R. Ornellas, R. M. A. Ando and P. H. Camargo, *Langmuir*, 2015, **31**, 10272-10278.
27. Y. Huang, Y. Fang, Z. Yang and M. Sun, *The Journal of Physical Chemistry C*, 2010, **114**, 18263-18269.
28. A. Sousa-Castillo, M. Comesaña-Hermo, B. Rodríguez-González, M. Pérez-Lorenzo, Z. Wang, X.-T. Kong, A. O. Govorov and M. A. Correa-Duarte, *The Journal of Physical Chemistry C*, 2016, **120**, 11690-11699.
29. E. Nalbant Esenturk and A. Hight Walker, *Journal of Raman Spectroscopy: An International Journal for Original Work in all Aspects of Raman Spectroscopy, Including Higher Order Processes, and also Brillouin and Rayleigh Scattering*, 2009, **40**, 86-91.
30. A. M. Fales, H. Yuan and T. Vo-Dinh, *The Journal of Physical Chemistry C*, 2014, **118**, 3708-3715.
31. J. Turkevich, P. C. Stevenson and J. Hillier, *Discussions of the Faraday Society*, 1951, **11**, 55-75.
32. S. Tanwar, K. K. Haldar and T. Sen, *Journal of the American Chemical Society*, 2017, **139**, 17639-17648.
33. K. K. Haldar, S. Tanwar, R. Biswas, T. Sen and J. Lahtinen, *Journal of Colloid and Interface Science*, 2019, **556**, 140-146.
34. T. Potlog, D. Duca and M. Dobromir, *Applied Surface Science*, 2015, **352**, 33-37.
35. S. W. Han, Y. Kim and K. Kim, *Journal of Colloid and Interface Science*, 1998, **208**, 272-278.
36. D. Zheng, C. Hu, T. Gan, X. Dang and S. Hu, *Sensors and Actuators B: Chemical*, 2010, **148**, 247-252.
37. K. K. Haldar, R. Biswas, S. Tanwar, T. Sen and J. Lahtinen, *ChemistrySelect*, 2018, **3**, 7882-7890.
38. M. Brust, M. Walker, D. Bethell, D. J. Schiffrin and R. Whyman, *Journal of the Chemical Society, Chemical Communications*, 1994, 801-802.
39. Y. Liu, D. Yang, Y. Zhao, Y. Yang, S. Wu, J. Wang, L. Xia and P. Song, *Heliyon*, 2019, **5**, e01545.
40. Y.-F. Huang, D.-Y. Wu, H.-P. Zhu, L.-B. Zhao, G.-K. Liu, B. Ren and Z.-Q. Tian, *Physical Chemistry Chemical Physics*, 2012, **14**, 8485-8497.
41. M. Sun, Y. Huang, L. Xia, X. Chen and H. Xu, *The Journal of Physical Chemistry C*, 2011, **115**, 9629-9636.
42. A. M. Gabudean, D. Biro and S. Astilean, *Journal of Molecular Structure*, 2011, **993**, 420-424.
43. Y. Yang, J. Shi, G. Kawamura and M. Nogami, *Scripta Materialia*, 2008, **58**, 862-865.
44. A. Garcia-Leis, J. V. Garcia-Ramos and S. Sanchez-Cortes, *The Journal of Physical Chemistry C*, 2013, **117**, 7791-7795.
45. N. Karthik, S. Asha and M. Sethuraman, *Journal of Sol-Gel Science and Technology*, 2016, **78**, 248-257.
46. S.-H. Nam, T. K. Kim and J.-H. Boo, *Catalysis Today*, 2012, **185**, 259-262.
47. F.-P. Du, N.-N. Cao, Y.-F. Zhang, P. Fu, Y.-G. Wu, Z.-D. Lin, R. Shi, A. Amini and C. Cheng, *Scientific Reports*, 2018, **8**, 6441.
48. N. Masnabadi, M. H. Ghasemi, M. H. Beyki and M. Sadeghinia, *Research on Chemical Intermediates*, 2017, **43**, 1609-1618.
49. H. Li and Y. Li, *Nanoscale*, 2009, **1**, 128-132.
50. R. Biswas, H. Singh, B. Banerjee and K. K. Haldar, *ChemistrySelect*, 2019, **4**, 4003-4007.

51. R. Biswas, S. Mete, M. Mandal, B. Banerjee, H. Singh, I. Ahmed and K. K. Haldar, *The Journal of Physical Chemistry C*, 2020, **124**, 3373-3388.
52. L.-N. Liu, J.-G. Dai, T.-J. Zhao, S.-Y. Guo, D.-S. Hou, P. Zhang, J. Shang, S. Wang and S. Han, *RSC Advances*, 2017, **7**, 35075-35085.
53. L.-N. Liu, J.-G. Dai, T.-J. Zhao, S.-Y. Guo, D.-S. Hou, P. Zhang, J. Shang, S. Wang and S. Han, *RSC Advances*, 2017, **7**, 35075-35085.
54. M. Ali, A. Mansha, S. Asim, M. Zahid, M. Usman and N. Ali, *Journal of Spectroscopy*, 2018, **2018**.

Chapter 4

Design of silica@Au hybrid nanostars for enhanced SERS and photothermal effect



4.1. Introduction

Localized surface plasmon resonance (LSPR) is a unique property of plasmonic nanostructures (made of Au and Ag) that have been the subject of intensive study over the past two decades.^{1, 2} The LSPR excitation gives these materials a remarkable ability to confine and modify light on the nanoscale.^{3, 4} Due to their distinctive optical properties from UV-Vis to near infrared (NIR), plasmonic nanoparticles/nanostructures have many promising applications in various fields such as biomedical domain,⁵ and detection of polynucleotides,⁶ SERS,⁷ photovoltaics.⁸

In recent years, scientists have been captivated by core-shell nanostructures due to the intriguing combination of properties from two very different materials.⁹⁻¹¹ Nanoparticles with an Au metal core and a SiO₂ dielectric shell, or a SiO₂ dielectric core and an Au metal shell, have been reported to be synthesized and used for various purposes, including cancer imaging and photothermal treatment.¹² By adjusting the shell thickness and core radius, the optical characteristics of these core-shell nanoparticles can be shifted from the visible to the infrared to the near infrared (IR).^{13, 14} These nanostructures, which can be thought of as a "core" surrounded by a "shell," combine the properties of two LSPRs, one of which is located inside the shell and the other outside.^{15, 16} Size variations between 10 nm and 100 nm are required to alter the LSPR position of spherical Au nanoparticles by a few nanometers.¹⁷ However, the biological window needs to be covered, so a wide spectrum of wavelengths from the visible to the infrared and near-infrared is required. As a result, when preparing the Au shell, the necessary tuning of the wavelength from the UV to the near IR region can be achieved by simply varying the thickness of the shell by a few nanometers.¹⁸ Dielectric silica is used as the core material in many published examples because it is thermally stable, chemically inert, and transparent in the visible spectrum. This means that it can serve as a platform for the creation of a wide range of nanostructures.¹⁹ The gold nanoshells surrounding a silica dielectric core with self-assembled monolayers were prepared and characterized by Pham et al.²⁰ The ideal SERS tag SiO₂@Au core-shell nanostructures for SERS based lateral flow immunoassay (LFA) were synthesized by Wang et al.²¹ The developed SiO₂@Au nanowires were put to use by Li et al. in high performance hydrogen peroxide sensors.²² Using p-mercaptoaniline as an analyte, Oldenberg et al.

demonstrated the SERS enhancement of metal shells.²³ Because of their SPR property, which causes them to show the SERS, spherical gold nanoshells have gained a lot of attention. The plasmons inside and outside the Au nanoshells resonate with one another, resulting in massively improved properties.¹⁸ When the Au nanoparticles have anisotropic shape, like nanostars or nanoflowers, a strong electromagnetic field is generated at the sharp edges via plasmon excitation under light irradiation, resulting in an increase in SERS enhancements.^{24, 25} Therefore, it is reasonable to expect a more pronounced SERS enhancement from anisotropic metal shells with dielectric cores.

One other amazing application of plasmonic nanostructures is in photothermal therapy (PTT).^{26, 27} NIR light is an extremely important light source for photothermal therapy, which is safe and noninvasive for normal tissues.²⁸ It was discovered that the morphology, the wavelength of the SPR, and the volume of the nanostructure all have a significant impact on the photothermal conversion efficiency of the Au nanostructures.²⁶ For example, by using spherical and anisotropic Au nanoparticles, Moustauoui et al. demonstrated the effect of shape and size on the photothermal heat elevation. They found that the anisotropic Au nanoparticles had a better photothermal effect due to their higher surface/volume ratio.²⁹ For the very first time, the Halas group described the thermal ablation therapy by utilizing the silica-gold nanoshell structures (SiO₂@Au core-shell spherical nanoparticles). They exploited the metal shells for the killing of human breast carcinoma cells and found the photothermal induced morbidity on exposure to NIR light (820nm, 35W/cm²).³⁰ After that, metal nanoshells started receiving immediate attention due to the efficient control that could be exerted over their shell thickness and their optical properties could be tuned.^{31, 32} Till now, either only isotropic/anisotropic pure Au nanoparticles or spherical core-shell nanostructures were used for photothermal therapy.

This chapter demonstrates the seed-mediated growth method to synthesize Au nanostars with sharp and controlled tips with a spherical silica core (SiO₂@Au NSs). Metallic nanostructures such as rings,³³ gaps,³⁴ bowties,^{35, 36} shells,³⁷ are known to provide SERS enhancements up to 10⁸ folds. So, the prepared SiO₂@Au NSs were explored for the SERS performance by using Rhodamine B (RhB) dye as a probe molecule. Also, plasmon band of our SiO₂@Au NSs lies in the biological window (700- 1200 nm).

Hence, we further investigated the photothermal effect of SiO₂@Au NSs by using 808 nm NIR laser line. Along with this, we have demonstrated the effect of concentration of nanostructures on the local temperature under NIR laser excitation. After that, these nanostructures were put to use in photothermal ablation of a breast cancer cell line in vitro. These research findings open up the possibilities for using nanostructures with a core-shell configuration for applications in SERS spectroscopy and photothermal cancer therapy.

4.2. Experimental Section

4.2.1. Materials

Phosphonium chloride (THPC) was purchased from TCI and Sodium chloride (NaCl) was purchased from Himedia. Tetraethyl orthosilicate (TEOS 98%), Ammonia solution (NH₃ 25%), (3-Aminopropyl)triethoxysilane (APTES 99%), Sodium Hydroxide (NaOH), Gold chloride trihydrate (HAuCl₄.3H₂O), L- Ascorbic acid, Silver nitrate (AgNO₃), Hydrochloric acid (HCl), Formaldehyde (HCHO), Potassium carbonate (K₂CO₃), and ethanol (EtOH) were purchased from Sigma- Aldrich, Tetrakis(hydroxymethyl) All the reagents are used without further purification.

4.2.2. Experimental procedures

4.2.2.1. Synthesis of spherical core-shell SiO₂@Au NPs

Au shell around the SiO₂ NP was prepared according to modified protocol as discussed the chapter 2 of the thesis.³¹ For this, aminated SiO₂ NPs were decorated with small sized Au nanoparticles. Small Au nanoparticles bonded to silica cores serve as nucleation sites for additional Au reduction via HAuCl₄ solution. As more Au is reduced, thicker coating forms on the silica nanoparticle's surface, and eventually Au spherical shell forms around the particle.

4.2.2.1.1. Preparation of silica nanoparticles (SiO₂-NPs)

SiO₂-NPs were prepared by modified Stober's method.³⁸ In brief, 64 mL of EtOH was added with 36 mL of H₂O and stirred for 10-15 min with constant temperature of 50°C.

Then 13.6 mL of NH_3 solution was added and the reaction mixture was stirred for 10 min. The TEOS solution was added to the reaction mixture in aliquots of 50 μL , 100 μL , and 150 μL at 5 min intervals. Afterwards, the reaction mixture was stirred for 3 hours at 50°C . and it was cooled to ambient temperature, centrifuged at 13000 rpm and washed three times with EtOH. In the end, white solid of SiO_2 -NPs was collected and dried in an oven at 60°C .

4.2.2.1.2. Preparation of aminated silica nanoparticles (SiO_2 - NH_2 NPs)

10 mg of SiO_2 -NPs was redispersed in 20 mL of EtOH using probe sonicator and added 10 μL of APTES solution to the reaction mixture and stirred slowly for overnight.³¹ Then on the next day, the reaction mixture was refluxed for 2 hours at 80°C in a round bottom flask (RBF). Then it was cooled to room temperature and washed three times with EtOH at 7500 rpm. After that, the residue was collected and dried in an oven at 60°C .

4.2.2.1.3. Synthesis of THPC Au NPs suspension

A THPC Au NPs suspension consisting of 2-3 nm Au colloid was synthesized as per the protocol given by Duff et al.³⁹ 1.5 mL of 0.2 M NaOH was added to 45.5 mL of H_2O under rapid stirring. 12 μL of 80% reducing agent THPC and 2 mL of 25 mM of HAuCl_4 aqueous solution were added in sequence. Small gold nanoparticles formed, as evidenced by the solution's sudden color change to a deep brown. The as prepared solution was sonicated for 10-15 min and then stored for 5 days at 4°C before use. The solution can be stable for months when stored at 4°C .

4.2.2.1.4. Synthesis of Au plating solution

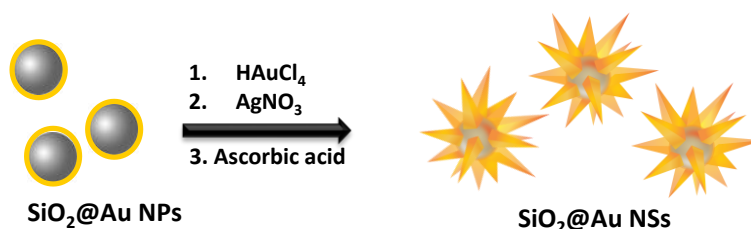
For the preparation of Au plating solution, 300 μL of 1 wt% HAuCl_4 aqueous solution was added to 20 mL of 1.8 mM aqueous K_2CO_3 .³¹ The solution was sonicated for 1-2 min and then stored for 5 days at 4°C before use.

Au shell around the SiO_2 NP was prepared according to modified protocol as discussed the chapter 2 of the thesis.³¹ Firstly, small Au NPs were decorated on SiO_2 NPs. In

order to achieve this, 40 mL of THPC Au NPs suspension was sonicated for 1-2 min. During the sonication, 4 mL of 1 M NaCl solution was added and then addition of 300 μ L of aqueous $\text{SiO}_2\text{-NH}_2$ NPs (probe sonicated) was done. The reaction mixture was sonicated for 2 min and left undisturbed at room temperature. After 5 days, the reaction mixture was centrifuged at 8500 rpm for 20 min to remove excess THPC solution and washed with H_2O . The so formed pellet (Au NPs decorated on SiO_2 NPs) was redispersed in H_2O . For the growth of Au shell from Au NPs decorated on SiO_2 NPs, Au plating solution was used. For this, Au plating solution was used in such a way that its volume was 10 times ($10\times$) than the redispersed pellet for the total volume of 2.2 mL. 11 μ L of formaldehyde solution was added and sonicated for 1-2 min, kept undisturbed for 10 min and centrifuged at 4100 rcf for 15 min and the obtained pellet was redispersed in water.

4.2.2.2. Synthesis of $\text{SiO}_2\text{@Au}$ NSs

The synthesized Au shells around the SiO_2 NPs ($\text{SiO}_2\text{@Au}$ NPs) were used as seeds with growth solution for the synthesis of silica core coated with Au nanostars shell ($\text{SiO}_2\text{@Au}$ NSs) (Scheme 4.1). For the synthesis of silica core coated with Au nanostars shell, 0.2 mM aqueous solution of HAuCl_4 was used with 1 N HCl. To this solution, synthesized $\text{SiO}_2\text{@Au}$ NPs seeds were added followed by the subsequent addition of 0.01 M AgNO_3 and 0.1 M ascorbic acid. Upon addition of ascorbic acid, blue color appeared indicating the formation of nanostars. After 10 min of stirring, the reaction mixture was centrifuged at 7500 rpm, and the formed pellet of $\text{SiO}_2\text{@Au}$ NSs was redispersed in H_2O .



Scheme 4.1. Schematic depiction of synthesis of $\text{SiO}_2\text{@Au}$ NSs.

4.2.2.3. Raman measurements

To evaluate the SERS performance of SiO₂@Au NSs, Rhodamine B (RhB) dye was used as a probe using both 785 nm and 633 nm laser line. The normal Raman spectrum of RhB dye was recorded by drop casting 1 mM solution of RhB dye on silicon wafer. After that, SiO₂@Au NSs solution was drop casted on silicon wafer followed by drop casting 1 μ M solution of RhB dye, and then the silicon wafer was dried and its SERS spectrum was recorded. The enhancement factor (EF) was calculated by using the equation 4.1.⁴⁰

$$EF = \frac{N_{bulk}}{N_{SERS}} \times \frac{I_{SERS}}{I_{bulk}} \quad \text{Equation 4.1}$$

where N_{bulk} is the number of RhB dye molecules in confocal volume contributing to Raman signal in normal Raman measurement using bulk RhB dye and N_{SERS} is the SERS measurements using RhB dye with SiO₂@Au NSs. I_{bulk} and I_{SERS} are the intensities of the vibrational signals in normal Raman and SERS measurements, respectively.

4.2.2.4. Photothermal transduction efficiency (η) studies

Different concentration (93.75, 187.75, 375, 562.5, 750 μ g/mL) of SiO₂@Au NSs were irradiated with NIR (808 nm) laser with power (2 W) and laser distance (2 cm). Further, photostability of NSs (750 μ g/mL) was explored after irradiation with the laser for three On-Off cycles. The heating and cooling cycles were recorded with FLIR Pro thermal imaging camera. The photothermal transduction efficiency was calculated using equation 4.2 (as in previous reports⁴¹).

$$\eta = \frac{hS(T_{max} - T_{Surr}) - Q_{dis}}{I(1 - 10^{-A_{800}})} \quad \text{Equation 4.2}$$

Where h and S are the heat transfer coefficient and the surface area of the container respectively. T_{Surr} (19.0°C) was surrounding temperature and T_{max} was the maximum steady temperature (63°C) of the solution. I , the laser power intensity which was set at

2.2 W/cm², the absorbance of the NSs at 800 nm was 0.181. Q_{Dis} expresses heat dissipated from the light absorbed by the solvent and container.

4.2.2.5. Hemocompatibility studies

Following IAEC approval of IISER Mohali (IISERM/SAFE/PRT/2021/023) and as per animal ethics guidelines, mice blood was utilized for hemocompatibility study. Briefly, 500 μ L of blood was dispersed in 4.5 mL of PBS and centrifuged at 1000 rpm for 5 min, further washed thrice with PBS until the clear supernatant was obtained. Final RBC's pellet was dispersed in 5 mL of PBS and stored at 4°C till use. Different concentration (25, 50, 100, 200, 400 μ g/mL) of SiO₂@Au NSs was incubated with 150 μ L of RBC for 1 hour at 37°C. After 1 hour, samples were pelleted down, supernatant was collected and absorbance was recorded at 575 and 655 nm with plate reader. Water and PBS were used as positive and negative control. Hemolysis percentage was calculated by using equation 4.3.

$$\text{Hemolysis (\%)} = ((A_{575} - A_{655}) - \text{PBS}) / (\text{water} - \text{PBS}) \times 100 \quad \text{Equation 4.3}$$

4.2.2.6. In vitro studies

Triple negative breast cancer cell line MDA-MB-231 and mouse fibroblast normal cell line L929 were acquired from National Centre for Cell Science (NCCS, Pune). The cells were cultured in Dulbecco's modified Eagle's medium (DMEM) supplemented with 10% fetal bovine serum and 1% antimycotic antibiotics solution in a humidified incubator supplied with 5% CO₂ at 37 °C.

4.2.2.7. In vitro biocompatibility

MTT assay was used to investigate the biocompatibility against L929 *cell line*. Cells (2.5×10^4 cells per well) were seeded in 96-well culture plates and cultured for 24 hours in the incubator with 5% CO₂ at 37°C. Different concentrations of the SiO₂@Au NSs (0-400 μ g/mL) were tested against the cells in triplicate and incubated for 24 hours at 37°C under 5% CO₂. After incubation, the sample was removed by washing the cells thrice with pre-warmed 1× PBS and further incubated with MTT solutions (5 mg/mL in

PBS). After 4 hours, the plates were centrifuged at 1500 rpm for 5 min at room temperature and DMSO was added to each well. To dissolve the formazan crystals, all the wells were aspirated before taking absorbance at 595 nm on an ELISA reader. Cell viability was calculated by means of the following equation 4.4.

$$\text{Cell viability (\%)} = \frac{\text{Absorbance of the treated cells}}{\text{Absorbance of the control cells}} \times 100 \quad \text{Equation 4.4}$$

4.2.2.8. In vitro photothermal therapy

Photothermal cytotoxicity was evaluated against MDA-MB-231 cells using an MTT assay. Cells (5×10^3 cells per well) were seeded in a 96-well culture plate at 37°C under 5% CO₂ for 24 hours. After overnight incubation, the cells were treated with different concentrations of SiO₂@Au NSs (0-300 µg/mL). After 6 hours, the cells were irradiated with 808 nm NIR laser for 10 min (power 2.2 W/cm²) and further incubated for 24 hours in the CO₂ humidified incubator. The cells were washed thrice with PBS buffer to remove traces of the sample and further incubated with MTT solutions (5 mg/mL in PBS) for 4 hours. After incubation for 4 hours, the plates were centrifuged at 1500 rpm for 5 min at room temperature and DMSO was added to dissolve the formazan crystals. All the wells were aspirated well and the absorbance of the suspension was measured at 595 nm on a microplate reader. Cell viability was calculated by the above-mentioned formula.

4.2.2.9. Cellular uptake study

The cellular uptake of SiO₂@Au NSs was quantified by ICP-MS analysis. Briefly, 1×10^5 cells (MDA-MB-231) were allowed to adhere in a 12 well plate under 5% CO₂ for 24 hours. After incubation, the cells were incubated with SiO₂@Au NSs (200 µg/mL) for 3, 6 and 24 hours. At the end of incubation, the cells were washed thrice with PBS buffer followed by trypsinization for the detachment of cells. The detached cells were centrifuged at 2000 rpm for 5 min. The cells were digested with ICP-MS grade nitric acid followed by dilution with double distilled water. The clear solution was analyzed with Inductive Coupled Plasma – Mass Spectrometer.

4.2.2.10. Cell morphology analysis

MDA-MB-231 cells and L929 cells were seeded onto the glass cover slips in 6 well plate with at a density of 1×10^5 cells per well and incubated with SiO₂@Au NSs (200 µg/mL) with and without laser. After 24 hours incubation, the cells were washed with PBS and fixed with 4% paraformaldehyde solution for 10–12 min. Following PBS wash, cells were stained by Hoechst 33342 and Ph-TRITC for staining the nuclei and cytoskeleton, respectively. Further, the cells were washed, mounted on a glass slide and examined under Zeiss LSM 880 confocal microscope (Carl Zeiss, Thornwood, New York).

As synthesized SiO₂ NPs, SiO₂@Au NPs, SiO₂@Au NSs, were characterized by UV-Vis spectrophotometer, DLS, FT-IR, powder XRD, TEM, and AFM as described in chapter 2 of this thesis.

4.3. Results and discussion

4.3.1. Optical and structural characterizations of SiO₂@Au NSs

For the synthesis of SiO₂@Au NSs, first core SiO₂ NPs were prepared. These were synthesized using TEOS in a water-EtOH mixture and amination of SiO₂ NPs was done using APTES to prepare SiO₂-NH₂ NPs. The optical and structural characterization of SiO₂ and SiO₂-NH₂ NPs was carried out using TEM, DLS, and powder XRD. From DLS measurements, the approximate hydrodynamic size for SiO₂ NPs and aminated SiO₂ NPs (SiO₂-NH₂ NPs) was evaluated.

As shown in Figure 4.1a, the average hydrodynamic size of SiO₂ NPs and SiO₂-NH₂ NPs was around 50 nm and 65 nm, respectively. The powder X-ray diffraction pattern of SiO₂ NPs was then collected. Figure 4.1b shows the XRD pattern of SiO₂ NPs showing a broad peak centered at 22.8° is indication of amorphous nature of as prepared SiO₂-NPs.⁴² Further, a zeta potentiometric study (Figure 4.1c) indicated a negative potential for SiO₂ NPs, but when amination was done using APTES to form SiO₂-NH₂ NPs, the potential was reversed to a positive value, displaying the successful amination of SiO₂ NPs. The amination of SiO₂ NPs was further affirmed using FT-IR analysis. The FT-IR spectra of SiO₂ NPs and SiO₂-NH₂ NPs are shown in Figure 4.1d. It was discovered that for SiO₂ NPs, the broad peak at 3353 cm⁻¹ corresponds to Si-O-H

stretching vibrations⁴² and in the case of SiO₂-NH₂ NPs, the medium peak at 3317 cm⁻¹ in the FT-IR spectrum was attributed to N-H stretching.⁴³ The peaks at 1625, 1104, and ~ 793 cm⁻¹ were due to the asymmetric and symmetric stretching vibrations of Si-O-Si, respectively.⁴² The peak at 480 cm⁻¹ was attributed with N-H wagging vibration in FT-IR spectrum SiO₂-NH₂ NPs. The analysis of zeta potentiometric and FT-IR studies demonstrated the successful amination of SiO₂ NPs. The average size of SiO₂ NPs as indicated from TEM images (depicted in Figure 4.1e and 4.1f) was 45 ± 5 nm which was consistent with the size obtained from DLS analysis. All these results demonstrate the successful synthesis of SiO₂ NPs and SiO₂-NH₂ NPs.

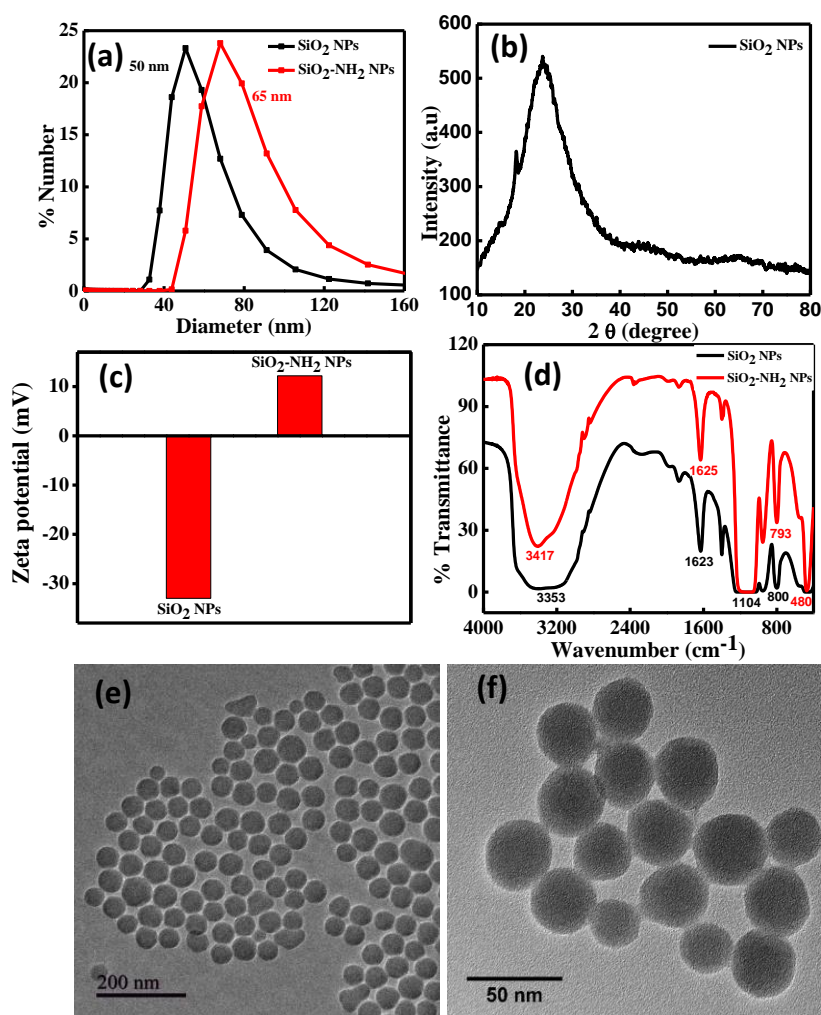


Figure 4.1. (a) Dynamic light scattering spectra of SiO₂ and SiO₂-NH₂ NPs, (b) XRD pattern of SiO₂ NPs, (c) Zeta potential, (d) Fourier-transform infrared spectra (FTIR) of SiO₂ and SiO₂-NH₂ NPs, and (e, f) TEM images of SiO₂ NPs.

Following the successful formation of $\text{SiO}_2\text{-NH}_2$ NPs, Au shell was deposited over $\text{SiO}_2\text{-NH}_2$ NPs subsequently forming core-shell $\text{SiO}_2\text{@Au}$ NPs. To achieve this, firstly small sized Au NPs prepared using THPC were decorated over the surface of $\text{SiO}_2\text{-NH}_2$ NPs. When the solution of $\text{SiO}_2\text{-NH}_2$ NPs was mixed with suspension of THPC Au NPs, small Au NPs were decorated on $\text{SiO}_2\text{-NH}_2$ NPs as a result of binding with the amine groups present on SiO_2 NPs. Then Au NPs decorated on the $\text{SiO}_2\text{-NH}_2$ NPs were grown into a shell around the SiO_2 core which results in formation of core-shell $\text{SiO}_2\text{@Au}$ NPs using Au plating solution. The extinction spectra of THPC Au NPs suspension and Au NPs decorated on $\text{SiO}_2\text{-NH}_2$ NPs were further measured.

Figure 4.2a shows the UV-Vis spectra of as synthesized THPC Au NPs suspension, Au NPs decorated on SiO_2 NPs, and $\text{SiO}_2\text{@Au}$ NPs. In case of THPC Au NPs suspension, the existence of a featureless absorbance which increases at lower wavelengths as well as the absence of any plasmon band in the 500-550 nm range strongly suggests the formation of small sized (< 3 nm) Au NPs.^{39, 44} The SPR band centered at 512 and 540 nm was credited to Au NPs decorated on $\text{SiO}_2\text{-NH}_2$ NPs²² and $\text{SiO}_2\text{@Au}$ NPs, respectively.²¹ The red shifting of the plasmon band from 512 nm to 540 nm indicated the successful formation of Au shell on SiO_2 NPs. The XRD pattern for $\text{SiO}_2\text{@Au}$ NPs is shown in Figure 4.2b. Along with the hump corresponding to amorphous SiO_2 NPs, the diffraction peak at 38.2° demonstrated that the Au NPs present on SiO_2 NPs were oriented in (111) plane. Peaks corresponding to (200), (220), and (311) are good suggestive of incorporation of Au NPs with SiO_2 NPs.⁴⁵ Further, the hydrodynamic size of as synthesized NPs was predicted using DLS. In case of THPC Au NPs suspension, it was observed that the diameter of Au NPs was 2-3 nm as shown in Figure 4.2c. When Au NPs were decorated on SiO_2 NPs, the size was found to be 100 nm (shown in Figure 4.2d). After the formation of Au shell, the hydrodynamic diameter (Figure 4.2d) was estimated to be 160 nm for $\text{SiO}_2\text{@Au}$ NPs. Hence, the DLS results confirmed the increase in the size of SiO_2 NPs when Au shell was formed which is consistent with the red shift of the plasmon band observed in the UV-Vis spectra of $\text{SiO}_2\text{@Au}$ NPs. TEM images (presented in Figure 4.2e and 4.2f) confirmed the successful formation of Au NPs decorated on SiO_2 with an average size of $\sim 60 \pm 5$ nm.

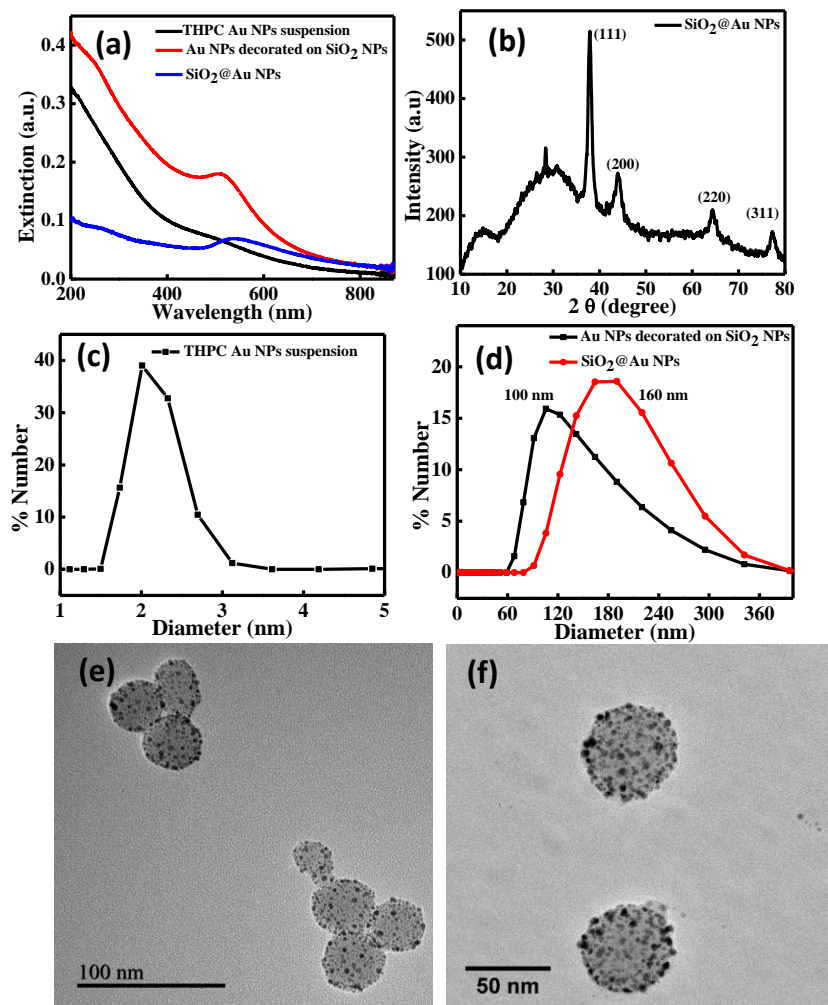


Figure 4.2. (a) UV-Vis extinction spectra of THPC Au NPs suspension, Au NPs decorated on SiO_2 NPs and SiO_2 @Au NPs, (b) XRD pattern of SiO_2 @Au NPs, (c) DLS spectrum of THPC Au NPs suspension, (d) DLS spectra Au NPs decorated on SiO_2 NPs and SiO_2 @Au NPs, and (e, f) TEM images of Au NPs decorated on SiO_2 NPs.

The as prepared core-shell SiO_2 @Au NPs were then used as seeds for growing the spherical Au shell into Au nanostar around the spherical SiO_2 NPs. The optical and structural characterizations of synthesized SiO_2 @Au NSs were performed.

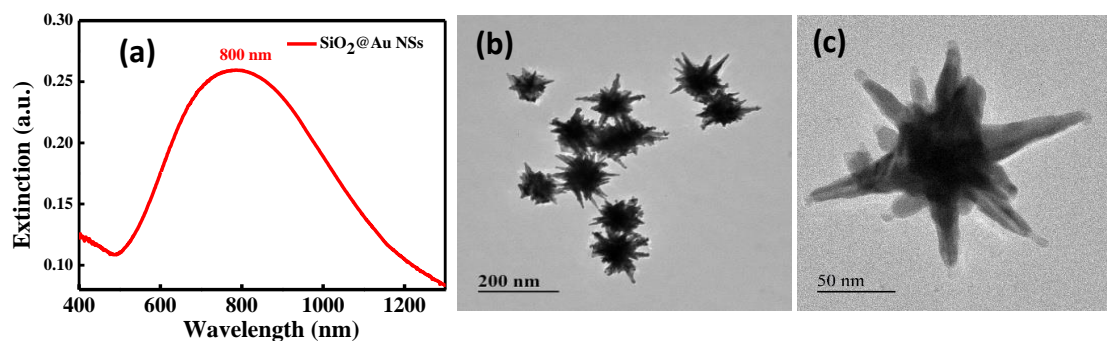


Figure 4.3. (a) UV- Vis-NIR spectrum of SiO₂@Au NSs, (b) Low resolution TEM images of SiO₂@Au NSs, and (c) TEM image of single SiO₂@Au NS.

Figure 4.3a shows the extinction spectrum of SiO₂@Au NSs depicting a broad SPR band centered at 800 nm indicating the formation of Au NSs on SiO₂ NPs core. The formation of SiO₂@Au NSs was further confirmed by TEM imaging (Figure 4.3b and 4.3c). As shown in Figure 4.3b, highly monodispersed SiO₂@Au NSs were formed with sharp and defined tips. The average size of SiO₂@Au NSs (tip to tip distance) as calculated from TEM images was 140 ± 5 nm (Figure 4.3c).

Further, high-angle annular dark-field imaging (HAADF-STEM) analysis of SiO₂@Au NSs was performed to determine the elemental composition of the structures. Figure 4.4a shows the HAADF-STEM image of SiO₂@Au NSs, and elemental mapping of SiO₂@Au NSs is shown in Figure 4.4b and 4.4c. The HAADF-STEM images proven the presence of both Si and Au in SiO₂@Au NSs and uniform deposition of Au around the Si core as well as tips of nanostars. The line scan analysis (Figure 4.4d) showed the presence of Si inside the core whereas Au is present as the outer shell and tips of SiO₂@Au NSs. The energy dispersive X-ray (EDX) spectrum further confirms the presence of both Si and Au in SiO₂@Au NSs (Figure 4.4e). Thus, these results confirm the successful formation of SiO₂@Au NSs. To the best of our knowledge, this is the first report on the surfactant-free synthesis of SiO₂@Au NSs.

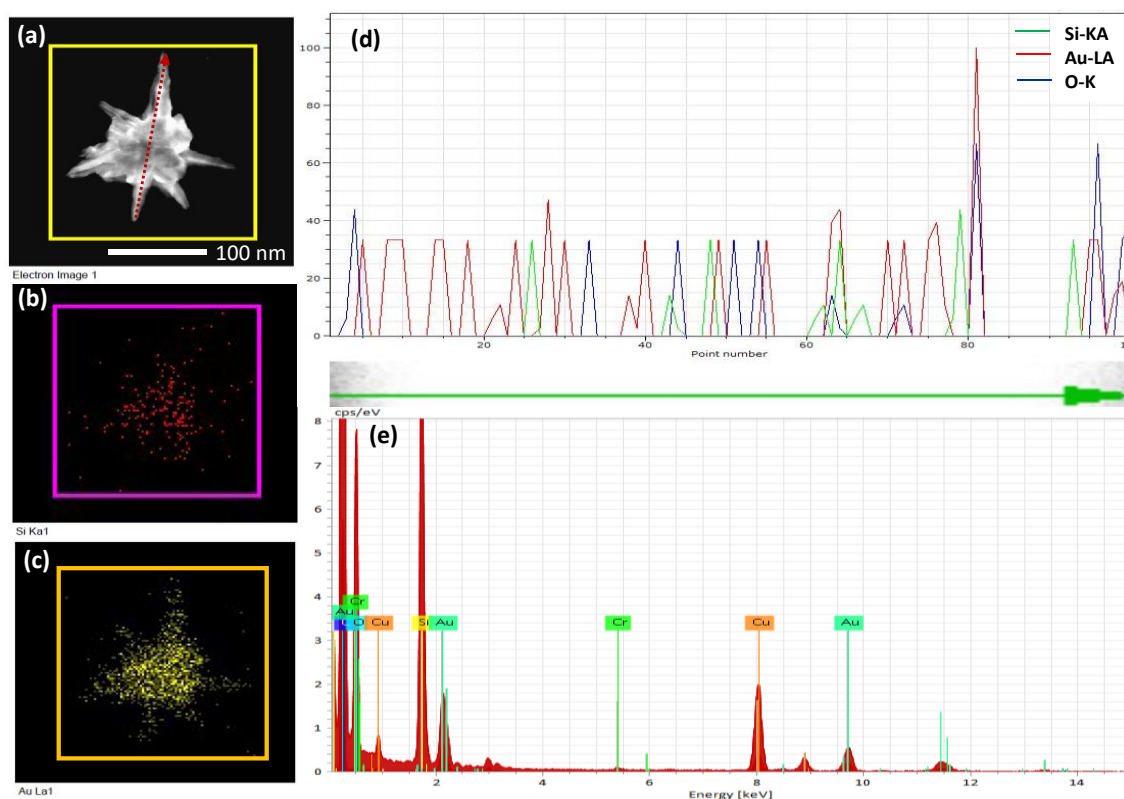


Figure 4.4. (a) HAADF-STEM image, (b,c) elemental mapping, (d) Line scan analysis of SiO₂@Au NS, and (e) EDX spectrum of SiO₂@Au NSs.

4.3.2. SERS performance of SiO₂@Au NSs

In order to check the potential of SiO₂@Au NSs for the enhancement of Raman signals, Rhodamine B (RhB) dye was chosen as a probe molecule to evaluate the SERS performance. The photoluminescence of RhB dye makes it challenging to capture its Raman signal. Therefore, the Raman signal of RhB dye can be greatly improved by employing plasmonic nanostructures as the SERS substrate. The normal Raman spectrum of bulk RhB dye was recorded by drop casting 1mM solution of RhB dye on silicon wafer using 785 nm laser (Figure 4.5a). It was discovered that peaks at 1642, 1536, and 1360 cm⁻¹ were related to aromatic C-C stretching vibrations, peak at 1283 cm⁻¹ was attributed to C-H bending, and peaks at 1195, 1520 cm⁻¹ were assigned to C-C bridge-band stretching.^{46, 47}

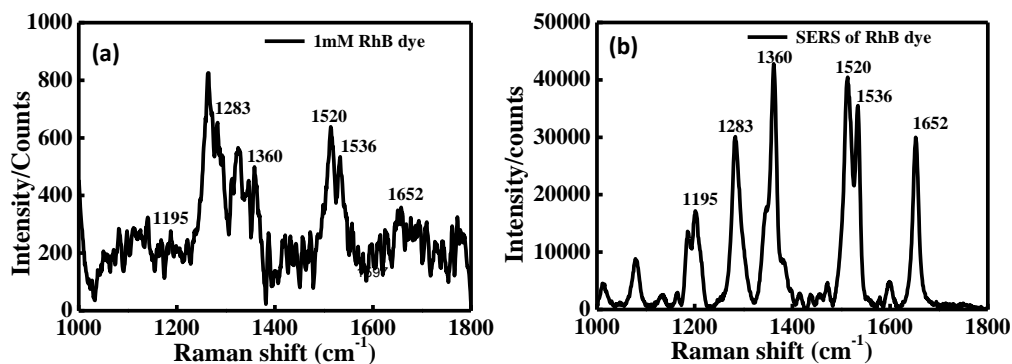


Figure 4.5. (a) Raman spectrum of RhB dye, and (b) SERS spectrum of 100 μ M RhB dye in SiO₂@Au NSs using 785 nm laser.

Figure 4.5b depicts the SERS spectrum of RhB dye using SiO₂@Au NSs which indicates the higher intensity of corresponding peaks as compared to the Raman spectrum of bulk RhB dye. This increase is credited to SERS enhancement of probe molecule (RhB dye) near plasmonic metal nanostructures due to the generation of intense electromagnetic fields arising from surface plasmon resonance.⁴⁸ Further, EF was calculated using equation 4.1 in which I_{SERS} and I_{bulk} are the intensities of strongest peak 1360 cm^{-1} in SERS spectrum and Raman spectrum of RhB dye, respectively (Figure 4.5). It was found that values of I_{SERS} and I_{bulk} are 43007 and 283 counts, respectively. The number of RhB dye molecules in the bulk (N_{bulk})^{40, 49} and in presence of SiO₂@Au NSs (N_{SERS})⁴⁰ were found to be 5.4×10^{10} and 5.7×10^6 , respectively. By substituting these values in equation 4.1, the calculated EF for RhB dye using SiO₂@Au NSs was estimated to be 1.37×10^6 . The EF values of solid Au NSs from the literature (Table 4.1) were compared to our prepared core-shell SiO₂@Au NSs. The obtained EF utilizing SiO₂@Au NSs (10^6) is found to be one order of magnitude higher as compared to pure Au nanostar (10^5). The high value of EF is attributed to the strong localized electromagnetic field at the sharp tips of nanostructure.⁵⁰ In our SiO₂@Au NSs, both star and shell type morphologies are present. In star morphology, strong coupling between plasmons of sharp tips of nanostar results in the creation of a large number of "hotspots," which are considered essential for elevated SERS enhancement.^{51, 52} Shell morphology involves the integration of localized plasmons present inside and outside of metal nanoshells, resulting in significantly increased field

strength that aids in increased SERS performance.¹⁸ So, our SiO₂@Au NSs (composed of shell and star morphology) show better EF value as compared to other shapes of similar λ_{max} position and excitation laser source.

Table 4.1. Enhancement factor comparison with literature.

Nanostructure	λ_{max}	Probe molecule	Laser used	EF	Reference
Multi branched Au NPs	850 nm	Rhodamine B	785 nm	Not calculated	⁵³
Au/Ag NSs	700 nm	Rhodamine 6G	785 nm	5.2×10^5	⁵⁴
Confeito-like Au NPs	655 nm	Rhodamine 6G	633 nm	1×10^5	⁵⁵
Au NSs	~ 800 nm	Rhodamine 6G	785 nm	4.1×10^5	⁵⁶
Au NSs	613 nm	Rhodamine B	633 nm	9.4×10^5	⁵⁷
Au NSs	704 nm	Rhodamine 6G	785 nm	1×10^5	⁵⁸
Dendritic Au rod	-	Rhodamine 6G	633 nm	1.5×10^5	⁵⁹
SiO₂@Au NSs	800 nm	Rhodamine B	785 nm 633 nm	1.37×10^6 3.5×10^4	This work

4.3.2.1. Effect of laser wavelength on SERS performance of SiO₂@Au NSs

Also, the same SERS measurements were done using laser 633 nm (Figure 4.6). It was found that values of I_{SERS} and I_{bulk} are 326 and 20 counts, respectively. The number of RhB dye molecules in the bulk (N_{bulk})^{40, 49} and in presence of SiO₂@Au NSs (N_{SERS})⁴⁰ was found to be 2.2×10^{10} and 1×10^7 , respectively and calculated EF was observed to be 3.5×10^4 . Hence, it is clear that using the resonant laser excitation wavelength of 785 nm with the LSPR band position of SiO₂@Au NSs (800 nm) leads to higher EF than using the off resonant wavelength of 633 nm which could be credited to the resonant SPR induced local field enhancement.⁶⁰ These results illustrate that SiO₂@Au NSs serve as an efficient SERS substrate demonstrating significant enhancement of Raman signals and thus can be possibly utilized for detection of a variety of target molecules.

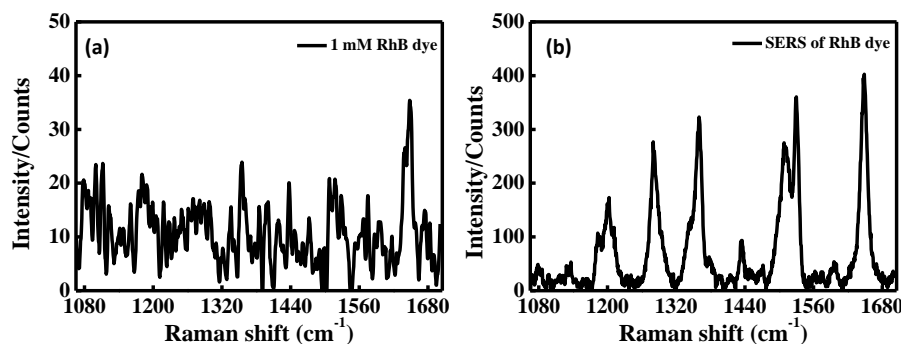


Figure 4.6. (a) Raman spectrum of RhB dye, and (b) SERS spectrum of 100 μM RhB dye in SiO₂@Au NSs using 633 nm laser.

4.3.3. Photothermal efficiency of SiO₂@Au NSs

The photothermal effect of as-prepared SiO₂@Au NSs is motivated by the significant SPR absorption in the NIR range. The SiO₂@Au NSs of different concentrations (93.75, 187.75, 375, 562.5, 750 μg/mL) were irradiated with 808 NIR laser with power 2.2 W/cm² for 5 min. It was demonstrated that there is concentration-dependent increase in the photothermal effect, with the highest temperature increment up to 63°C for 750 μg/mL (Figure 4.7a). Further, the colloidal SiO₂@Au NSs also possessed excellent photothermal stability for up to three consecutive Laser On-Off cycles (Figure 4.7b). The photothermal transduction efficiency (η) of SiO₂@Au NSs was calculated according to equation 4.2 and found to be ~72%. The η value of some other shapes from literature with comparable sizes and LSPR band positions are listed in Table 4.2.

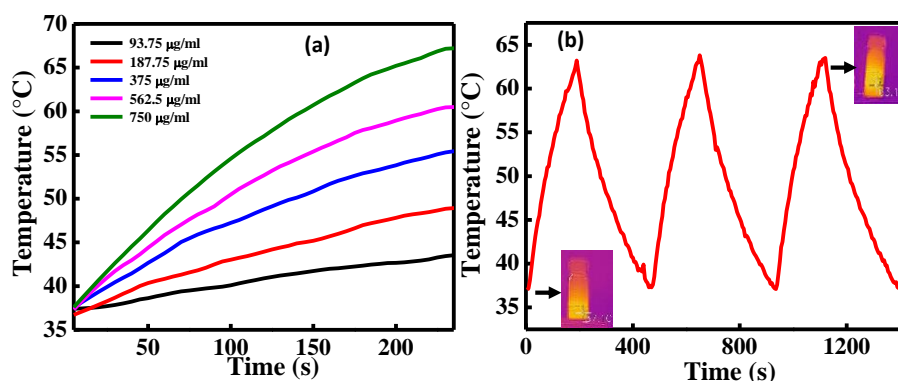


Figure 4.7. (a) Heating curves of various concentrations of SiO₂@Au NSs under laser irradiation and, (b) Photostability of SiO₂@Au NSs under three cycles of laser irradiation.

This is made clear by the fact that our anisotropic shaped shell morphology is more efficient at photothermal conversion than others Au nanostructures such as Au nanostars, nanobipyramids, and nanovesicles. The value of η for solid Au NSs is 34%⁶¹, while our core-shell SiO₂@Au NSs has a significantly higher value of 72% which is more than twice as much as pure Au nanostars (Table 4.2). Furthermore, as compared to spherical Au nanoshell of similar size and LSPR position, the anisotropic core-shell SiO₂@Au NSs exhibit higher η value owing to the unique shell type anisotropic shape. Sharp tipped or star shape morphology is considered to be the most effective for converting photon energy to heat energy due to their high values of the ratio of absorption and scattering of light.²⁷ Also, having a spherical nanoshells morphology that can maintain high absorption cross sections, leads to high photothermal conversion efficiencies.⁶² There are both shell and star morphologies exist in our SiO₂@Au NSs. So, when NIR light incident on the SiO₂@Au NSs, then high absorption cross sections of nanoshell and near field enhancement at the sharp tips cause the local temperature to increase enough to produce heat and this generated heat is used to destroy cancer cells.

Table 4.2. Photothermal Transduction Efficiency (η) comparison with literature.

Nanostructure	Nanoparticle size	λ_{\max}	NIR irradiation Conditions	η	Reference
Au nanostars	~ 200 nm	770 nm	CW laser, 808 nm	34 %	⁶¹
Au nanoshells	152 nm	796 nm	CW laser, 2 W/cm ² , 810 nm	39 %	⁶²
Au nano bipyramids	77 × 173 nm	809 nm	CW laser, 809 nm	51 %	⁶³
Au nanoshell	145 nm	780 nm	2 W/cm ² , 808 nm	25 %	⁶⁴
SiO ₂ /Au nanoshells	154 nm	815 nm	815 nm	30 %	⁶⁵
Au nanovesicles	207 nm	800 nm	1 W/cm ² , 808 nm	37 %	⁶⁶
SiO₂@Au nanostars	140 nm	800 nm	2.2 W/cm², 808 nm	72 %	Our work

4.3.4. *In vitro* studies

The biocompatibility of SiO₂@Au NSs at varying concentrations (25, 50, 100, 200, 400 µg/mL) was evaluated against L929 cell lines. SiO₂@Au NSs showed >80% cell survival even at higher concentration of 400 µg/mL (Figure 4.8a). Further, the SiO₂@Au NSs showed negligible hemolysis similar to negative control at all tested concentrations (Figure 4.8b).

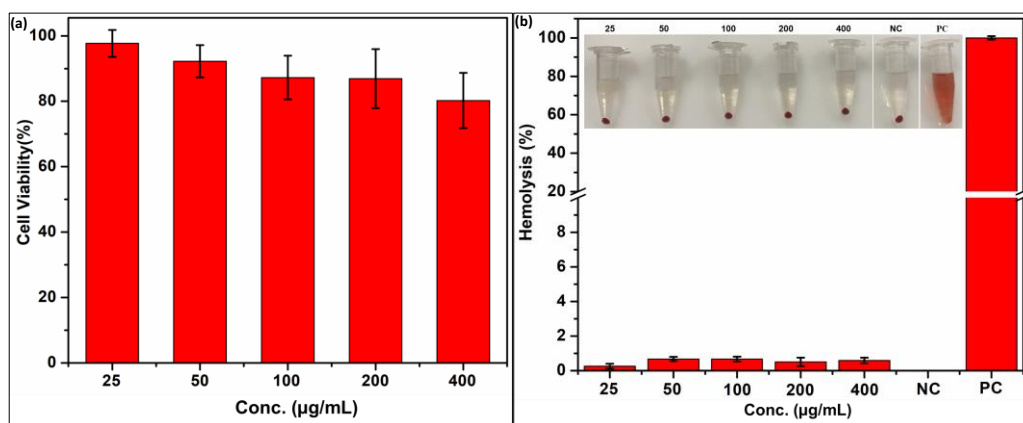


Figure 4.8. (a) *Biocompatibility of SiO₂@Au NSs with L929 cells*, and (b) *Hemocompatibility of SiO₂@Au NSs*.

Next, we analyzed the cytotoxicity of SiO₂@Au NS against triple negative breast cancer cell line MDA-MB-231. The SiO₂@Au NS significantly reduced the cell viability in a dose-dependent manner after 24 hours of incubation, with ≤50% cell viability at a concentration of 400 µg/mL. However, cytotoxicity further enhanced following 5 min of NIR laser irradiation with cell viability dropping below ~10% at same concentration (Figure 4.9a). Subsequently, it was observed that photothermal toxicity could be significantly increased at lower concentrations (200, 250 and 300 µg/mL) with 10 min of laser irradiation (Figure 4.9b). Moreover, when cells treated with 200 µg/mL of SiO₂@Au NSs and irradiated for different time period (2.5, 5, 7.5, 10 min), the survival rate decreased sharply to ~20% within 10 min of laser irradiation (Figure 4.9c). Further, the uptake of SiO₂@Au NSs by cancer cells as quantified by the ICP-MS analysis showed that the extent of association of the NSs with the cancer cells proportionally increased with time of incubation (Figure 4.9d).

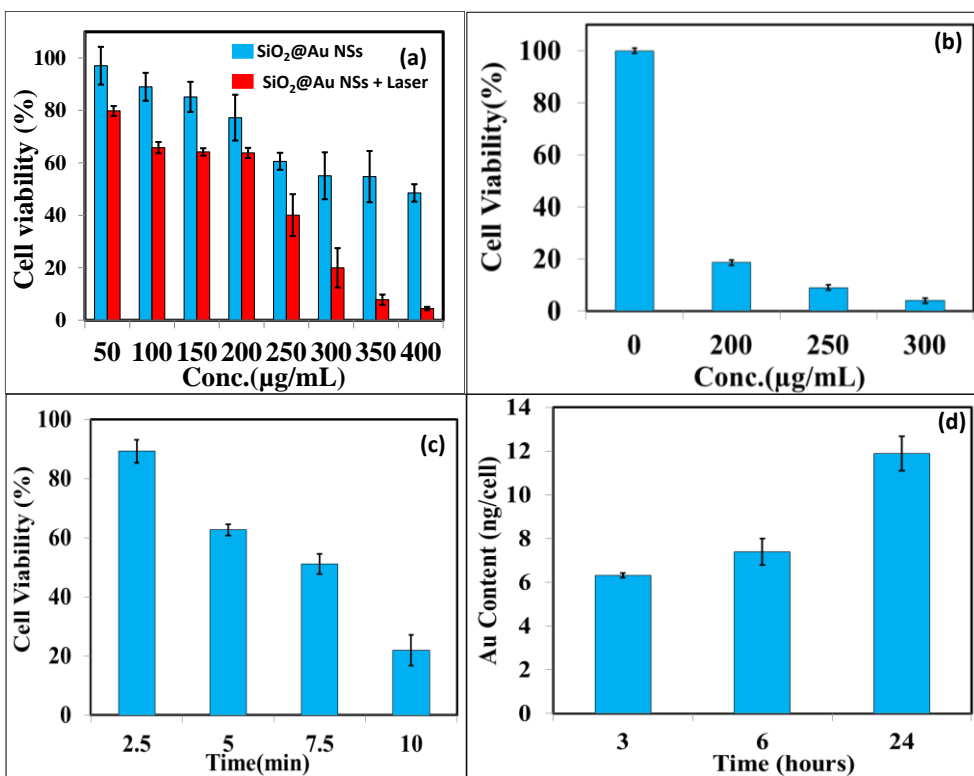


Figure 4.9. Cytotoxicity of SiO₂@Au NSs (a) at varying concentrations with and without 5 min of laser irradiation, (b) at varying concentrations with laser irradiation for 10 min, (c) cell viability at different laser irradiation time (conc. 200 μg/mL), and (d) time dependent cellular uptake of SiO₂@Au NSs.

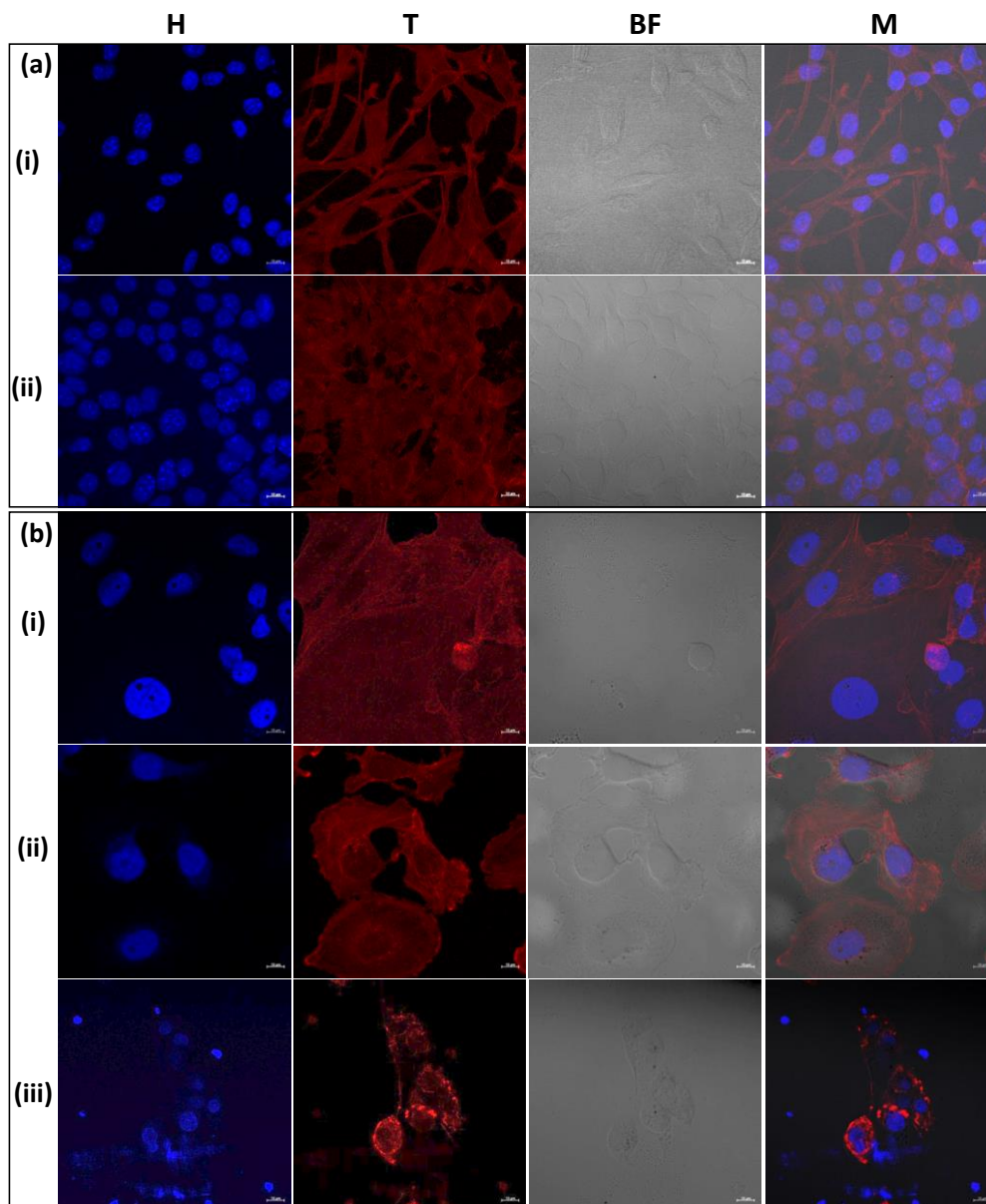


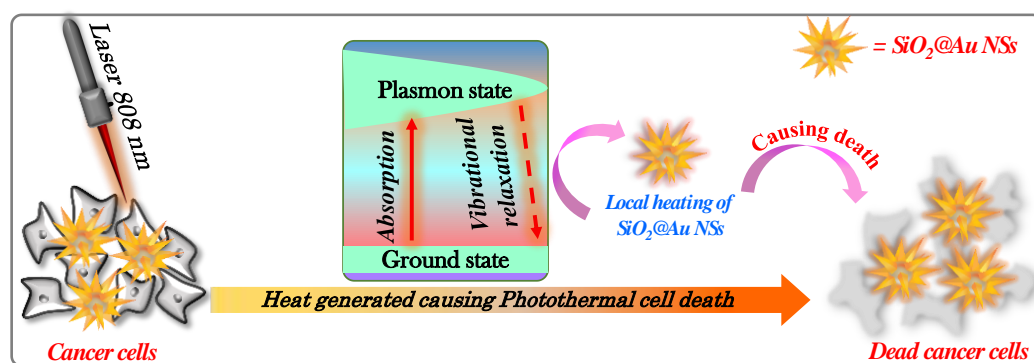
Figure 4.10. Confocal microscopic images of (i) untreated, (ii) SiO₂@Au NSs treated L929 cells (a), and (i) untreated, (ii) SiO₂@Au NSs, (iii) SiO₂@Au NSs + laser treated MDA-MB-231 cells (b). (H-Hoechst; T-phalloidin-TRITC; BF-Bright Field; M-Merged).

The concentration dependent cancer cell specific dark toxicity was confirmed with confocal microscopy. While L929 cells were predominantly found to retain their cellular features with no significant loss of cell density, MDA MB 231 cells showed shrinkage of cell size. These observations support the cytotoxicity results. Previous

studies have shown that nanoparticles with high surface curvatures such as nanorods exhibit enhanced uptake efficiency than nanospheres⁶⁷ owing to stronger cell affinity due to more points of contact with plasma membrane than nanosphere.⁶⁸ It has also been indicated that cancer cells possess lower stiffness than the normal cells as investigated by atomic force microscopy.⁶⁹ Considering nanostars to possess both high surface curvature and their interaction with cancer cell membrane via pointed sharp ends could have caused subsequent cancer cell damage and decreased viability. Further, laser irradiation after 6 hours of incubation with SiO₂@Au NSs significantly distorted the cell membrane and caused visible nuclear fragmentation (Figure 4.10).

4.4. Plausible mechanism of photothermal effect of SiO₂@Au NSs

When light incidents on plasmonic nanostructures, these exhibit a variety of mechanisms during the excitation and decay processes of LSP.^{70, 71} During the decay process of hot carriers generated by excitation, electron-electron or electron-phonon interactions occur to achieve the energy distributions. These vibrational relaxations result in heat dissipation in the surrounding plasmonic nanostructures which is enough to carry out various thermal processes or thermal reactions. So, such type of nanostructures can act as an efficient agent for the photothermal effect for cancer therapy. The photothermal effect is more pronounced in the case of anisotropic shapes such as nanostars as discussed by Chatterjee et. al owing to their sharp tip heads.²⁷ The mechanistic pathway for the death of cancer cells using the photothermal effect of SiO₂@Au NSs on NIR laser illumination is depicted (Scheme 4.2).



Scheme 4.2. Schematic for the mechanism of the photothermal effect of SiO₂@Au NSs to kill cancer cells on laser illumination.

4.5. Conclusion

To sum up, we have created an easy-to-use, surfactant-free method for the synthesis of anisotropic core-shell nanostructures, wherein SiO₂ NPs serve as the core and Au NSs serve as the shell. The optical and structural characterizations demonstrated the successful synthesis of SiO₂@Au NSs with an average size of 140 ± 5 nm. The SiO₂@Au NSs was discovered to have good SERS performance in addition to having excellent biocompatibility and PT effect. Due to the generation of strong electromagnetic fields by the sharp tips of Au nanostar shell, the SERS EF of RhB dye using SiO₂@Au NSs as substrate was determined to be 1.37×10^6 . The branched SiO₂@Au NSs display strong SPR absorption in the near-infrared region, which makes them an excellent candidate for the PT effect. The SiO₂@Au NSs exhibit remarkable photothermal conversion efficiency of up to 72% which is higher than other Au nanostructures of comparable size, as well as excellent thermal stability. It was observed that local temperature rises in a concentration-dependent manner on irradiating SiO₂@Au NSs with 808 nm laser line. The local heat produced in proximity of SiO₂@Au NSs was utilized for photothermal eradication of breast cancer cells in vitro. These core-shell anisotropic nanostructures have the ability to be an attractive contender for SERS-based enhancements and photothermal therapy agents, in addition to their potential use as biosensors and catalysts.

Note:

- ✓ **Gagandeep Kaur**, Vishaldeep Kaur, Charanleen Kaur, Navneet Kaur, Asifkhan Shanavas, and Tapasi Sen “Design of silica@gold hybrid nanostars for enhanced SERS and photothermal effect” (**Revised manuscript submitted**).

References

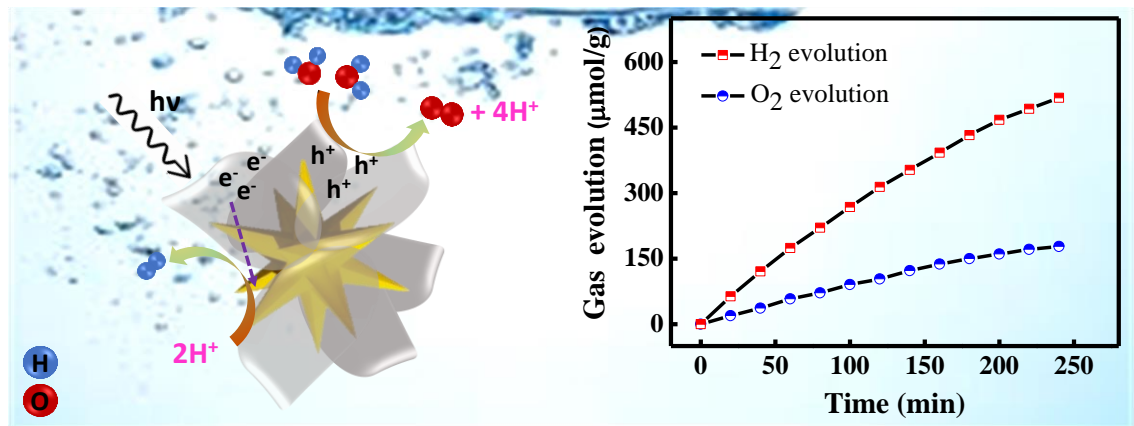
1. E. Hutter and J. H. Fendler, *Advanced Materials*, 2004, **16**, 1685-1706.
2. J. A. Schuller, E. S. Barnard, W. Cai, Y. C. Jun, J. S. White and M. L. Brongersma, *Nature Materials*, 2010, **9**, 193-204.
3. K. L. Kelly, E. Coronado, L. L. Zhao and G. C. Schatz, *Journal of Physical Chemistry B*, 2003, **107**, 668-677.
4. S. Underwood and P. Mulvaney, *Langmuir*, 1994, **10**, 3427-3430.
5. N. G. Khlebtsov and L. A. Dykman, *Journal of Quantitative Spectroscopy and Radiative Transfer*, 2010, **111**, 1-35.
6. R. Elghanian, J. J. Storhoff, R. C. Mucic, R. L. Letsinger and C. A. Mirkin, *Science*, 1997, **277**, 1078-1081.
7. L. Guerrini and D. Graham, *Chemical Society Reviews*, 2012, **41**, 7085-7107.
8. S. A. Pillai and M. Green, *Solar Energy Materials and Solar Cells*, 2010, **94**, 1481-1486.
9. J. Xue, C. Wang and Z. Ma, *Materials Chemistry and Physics*, 2007, **105**, 419-425.
10. S. Mandal and K. M. Krishnan, *Journal of Materials Chemistry*, 2007, **17**, 372-376.
11. Z. Lyu, M. Xie, E. Aldama, M. Zhao, J. Qiu, S. Zhou and Y. Xia, *ACS Applied Nano Materials*, 2019, **2**, 1533-1540.
12. C. Loo, A. Lin, L. Hirsch, M.-H. Lee, J. Barton, N. Halas, J. West and R. Drezek, *Technology in Cancer Research & Treatment*, 2004, **3**, 33-40.
13. S. Oldenburg, R. Averitt, S. Westcott and N. Halas, *Chemical Physics Letters*, 1998, **288**, 243-247.
14. B. J. Jankiewicz, D. Jamiola, J. Choma and M. Jaroniec, *Advances in Colloid and Interface Science*, 2012, **170**, 28-47.
15. H. Wang, D. W. Brandl, F. Le, P. Nordlander and N. J. Halas, *Nano Letters*, 2006, **6**, 827-832.
16. O. Peña, U. Pal, L. Rodríguez-Fernández and A. Crespo-Sosa, *JOSA B*, 2008, **25**, 1371-1379.
17. Y. Sun and Y. Xia, *Analyst*, 2003, **128**, 686-691.
18. E. Prodan, C. Radloff, N. J. Halas and P. Nordlander, *Science*, 2003, **302**, 419-422.
19. Y. Piao, A. Burns, J. Kim, U. Wiesner and T. Hyeon, *Advanced Functional Materials*, 2008, **18**, 3745-3758.
20. T. Pham, J. B. Jackson, N. J. Halas and T. R. Lee, *Langmuir*, 2002, **18**, 4915-4920.
21. K. Wang, Y. Wang, C. Wang, X. Jia, J. Li, R. Xiao and S. Wang, *RSC Advances*, 2018, **8**, 30825-30831.
22. Y. Li, L. Zu, G. Liu, Y. Qin, D. Shi and J. Yang, *Particle & Particle Systems Characterization*, 2015, **32**, 498-504.
23. S. J. Oldenburg, S. L. Westcott, R. D. Averitt and N. J. Halas, *The Journal of Chemical Physics*, 1999, **111**, 4729-4735.
24. S. Eustis and M. A. El-Sayed, *Chemical Society Reviews*, 2006, **35**, 209-217.
25. E. C. Le Ru, M. Meyer, E. Blackie and P. G. Etchegoin, *Journal of Raman Spectroscopy*, 2008, **39**, 1127-1134.
26. X. Wang, G. Li, Y. Ding and S. Sun, *RSC Advances*, 2014, **4**, 30375-30383.
27. H. Chatterjee, D. S. Rahman, M. Sengupta and S. K. Ghosh, *The Journal of Physical Chemistry C*, 2018, **122**, 13082-13094.
28. G. Xu, S. Liu, H. Niu and W. Lv, *RSC Advances*, 2014, **4**, 33986-33997.
29. H. Moustauoui, J. Saber, I. Djeddi, Q. Liu, A. T. Diallo, J. Spadavecchia, M. Lamy de la Chapelle and N. Djaker, *The Journal of Physical Chemistry C*, 2019, **123**, 17548-17554.

30. L. R. Hirsch, R. J. Stafford, J. A. Bankson, S. R. Sershen, B. Rivera, R. Price, J. D. Hazle, N. J. Halas and J. L. West, *Proceedings of the National Academy of Sciences*, 2003, **100**, 13549-13554.
31. B. E. Brinson, J. B. Lassiter, C. S. Levin, R. Bardhan, N. Mirin and N. J. Halas, *Langmuir*, 2008, **24**, 14166-14171.
32. Q. Li, W. Zhang, D. Zhao and M. Qiu, *Plasmonics*, 2014, **9**, 623-630.
33. A. A. Semenova, E. A. Goodilin, N. A. Brazhe, V. K. Ivanov, A. E. Baranchikov, V. A. Lebedev, A. E. Goldt, O. V. Sosnovtseva, S. V. Savilov, A. V. Egorov, A. R. Brazhe, E. Y. Parshina, O. G. Luneva, G. V. Maksimov and Y. D. Tretyakov, *Journal of Materials Chemistry*, 2012, **22**, 24530-24544.
34. D. R. Ward, N. K. Grady, C. S. Levin, N. J. Halas, Y. Wu, P. Nordlander and D. Natelson, *Nano Letters*, 2007, **7**, 1396-1400.
35. S. Dodson, M. Haggui, R. Bachelot, J. Plain, S. Li and Q. Xiong, *The Journal of Physical Chemistry Letters*, 2013, **4**, 496-501.
36. X. Yao, S. Jiang, S. Luo, B.-W. Liu, T.-X. Huang, S. Hu, J. Zhu, X. Wang and B. Ren, *ACS Applied Materials & Interfaces*, 2020, **12**, 36505-36512.
37. S. Pande, S. K. Ghosh, S. Praharaj, S. Panigrahi, S. Basu, S. Jana, A. Pal, T. Tsukuda and T. Pal, *The Journal of Physical Chemistry C*, 2007, **111**, 10806-10813.
38. W. Stöber, A. Fink and E. Bohn, *Journal of Colloid and Interface Science*, 1968, **26**, 62-69.
39. D. G. Duff, A. Baiker and P. P. Edwards, *Langmuir*, 1993, **9**, 2301-2309.
40. Y. Xu, M. P. Konrad, J. L. Trotter, C. P. McCoy and S. E. J. Bell, *Small*, 2017, **13**, 1602163.
41. X. Liu, B. Li, F. Fu, K. Xu, R. Zou, Q. Wang, B. Zhang, Z. Chen and J. Hu, *Dalton Transactions*, 2014, **43**, 11709-11715.
42. L. Singh, S. Bhattacharyya, G. Mishra and S. Ahalawat, *Applied Nanoscience*, 2011, **1**, 117-122.
43. Y. Wu, S. Chen, Y. Liu, Z. Lu, S. Song, Y. Zhang, C. Xiong and L. Dong, *Journal of Materials Science & Technology*, 2020, **50**, 139-146.
44. A. E. Di Mauro, V. Villone, C. Ingrosso, M. Corricelli, L. Oria, F. Pérez-Murano, A. Agostiano, M. Striccoli and M. L. Curri, *Journal of Materials Science*, 2014, **49**, 5246-5255.
45. D. Shao, H. Sun, M. Yu, J. Lian and S. Sawyer, *Nano Letters*, 2012, **12**, 5840-5844.
46. T. Xia, H. Luo, S. Wang, J. Liu, G. Yu and R. Wang, *CrystEngComm*, 2015, **17**, 4200-4204.
47. T. D. T. Ung, T. H. Nguyen and Q. L. Nguyen, *Advances in Natural Sciences: Nanoscience and Nanotechnology*, 2016, **7**, 035013.
48. J. Zhang, X. Li, X. Sun and Y. Li, *The Journal of Physical Chemistry B*, 2005, **109**, 12544-12548.
49. F. Adar, E. Lee, S. Mamedov and A. Whitley, *Microscopy and Microanalysis*, 2010, **16**, 360-361.
50. E. Nalbant Esenturk and A. R. Hight Walker, *Journal of Raman Spectroscopy*, 2009, **40**, 86-91.
51. G. Kaur, S. Tanwar, V. Kaur, R. Biswas, S. Saini, K. K. Haldar and T. Sen, *Journal of Materials Chemistry C*, 2021, **9**, 15284-15294.
52. S. Tanwar, K. K. Haldar and T. Sen, *Journal of the American Chemical Society*, 2017, **139**, 17639-17648.
53. A. Ceja-Fdez, T. López-Luke, A. Torres-Castro, D. A. Wheeler, J. Z. Zhang and E. De la Rosa, *RSC Advances*, 2014, **4**, 59233-59241.
54. A. Childs, E. Vinogradova, F. Ruiz-Zepeda, J. J. Velazquez-Salazar and M. Jose-Yacaman, *Journal of Raman Spectroscopy*, 2016, **47**, 651-655.

55. M. Ujihara, N. M. Dang and T. Imae, *Sensors (Basel)*, 2017, **17**.
56. H. Yuan, A. M. Fales, C. G. Khoury, J. Liu and T. Vo-Dinh, *Journal of Raman Spectroscopy*, 2013, **44**, 234-239.
57. F. Zhang, X. Yang, D. Wang, L. Yu, Y. Hu, A. Zhu, C. Zhang, Y. Zheng, T. Yin, Y. Zhang and W. Xie, *Journal of Raman Spectroscopy*, 2022, **53**, 1227-1237.
58. Q. Su, X. Ma, J. Dong, C. Jiang and W. Qian, *ACS Applied Materials & Interfaces*, 2011, **3**, 1873-1879.
59. S. Choi, M. Ahn and J. Kim, *Analytica Chimica Acta*, 2013, **779**, 1-7.
60. J. Zhu, J. Gao, J.-J. Li and J.-W. Zhao, *Applied Surface Science*, 2014, **322**, 136-142.
61. J. Depciuch, M. Stec, A. Maximenko, M. Pawlyta, J. Baran and M. Parlinska-Wojtan, *International Journal of Molecular Sciences*, 2019, **20**, 5011.
62. C. Ayala-Orozco, C. Urban, M. W. Knight, A. S. Urban, O. Neumann, S. W. Bishnoi, S. Mukherjee, A. M. Goodman, H. Charron, T. Mitchell, M. Shea, R. Roy, S. Nanda, R. Schiff, N. J. Halas and A. Joshi, *ACS Nano*, 2014, **8**, 6372-6381.
63. H. Chen, L. Shao, T. Ming, Z. Sun, C. Zhao, B. Yang and J. Wang, *Small*, 2010, **6**, 2272-2280.
64. V. P. Pattani and J. W. Tunnell, *Lasers in Surgery and Medicine*, 2012, **44**, 675-684.
65. J. R. Cole, N. A. Mirin, M. W. Knight, G. P. Goodrich and N. J. Halas, *The Journal of Physical Chemistry C*, 2009, **113**, 12090-12094.
66. P. Huang, J. Lin, W. Li, P. Rong, Z. Wang, S. Wang, X. Wang, X. Sun, M. Aronova, G. Niu, R. D. Leapman, Z. Nie and X. Chen, *Angew Chem Int Ed Engl*, 2013, **52**, 13958-13964.
67. H. Dong, X. Xu, L. Wang and R. Mo, *Biomaterials Science*, 2020, **8**, 2344-2365.
68. S. Dasgupta, T. Auth and G. Gompper, *Nano Letters*, 2014, **14**, 687-693.
69. S. E. Cross, Y.-S. Jin, J. Rao and J. K. Gimzewski, *Nature Nanotechnology*, 2007, **2**, 780-783.
70. L. V. Besteiro, P. Yu, Z. Wang, A. W. Holleitner, G. V. Hartland, G. P. Wiederrecht and A. O. Govorov, *Nano Today*, 2019, **27**, 120-145.
71. E. Kazuma and Y. Kim, *Angewandte Chemie*, 2019, **131**, 4850-4858.

Chapter 5

Design of plasmonic - semiconductor hybrid nanostructures for photochemical water splitting



5.1. Introduction

Research into developing noble metal and semiconductor composite nanostructures for various applications, such as photocatalysis, gas sensing, fuel generation, and water splitting has increased in recent years.¹⁻³ Photocatalysts are crucial in the photocatalytic process because they convert the energy from light into chemical reactions, either the synthesis or breakdown of molecules. The photocatalytic material should have the right valence and conduction band positions and a large enough band gap to facilitate redox reactions via electron-hole pairs created by photoexcitation. Numerous photocatalysts have already been intensively designed to effectively utilize solar energy for water splitting which is an alternative way for production of hydrogen energy. Since ZnO can be grown into nanoparticles of varying morphologies via low-cost chemical routes, it has emerged as a promising photocatalyst.⁴ To effectively convert solar light in useful energy, it is crucial to find ways to increase light absorption and minimize charge recombination. This can be achieved by using highly efficient photocatalysts which segregate electron-hole pairs easily and facilitate their transfer to the liquid/semiconductor junction and have abundance of catalytically active sites that allow the water splitting half-reactions to proceed with low activation barriers. In order to overcome these limitations, semiconductors have been integrated mostly with plasmonic metal nanostructures.⁵⁻⁷ In the context of photocatalytic water splitting, plasmonic Au nanoparticles, due to its remarkable optical, electrical and catalytic properties,⁸ are integrated with semiconductors. Silva et al. found that P25 titania decorated with Au nanoparticles showed better photocatalytic activity for H₂ generation as compared to TiO₂ only.⁹ These semiconductors-plasmonic integrated nanostructures have exhibited superior photocatalytic activity in either the oxygen or hydrogen evolution.¹⁰⁻¹² Wu et al. fabricated Au/TiO₂ dumbbell shaped nanorods which were further exploited for H₂ evolution from water reduction under visible and near infrared light.¹³ It was deduced that Au/TiO₂ dumbbell shaped nanorods possess superior performance for H₂ evolution than physical mixture of Au nanorods and amorphous TiO₂. Research by Haro et al., in contrast to the aforementioned studies, has shown that

the major impact of Au nanoparticles to the improved photocurrent has a catalytic origin, as evidenced by the faster charge transfer kinetics.¹⁴

It has been demonstrated that the presence of noble metal nanoparticles increases the overall efficiency of photocatalysts due to the efficient charge transfer that occurs as a direct result of the formation of Schottky junctions at the metal-semiconductor interface. Hence, interfacial area effects the coupling between plasmonic nanomaterial and semiconductor components which results in a synergy of properties in nanohybrids. Consequently, Au-ZnO nanocomposites with a variety of morphologies are being investigated for use in photocatalysis.¹⁵ Noble metal@semiconductor core-shell nanostructures provide 3D contact between the core and shell, resulting in a wider interfacial area, which results in strengthening the direct interfacial electronic exchange between the core and shell. Also, development of Au@semiconductor core-shell nanostructures is an innovative approach to shield the Au nanocrystal core from agglomeration and chemical corrosion during harsh reaction conditions and provide the maximum and profound interface between Au and the semiconductor, which is essential for separation of charge carriers and their transport.^{16, 17} While many investigations into ZnO with Au nanoparticles have been conducted,¹⁸⁻²² but still there is a lot of room to investigate simple and rational synthetic strategies for obtaining these core-shell nanomaterials which provide significantly improved photocatalytic activity especially in case of photocatalytic water splitting. Absorption of UV light, creation of electron hole pairs, transfer of electrons from conduction band of ZnO to metal and catalytic reactions by these hybrid nanocomposites lead to the evolution of H₂ or O₂ comprise the mechanism for photo-catalytic water splitting. Hence, these integrated nanocomposites will help in understanding optical absorption, charge carrier excitation, as well as transfer in photocatalytic applications

Motivated by the aforementioned concepts, this chapter of the thesis provides a new synthetic approach to design a novel nanocomposite (NC) of ZnO nanopetals with Au nanostar at its core (Au@ZnO NC). Further confirmation of the prepared NCs was done by using different optical and structural characterizations. The synthesized Au@ZnO

NCs was utilized as a catalyst for photocatalytic water splitting for H₂ and O₂ production.

5.2. Experimental Section

5.2.1. Materials

Zinc Nitrate hexahydrate (Zn(NO₃)₂·6H₂O), Sodium Hydroxide (NaOH), Gold chloride trihydrate (HAuCl₄·3H₂O), Trisodium citrate dihydrate (TSC), Silver nitrate (AgNO₃), L- Ascorbic acid (AA), Hydrochloric acid (HCl), and Sodium dodecyl sulphate (SDS) were purchased from Sigma-Aldrich. All the reagents were used without further purification. Milli-Q (MQ) water was used during the experiment. Glass apparatus was cleaned thoroughly with aqua regia and rinsed with MQ water.

5.2.2. Experimental procedures

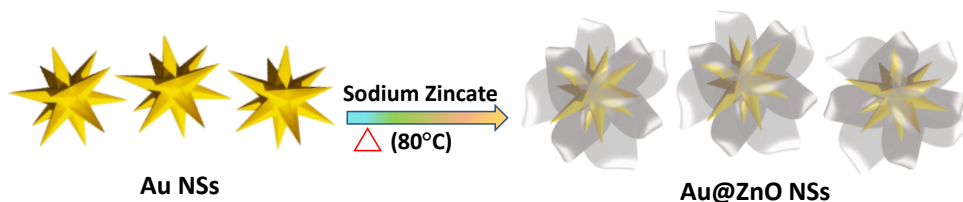
5.2.2.1. Synthesis of Au nanostars

We have followed the same procedure as mentioned in chapter 3 of the thesis for the synthesis of Au nanostars.

5.2.2.2. Synthesis of Au@ZnO NCs

Au@ZnO NCs, a novel metal-semiconductor nanostructures, were synthesized in aqueous phase under subtle conditions, without the inclusion of any corrosive chemicals or severe reaction conditions (Scheme 5.1). Two key concepts underpin our approach: first, to use Au nanostars as the core material, and second, to use a solution of Na₂(ZnO)₂ as the source for ZnO to grow shell in nanopetal shape around the core. Before initiating the synthesis of the Au@ZnO NCs, the solution of sodium zincate needed to be prepared. In order to accomplish this, 10 mL of 10 mM solution of Zn(NO₃)₂·6H₂O was prepared and 2 M of NaOH solution was added under stirring. On addition of NaOH solution, white precipitates of Zn(OH)₂ were formed in the solution. These white precipitates were dissolved by adding excessive amount of 2 M NaOH solution which led to the formation of sodium zincate (Na₂ZnO₂). Now, to prepare

Au@ZnO NCs, 1 mL of Na_2ZnO_2 solution (aged for 24 hours) was diluted with 4 mL of H_2O and added to 10 mL solution of Au nanostars prepared in section 2.2 under stirring at 80°C . After 30 min, the heat was turned off, and the reaction mixture was stirred overnight. Next, the reaction mixture was centrifuged at 3000 RPM for 10 min at 20°C , collected the residue, redispersed it in H_2O and lyophilized it to obtain the powder form of Au@ZnO NCs.



Scheme 5.1. Schematic depiction for synthesis of Au@ZnO NCs.

5.2.2.3. Photocatalytic water splitting experiments

For the photocatalytic H_2 production, 30 mg of Au/ZnO photocatalyst was well-dispersed in 50 mL of aqueous solution containing 0.3 M Na_2SO_3 which serves as hole scavenger. The scavengers can consume the photo-generated hole on the surface of the catalysts and prevent the recombination of photo-generated electrons and holes. For the photocatalytic O_2 evolution, 30 mg of catalyst was well-dispersed in 50 mL of aqueous solution containing 0.1 M $\text{Na}_2\text{S}_2\text{O}_8$ which acts as sacrificial electron acceptor.

The prepared Au nanostars and Au@ZnO NCs were characterized by UV-Vis spectrophotometer, TEM, XPS, and PXRD as mentioned in chapter 2 of the thesis. The photocurrent response was measured with using a Metrohm Autolab (Multichannel-204) connected to a standard three-electrode electrochemical cell using Nova 2.1.4 software as described in chapter 2. For this, a standard three-electrode framework with a 0.05 M Na_2SO_4 electrolyte solution, Pt wire as the counter electrode and an Ag/AgCl (3 M KCl) electrode as the reference electrode was employed.

5.3. Results and discussion

5.3.1. Optical and structural characterizations of Au@ZnO NCs

The process of ZnO shell around the Au nanostar core is monitored by UV-Vis absorption/extinction spectroscopy. Figure 5.1 shows the UV-Vis extinction spectra of prepared pure Au nanostars, ZnO nanopetals without core, and core-shell Au@ZnO NCs which are formed by mixing of Na_2ZnO_2 and Au nanostars after heat treatment. An extinction band position at 730 nm is observed for Au nanostars, which is redshifted to 800 nm after the formation of ZnO shell in nanopetal form. The formation of ZnO shell on Au NPs cores is responsible for this red shift because their refractive index (2.003) is larger than that of water (1.33).²³ Extinction position of pure ZnO is found at 350 nm which is attributed to excitonic band²⁴⁻²⁶ of pure ZnO nanoparticles. The extinction peak of ZnO is intact in Au@ZnO NCs indicating the incorporation of Au nanostars and ZnO nanopetals. In Au@ZnO NCs, the formation of a thick ZnO shell may account for the lower extinction intensity measured for Au nanostars.²³

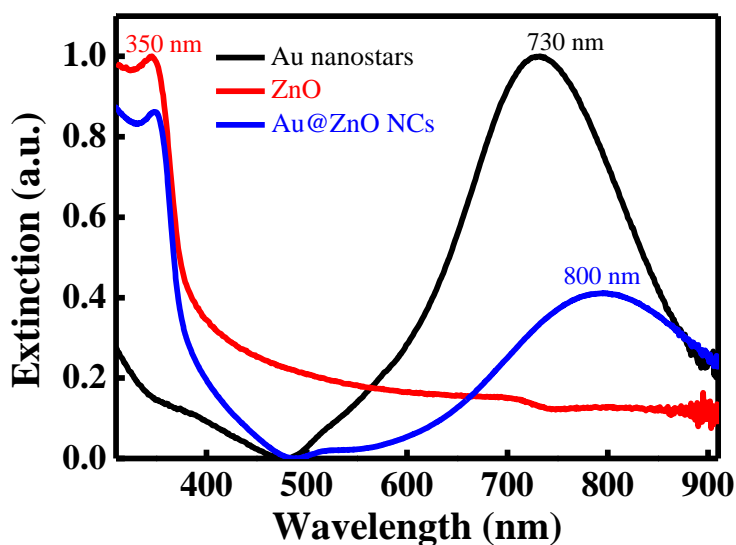


Figure 5.1. Normalized UV-vis extinction spectra of Au nanostars (black), ZnO nanoparticles (red), and Au@ZnO NCs (blue).

The crystalline nature and crystal faces of Au@ZnO NCs were analyzed by powder X-ray diffraction (PXRD) study. As can be seen in Figure 5.2, Au@ZnO NCs exhibit characteristic diffraction peaks at $2\theta = 38.12^\circ$, 44.28° , 64.53° , and 77.56° ,

corresponding to (111), (200), (220), and (311), respectively, indicating the existence of Au (JCPDS no. 01-1174).^{20, 27} Other peaks have been found at angles 31.70°, 34.80°, 36.22°, 47.60°, 56.60°, 62.76°, 66.43°, 67.95°, and 69.15° corresponding to (100), (002), (101), (102), (110), (103), (200), (112), and (201), respectively. These peaks indicate the presence of ZnO (JCPDS 36-1451)^{20, 28} in Au@ZnO NCs. In nanocomposites of Au@ZnO, the presence of peaks corresponding to both Au and ZnO, as well as the sharpness of those peaks, indicate that both components are present, and also the nanocomposites are of a highly crystalline nature. Hence, the nanocomposites are composed of face centered cubic phase of Au and hexagonal wurtzite structure of ZnO. There was also no detectable change in the position of any diffraction peak or the presence of any other crystalline impurities.

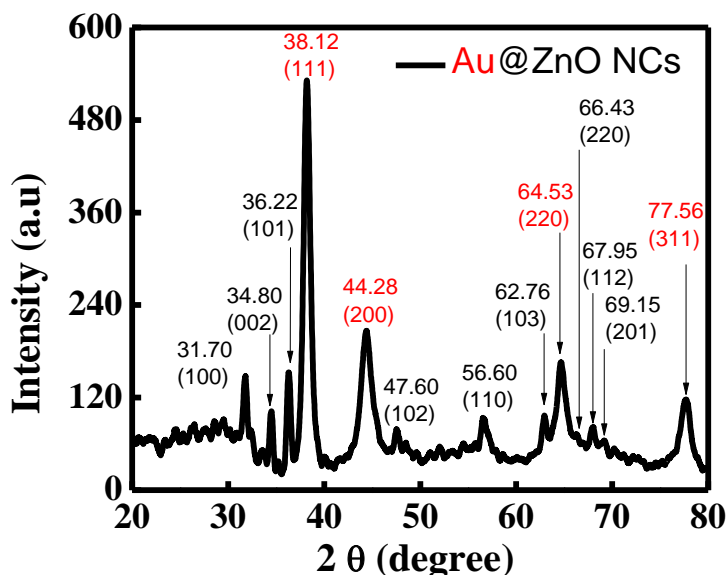


Figure 5.2. Powder XRD pattern of Au@ZnO NCs.

The chemical composition and electronic structure of the Au@ZnO NCs were analyzed using X-ray photoelectron spectroscopy (XPS). Figure 5.3a shows the wide XPS survey spectrum, which clearly displays the elemental peaks of Zn, Au, and O. High-resolution XPS spectra of the Au 4f (Figure 5.3b) shows two peaks at 84.01 eV and 87.66 eV corresponding to Au 4f_{7/2} and Au 4f_{5/2}, respectively. This binding energy attributes to the presence of metallic Au with zero oxidation state. The other two peaks 89.20 eV and 91.41 eV corresponds to Zn 3p_{3/2} and Zn 3p_{1/2}. These peaks are ascribed to +2 oxidation

state of Zn.²⁶ Also, the peaks in Figure 5.3c are positioned at 1021.63 and 1044.75 eV, which are attributed to the Zn 2p_{3/2} and Zn 2p_{1/2} of Zn⁺².²⁹ In Figure 5.3d, the peak positioned at 530.40 eV binding energy is attributed to lattice oxygen present in ZnO.³⁰ Moreover, the oxygen species present in the hydroxyl groups which are adsorbed on surface of Au@ZnO NCs are responsible for the peak centred at binding energy of 532.01 eV.^{30, 31} Hence, XPS study reveals that the Au@ZnO NCs are purely the combination of components Au and ZnO.

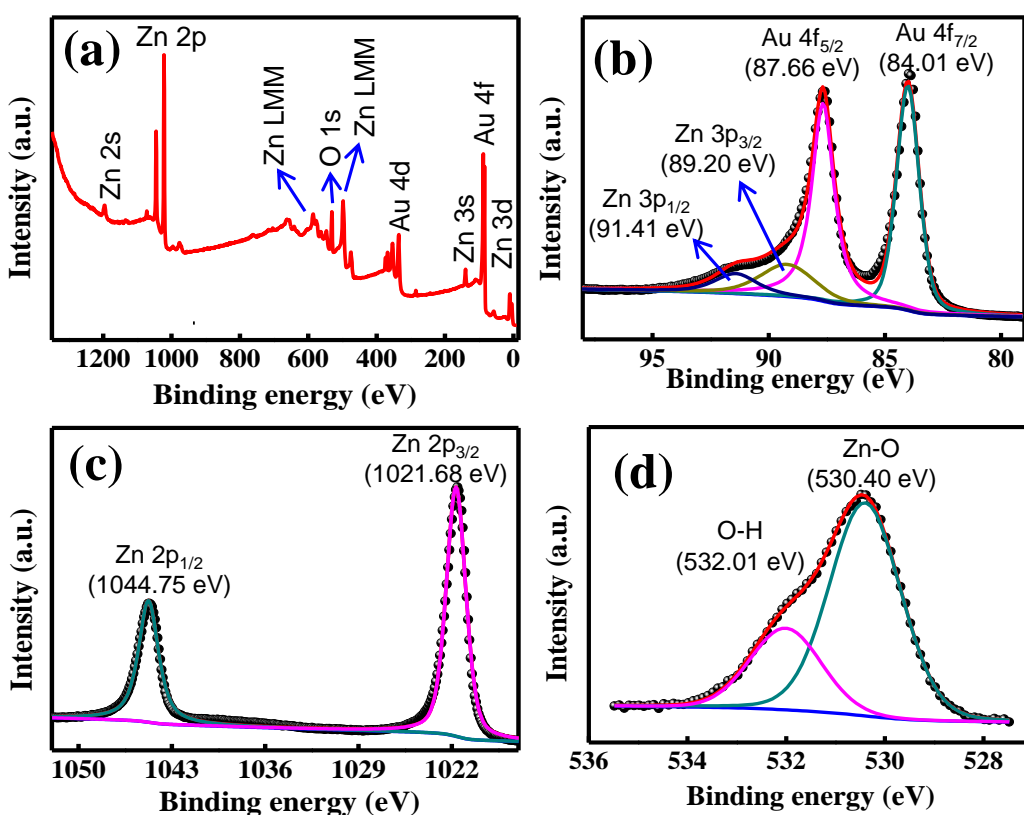


Figure 5.3. (a) wide XPS survey spectrum of Au@ZnO NCs, High resolution XPS spectra of (b) Au 4f, Zn 3p, (c) Zn 2p, and (d) O 1s elements present in Au@ZnO NCs.

Transmission electron microscopy (TEM) was used to examine the morphology, size, and composition of as synthesized Au@ZnO NCs. Figures 5.4a and b show TEM images of Au@ZnO NCs, with dark contrast at the core corresponding to the Au nanostar core and light contrast corresponding to the ZnO in nanopetal shape surrounding the core component. It has been observed that as synthesized Au@ZnO

NCs, without size sorting, are highly monodisperse in nature. Overall, the average size of Au@ZnO NCs was estimated to be 125 ± 10 nm, while the average size of the Au nanostar core was found to be 80 ± 5 nm. Figure 5.4c and d of Au@ZnO NC shows the lattice d spacing of 2.42\AA corresponding to (101) plane indicating that ZnO atoms are arranged in a hexagonal wurtzite structure.³²

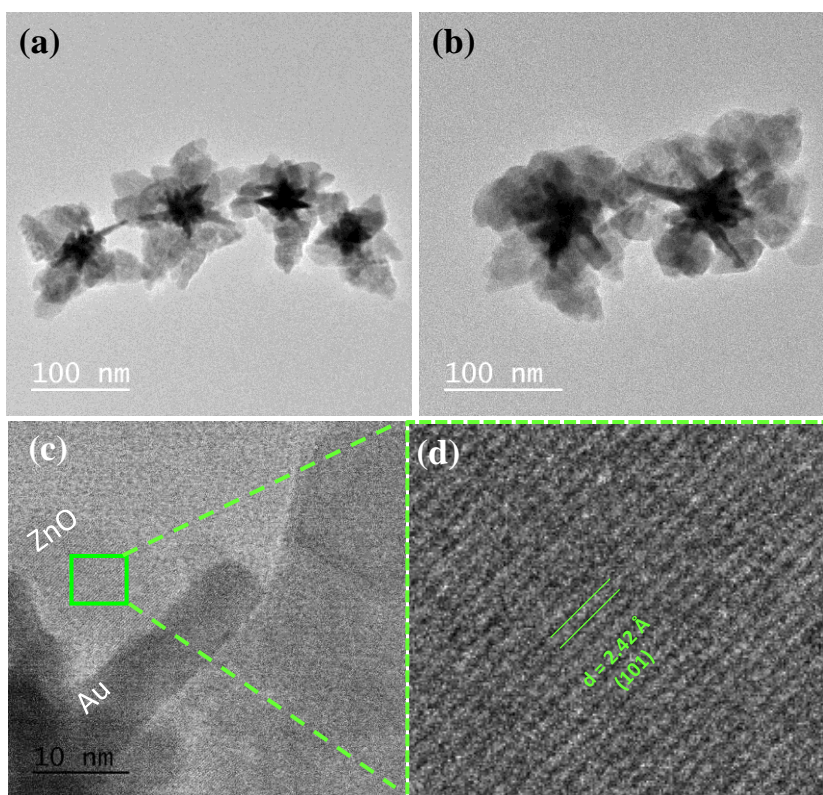


Figure 5.4. (a-b) TEM images of Au/ZnO core shell nanostructures, (c) HRTEM image of Au/ZnO, and (d) Zoom in image showing the inter planer d spacing of marked area in (c).

The elemental composition of Au@ZnO NCs was further confirmed by Energy dispersive X-Ray (EDX) spectrum shown in Figure 5.5. It was confirmed that elements Au, Zn, and O are present in Au@ZnO NCs (Copper grid is the source of the Cu signal in Figure 5.5). In order to gain a better understanding of the composition of these Au@ZnO NCs, high-angle annular dark-field scanning transmission electron microscopy (TEM) was also performed (HAADF-STEM) and depicted in Figure 5.6. Element mapping analysis clearly demonstrated that Au, Zn, and O are the primary

constituents present in the Au@ZnO NCs (Figures 5.6b-5.6d), and it was also observed that the ZnO components are dispersed all over the core Au nanostar.

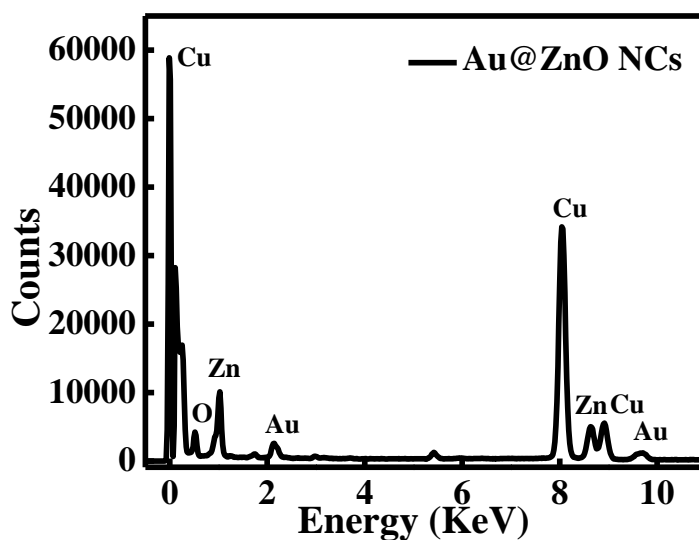


Figure 5.5. EDX spectrum of Au@ZnO NCs.

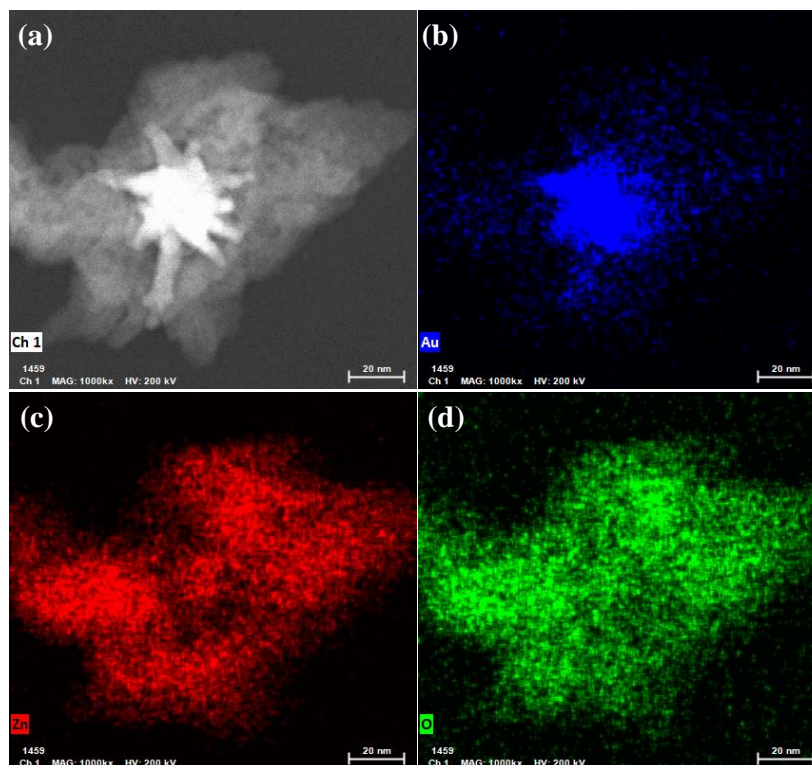


Figure 5.6. (a) HAADF-STEM image of single Au@ZnO NC and corresponding EDX elemental mapping of Au (b), Zn (c), and O (d).

5.3.2. Photocatalytic water splitting

5.3.2.1. Au@ZnO NCs as photocatalyst for H₂ and O₂ evolution reactions

With the stable dispersion of Au@ZnO NCs, we have performed the photocatalytic water splitting under 360 nm laser irradiation for H₂ and O₂ evolution using Na₂SO₃ and Na₂S₂O₈ as sacrificial agents, respectively. The time-dependent photocatalytic oxygen and hydrogen evolutions for Au@ZnO NCs are depicted in the Figure 5.7a. The oxygen and hydrogen evolution efficiencies using Au@ZnO NCs as a catalyst were significantly increased to 19, and 63 $\mu\text{mol/g}$ after 20 min of irradiation, respectively. After 4 h, the oxygen and hydrogen evolution efficiencies were observed to be 177, and 518 $\mu\text{mol/g}$, respectively. It is clear from this observation that the synthesized Au@ZnO NCs act as good photocatalyst for the H₂ and O₂ productions from water splitting. In addition, the kinetics of H₂ evolution on this catalyst is investigated by means of electrochemical impedance spectroscopy (EIS) when exposed to light. Figure 5.7b depicts a Nyquist plot of an EIS spectrum, and the inset of this figure proposes a simplified equivalent circuit that can be used to fit this spectrum. The charge transfer resistance was determined to be 33.46 ohm. A lower charge transfer resistance indicates a higher rate of charge transfer using Au@ZnO NCs photocatalyst during photocatalytic water splitting.

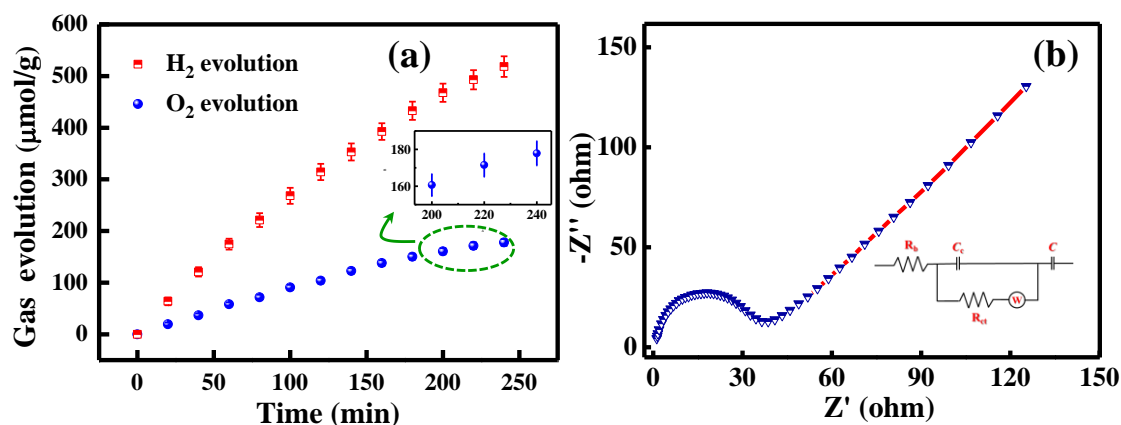


Figure 5.7. (a) Time-dependent photocatalytic hydrogen and oxygen gas production profiles of Au@ZnO NCs (Error bars indicate standard deviation for three measurements), and (b) Impedance spectrum of Au@ZnO NCs.

5.3.2.2. Recycling test of catalyst Au@ZnO NCs for H₂ and O₂ production activity

Moreover, recycling test was performed on the both oxygen and hydrogen production activity of Au/ZnO nanostructure to evaluate the stability of the catalyst. After five cycles, there is no considerable decrease observed in the H₂ production (Figure 5.8a), whereas 4.4% decrease in O₂ production efficiency was observed (Figure 5.8b), indicating the good stability of the catalyst during the photocatalytic water splitting.

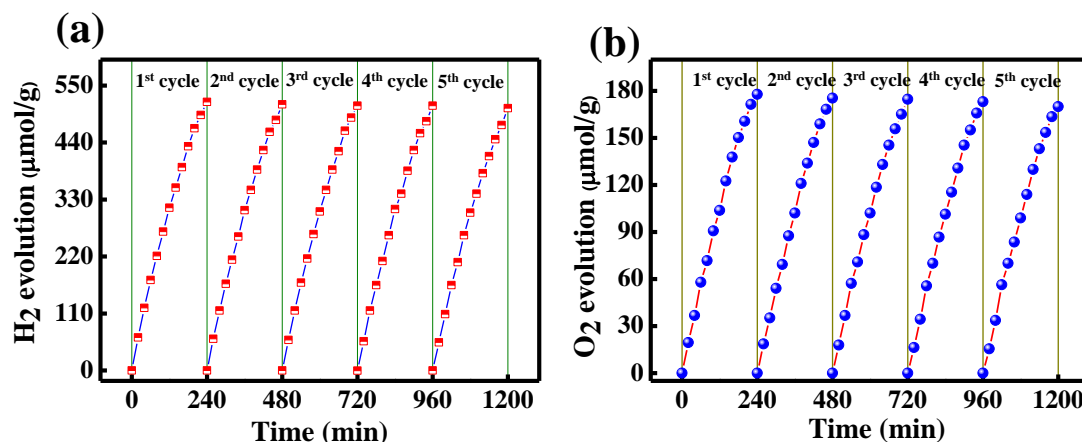


Figure 5.8. Stability of Au@ZnO NCs for photocatalytic H₂ (a), and O₂ gas production (b) for five cycles.

5.3.3. Plausible mechanism for the photocatalytic water splitting

To get mechanistic insights for the photocatalytic water splitting into H₂ and O₂ using Au@ZnO NCs, it is important to have idea about the valence band (VB) and conduction band (CB) alignments within the catalyst. For this, the Tauc plot of $(\alpha h\nu)^2$ vs $h\nu$ was plotted for the calculation of band gap energy of Au@ZnO NCs and it was estimated that optical band gap energy between VB and CB was 3.31 eV (Figure 5.9a). Now, to know the position of Fermi level (E_f) or work function (ϕ), ultraviolet photoelectron spectroscopy (UPS) was carried out and ϕ was found to be 4.17 eV (Figure 5.9b) and further to evaluate the position of VB from E_f , valence band scan from X-ray photoelectron spectroscopy (XPS) was recorded and position of valence band was found to be 2.03 eV (Figure 5.9c).

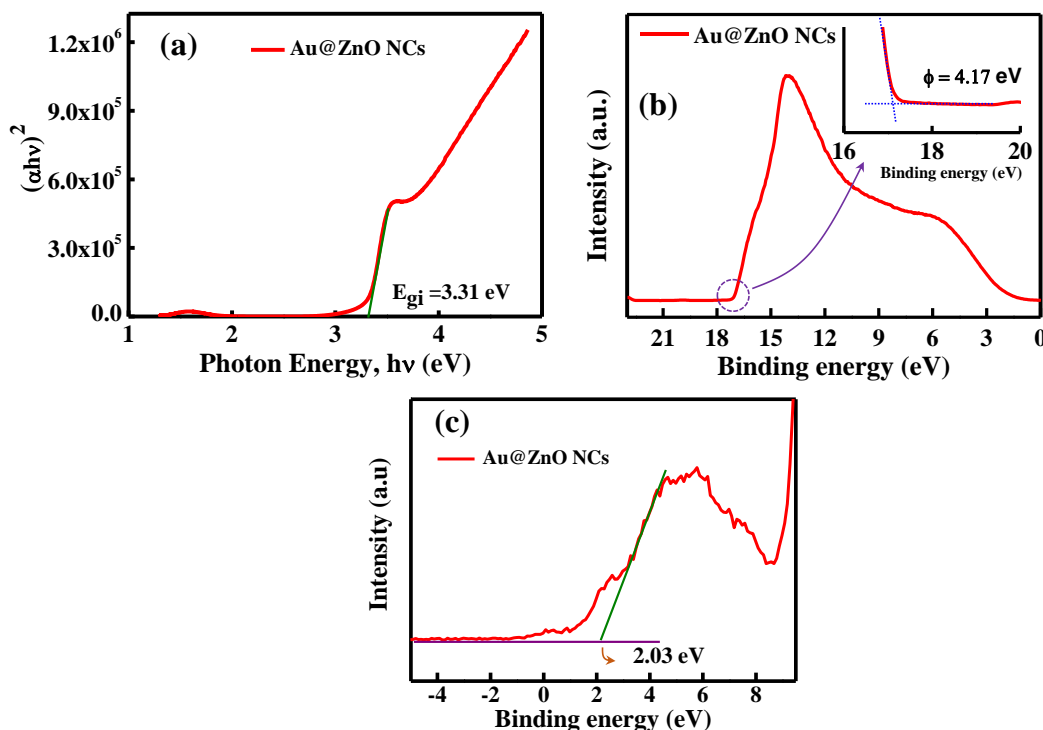


Figure 5.9. (a) Tauc plot indicating optical band gap, (b) UPS spectrum indicating work function, and XPS valence band spectrum indicating position of VB from E_f of catalyst Au@ZnO NC.

On the basis of the above observations, the possible mechanism of the photocatalytic water splitting for H_2 and O_2 evolution using photocatalyst Au@ZnO NC is elucidated based on the alignments of bands of Au@ZnO NC depicted in Figure 5.10.^{33, 34} As the water splitting reaction takes place in two half reactions: H_2 evolution reaction and O_2 evolution reaction. Under UV light illumination, photogenerated electrons are created in the VB of ZnO and travel through the nanocomposite to the CB, leaving behind positive holes. Multiple consumers exist for these electrons. They can either combine with the material's internal voids and surface species to form new particles, or they can react with protons to yield H_2 gas. For the photocatalytic H_2 production, Na_2SO_3 serves as hole scavenger for the holes left behind in VB (Figure 5.10a). As the E_f lies lower than the CB, the electrons also transfer from CB to Au which acts as a sink for electrons. The electrons accumulated in the Au are being utilized for the H_2 production. For the O_2 evolution, $Na_2S_2O_8$ serves as electron scavenger for the electrons in CB of ZnO and E_f of Au. The holes left behind in the VB are being utilized for the O_2 evolution (Figure

5.10b). Conclusions drawn from the aforementioned indicate that the hydrogen and oxygen production rates can be significantly increased by using Au as a sink for electrons to effectively suppress the recombination of electrons and holes.

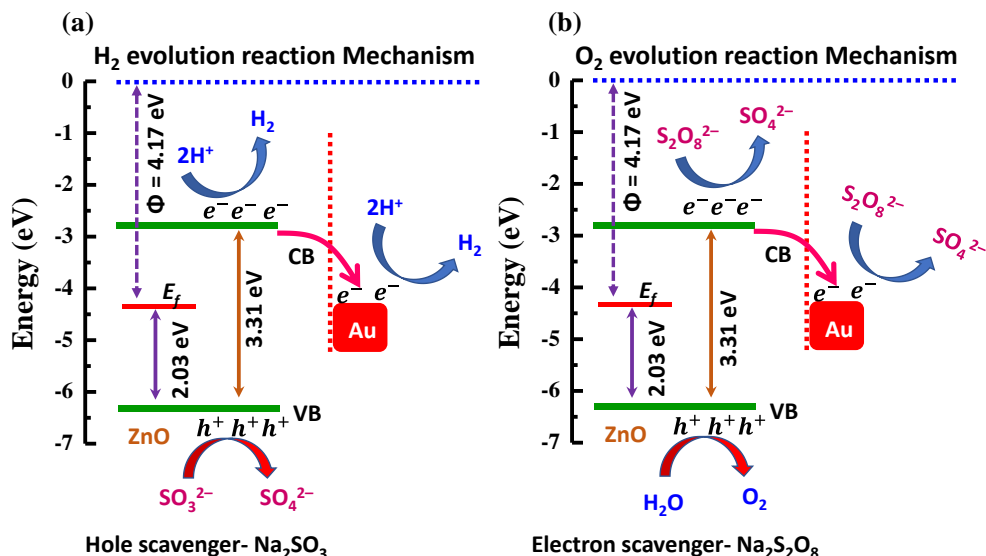


Figure 5.10. Schematic diagram of band alignments in Au@ZnO NC and mechanism of photo-generated charge separation for (a) H₂ evolution reaction, and (b) O₂ evolution reaction.

5.3.4. Conclusion

In conclusion, a simple solution phase methodology was used to successfully synthesize a petal-shaped Au@ZnO hybrid nanocomposite which are further confirmed with optical and structural characterizations. The prepared catalyst was used for photocatalytic water splitting under light illumination. Au@ZnO NCs exhibited hydrogen and oxygen evolution up to 518 and 177 μmol g⁻¹, respectively. Charge separation in ZnO shells was significantly accelerated due to presence of Au, which acts as electron sink. Because of this, the photocatalyst was effective at producing H₂ and O₂. In this study, Au@ZnO NCs were found to be promising for photocatalytic water splitting, which could have significant implications for the field of energy conversion.

Note:

✓ This manuscript is under preparation.

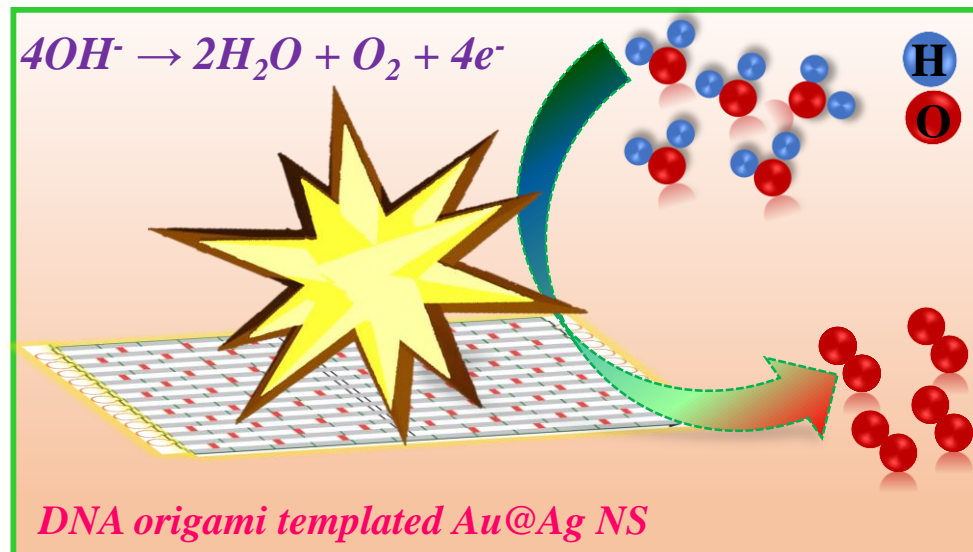
References

1. M. Valenti, M. Jonsson, G. Biskos, A. Schmidt-Ott and W. Smith, *Journal of Materials Chemistry A*, 2016, **4**, 17891-17912.
2. W. Hou and S. B. Cronin, *Advanced Functional Materials*, 2013, **23**, 1612-1619.
3. H. Liu, Y. Hu, Z. Zhang, X. Liu, H. Jia and B. Xu, *Applied Surface Science*, 2015, **355**, 644-652.
4. C. Acar, I. Dincer and G. F. Naterer, *International Journal of Energy Research*, 2016, **40**, 1449-1473.
5. A. Primo, T. Marino, A. Corma, R. Molinari and H. Garcia, *Journal of the American Chemical Society*, 2011, **133**, 6930-6933.
6. J.-J. Chen, J. C. Wu, P. C. Wu and D. P. Tsai, *The Journal of Physical Chemistry C*, 2011, **115**, 210-216.
7. S. Linic, P. Christopher and D. B. Ingram, *Nature Materials*, 2011, **10**, 911-921.
8. Y. Tan, Y. Zhang, L. Kong, L. Kang and F. Ran, *Journal of Alloys and Compounds*, 2017, **722**, 1-7.
9. C. U. Gomes Silva, R. Juárez, T. Marino, R. Molinari and H. García, *Journal of the American Chemical Society*, 2011, **133**, 595-602.
10. J. Zhang, X. Jin, P. I. Morales-Guzman, X. Yu, H. Liu, H. Zhang, L. Razzari and J. P. Claverie, *ACS Nano*, 2016, **10**, 4496-4503.
11. E. Ha, L. Y. S. Lee, J. Wang, F. Li, K.-Y. Wong and S. C. E. Tsang, *Advanced Materials*, 2014, **26**, 3496-3500.
12. E. Ha, L. Y. S. Lee, H.-W. Man, S. C. E. Tsang and K.-Y. Wong, *ACS Applied Materials & Interfaces*, 2015, **7**, 9072-9077.
13. B. Wu, D. Liu, S. Mubeen, T. T. Chuong, M. Moskovits and G. D. Stucky, *Journal of the American Chemical Society*, 2016, **138**, 1114-1117.
14. M. Haro, R. Abargues, I. Herraiz-Cardona, J. Martínez-Pastor and S. Giménez, *Electrochimica Acta*, 2014, **144**, 64-70.
15. N. Zhang, S. Liu, X. Fu and Y.-J. Xu, *The Journal of Physical Chemistry C*, 2011, **115**, 9136-9145.
16. D. Zheng, X. Pang, M. Wang, Y. He, C. Lin and Z. Lin, *Chemistry of Materials*, 2015, **27**, 5271-5278.
17. C. Fang, H. Jia, S. Chang, Q. Ruan, P. Wang, T. Chen and J. Wang, *Energy & Environmental Science*, 2014, **7**, 3431-3438.
18. H. J. Jung, R. Koutavarapu, S. Lee, J. H. Kim, H. C. Choi and M. Y. Choi, *Journal of Alloys and Compounds*, 2018, **735**, 2058-2066.
19. B. Li, R. Wang, X. Shao, L. Shao and B. Zhang, *Inorganic Chemistry Frontiers*, 2017, **4**, 2088-2096.
20. M. Misra, P. Kapur and M. L. Singla, *Applied Catalysis B: Environmental*, 2014, **150-151**, 605-611.
21. Y. Chen, D. Zeng, M. B. Cortie, A. Dowd, H. Guo, J. Wang and D. L. Peng, *Small*, 2015, **11**, 1460-1469.
22. Y. Chen, D. Zeng, K. Zhang, A. Lu, L. Wang and D.-L. Peng, *Nanoscale*, 2014, **6**, 874-881.
23. S. M. Majhi, P. Rai and Y.-T. Yu, *ACS Applied Materials & Interfaces*, 2015, **7**, 9462-9468.
24. X. Wang, X. Kong, Y. Yu and H. Zhang, *The Journal of Physical Chemistry C*, 2007, **111**, 3836-3841.
25. P. Li, Z. Wei, T. Wu, Q. Peng and Y. Li, *Journal of the American Chemical Society*, 2011, **133**, 5660-5663.

26. R. Biswas, B. Banerjee, M. Saha, I. Ahmed, S. Mete, R. A. Patil, Y.-R. Ma and K. K. Haldar, *The Journal of Physical Chemistry C*, 2021, **125**, 6619-6631.
27. M. Zhang, J. Pan, X. Xu, G. Fu, L. Zhang, P. Sun, X. Yan, F. Liu, C. Wang, X. Liu and G. Lu, *Analytical Chemistry*, 2022, **94**, 4850-4858.
28. V. V. Pham, T. D. Nguyen, P. P. Ha La and M. Thi Cao, *Advances in Natural Sciences: Nanoscience and Nanotechnology*, 2020, **11**, 015005.
29. D.-X. Ju, H.-Y. Xu, Z.-W. Qiu, Z.-C. Zhang, Q. Xu, J. Zhang, J.-Q. Wang and B.-Q. Cao, *ACS Applied Materials & Interfaces*, 2015, **7**, 19163-19171.
30. P. She, K. Xu, Y. Shang, Q. He, S. Zeng, S. Yin, G. Lu, S. Liang, H. Sun and Z. Liu, *New Journal of Chemistry*, 2018, **42**, 3315-3321.
31. Z. Jiang, W. Wei, D. Mao, C. Chen, Y. Shi, X. Lv and J. Xie, *Nanoscale*, 2015, **7**, 784-797.
32. R. Peng, Y. Li, J. Chen, P. Si, J. Feng, L. Zhang and L. Ci, *Sensors and Actuators A: Physical*, 2018, **283**, 128-133.
33. Y. Zeng, Z. Ye, B. Lu, W. Dai and X. Pan, *Applied Physics A*, 2016, **122**, 296.
34. P. Fageria, S. Gangopadhyay and S. Pande, *RSC Advances*, 2014, **4**, 24962-24972.

Chapter 6

DNA origami-templated bimetallic core-shell nanostructures for enhanced Oxygen Evolution Reaction



6.1. Introduction

A rise in energy consumption is inevitable, given the expanding human population and the burgeoning pace of modern society. Along with photocatalytic water splitting to produce H_2 (As mentioned in chapter 5 of the thesis), Electrochemical hydrogen production is another practical approach which has the potential to effectively lessen global energy crises and lead to a long-term solution. Since the anodic oxygen evolution reaction (OER) has a slow kinetics, it is still a concern for large-scale hydrogen synthesis via electrochemical water splitting.¹⁻⁵ OER requires a greater overpotential than HER to overcome the kinetic energy barrier. Conventional electrocatalysts based on noble-metal oxides such as IrO_2 and RuO_2 , are considered as benchmark catalysts for the OER reaction exhibiting high activity in both acidic and alkaline electrolytes,⁶ but these materials are less abundant and suffer from poor sustainability.⁷⁻⁹ Other transition metal based nanostructures have also been reported for their extensive uses in electrocatalysis for OER due to low-cost and good stability.¹⁰⁻¹⁸

Othman et al. illustrated the use of Au nanoparticles modified glassy carbon electrodes in OER.¹⁹ Au nanoparticles are assumed to speed up the affirmative adsorption of OH^- which is necessary step for OER. Thus, the charge transfer during the transformation of water into oxygen molecule can be obtained at reasonably less positive potential accelerating OER.²⁰ It has also been reported that the conductivity can be enhanced and the necessary active sites for OER can be formed by combining silver (Ag) nanoparticles with double-layered metal hydroxide nanosheets.²¹ We found that the kinetics of electrocatalytic reactions could be altered by the cooperative effect of bimetallic nanostructures, as opposed to those made of a single metal. For example, Zhuang et al. demonstrated that the core-shell type $Au@Co_3O_4$ nanocrystals exhibited enhanced OER current density as compared to Au and Co_3O_4 nanocrystals alone.²² Hou et al. showed $Ag@Co_xP$ core-shell type heterogeneous nanostructures as better catalyst for excellent OER activity and stability in preference to only Co_2P nanoparticles.²³ It has been observed experimentally that systems involving the integration of two distinct materials achieve higher levels of electrocatalytic activity.²⁴⁻²⁷ Only a small number of

reports have been published so far on the use of pure plasmonic nanoparticles as catalysts for OER and HER in the context of electrocatalytic water splitting, indicating that this area of research is still in its infancy.^{19, 28, 29} Therefore, it is of great interest to design novel catalysts by changing the geometry and electronic structure of the plasmonic nanostructures to achieve excellent sustainability and high efficiency in breaking the kinetic barrier and speeding up the OER process.

In traditional electrocatalytic OER, Binders are used to physically connect the active material and conducting material. Electrochemical performance can be hindered when the binder material prevents ions from moving freely.³⁰ So, a binder material should be conductive for the transport of required ions. Commonly used binders like Nafion, however, have a low conductivity towards the transport of hydroxide ions^{31, 32}, resulting in swelling of catalytically active sites can poison the activity of the catalyst.³³ Recently, a few research teams have shown that DNA can be used to enhance the activity of metal catalysts in water splitting electrocatalysis,^{34, 35} methanol oxidation,³⁶ oxygen evolution reaction,³⁷ electrocatalytic water oxidation with the use of any external binder.^{38, 39} Binding DNA with metal nanostructures provides stability to catalysts when stored in refrigerator. The presence of phosphate backbones in the DNA scaffold also increases its activity, from an OER perspective. This provides the advantage of low loading of catalyst as compared to conventional loading.³³ Thus, DNA can function as a binder and stabilizer, demonstrating superior electrocatalysis when combined with metals.⁴⁰⁻⁴² DNA origami is a recently developed, highly effective method for controlling the precise placement of nanoparticles during the assembly of various nanostructures.⁴³⁻⁴⁶ These methods of assembly are more efficient and less expensive than the conventional top-down lithographic methods of positioning metal nanoparticles.⁴⁷ DNA origami provides very long phosphate backbone for the adsorption of metal ions resulting in increased surface area.^{48, 49} In this way, the electrochemical surface area and the density of energetic/active sites are both increased through the controlled assembly of nanostructures on a DNA origami template, which in turn improves electrocatalysis.

The work in this chapter presents the fabrication of DNA origami templated Au@Ag nanostars. These DNA origami templated nanostructures were then used in electrocatalytic oxygen evolution reactions. For an electrocatalyst to be effective for OER, its stability, activity, and charge kinetics are crucial aspects that need to be taken into consideration. Hence, the overpotentials required to generate a current density of 10 mA cm^{-2} and Tafel slope values for DNA origami templated Au@Ag nanostars, ss-DNA functionalized Au@Ag nanostars and Au@Ag nanostars with external binder were compared. Mainly we have observed the effect of incorporation of DNA origami and Ag coating over the Au nanostars on OER performance. Along with this, OER performance of DNA origami templated Au nanostars was compared with that of ss-DNA functionalized Au nanostars and only Au nanostars with external binder. This study fills in a gap by explaining how DNA origami can act as a binder and stabilizer, and how a conducting Ag coating over Au nanostars can boost OER activity which remained unexplored earlier.

6.2. Experimental section

6.2.1. Materials

Gold chloride trihydrate ($\text{HAuCl}_4 \cdot 3\text{H}_2\text{O}$), Tri-sodium citrate (TSC), L- Ascorbic acid, Silver nitrate (AgNO_3), Hydrochloric acid (HCl), Ammonium hydroxide solution (NH_4OH) 25%, Tris-(carboxyethyl) phosphine hydrochloride (TCEP.HCl), Magnesium chloride hexa-hydrate ($\text{MgCl}_2 \cdot 6\text{H}_2\text{O}$), Sodium dodecyl sulphate (SDS) and Sodium chloride (NaCl) were purchased from Sigma- Aldrich and used as received. M13mp18 single stranded DNA was procured from New England Biolabs and was used without further purification. All the DNA oligonucleotides were purchased from Integrated DNA technologies (IDT) with HPLC purification. Tween 20, and Acetic acid (CH_3COOH) were purchased from Merck. Buffer solutions tris (hydroxymethyl)aminomethane (Tris base), 1 M potassium phosphate monobasic solution (KH_2PO_4), 1 M potassium phosphate dibasic solution (K_2HPO_4), ethylenediaminetetraacetic acid disodium (EDTA) were purchased from Sigma Aldrich and used without further purification. Sephacryl S-300 high resolution resin was bought

from GE Healthcare. 5 % Nafion™ 117 solution (Sigma-Aldrich), potassium hydroxide (KOH, Loba Chemie) and MilliQ water was used to carry out all the experiments. All the glasswares were cleaned with aqua regia, water, and MilliQ water before using for experiments.

6.2.2. Experimental procedures

6.2.2.1. Synthesis of Au nanostars and Au nanostars coated with Ag layer (Au@Ag nanostars)

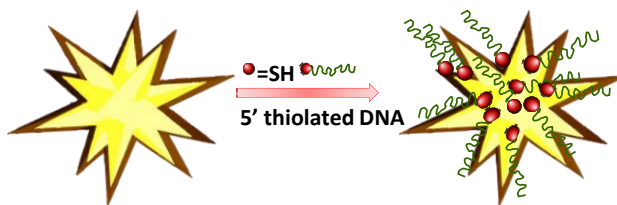
The procedure which was followed for the synthesis of Au nanostars and Au@Ag nanostars was same as described in chapter 3 of the thesis.

6.2.2.2. Synthesis of rectangular DNA Origami

The DNA origami having rectangular shape was synthesized by the methodology explained in chapter 2 of the thesis.

6.2.2.3. Synthesis of ss-DNA functionalized Au@Ag nanostars

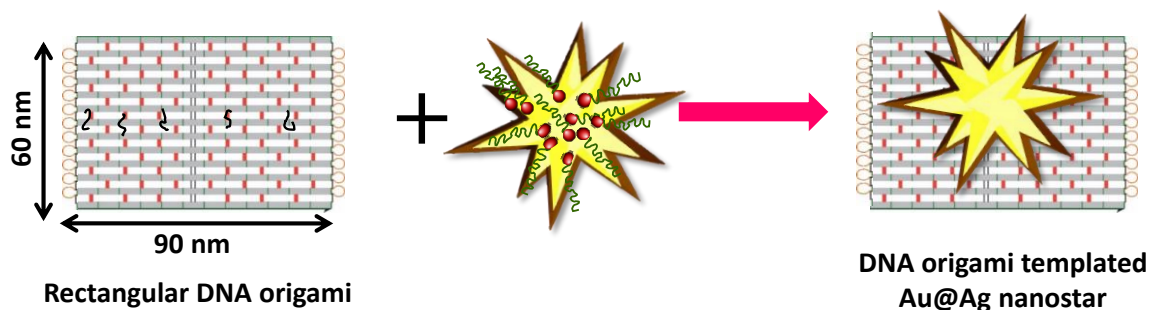
DNA functionalization of Au@Ag nanostars was carried out by using a fast pH assisted method as described in our earlier report and as mentioned in chapter 2.⁴⁵ First, to deprotect the DNA oligonucleotides, S-S bond of disulfide protected DNA oligonucleotides were cleaved by incubating it with 200× molar excess of TCEP.HCl at room temperature for 3 hours. Afterward, to 1 mL solution of Au@Ag nanostars, the addition of 5' thiol terminated deprotected ss-DNA oligonucleotides with the DNA sequence: 5'-SH-CGTCGTATTCGATAGCTTAG-3' was done which further tailed by stirring for 10 min. After that, 10% Tween 20 solution was added and again stirred for 10 min and after this, a 4:5 mixture of KH₂PO₄ and K₂HPO₄ buffers was added to the solution. After leaving this reaction mixture for overnight incubation with stirring, stepwise additions of PBS solution containing 2 M NaCl and 0.1% Tween were carried out till the final concentration of NaCl was reached to 750 mM. Then the so obtained solution was slowly stirred for few hours at room temperature and purification was done by centrifugation followed by redispersion in 0.5×TAE. Scheme 6.1 shows the schematic for the synthesis of ss-DNA functionalized Au@Ag nanostars.



Scheme 6.1. Schematic illustration for the synthesis of ss-DNA functionalized Au@Ag nanostars.

6.2.2.4. Synthesis of DNA origami templated Au@Ag nanostars assemblies

For the hybridization of ss-DNA functionalized Au@Ag nanostars with rectangular DNA origami, DNA origami was mixed with ss-DNA functionalized Au@Ag nanostars in a 1:2 molar ratio in 0.5×TAE buffer containing 300 mM NaCl. The above-mentioned solution mixture was kept in a PCR thermocycler (Bio-rad C1000) and heated repeatedly between 20°C and 40°C for about 12 hours for the formation of assemblies of DNA origami templated Au@Ag nanostars (Scheme 6.2). Using similar method, DNA origami templated pure Au nanostars were also prepared.



Scheme 6.2. Schematic illustration for the synthesis of DNA origami templated Au@Ag nanostar assemblies.

6.2.2.5. Preparation of TEM samples

For recording the TEM images of Au@Ag nanostars, the sample solution was directly drop casted on the carbon coated copper grids and dried in vacuum desiccator. For the imaging of DNA origami and DNA origami templated Au@Ag nanostars assemblies, firstly the carbon coated copper grid was activated by 6 μ L of 1 M $MgCl_2$. After that 6

μL of the sample was dropped over the grid and wicked after 3 min. The grid was negatively strained with uranyl acetate solution (2% w/v) and then dried for some time.

6.2.2.6. Preparation of AFM samples

AFM imaging of the DNA origami and DNA origami templated Au@Ag nanostars assemblies were carried out by preparing the samples onto mica sheets of V1 quality. For this, firstly mica surface was cleaved then activated by using 50 mM MgCl_2 and after 10 min washed with water and dried in air. After this, 20 μL of purified sample was drop casted over the mica surface and after 10 min, washed with water and dried by using nitrogen gun gently.

6.2.2.7. Electrochemical measurements

All the electrochemical measurements were carried out at room temperature using Metrohm Autolab (Multichannel-204) connected to a standard three-electrode system using Nova 2.1.4 software. Platinum (Pt) electrode and Ag/AgCl (3M KCl) electrode were used as a counter electrode and reference electrode for the electrochemical OER studies, respectively. For the measurements, 5 μL aqueous solution of catalyst was drop casted on the glassy carbon (GC, diameter 3 mm) electrode and catalyst loaded GC was kept in vacuum desiccator for overnight drying. For the preparation of catalyst ink of Au nanostars and Au@Ag nanostars, 20 μL 5% Nafion solution used. Notably, Nafion solution was not used for the ink preparation of ss-DNA functionalized Au@Ag nanostars, DNA origami templated Au@Ag nanostars and DNA origami templated Au nanostars catalysts. The dried electrode was then used as working electrode (WE) for the study of oxygen evolution reaction (OER). All the electrochemical experiments were performed at the room temperature in 1 M KOH solution ($\text{pH} = 13.8$) as an electrolyte. The loading of catalyst on GC surface was 0.321 mg cm^{-2} . Linear sweep voltammetry (LSV) analysis was performed in potential range of 0 to 1 V vs. Ag/AgCl electrode with a scan rate of 10 mV s^{-1} and cyclic voltammetry (CV) experiments were carried in the potential range of 0.15 V to 0.25 V with scan rate varying from 10 to 50

mV s⁻¹. The Nyquist plot was performed at frequencies from 100 kHz to 0.1 Hz. All potentials were calibrated versus RHE using the following Nernst Equation (6.1).

$$E_{RHE} = E_{\left(\frac{Ag}{AgCl}\right)} + 0.059pH + E_{Ref} \quad \text{Equation 6.1}$$

The electrochemically active surface area (ECSA) is proportional to the electrochemical double layer capacitance (C_{dl}) of the material and the value of ECSA can be easily calculated using the following equation (6.2).⁵⁰⁻⁵²

$$ECSA = C_{dl} / C_s \quad \text{Equation 6.2}$$

Here, C_s is the specific capacitance of flat working electrode and its value is 40 $\mu\text{F cm}^{-2}$ per cm^2_{ECSA} for the flat electrode. The double-layer capacitance (C_{dl}) was calculated from the slope of anodic current (J_a) and cathodic current (J_c) vs scan rate plot.

As synthesized Au nanostars, Au@Ag nanostars, DNA origami, DNA origami templated Au@Ag nanostars were characterized by UV-Vis spectrophotometer, TEM, and AFM, as described in chapter 2 of this thesis.

6.3. Results and discussion

6.3.1. Structural and optical characterizations of DNA origami templated Au@Ag nanostars

To begin, a rectangular DNA origami was synthesized by employing M13MP18 single-stranded DNA scaffold and utilizing the small staple strands. The purified/ filtered DNA origami was characterized with help of AFM and TEM imaging. The fabrication of the DNA origami was confirmed by AFM and TEM images as shown in Figure 6.1. AFM images in Figure 6.1a, b indicate the formation of DNA origami of dimensions $\sim 90 \times 60$ nm. Height profile of rectangular DNA origami is illustrated in Figure 6.1c indicating the height of DNA origami about 2 nm. TEM images of DNA origami as shown in Figure 6.1d, e also confirm the rectangular shape of DNA origami with $\sim 90 \times 60$ nm dimensions.

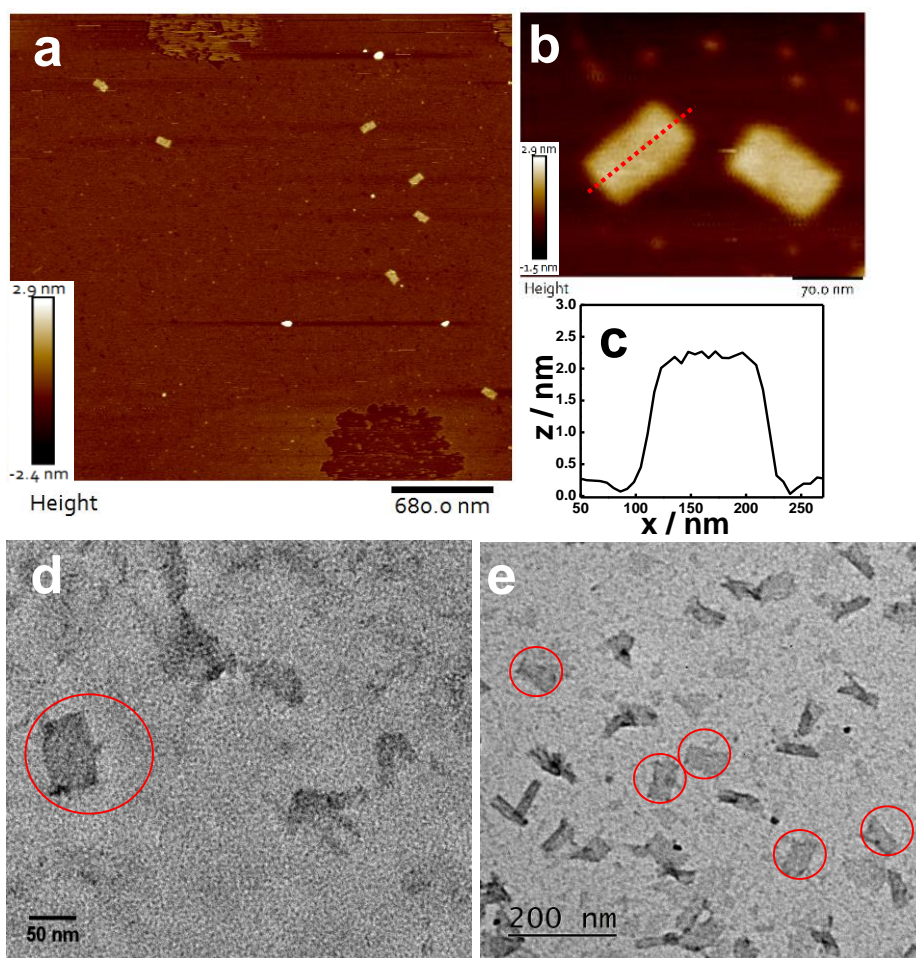


Figure 6.1. (a, b) AFM images of rectangular DNA origami, (c) corresponding height profile, and (d, e) TEM images of rectangular DNA origami.

The bimetallic silver coated Au nanostars that were utilized in this investigation were synthesized by adhering to a procedure under mild conditions. Due to the fact that gold and silver both have similar lattice fringes, the use of gold nanostars as the core material for the application of silver coating was deemed appropriate. This results in the coating over the Au nanostars leaving their shape and size intact. The process of Ag coating over the Au nanostars was monitored through the UV-vis absorption/extinction spectroscopy and the required extinction spectra is illustrated by Figure 6.2. Figure 6.2 shows the extinction spectrum of Au nanostars which indicated the plasmon resonance peak at 730 nm. However, after the coating with Ag, the extinction peak of Au@Ag nanostars was blue shifted to 524 nm as depicted in Figure 6.2 covering the entire

visible range which indicates the formation of Ag coated Au nanostars. Also, the digital images of as prepared Au nanostars and Au@Ag nanostars are shown in the inset of Figure 6.2. The plasmon resonance extinction peaks observed in UV-vis spectra are in agreement with the previously published reports.⁵³⁻⁵⁸

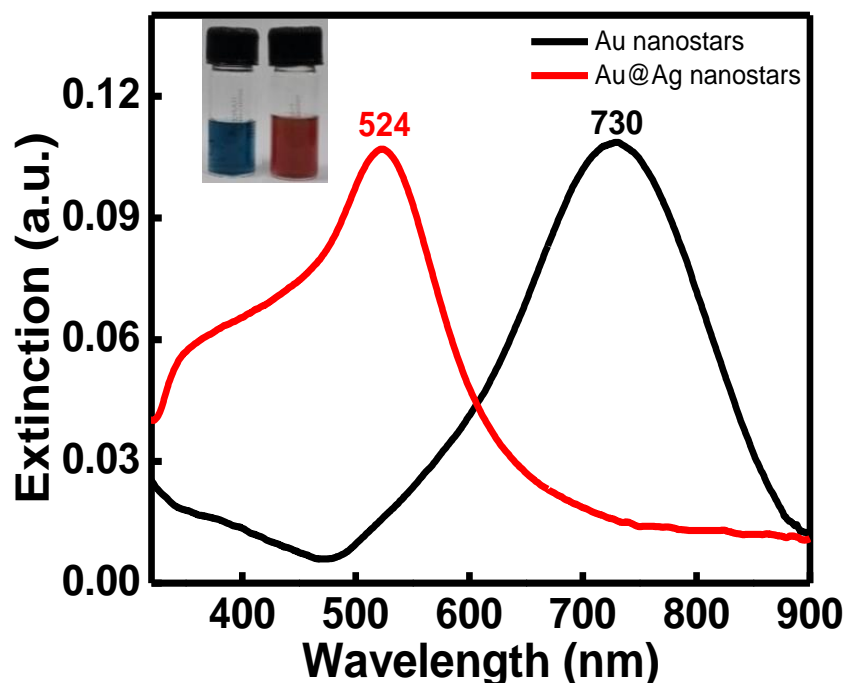


Figure 6.2. UV-vis extinction spectra of Au nanostars and Au@Ag nanostars (the inset shows digital images of nanostar solutions).

To check the morphology and shape, TEM imaging of Au nanostars and Au@Ag nanostars was conducted (Figure 6.3). Figure 6.3a, b depicts that the Au nanostars are formed with high uniformity and sharp tips. It was also revealed from the TEM images that the average size Au nanostars from tip to tip was found to be around 75 ± 5 nm. As it is clear from the TEM images that the tips and core of Au nanostars are well coated with Ag shell. Without the size sorting, Figure 6.3c, d depicts that the Au@Ag nanostars attain the well monodispersity. It has been observed that the average size for these nanoparticles was found to be 80 ± 5 nm.

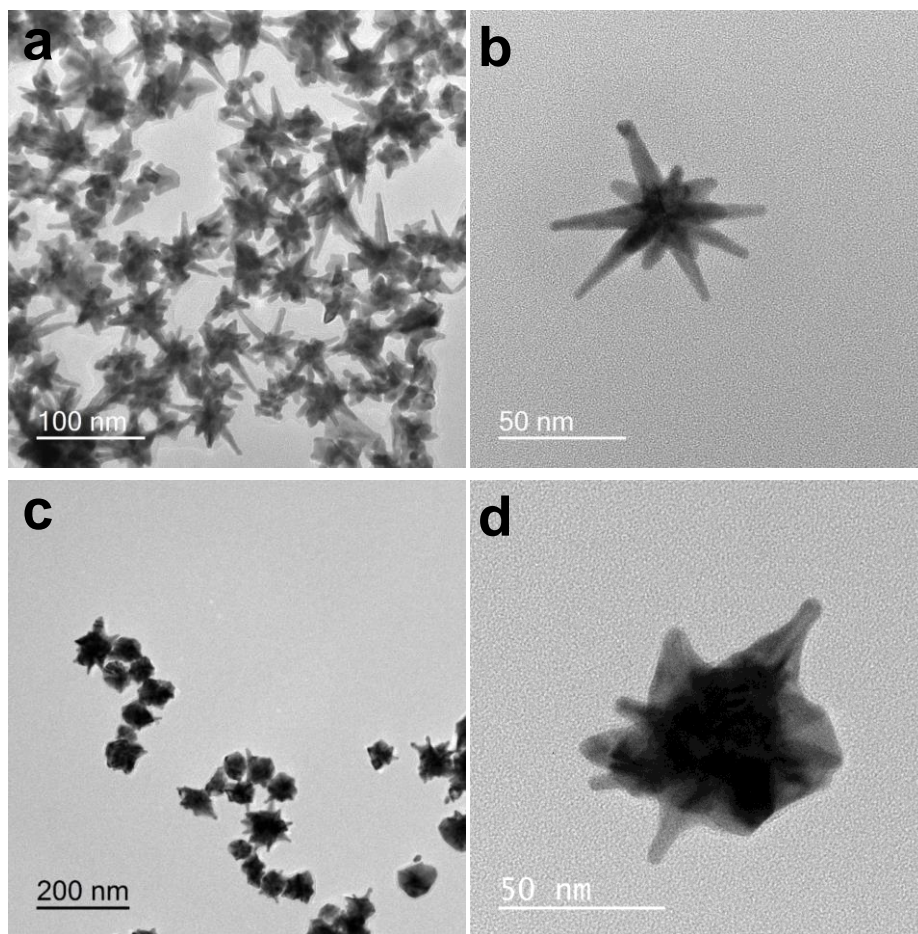


Figure 6.3. TEM images of Au nanostars (a and b), and Au@Ag nanostars (c and d).

The HAADF- STEM image of Au@Ag nanostars is shown in Figure 6.4a and elemental mapping images are presented in Figure 6.4b, c which clearly illustrate the presence of Au in core and Ag in shell in the Au@Ag nanostars. Also, The TEM- Energy dispersive X-ray (EDX) study (Figure 6.5) also showed that both Au and Ag are incorporated in Au@Ag nanostars, signifying their successful formation.

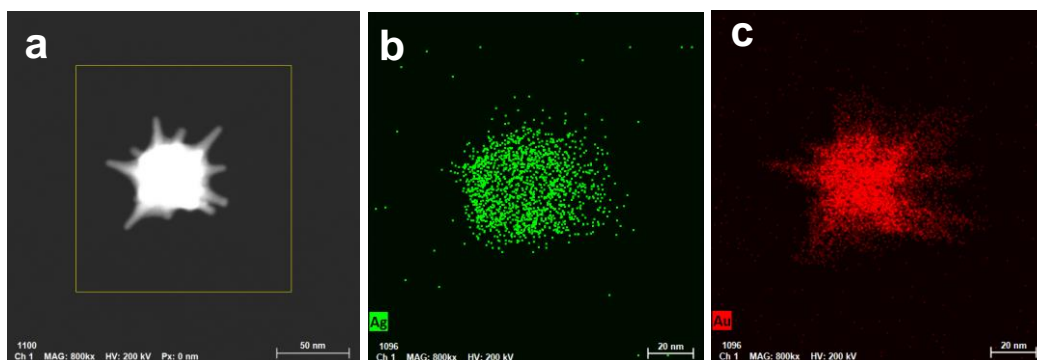


Figure 6.4. (a) HAADF-STEM image, and (b, c) the elemental mapping images of Au@Ag nanostars.

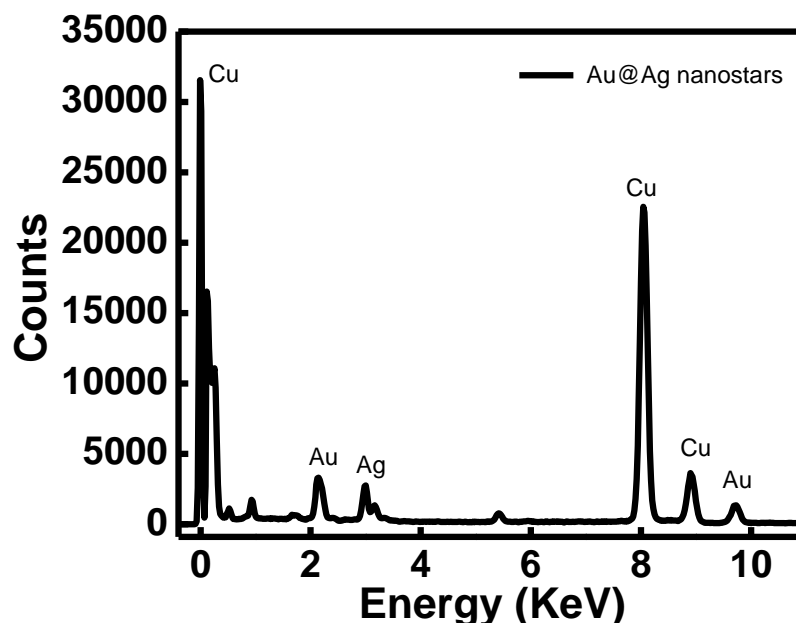


Figure 6.5. Energy Dispersive X-Ray (EDX) spectrum of Au@Ag nanostars.

After the successful synthesis and characterization of Au@Ag nanostars, these were functionalized with thiol modified ss-DNA oligonucleotides by using salt ageing method. UV-vis spectra of Au@Ag nanostars before and after the DNA functionalization are shown in Figure 6.6 which indicates some red shifting from 524 nm to 533 nm due to the change in dielectric constant of surrounding medium after the DNA functionalization of Au@Ag nanostars. This result is in consistent with previous reports by our group.^{45, 46}

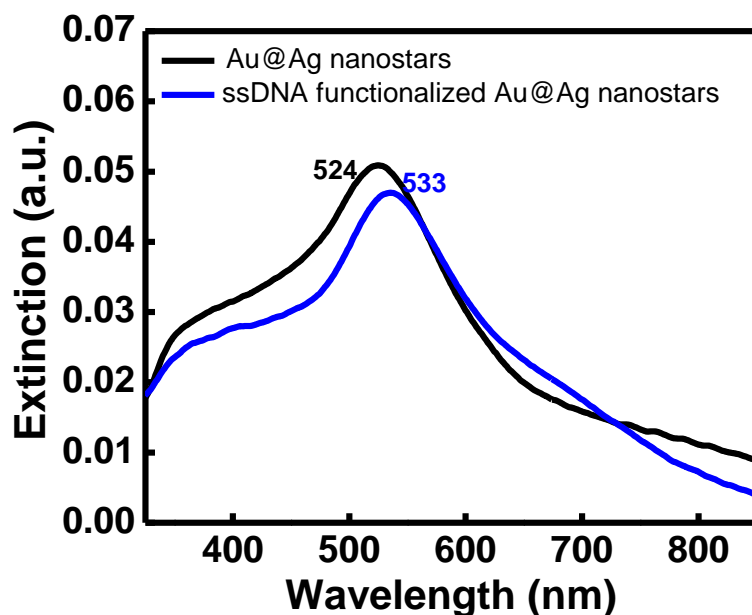


Figure 6.6. UV-Vis extinction spectra of Au@Ag nanostars before and after ss-DNA functionalization.

Now, the prepared rectangular DNA origami was used to immobilize the ss-DNA-functionalized Au@Ag nanostars. For fabrication of nanostar monomer immobilized on DNA origami, there are some predefined positions as explained in our previous report⁴⁹ on DNA origami with the help of capturing strands hanging on the surface of DNA origami. As it can be observed that the dimensions of DNA origami and size of prepared nanostructures are almost similar so each DNA origami is able to hold a single Au@Ag nanostars. This was further demonstrated by AFM images shown in Figure 6.7a and corresponding height profile is illustrated inset of Figure 6.7a indicating the immobilization of single nanostar over the DNA origami. The origami template is not clearly visible because it is completely hidden under the nanostars. Also, TEM images illustrated in Figure 6.7b indicates the successful formation of nanostar monomers over the DNA origami. In Figure 6.7c, origami template is also clearly visible holding a single Au@Ag nanostar. All these structural and characterizations confirm the successful formation of the DNA origami templated Au@Ag nanostars assemblies.

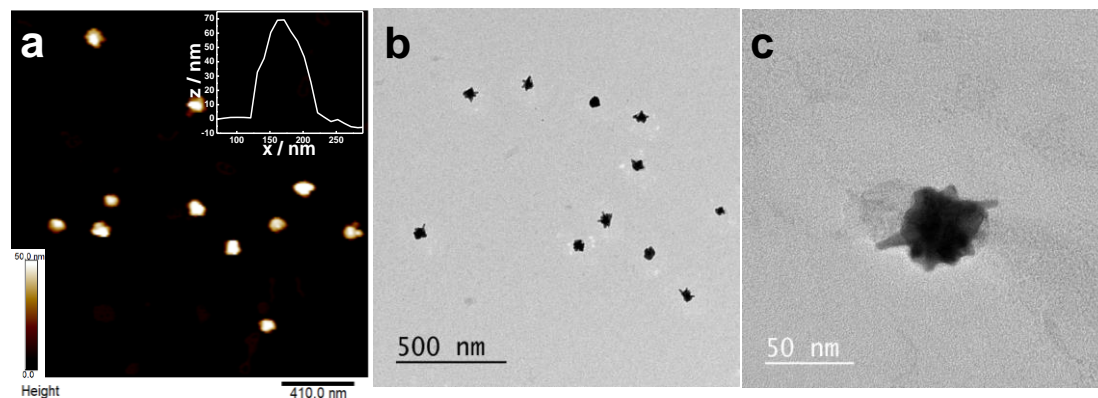


Figure 6.7. (a) AFM images of DNA origami-templated Au@Ag nanostar assemblies (the inset shows the corresponding height profile) and (b and c) TEM images of DNA origami-templated Au@Ag nanostar assemblies.

6.3.2. Electrochemical OER performance

After the successful synthesis of Au nanostars, Au@Ag nanostars, ss-DNA functionalized Au@Ag nanostars, and DNA origami templated Au@Ag nanostars, their electrocatalytic activities were studied toward oxygen evolution reaction (OER) in 1 M KOH solution using a typical three-electrode system at room temperature (Figure 6.8). For the control set of OER studies, we have also carried out the OER activity of DNA origami templated Au nanostars, ss-DNA functionalized Au nanostars and DNA origami (Figure 6.9). To evaluate the OER activity we have performed linear sweep voltammetry (LSV) study of the catalysts and it has been found that DNA origami templated Au@Ag nanostars exhibited lowest overpotential of 266 mV than ss-DNA functionalized Au@Ag nanostars (294 mV), Au@Ag nanostars (309 mV), DNA origami templated Au nanostars (336 mV), IrO₂ (353 mV), ss-DNA functionalized Au nanostars (377 mV), Au nanostars (394 mV) and DNA origami (505 mV) to achieve a current density of 10 mA cm⁻² (Figure 6.8a).

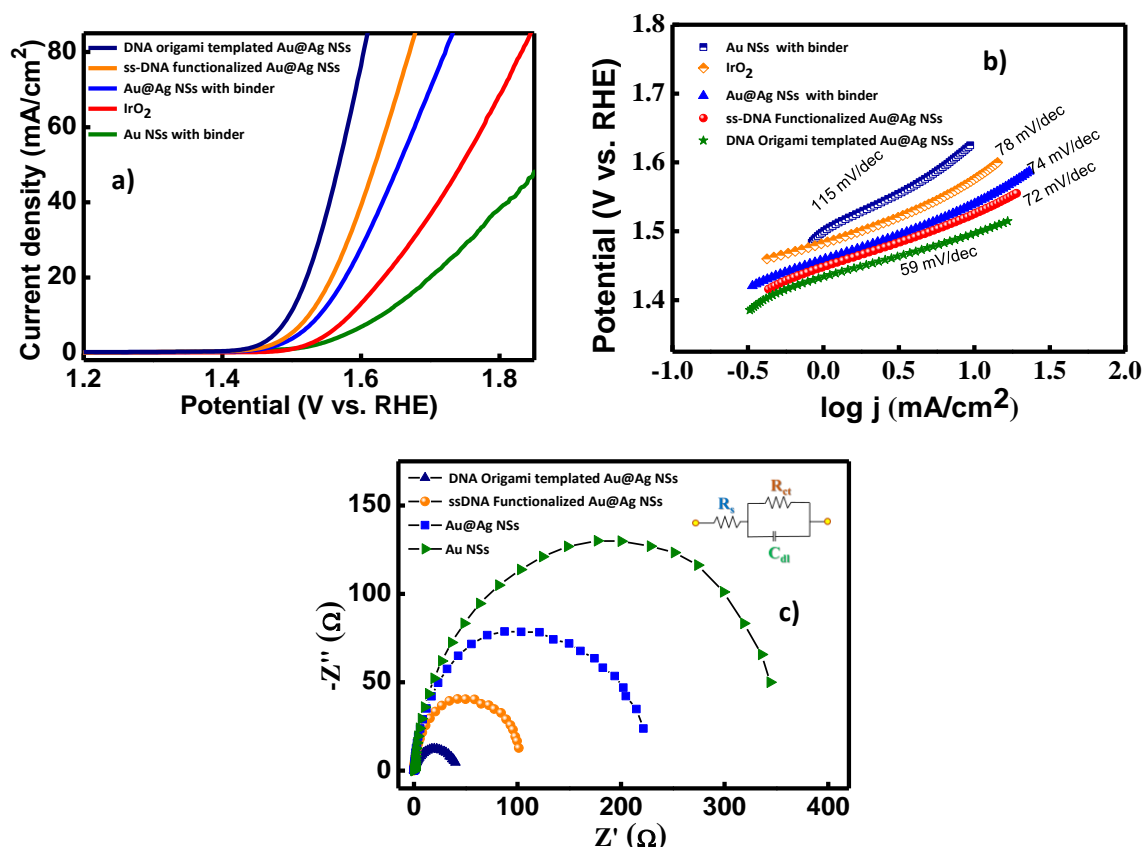


Figure 6.8. (a) Polarization curves (LSV) and (b) corresponding Tafel plots of Au nanostars, IrO₂, Au@Ag nanostars, ss-DNA-functionalized Au@Ag nanostars, and DNA origami-templated Au@Ag nanostars. (c) Electrochemical impedance spectra of the catalysts recorded at 350 mV (Ag/AgCl).

The kinetics or rate of activity of the as synthesized catalysts towards OER was evaluated by the Tafel slope analysis as shown in Figure 6.8b and Figure 6.9. Tafel slope of DNA origami templated Au@Ag nanostars was calculated to be 59 mV/dec which was smallest than ss-DNA functionalized Au@Ag nanostars (72 mV/dec), Au@Ag nanostars (74 mV/dec), DNA origami templated Au nanostars (75 mV/dec), ss-DNA functionalized Au nanostars (83 mV/dec), IrO₂ (78 mV/dec), Au nanostars (115 mV/dec), and DNA origami (168 mV/dec). So, except Au nanostars rest of the catalyst showed superior OER activity in alkaline medium.

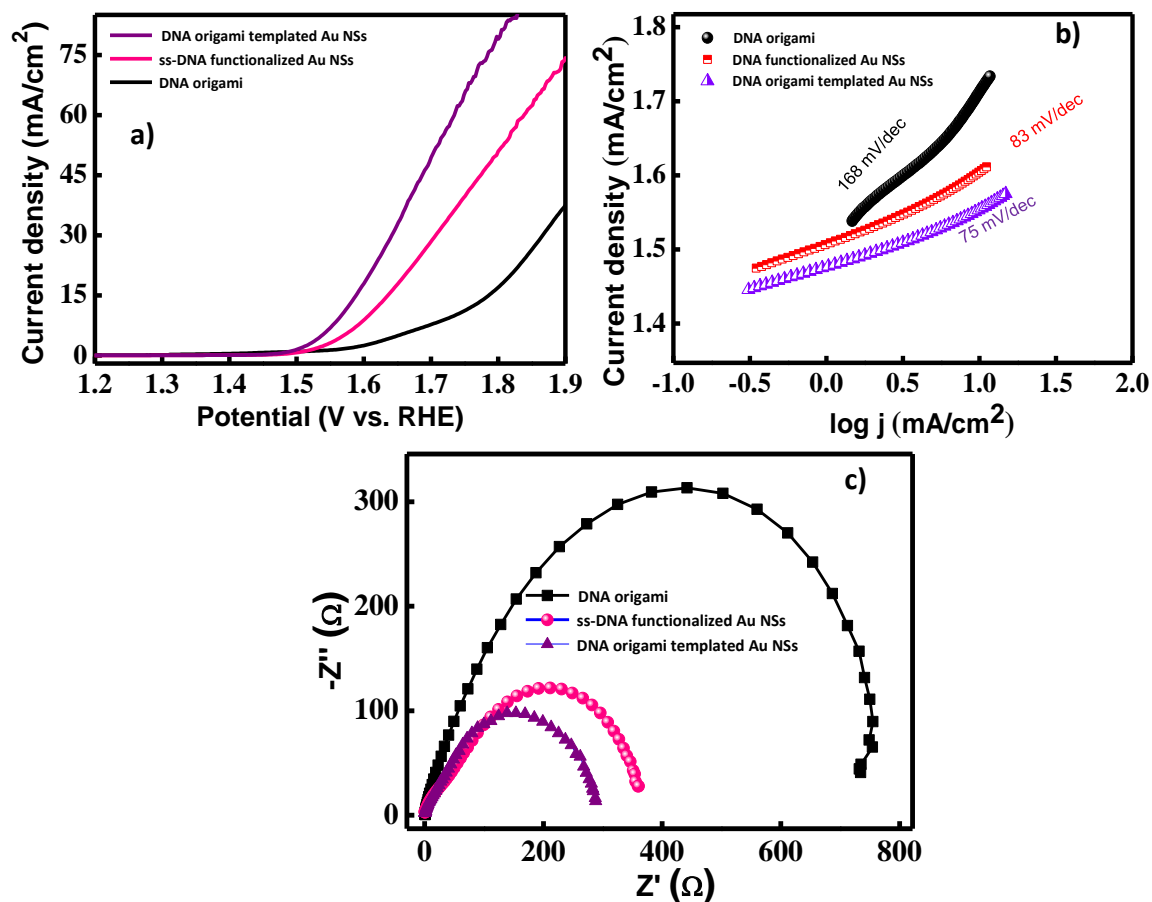


Figure 6.9. (a) polarization curves (LSV), and (b) corresponding Tafel plots of DNA origami templated Au nanostars, ss-DNA functionalized Au nanostars and Au nanostars, respectively. (c) Electrochemical impedance spectra of the catalysts at 350 mV (Ag/AgCl).

To further get into detailed information for superior OER activity and the role of DNA toward electrochemical OER process, we have studied electrochemical impedance spectroscopy (EIS). EIS spectra were fitted using an equivalent circuit model (Figure 6.8c, inset). From EIS study, solution resistance (R_s) and charge-transfer resistance (R_{ct}) of the catalysts were calculated and it has been found that DNA origami templated Au@Ag nanostars possessed very small R_{ct} value of 39.23 Ω. R_{ct} values of ss-DNA functionalized Au@Ag nanostars, Au@Ag nanostars, DNA origami templated Au nanostars, ss-DNA functionalized Au nanostars, Au nanostars, and DNA origami were found to be 98.17, 217.69, 283.15, 339.86, 342.54, and 711.36 Ω, respectively (Figure

6.8c and Figure 6.9c). So lower R_{ct} value facilitates the charge transfer process from the catalyst surface to electrolyte during OER process under an applied potential. So, LSV, Tafel analysis, and EIS study showed that ss-DNA functionalized Au@Ag nanostars and DNA origami templated Au@Ag nanostars exhibited much better OER performances than Au@Ag nanostars without DNA functionalization with binder and same trend of results also achieved by ss-DNA functionalized Au nanostars, DNA origami templated Au nanostars and Au nanostars without DNA with binder. So, it is clearly indicating that DNA has a significant influence towards OER activity. Transport of ions and electrons is another important step in the OER process, DNA origami acts as a superior transporter of hydroxide ions and electrons due to having numerous binding sites (PO_4^{3-} , $-NH_2$ etc) in DNA origami, followed by the synergism assisted by PO_4^{3-} from DNA also enhance the overall OER activity.⁴² Most importantly, instead of using binder, electrochemically active surface area (ECSA) of Au@Ag nanostars was also increased when Au@Ag nanostars was functionalized with DNA. ECSA values of DNA origami templated Au@Ag nanostars, ss-DNA functionalized Au@Ag nanostars, Au@Ag nanostars, DNA origami templated Au nanostars, ss-DNA functionalized Au nanostars, Au nanostars, and DNA origami were calculated to be 78.87, 55.00, 27.5, 18.37, 14.37 and 8.37 cm^2 , respectively (Figure 6.10, 6.11 and Table 6.1). So external binder such as nafion was not only blocking the active sites of the catalyst but also inhibiting the charge transfer rates at the interface between catalyst and electrolyte during OER process.^{37, 41} Due to the presence of very long phosphate backbone in DNA origami structures (consisting of ~7800 base pairs), the OER activity of DNA origami-templated nanostars were found to be higher compared to ss-DNA functionalized nanostars. Comparison with literature is shown in Table 6.2.

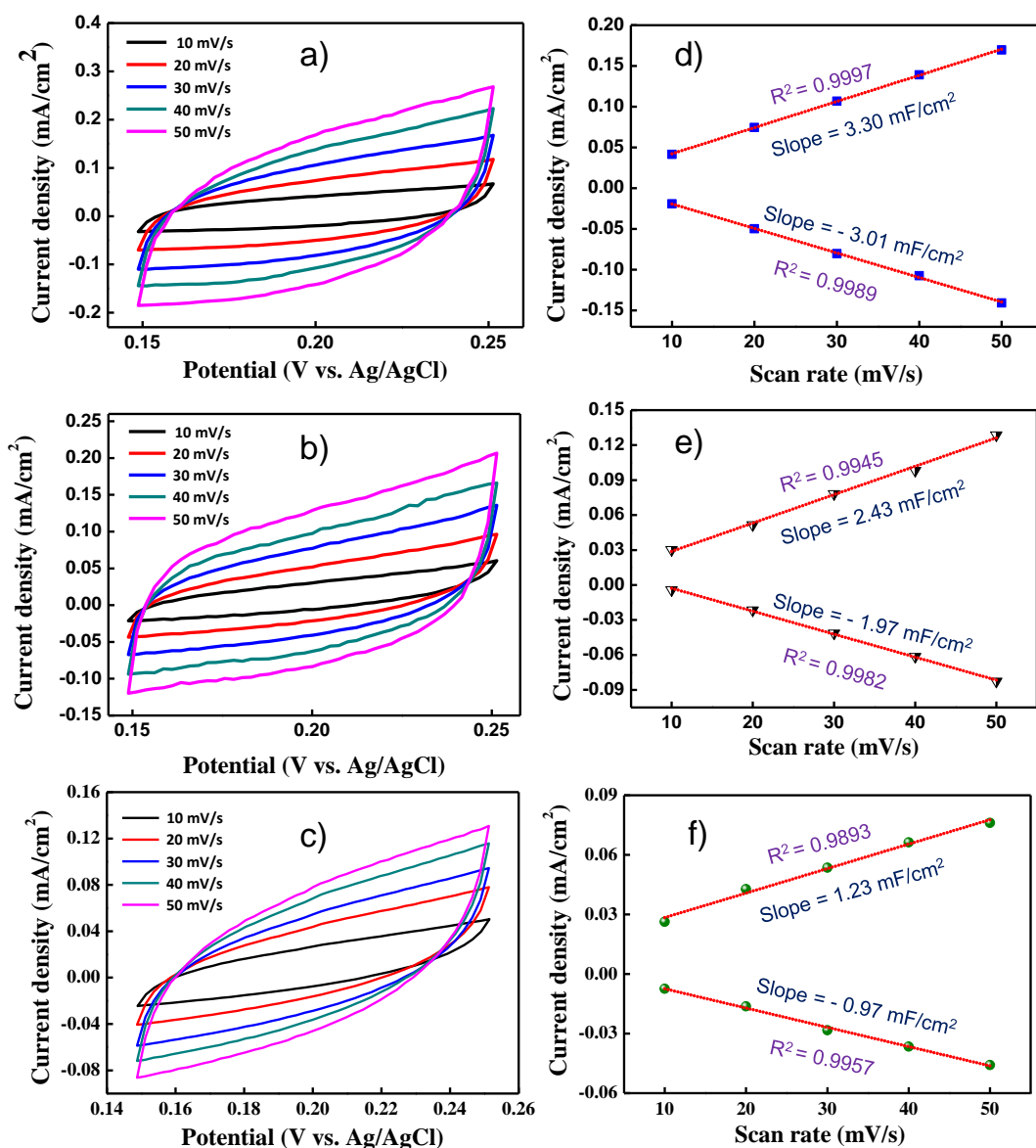


Figure 6.10. (a-b) Cyclic voltammetry curves and (d-e) plot of anodic current density (J_a) and cathodic current density (J_c) against scan rate for the determination of double layer capacitance (C_{dl}) of DNA origami templated Au@Ag nanostars, ss-DNA functionalized Au@Ag nanostars and Au@Ag nanostars, respectively.

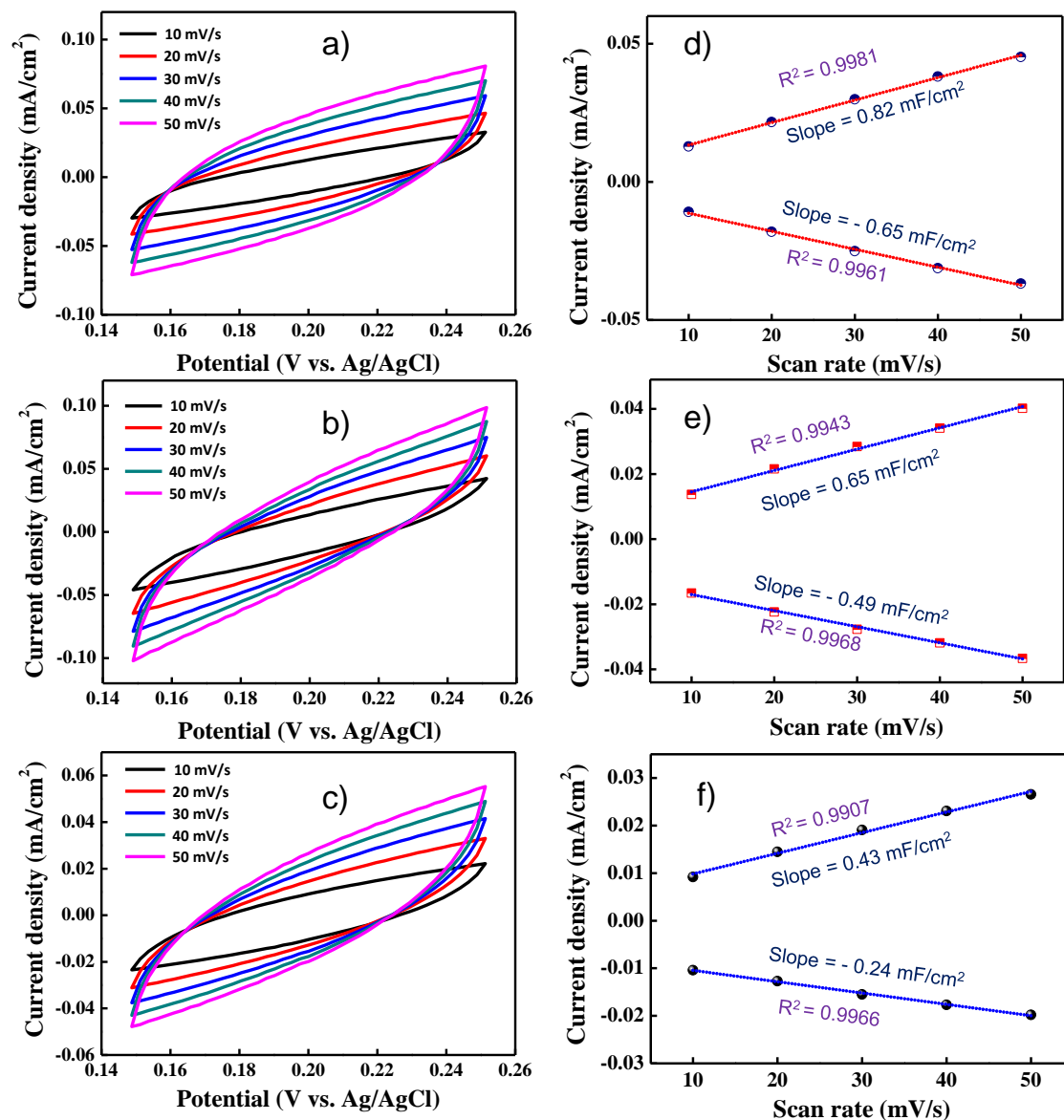


Figure 6.11. (a-b) Cyclic voltammetry curves and (d-e) plot of anodic current density (J_a) and cathodic current density (J_c) against scan rate for the determination of double layer capacitance (C_{dl}) of DNA origami templated Au nanostars, ss-DNA functionalized Au nanostars and Au nanostars, respectively.

Table 6.1. Summary of electrochemical OER performance of Au nanostars, Au@Ag nanostars, and ss-DNA functionalized Au@Ag nanostars, and DNA origami templated Au@Ag nanostars catalysts in 1 M KOH.

System	Overpotential at 10 mA cm⁻²	Tafel slope (mV dec⁻¹)	R_{ct} (Ω)	R_s (Ω)	C_{dl} (mFcm⁻²)	ECSA (cm²)
DNA origami	505 mV	168	711.36	0.35	-	-
Au nanostars with binder	394 mV	115	342.54	0.27	0.335	8.37
ss-DNA functionalized Au nanostars	377 mV	83	339.86	0.32	0.570	14.25
IrO ₂	353 mV	78	-	-	-	-
DNA origami templated Au nanostars	336 mV	75	283.15	0.28	0.735	18.37
Au@Ag nanostars with binder	309 mV	74	217.69	0.24	1.100	27.5
ss-DNA functionalized Au@Ag nanostars	294 mV	72	98.17	0.18	2.200	55.00
DNA origami templated Au@Ag nanostars	266 mV	59	39.23	0.21	3.155	78.87

Table 6.2. Comparison of OER activity of as synthesized DNA origami templated Au@Ag nanostars with some reported Au or Ag or DNA based catalysts.

Catalyst	Overpotential (mV) at 10 mA cm⁻²	Tafel slope	Electrolyte	References
Co ₂ P/Co ₂ N@CNF-DNA(C)	360	107.42	1 MKOH	³⁵
CoSe-DNA	383	71	1 MKOH	³⁸
Ag-Co(OH) ₂ @DNA	260*	72	1 MKOH	³⁷
Ir-Ag Nanotubes	285	61.1	0.5 M H ₂ SO ₄	⁵⁹
Au-Fe Nanoalloys	800	-	1 MKOH	⁶⁰
Au-Ir	393	49	0.1 M HClO ₄	⁶¹
AuCu@IrNi	308	58	0.1 M HClO ₄	⁶²
DNA origami templated nanostars Au@Ag	266	59	1 M KOH	This work

* Overpotential at 50 mA cm⁻²

6.3.2.1. Stability studies

Moreover, we have studied the stability of DNA origami templated Au@Ag nanostars by performing 2500 continuous LSV cycles using 1M KOH electrolyte at a constant scan rate of 50 mV s⁻¹ (Figure 6.12). After 2500 LSV cycles, the change in overpotential at current density of 10 mA cm⁻² was only 4 mV (from 266 mV to 270 mV) which confirmed the superior durability of DNA origami templated Au@Ag nanostars toward OER activity.

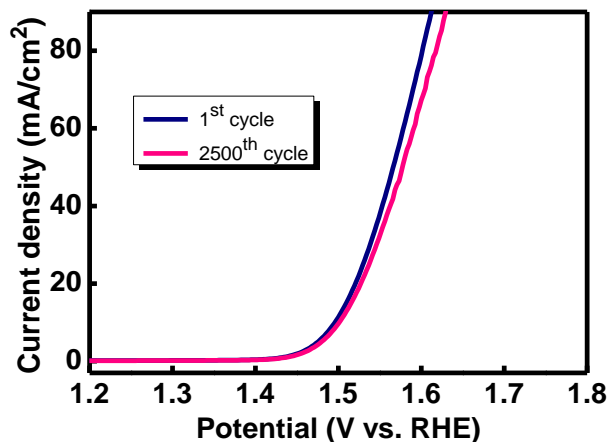


Figure 6.12. Stability test: LSV curves of DNA origami-templated Au@Ag nanostars of first and 2500th cycles of continuous operation.

Intriguingly, the chronoamperometric study of Au@Ag nanostars was severely hampered by the fact that the binder clogged the catalyst's active site. Chronoamperometric study of Au@Ag nanostars exhibited a loss of 15.3% current density after 15 h stability test (Figure 6.13a), whereas DNA origami templated Au@Ag nanostars showed 9.2 % loss of current density at a constant applied potential of 266 mV for 15 h (Figure 6.13b). To further confirm the positive influence of DNA towards the stability of OER performance of DNA origami templated Au@Ag nanostars. We have also studied a series of chronopotentiometric measurements of DNA origami templated Au@Ag nanostars in 1 M KOH for a total of 15 h with 3 h interval at different current density values (20 to 100 mA cm⁻²) (Figure 6.13c). DNA origami templated Au@Ag nanostars showed a constant overpotential of 291, 324, 351, 373, and 394 mV at applied current density of 20, 40, 60, 80, and 100 mA cm⁻², respectively. Chronopotentiometric stability test showed that at different applied current density the obtained overpotential of DNA origami templated Au@Ag nanostars for OER activity remained almost constant. Thus, DNA serves as a binder, contributing to the catalyst's excellent stability performance across a broad potential and current gradient.

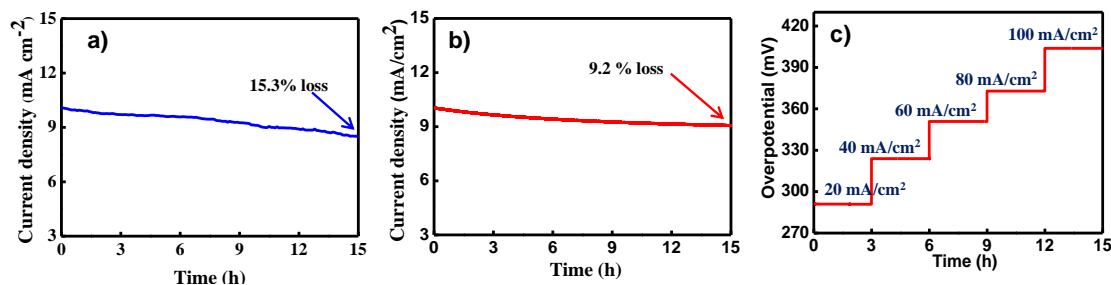


Figure 6.13. Chronoamperometry study of (a) Au@Ag nanostars (using binder) at an overpotential of 309 mV for 15 h, (b) DNA origami templated Au@Ag nanostars at an overpotential of 266 mV for 15 h, and (c) Chronopotentiometric study of DNA origami templated Au@Ag nanostars for OER activity in 1.0 M KOH as a function of current density (20-100 mA/cm²).

6.3.2.2. Effect of OER on morphology of Au@Ag nanostars

After the OER study, the morphology of DNA origami-templated Au@Ag nanostars was also investigated using TEM analysis which is depicted in Figure 6.14. No morphological deformation of Au@Ag was observed. After conducting the stability test, it was discovered that there was no aggregation of nanostars. In addition, the DNA origami template that was holding the nanostar could be seen in the TEM images.

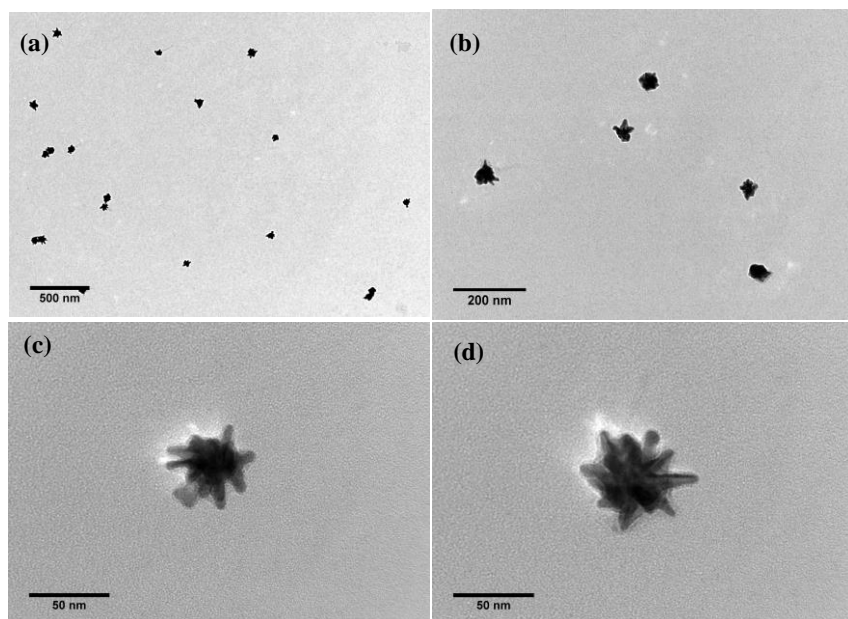
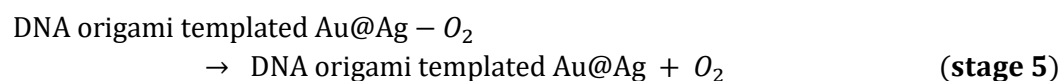
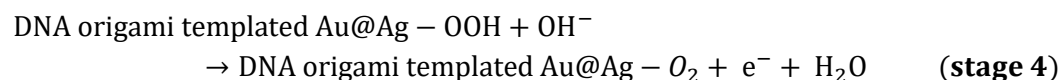
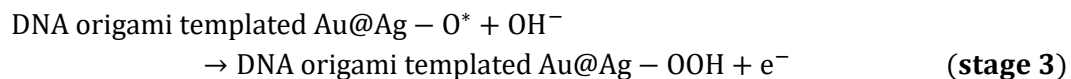


Figure 6.14. TEM images of DNA origami templated Au@Ag nanostars after chronoamperometry stability.

6.3.2.3. Most possessable mechanistic pathway for OER activity



Here, the main active sites of DNA origami templated Au@Ag nanostars catalyst are the metal center i.e., Au and Ag for the electrochemical OER activity in alkaline medium. Transport of ions and electrons is another important step in the OER process, DNA origami boost the conductivity as well as acts as a superior transporter of hydroxide ions and electrons due to abundance of binding sites (such as PO_4^{3-} , $-\text{NH}_2$ etc) in DNA origami, furthermore the synergism assisted by PO_4^{3-} from DNA also enhance the overall OER activity.⁴²

6.4. Conclusion

In conclusion, this chapter lays out a straightforward synthetic method for developing Au@Ag nanostars monomer bound to a rectangular DNA origami template, which were then probed in electrochemical OER studies. It was found that the overpotential required at a current density of 10 mA cm^{-2} was 266 mV for DNA origami templated Au@Ag nanostars. Existence of lots of phosphate groups in DNA origami structure improved the activity of the DNA origami templated Au@Ag nanostars. The Tafel slope value was found to be lowest for DNA origami templated Au@Ag nanostars (59 mV dec^{-1}) which revealed that the charge transfer kinetics was facile in DNA origami templated Au@Ag nanostars. DNA origami templated Au@Ag nanostars exhibited almost constant current density at a constant applied potential of 266 mV for 15 h. This study reveals that core shell Au@Ag nanostars are better catalyst as compared to only

core Au nanostars due to the presence of highly conductive Ag layer on Au core. Further, with the introduction of DNA origami to the Au@Ag nanostars resulted in more pronounced and improved effect on OER reaction. Results from the combined studies unmistakably demonstrated that DNA origami templated Au@Ag nanostars exhibited higher OER activity and stability than other nanostars without DNA origami structures. Thus, this research avenue opens up new possibilities for investigating assemblies of metal nanostructures with DNA origami for potential application in the developing field of hydrogen energy generation, in addition to other fields like supercapacitors and sensors.

Note:

- ✓ Authors and the corresponding author of paper gave their approval for inclusion of this work in present thesis. The corresponding publication is:

Gagandeep Kaur, Rathindranath Biswas, Krishna Kanta Haldar, Tapasi Sen “DNA Origami-templated Bimetallic Core-shell Nanostructures for Enhanced Oxygen Evolution Reaction” *The Journal of Physical Chemistry C* 2022, 126 (16), 6915-692.

References

1. M. Ramadoss, Y. Chen, X. Chen, Z. Su, M. Karpuraranjith, D. Yang, M. A. Pandit and K. Muralidharan, *The Journal of Physical Chemistry C*, 2021, **125**, 20972-20979.
2. C. C. McCrory, S. Jung, I. M. Ferrer, S. M. Chatman, J. C. Peters and T. F. Jaramillo, *Journal of the American Chemical Society*, 2015, **137**, 4347-4357.
3. S. Chen, J. Duan, M. Jaroniec and S. Z. Qiao, *Advanced Materials*, 2014, **26**, 2925-2930.
4. R. Biswas, P. Thakur, G. Kaur, S. Som, M. Saha, V. Jhahria, H. Singh, I. Ahmed, B. Banerjee and D. Chopra, *Inorganic Chemistry*, 2021, **60**, 12355-12366.
5. H. Jia, N. Shang, J. Chen, Q. Yang, M. Su, M. Li and Y. Zhang, *Journal of Colloid and Interface Science*, 2021, **601**, 338-345.
6. Z. Duan, X. Tan, Y. Sun, W.-C. Zhang, A. Umar and X. Wu, *ACS Applied Nano Materials*, 2021, **4**, 10791-10798.
7. R. Frydendal, E. A. Paoli, B. P. Knudsen, B. Wickman, P. Malacrida, I. E. Stephens and I. Chorkendorff, *ChemElectroChem*, 2014, **1**, 2075-2081.
8. Y. Lee, J. Suntivich, K. J. May, E. E. Perry and Y. Shao-Horn, *The Journal of Physical Chemistry Letters*, 2012, **3**, 399-404.
9. K. Klyukin, A. Zagalskaya and V. Alexandrov, *The Journal of Physical Chemistry C*, 2019, **123**, 22151-22157.
10. W. Xu, W. Xie and Y. Wang, *ACS Applied Materials & Interfaces*, 2017, **9**, 28642-28649.
11. B. Zhang, G. Liu, X. Yao, X. Li, B. Jin, L. Zhao, X. Lang, Y. Zhu and Q. Jiang, *ACS Applied Nano Materials*, 2021, **4**, 5383-5393.
12. R. Biswas, A. Kundu, M. Saha, V. Kaur, B. Banerjee, R. S. Dhayal, R. A. Patil, Y.-R. Ma, T. Sen and K. K. Halder, *New Journal of Chemistry*, 2020, **44**, 12256-12265.
13. I. Ahmed, R. Biswas, R. A. Patil, K. K. Halder, H. Singh, B. Banerjee, B. Kumar, Y.-R. Ma and K. K. Halder, *ACS Applied Nano Materials*, 2021, **4**, 12672-12681.
14. M. Dai, H. Liu, D. Zhao, X. Zhu, A. Umar, H. Algarni and X. Wu, *ACS Applied Nano Materials*, 2021, **4**, 5461-5468.
15. K.-L. Ng, K.-Y. Kok and B.-H. Ong, *ACS Applied Nano Materials*, 2018, **1**, 401-409.
16. H.-J. Yin, K. Yuan, Y.-L. Zheng, X.-C. Sun and Y.-W. Zhang, *The Journal of Physical Chemistry C*, 2021, **125**, 16516-16523.
17. L. Wang, T. Meng, C. Chen, Y. Fan, Q. Zhang, H. Wang and Y. Zhang, *Journal of Colloid and Interface Science*, 2018, **532**, 650-656.
18. H. Singh, R. Biswas, I. Ahmed, P. Thakur, A. Kundu, A. R. Panigrahi, B. Banerjee, K. K. Halder, J. Lahtinen and K. Mondal, *ACS Applied Materials & Interfaces*, 2022.
19. S. H. Othman, M. S. El-Deab and T. Ohsaka, *Int. J. Electrochem. Sci*, 2011, **6**, 6209-6219.
20. I. M. Al-Akraa, A. M. Mohammad, M. S. El-Deab and B. E. El-Anadoul, *Arabian Journal of Chemistry*, 2017, **10**, 877-884.
21. S. A. Chala, M.-C. Tsai, W.-N. Su, K. B. Ibrahim, A. D. Duma, M.-H. Yeh, C.-Y. Wen, C.-H. Yu, T.-S. Chan, H. Dai and B.-J. Hwang, *ACS Catalysis*, 2019, **9**, 117-129.
22. Z. Zhuang, W. Sheng and Y. Yan, *Advanced Materials*, 2014, **26**, 3950-3955.
23. Y. Hou, Y. Liu, R. Gao, Q. Li, H. Guo, A. Goswami, R. Zboril, M. B. Gawande and X. Zou, *ACS Catalysis*, 2017, **7**, 7038-7042.
24. C.-J. Zhong and M. M. Maye, *Advanced Materials*, 2001, **13**, 1507-1511.
25. T. Hirakawa and P. V. Kamat, *Journal of the American Chemical Society*, 2005, **127**, 3928-3934.
26. V. Mazumder, M. Chi, K. L. More and S. Sun, *Journal of the American Chemical Society*, 2010, **132**, 7848-7849.

27. P. Strasser, S. Koh, T. Anniyev, J. Greeley, K. More, C. Yu, Z. Liu, S. Kaya, D. Nordlund and H. Ogasawara, *Nature Chemistry*, 2010, **2**, 454-460.
28. G. Liu, P. Li, G. Zhao, X. Wang, J. Kong, H. Liu, H. Zhang, K. Chang, X. Meng and T. Kako, *Journal of the American Chemical Society*, 2016, **138**, 9128-9136.
29. Y. Wei, X. Zhang, Z. Liu, H.-S. Chen and P. Yang, *Journal of Power Sources*, 2019, **425**, 17-26.
30. M. Gong, Y. Li, H. Wang, Y. Liang, J. Z. Wu, J. Zhou, J. Wang, T. Regier, F. Wei and H. Dai, *Journal of the American Chemical Society*, 2013, **135**, 8452-8455.
31. M. Arif, G. Yasin, M. Shakeel, M. A. Mushtaq, W. Ye, X. Fang, S. Ji and D. Yan, *Journal of Energy Chemistry*, 2021, **58**, 237-246.
32. R. Gao, Q. Dai, F. Du, D. Yan and L. Dai, *Journal of the American Chemical Society*, 2019, **141**, 11658-11666.
33. K. Karthick, S. Anantharaj, S. R. Ede, S. S. Sankar, S. Kumaravel, A. Karmakar and S. Kundu, *Advances in Colloid and Interface Science*, 2020, **282**, 102205.
34. S. Kumaravel, M. P. Kumar, P. Thiruvengadam, N. Bandla, S. S. Sankar, S. Ravichandran and S. Kundu, *Inorganic Chemistry*, 2020, **59**, 14501-14512.
35. H. Li, X. Kong, X. Geng, C. Gu, Z. Liu and J. Wang, *Electrochimica Acta*, 2021, **367**, 137562.
36. S. Kumaravel, M. Subramanian, K. Karthick, A. Sakthivel, S. Kundu and S. Alwarappan, *ACS Omega*, 2021, **6**, 19162-19169.
37. A. Karmakar, K. Karthick, S. S. Sankar, S. Kumaravel, M. Ragunath and S. Kundu, *Inorganic Chemistry*, 2021, **60**, 2680-2693.
38. K. Karthick, S. N. Jagadeesan, P. Kumar, S. Patchaiammal and S. Kundu, *Inorganic Chemistry*, 2019, **58**, 6877-6884.
39. H. Singh, I. Ahmed, R. Biswas, S. Mete, K. K. Halder, B. Banerjee and K. K. Haldar, *RSC Advances*, 2022, **12**, 3738-3744.
40. K. Karthick, S. Anantharaj, P. E. Karthik, B. Subramanian and S. Kundu, *Inorganic Chemistry*, 2017, **56**, 6734-6745.
41. S. Anantharaj, P. E. Karthik, B. Subramanian and S. Kundu, *ACS Catalysis*, 2016, **6**, 4660-4672.
42. S. Anantharaj, P. Karthik and S. Kundu, *Journal of Materials Chemistry A*, 2015, **3**, 24463-24478.
43. G. P. Acuna, M. Bucher, I. H. Stein, C. Steinhauer, A. Kuzyk, P. Holzmeister, R. Schreiber, A. Moroz, F. D. Stefani and T. Liedl, *ACS Nano*, 2012, **6**, 3189-3195.
44. S. Tanwar, K. K. Haldar and T. Sen, *Journal of the American Chemical Society*, 2017, **139**, 17639-17648.
45. V. Kaur, S. Tanwar, G. Kaur and T. Sen, *ChemPhysChem*, 2020, **22**, 160-167.
46. S. Tanwar, V. Kaur, G. Kaur and T. Sen, *The Journal of Physical Chemistry Letters*, 2021, **12**, 8141-8150.
47. J. Prinz, C. Heck, L. Ellerik, V. Merk and I. Bald, *Nanoscale*, 2016, **8**, 5612-5620.
48. P. Wang, T. A. Meyer, V. Pan, P. K. Dutta and Y. Ke, *Chem*, 2017, **2**, 359-382.
49. P. W. Rothmund, *Nature*, 2006, **440**, 297-302.
50. H. Deng, C. Zhang, Y. Xie, T. Tumlin, L. Giri, S. P. Karna and J. Lin, *Journal of Materials Chemistry A*, 2016, **4**, 6824-6830.
51. C. C. L. McCrory, S. Jung, J. C. Peters and T. F. Jaramillo, *Journal of the American Chemical Society*, 2013, **135**, 16977-16987.
52. R. Prasannachandran, T. V. Vineesh, A. Anil, B. M. Krishna and M. M. Shaijumon, *ACS Nano*, 2018, **12**, 11511-11519.
53. A. M. Fales, H. Yuan and T. Vo-Dinh, *The Journal of Physical Chemistry C*, 2014, **118**, 3708-3715.
54. Y. Yang, J. Shi, G. Kawamura and M. Nogami, *Scripta Materialia*, 2008, **58**, 862-865.

55. Y. Ran, P. Strobbia, V. Cupil-Garcia and T. Vo-Dinh, *Sensors and Actuators B: Chemical*, 2019, **287**, 95-101.
56. K. K. Haldar, S. Tanwar, R. Biswas, T. Sen and J. Lahtinen, *Journal of Colloid and Interface Science*, 2019, **556**, 140-146.
57. K. K. Haldar, S. Kundu and A. Patra, *ACS Applied Materials & Interfaces*, 2014, **6**, 21946-21953.
58. D. Paital, T. Sen, A. Patra and K. K. Haldar, *Gold Bulletin*, 2017, **50**, 313-317.
59. M. Zhu, Q. Shao, Y. Qian and X. Huang, *Nano Energy*, 2019, **56**, 330-337.
60. I. Vassalini, L. Borgese, M. Mariz, S. Polizzi, G. Aquilanti, P. Ghigna, A. Sartorel, V. Amendola and I. Alessandri, *Angewandte Chemie International Edition*, 2017, **56**, 6589-6593.
61. P.-C. Chen, M. Li, J. Jin, S. Yu, S. Chen, C. Chen, M. Salmeron and P. Yang, *ACS Materials Letters*, 2021, **3**, 1440-1447.
62. J. Park, S. Choi, A. Oh, H. Jin, J. Joo, H. Baik and K. Lee, *Nanoscale Horizons*, 2019, **4**, 727-734.

Chapter 7

Conclusion

7.1. Summary of this thesis

This thesis is set out to explore the synthesis of unique shaped plasmonic nanoparticles and their integrated structures with dielectric materials and semiconductors for applications in numerous fields, including catalysis, therapeutics, and energy. Plasmonic nanostructures offer the unique optical characteristics, such as absorption, scattering, and field enhancements. These properties own to their LSPR which is dependent on shape, size, and surrounding environment. The excitation and decay of generated localized surface plasmons in plasmonic nanoparticles offer three excitation sources including electric field, electron-hole pairs, and heat which can be exploited in different fields. Therefore, plasmonic nanostructures' shape selection and integration with other materials, including semiconductors, can aid in enhancing their properties, which in turn contribute to improved applications. There are a total of six chapters which compose this thesis, including chapter 7.

In the first chapter, an introduction to the optical properties of gold nanoparticles and their bimetallic or integrated structures is presented. This chapter provides an overview of the various mechanisms exhibited by plasmonic nanoparticles on light irradiation. It also discusses the significance of plasmonic nanoparticles-based applications in a variety of fields, such as photocatalysis, SERS, photothermal therapy, and photocatalytic water splitting. In addition to that, there is a discussion on the role played in electrocatalytic OER. The DNA origami method is also discussed in relation to its potential use in the precise positioning and controlled assembly of nanostructures for improved sensing applications. It provides very long phosphate backbone for the adsorption of metal ions resulting in increased surface area which provide stability, facile charge transfer. The synthetic protocols and characterization methods that were utilized for the work presented in this thesis are outlined and discussed in the second chapter of the thesis. In this chapter, we describe the solution-based synthesis of several distinct gold nanostructures including Au nanostars, Ag coated Au nanostars, and hybrid nanostructures of Au combined with semiconductors. In addition to that, the synthesis of DNA origami and the immobilization of nanoparticles on DNA origami are covered in this chapter. The remaining four chapters focus on novel plasmonic nanostructure design

and their applications in photocatalysis, signal enhancement through SERS, photothermal therapy, photocatalytic water splitting, and electrocatalytic oxygen evolution reaction.

The most significant results of this work can be summed up as follows:

1. The bimetallic Au/Ag nanostars show superior photocatalytic activity due to combination of the best features of both metals i.e., chemical stability of Au and better plasmonic properties of Ag owing to its high extinction coefficient. Epitaxial growth of Ag over previously synthesized Au nanostars yielded the resulting Au/Ag nanostars. These were put to use in the plasmon mediated dimerization reaction of PATP, serving as both a SERS substrate and a catalyst propelled by plasmons. Employing the SERS monitoring, it has been found that PATP rapidly converts into its dimerized product DMAB within few seconds by photochemical reaction using Au/Ag core-shell nanostars. When compared with pure metallic counterparts (i.e., only Au nanostars or only Ag nanostars), the photocatalytic activity of the conversion reaction was found to be significantly improved by bimetallic core-shell Au/Ag nanostars. Due to a higher electric field at the tips of the bimetallic nanostructures according to FDTD simulations, Au/Ag nanostars had better photocatalytic activity than pure Au nanostars. The conversion reaction using bimetallic core-shell Au/Ag nanostars is affected by the thickness of the Ag layer, and optimum thickness was found to be $\sim 7 \pm 1$ nm. Under basic pH, 9 pM concentration of Au/Ag nanostars was enough to dimerize PATP into DMAB, which is low as compared to neutral and acidic pH.
2. A simple and effective seed-mediated surfactant free approach has been developed for the synthesis of anisotropic core-shell nanostructures with SiO₂ nanoparticle as a core and Au nanostar as a shell. Plasmonic nanoparticles, with their distinctive localized surface plasmon resonance (LSPR), are being put to use as SERS based detectors of pollutants and photothermal (PT) agents in cancer therapy. Therefore, the SERS performance of as-synthesized anisotropic SiO₂@Au nanostars was analyzed by employing Rhodamine B (RhB) dye as a Raman probe, and the results showed a robust enhancement factor of 1.37×10^6 . Due to the biocompatible nature and NIR activity of prepared nanostars, these

were employed for the photothermal killing of breast cancer cells. The photothermal effect of the SiO₂@Au nanostars increased with increasing concentration, and demonstrated a photothermal conversion efficiency of up to 72%.

3. It has been discovered how to efficiently and effectively create Au@ZnO hybrid nanocomposites (NCs), which consist of a core Au nanostar surrounded by ZnO nanopetals. In order to validate the photocatalytic potential of these nanostructures, photocatalytic water splitting was carried out. Au@ZnO NCs exhibited hydrogen and oxygen evolution up to 518.36 and 177.86 $\mu\text{mol g}^{-1}$, respectively. This is because the strong electron scavenging activity of the Au nanoparticles preventing the recombination of photogenerated charge carriers in ZnO.
4. The design of assembling core-shell Au@Ag nanostar structure on rectangular DNA origami has been demonstrated. These assemblies were investigated for electrocatalytic activities through OER which remained unexplored earlier. Excellent OER activity and high stability were observed in the DNA origami templated bimetallic nanostar catalyst, which also displayed a current density of 10 mA cm^{-2} at a low overpotential of 266 mV without the use of any external binder. Due to the highly conductive Ag layer, the electrocatalytic performance of DNA origami templated Au@Ag nanostars was significantly higher than that of pure core Au nanostars immobilized on DNA origami. Being long phosphate backbone, DNA origami helped in the facile transfer of hydroxide ions and electron for oxygen evolution. In addition, the controlled assembly of bimetallic nanostructures on the DNA origami template increased the density of active sites and the electrochemical surface area, leading to improved electrocatalysis.

Thus, the morphology control over the plasmonic nanostructures and their integration with other metals or semiconductors results in the development of new and advanced catalysts which allow their use in various applications such as photocatalysis, sensing, fuel generation, and water splitting.

7.2. Scope for the future work

This thesis explains how to use different morphologies of plasmonic nanostructures and their hybrid nanostructures in photocatalysis, sensing, and water splitting applications. When it comes to nanotechnology, there are a lot of different avenues that still need to be investigated before we determine whether or not these findings have any real-world applications.

1. With the right knowledge of optical features, combining plasmonic nanoparticles with other metals (like Cu and Al) can greatly aid in the creation of low-cost and high-performance optical platforms. It is important to focus on modifying fabrication and post-fabrication techniques to realize highly tunable and economically viable nanostructures for specific purposes.
2. An important step toward clinical application is the development of multi-functional plasmonic nanostructured materials for establishing a safe and effective therapeutic approach.
3. The attractive optical features of plasmonic nanostructures are expected to lead to further major discoveries, particularly in the designing of more specific visible-light driven catalysts.
4. The assembly of metal nanostructures-DNA could also be considered for use in other fields, such as sensors, SERS studies, and supercapacitors. The electrocatalytic research can be performed more easily through the use of metal nanostructures templated on DNA origami. DNA also behaves as an effective stabilizer in this context and can be employed for future applications.

More research into plasmonics will improve the properties and characteristics of nanostructured materials, making it easier to design application-focused plasmonic nanostructures.

Appendix A

Appendix A

Table 1: Sequences of staple strands

The colored sequences represent the sequences extended at the 3' end of staples 80, 81, 82, 83, 85, 86, 87, and 111 for immobilization of Ag coated Au nanostars on DNA origami.

Name	Sequence (5' to 3')
2	ACGTTAGTAAATGAATTTTCTGTAAGCGGAGT
3	CGTAACGATCTAAAGTTTTGTCGTGAATTGCG
4	TGTAGCATTCCACAGACAGCCCTCATCTCCAA
5	TGAGTTTCGTCACCAGTACAACTTAATTGTA
6	CAAGCCCAATAGGAACCCATGTACCGTAACAC
7	CTCAGAGCCACCACCCTCATTTTCCTATTATT
8	CCCTCAGAACCGCCACCCTCAGAACTGAGACT
9	TATCACCGTACTCAGGAGGTTTAGCGGGGTTT
10	TATAAGTATAGCCCGGCCGTCGAG
11	GAGAATAGCTTTTGCGGGATCGTCGGGTAGCA
12	AATAATAAGGTCGCTGAGGCTTGCAAAGACTT
13	AAAAAAGGACAACCATCGCCACGCGGGTAAA
14	TCGGTTTAGCTTGATACCGATAGTCCAACCTA
15	AATGCCCCGTAACAGTGCCCGTATGTGAATTT
16	CTGAAACAGGTAATAAGTTTTAACCCCTCAGA
17	CCTCAAGAATACATGGCTTTTGATAGAACCAC
18	AGGGTTGAATAAATCCTCATTAATGATATTC
19	CAGCGAAAACTTTCAACAGTTTCTGGGATTTTGCTAAAC
20	AAAGGCCGAAAGGAACAATAAGCTTTCCAG
21	ATATATTCTTTTTTCACGTTGAAAATAGTTAG
22	CAATGACACTCCAAAAGGAGCCTTACAACGCC
23	CTTAAACATCAGCTTGCTTTTCGAGAAACAGTT
24	TGCCTTGACTGCCTATTTTCGGAACAGGGATAG
25	AGTGTACTTGAAAGTATTAAGAGGCCGCCACC

26	TAAGCGTCGAAGGATTAGGATTAGTACCGCCA
27	GGAAAGCGACCAGGCGGATAAGTGAATAGGTG
28	ACGGCTACTTACTTAGCCGGAACGCTGACCAA
29	TTTCATGAAAATTGTGTCGAAATCTGTACAGA
30	ATACGTAAAAGTACAACGGAGATTTTCATCAAG
31	AAACGAAATGACCCCCAGCGATTATTCATTAC
32	GAGCCGCCCCACCACCGGAACCGCCTAAAACA
33	GCCACCACTCTTTTCATAATCAAACCGTCACC
34	CACCAGAGTTCGGTCATAGCCCCCGCCAGCAA
35	TGAGGCAGGCGTCAGACTGTAGCGTAGCAAGG
36	ACAAACAAAATCAGTAGCGACAGATCGATAGC
37	ACGGTCAAGACAGCATCGGAACGAACCCTCAG
38	CGCCTGATGGAAGTTTCCATTAAACATAACCG
39	GCGAAACATGCCACTACGAAGGCATGCGCCGA
40	CTCATCTTGAGGCCAAAAGAATACACTCCCTCA
41	AACCAGAGACCCTCAGAACCGCCAGGGGTCAG
42	GTTTGCCACCTCAGAGCCGCCACCGATACAGG
43	TCGGCATTCCGCCGCCAGCATTGACGTTCCAG
44	TGCCTTTAGTCAGACGATTGGCCTGCCAGAAT
45	CTTTGAAAAGAACTGGCTCATTATTTAATAAA
46	CCAGGCGCTTAATCATTGTGAATTACAGGTAG
47	AGTAATCTTAAATTGGGCTTGAGAGAATACCA
48	CCAAATCACTTGCCCTGACGAGAACGCCAAAA
49	TTATTCATAGGGAAGGTAAATATTCATTTCAGT
50	GACTTGAGAGACAAAAGGGCGACAAGTTACCA
51	AATCACCAAATAGAAAATTCATATATAACGGA
52	CCGGAAACACACCACGGAATAAGTAAGACTCC
53	AGCACCGTTAAAGGTGGCAACATAGTAGAAAA
54	GGACGTTGTCATAAGGGAACCGAAAGGCGCAG
55	CGATTTTAGAGGACAGATGAACGGCGCGACCT

56	TTTCAACTATAGGCTGGCTGACCTTGTATCAT
57	GAATAAGGACGTAACAAAGCTGCTGACGGAAA
58	ATTGAGGGTAAAGGTGAATTATCAATCACCGG
59	AGCGCCAACCATTTGGGAATTAGATTATTAGC
60	TCACAATCGTAGCACCATTACCATCGTTTTCA
61	ACGCAAAGGTCACCAATGAAACCAATCAAGTT
62	ACGAAGTAGCGTCCAATACTGCGGAATGCTTT
63	AAAGATTTCAGGGGGTAATAGTAAACCATAAAT
64	CATTCAACGCGAGAGGCTTTTGCATATTATAG
65	GGAATTACTCGTTTACCAGACGACAAAAGATT
66	AAAAGTAATATCTTACCGAAGCCCAACACTAT
67	GAAGGAAAATAAGAGCAAGAAACAACAGCCAT
68	ATACCCAAGATAACCCACAAGAATAAACGATT
69	TTATTACGGTCAGAGGGTAATTGAATAGCAGC
70	TACATACAGACGGGAGAATTAACCTACAGGGAA
71	TAAATATTGGAAGAAAAATCTACGACCAGTCA
72	ACTGGATAACGGAACAACATTATTACCTTATG
73	TTTGCCAGATCAGTTGAGATTTAGTGGTTTAA
74	CCAAAATATAATGCAGATACATAAACACCAGA
75	CATAACCCGAGGCATAGTAAGAGCTTTTTAAG
76	GCAATAGCGCAGATAGCCGAACAATTCAACCG
77	GCCCAATACCGAGGAAACGCAATAGGTTTACC
78	ATCAGAGAAAGAACTGGCATGATTTTATTTTG
79	TGAACAAACAGTATGTTAGCAAACCTAAAAGAA
80	AAACAGTTGATGGCTTAGAGCTTATTTAAATA
81	CAAAAATCATTGCTCCTTTTGATAAGTTTCAT
82	TCAGAAGCCTCCAACAGGTCAGGATCTGCGAACTAAGCTATCGA
83	AAGAGGAACGAGCTTCAAAGCGAAGATACATTCTAAGCTATCGA
84	CCTAATTTACGCTAACGAGCGTCTATATCGCG
85	ATTATTTAACCCAGCTACAATTTTCAAGAACGCTAAGCTATCGA

86	TTTTGTTTAAGCCTTAAATCAAGAATCGAGAACTAAGCTATCGA
87	CTTTACAGTTAGCGAACCTCCCGACGTAGGAA
88	GCGCATTAGCTTATCCGGTATTCTAAATCAGA
89	ATATAATGCATTGAATCCCCCTCAAATCGTCA
90	TTTTTGCGCAGAAAACGAGAATGAATGTTTAG
91	TACCTTTAAGGTCTTTACCCTGACAAAGAAGT
92	GAAGCAAAAAAGCGGATTGCATCAGATAAAAA
93	TTTTAATTGCCCGAAAGACTTCAATTCCAGAG
94	TCTTACCAGCCAGTTACAAAATAAATGAAATA
95	TATTTTGCTCCCAATCCAAATAAGTGAGTTAA
96	AGGTTTTGAACGTCAAAAATGAAAGCGCTAAT
97	GAGGCGTTAGAGAATAACATAAAAGAACACCC
98	TGCAACTAAGCAATAAAGCCTCAGTTATGACC
99	TCCATATACATACAGGCAAGGCAACTTTATTT
100	CGAGTAGAACTAATAGTAGTAGCAAACCCTCA
101	TCGCAAATGGGGCGCGAGCTGAAATAATGTGT
102	ATCGGCTGCGAGCATGTAGAAACCAGCTATAT
103	GGTATTAAGAACAAGAAAAATAATTAAAGCCA
104	CAAGCAAGACGCGCCTGTTTATCAAGAATCGC
105	TCATTACCCGACAATAAACAACATATTTAGGC
106	TATAGAAGCGACAAAAGGTAAAGTAGAGAATA
107	GCTAAATCCTGTAGCTCAACATGTATTGCTGA
108	CAAAATTAAAGTACGGTGTCTGGAAGAGGTCA
109	CAATAAATACAGTTGATTCCCAATTTAGAGAG
110	TCAATTCTTTTAGTTTGACCATTACCAGACCG
111	TTTCATTTGGTCAATAACCTGTTTAATCAATACTAAGCTATCGA
112	CTAATTTATCTTTCCTTATCATTATCCTGAA
113	TAAGTCCTACCAAGTACCGCACTCTTAGTTGC
114	AATGCAGACCGTTTTTATTTTCATCTTGCGGG
115	CCAGACGAGCGCCCAATAGCAAGCAAGAACGC

116	CTGTAATATTGCCTGAGAGTCTGGAAAAC TAG
117	CAACGCAATTTTTGAGAGATCTACTGATAATC
118	TATATTTTAGCTGATAAATTAATGTTGTATAA
119	AGGTAAAGAAATCACCATCAATATAATATTTT
120	GCGTTATAGAAAAAGCCTGTTTAGAAGGCCGG
121	ACGCTCAAAATAAGAATAAACACCGTGAATTT
122	CATATTTAGAAATACCGACCGTGTTACCTTTT
123	AGAGGCATAATTTTCATCTTCTGACTATAACTA
124	TAAAGTACCGCGAGAAAAC TTTTATCGCAAG
125	AGAGAATCGGTTGTACCAAAAACAAGCATAAA
126	TCAGGTCAC TTTTGCGGGAGAAGCAGAATTAG
127	GGTAGCTAGGATAAAAAATTTTAGTTAACATC
128	ACCGTTCTAAATGCAATGCCTGAGAGGTGGCA
129	AGACAGTCATTCAAAGGGTGAGATATCATAT
130	AATTACTACAAATTCTTACCAGTAATCCCATC
131	AGGCGTTACAGTAGGGCTTAATTGACAATAGA
132	AATGGTTTACAACGCCAACATGTAGTTCAGCT
133	TTTTAGTTTTTTCGAGCCAGTAATAAATTCTGT
134	CATGTCAAGATTCTCCGTGGGAACCGTTGGTG
135	AGAAAAGCAACATTAAATGTGAGCATCTGCCA
136	GCAAATATCGCGTCTGGCCTTCCTGGCCTCAG
137	GT TAAAATTTTAACCAATAGGAACCCGGCACC
138	TTAAGACGTTGAAAACATAGCGATTTAAATCA
139	ATCAAAATCGTCGCTATTAATTAACGGATTCTG
140	TAACCTCCATATGTGAGTGAATAAACAAAATC
141	TATGTAAACCTTTTTTAATGGAAAAATTACCT
142	ACAAAGAAATTAATTACATTTAACACATCAAG
143	GATTGACCGATGAACGGTAATCGTAGCAAACA
144	ACCCGTCGTCATATGTACCCCGGTAAAGGCTA
145	CTTTCATCCCCAAAAACAGGAAGACCGGAGAG

146	AAATAATTTTAAATTGTAAACGTTGATATTCA
147	GCTCATTTTTCGCATTAAATTTTGTAGCTTAGA
148	TAGAATCCCTGAGAAGAGTCAATAGGAATCAT
149	CTGTAAATCATAGGTCTGAGAGACGATAAATA
150	AAATCAATGGCTTAGGTTGGGTTACTAAATTT
151	TTGAATTATGCTGATGCAAATCCACAAATATA
152	TAGATGGGGGGTAACGCCAGGGTTGTGCCAAG
153	GTTTGAGGGAAAGGGGGATGTGCTAGAGGATC
154	GAAGATCGGTGCGGGCCTCTTCGCAATCATGG
155	GCTTCTGGTCAGGCTGCGCAACTGTGTTATCC
156	CTTTTACACAGATGAATATACAGTAAGCGCCA
157	CCTGATTGAAAGAAATTGCGTAGACCCGAACG
158	GCGCAGAGATATCAAAATTATTTGACATTATC
159	GAGCAAAAACCTTCTGAATAATGGAAGAAGGAG
160	AAAACAAATTCATCAATATAATCCTATCAGAT
161	CACGACGTGTAATGGGATAGGTCAAAACGGCG
162	ATTAAGTTCGCATCGTAACCGTGCGAGTAACA
163	CAGCTGGCGGACGACGACAGTATCGTAGCCAG
164	GGCGATCGCACTCCAGCCAGCTTTGCCATCAA
165	TTCGCCATTGCCGGAACCCAGGCACACAGTAC
166	TTTAACGTTTCGGGAGAAACAATAATTTTCCCT
167	ACAGAAATCTTTGAATACCAAGTTCCTTGCTT
168	AACCTACCGCGAATTATTCATTTCCAGTACAT
169	TGGATTATGAAGATGATGAAACAAAATTTTCAT
170	CTTGCAATGCATTAATGAATCGGCCCGCCAGGG
171	CCCGGGTACTTTCCAGTCGGGAAACGGGGCAAC
172	TCATAGCTACTCACATTAATTGCGCCCTGAGA
173	GCTCACAATGTAAAGCCTGGGGTGGGTTTGCC

174	CGACAAC TAAGTATTAGACTTTACAGCCGGAA
175	TTATTAATGCCGTCAATAGATAATCAGAGGTG
176	ATTTTGCGTCTTTAGGAGCACTAAGCAACAGT
177	CGGAATTATTGAAAGGAATTGAGGTGAAAAAT
178	GATGGCAAAATCAATATCTGGTCACAAATATC
179	GGGAGAGGTGTAAAACGACGGCCATTCCCAGT
180	GCCAGCTGCCTGCAGGTCGACTCTGCAAGGCG
181	ACTGCCCCGCCGAGCTCGAATTCGTTATTACGC
182	GTGAGCTAGTTTCCTGTGTGAAATTTGGGAAG
183	GCATAAAGTTCCACACAACATACGAAACAATT
184	GGATTTAGCGTATTAAATCCTTTGTTTTTCAGG
185	AGATTAGATTTAAAAGTTTGAGTACACGTAAA
186	CTAAAATAGAACAAAGAAACCACCAGGGTTAG
187	ATCAACAGTCATCATATTCCTGATTGATTGTT
188	TGGTTTTTAACGTCAAAGGGCGAAGAACCATC
189	AGCTGATTACAAGAGTCCACTATTGAGGTGCC
190	GAGTTGCACGAGATAGGGTTGAGTAAGGGAGC
191	CCAGCAGGGGCAAAATCCCTTATAAAGCCGGC
192	ACGAACCAAAACATCGCCATTAAATGGTGGTT
193	AGGCGGTCATTAGTCTTTAATGCGCAATATTA
194	GCCACGCTATACGTGGCACAGACAACGCTCAT
195	CTAAAGCAAGATAGAACCCTTCTGAATCGTCT
196	AAACCCTCACCAGTAATAAAAGGGATTACACAGTCACACG
197	TATCAGGGCGGTTTGCGTATTGGGAACGCGCG
198	TGGACTCCCTTTTCACCAGTGAGACCTGTCGT
199	AGTTTGGAGCCCTTCACCGCCTGGTTGCGCTC
200	GAATAGCCGCAAGCGGTCCACGCTCCTAATGA

201	CCGAAATCCGAAAATCCTGTTTGAAATACCGA
202	TAGCCCTACCAGCAGAAGATAAAAACATTTGA
203	GAATGGCTAGTATTAACACCGCCTCAACTAAT
204	GCGTAAGAGAGAGCCAGCAGCAAAAAGGTTAT
205	GCCAACAGTCACCTTGCTGAACCTGTTGGCAA
206	CGATGGCCCACTACGTAAACCGTC
207	ACCCAAATCAAGTTTTTTGGGGTCAAAGAACG
208	GTAAAGCACTAAATCGGAACCCTAGTTGTTCC
209	CCCCGATTTAGAGCTTGACGGGGAAATCAAAA
210	GAACGTGGCGAGAAAGGAAGGGAACAACTAT
211	CGGCCTTGCTGGTAATATCCAGAACGAACTGA
212	CCGCCAGCCATTGCAACAGGAAAAATATTTTT
213	GGAAATACCTACATTTTGACGCTCACCTGAAA
214	GAAATGGATTATTTACATTGGCAGACATTCTG

Table 2: Sequences of edge staple strands (edge A) for DNA origami

Name	Sequence (5' to 3')
Edge 19	CAGCGAAATTTTTTTTAACTTTCAACAGTTTCTGGGATTTTGC TAAACTTTTT
Edge 37	ACGGTCAATTTTTTTTTTTGACAGCATCGGAACGAACCCTCAG
Edge 54	GGACGTTGTTTTTTTTTTTCATAAGGGAACCGAAAGGCGCAG
Edge71	TAAATATTTTTTTTTTGAAGAAAAATCTACGACCAGTCA
Edge 89	ATATAATGTTTTTTTTTCATTGAATCCCCCTCAAATCGTCA
Edge 107	GCTAAATCTTTTTTTTTTTCTGTAGCTCAACATGTATTGCTGA
Edge 125	AGAGAATCTTTTTTGGTTGTACCAAAAACAAGCATAAA
Edge 143	GATTGACCTTTTTTTTTTTGATGAACGGTAATCGTAGCAAACA
Edge 161	CACGACGTTTTTTTTTTTGTAAATGGGATAGGTCAAAACGGCG

Edge 179	GGGAGAGGTTTTTTTTTTTGTAAAACGACGGCCATTCCCAGT
Edge 197	TATCAGGGTTTTTTTCGGTTTGCCTATTGGGAACGCGCG
Edge 206	TTTTTTTCGATGGCCCACTACGTAAACCGTC

Table 3: Sequences of edge staple strands (edge B) for DNA origami

Name	Sequence (5' to 3')
Edge 10	TTTTTTTTTTTATAAGTATAGCCCGGCCGTCGAG
Edge 18	AGGGTTGATTTTTTATAAATCCTCATTAAATGATATTC
Edge 36	ACAAACAATTTTTTTTTTTAATCAGTAGCGACAGATCGATAGC
Edge53	AGCACCGTTTTTTTTTTTAAAGGTGGCAACATAGTAGAAAA
Edge70	TACATACATTTTTTTTTTTGACGGGAGAATTAACACTACAGGGAA
Edge88	GCGCATTATTTTTTTTTTTTGCTTATCCGGTATTCTAAATCAGA
Edge106	TATAGAAGTTTTTTTTTTTCGACAAAAGGTAAAGTAGAGAATA
Edge124	TAAAGTACTTTTTTCGCGAGAAAACCTTTTTATCGCAAG
Edge142	ACAAAGAATTTTTTTTATTAATTACATTTAACACATCAAG
Edge160	AAAACAAATTTTTTTTTTTTCATCAATATAATCCTATCAGAT
Edge178	GATGGCAATTTTTTTTTTTTAATCAATATCTGGTCACAAATATC
Edge196	AAACCTCTTTTTTTTTTTTACCAGTAATAAAAGGGATTACCA GTCACACGTTTTT

Table 4: Sequence for thiol labeled DNA

Name	Sequence (5' to 3')
Thiol labeled DNA	5'Thiol-CGTCGTATTCGATAGCTTAG

List of publications:**Included in thesis:**

1. **Gagandeep Kaur**, Swati Tanwar, Vishaldeep Kaur, Rathindranath Biswas, Sangeeta Saini, Krishna Kanta Haldar, and Tapasi Sen “Interfacial design of gold/silver core-shell nanostars for plasmon-enhanced photocatalytic coupling of 4-aminothiophenol” *Journal of Materials Chemistry C* 2021, 9 (42), 15284-15294.
2. **Gagandeep Kaur**, Rathindranath Biswas, Krishna Kanta Haldar, and Tapasi Sen “DNA Origami-templated Bimetallic Core-shell Nanostructures for Enhanced Oxygen Evolution Reaction” *The Journal of Physical Chemistry C* 2022, 126 (16), 6915-6924.
3. **Gagandeep Kaur**, Vishaldeep Kaur, Navneet Kaur, Charanleen Kaur, Asifkhan Shanavas, and Tapasi Sen, “Design of silica@gold hybrid nanostars for enhanced SERS and photothermal effect”. **(Revised manuscript submitted)**
4. **Gagandeep Kaur**, Rathindranath Biswas, Krishna Kanta Haldar, and Tapasi Sen “Design of Au@ZnO plasmonic & semiconductor hybrid nanopetal shaped structures for photochemical water splitting”. **(Manuscript to be communicated)**

Not included in thesis:

5. Vishaldeep Kaur, Swati Tanwar, **Gagandeep Kaur**, and Tapasi Sen “DNA-Origami-Based Assembly of Au@Ag Nanostar Dimer Nanoantennas for Label-Free Sensing of Pyocyanin” *ChemPhysChem* 2021, 22 (2), 160-167.
6. Swati Tanwar, Vishaldeep Kaur, **Gagandeep Kaur**, and Tapasi Sen “Broadband SERS Enhancement by DNA Origami Assembled Bimetallic Nanoantennas with Label-Free Single Protein Sensing” *The Journal of Physical Chemistry Letters* 2021, 12 (33), 8141-8150.
7. Rathindranath Biswas, Pooja Thakur, **Gagandeep Kaur**, Shubham Som, Monochura Saha, Vandna Jhahria, Harjinder Singh, Imtiaz Ahmed, Biplab Banerjee, Deepak Chopra, Tapasi Sen, and Krishna Kanta Haldar “Interfacial Engineering of CuCo₂S₄/g-C₃N₄ Hybrid Nanorods for Efficient Oxygen Evolution Reaction” *Inorganic Chemistry* 2021, 60 (16), 12355-12366.
8. Charanleen Kaur, **Gagandeep Kaur**, Shikha Rai, Tapasi Sen “Gold core-silver shell nanobipyramids: efficient candidate for plasmon enhanced C-B bond cleavage” **(Manuscript to be communicated)**

Conferences

1. “Design of hybrid plasmonic nanostructures for enhanced photocatalytic activity” **Gagandeep Kaur**, and Tapasi Sen, poster presentation delivered at “**Chem@Nano’22**” (27th August, 2022) organized by INST Mohali, India.
2. “Design of hybrid plasmonic nanostructures for enhanced catalytic activity” **Gagandeep Kaur**, and Tapasi Sen, poster presentation delivered at “**2nd Research Scholar’s Day 2022**” (31th March, 2022) organized by INST Mohali, India.
3. “Design of hybrid plasmonic nanostructures for enhanced catalytic activity” **Gagandeep Kaur**, and Tapasi Sen, poster presentation delivered at “**INST-CSIR-CSIO 1st Bilateral Meeting 2022**” (25th March, 2022) organized by INST Mohali, India.
4. “Design of hybrid plasmonic nanostructures for enhanced catalytic activity” **Gagandeep Kaur**, and Tapasi Sen, poster presentation delivered at “**INST-IISER 1st Bilateral Meeting 2022**” (15th March, 2022) organized by INST Mohali, India.
5. “Design of hybrid plasmonic nanostructures for enhanced catalytic activity” **Gagandeep Kaur**, and Tapasi Sen, poster presentation delivered at “**Nanoday 2021**” (31th December, 2021) organized by INST Mohali, India.
6. “Design of hybrid plasmonic nanostructures for sensing and photocatalysis applications” Vishaldeep Kaur, **Gagandeep Kaur**, and Tapasi Sen, poster presentation delivered at “**1st Research Scholar’s Day 2021**” (26th February, 2021) organized by INST Mohali, India.
7. “Design of bimetallic and core-shell plasmonic nanostructures for enhanced photocatalytic activity” **Gagandeep Kaur**, Swati Tanwar, and Tapasi Sen, poster presentation delivered at “**ICONSAT (International Conference on Nano Science and Technology) 2020**” (5th - 7th March 2020), organized by S. N. Bose National Centre for Basic Sciences, Kolkata, India.
8. “Design of bimetallic and core-shell plasmonic nanostructures for enhanced photocatalytic activity” **Gagandeep Kaur**, and Tapasi Sen, poster presentation delivered at “**1st CRIKC Chemistry Symposium 2019**” (9th - 10th November 2019), organized by IISER Mohali, India.

Gagandeep Kaur

Ph.D. Research Scholar

Institute of Nanoscience and Technology

& Indian Institute of Science Education and Research,

Mohali (Punjab), India



Gagandeep Kaur completed her Bachelor's degree in Chemistry in 2014 and her Master's degree in Inorganic Chemistry in 2016 from the Department of Chemistry, Panjab University Chandigarh. In January 2018 she joined Institute of Nanoscience and Technology as a Ph.D. research scholar under the guidance of Dr. Tapasi Sen. She published a number of articles based on her research and presented her research work at a number of conferences on both national and international level. Her research interest includes the synthesis and design of hybrid plasmonic metal nanostructures for their enhanced photocatalytic applications.





RightsLink



Home



Help ▾



Live Chat



Sign in



Create Account

DNA Origami-Templated Bimetallic Core-Shell Nanostructures for Enhanced Oxygen Evolution Reaction



Author: Gagandeep Kaur, Rathindranath Biswas, Krishna Kanta Halder, et al

Publication: The Journal of Physical Chemistry C

Publisher: American Chemical Society

Date: Apr 1, 2022

Copyright © 2022, American Chemical Society

PERMISSION/LICENSE IS GRANTED FOR YOUR ORDER AT NO CHARGE

This type of permission/license, instead of the standard Terms and Conditions, is sent to you because no fee is being charged for your order. Please note the following:

- Permission is granted for your request in both print and electronic formats, and translations.
- If figures and/or tables were requested, they may be adapted or used in part.
- Please print this page for your records and send a copy of it to your publisher/graduate school.
- Appropriate credit for the requested material should be given as follows: "Reprinted (adapted) with permission from {COMPLETE REFERENCE CITATION}. Copyright {YEAR} American Chemical Society." Insert appropriate information in place of the capitalized words.
- One-time permission is granted only for the use specified in your RightsLink request. No additional uses are granted (such as derivative works or other editions). For any uses, please submit a new request.

If credit is given to another source for the material you requested from RightsLink, permission must be obtained from that source.

[BACK](#)[CLOSE WINDOW](#)